ABSTRACT

Title of dissertation: CRITICAL EVALUATION AND DEVELOPMENT OF ONE-EQUATION NEAR-WALL TURBULENCE MODELS

Ricardo Heinrich Diaz, Doctor of Philosophy, 2003

Dissertation directed by: Professor Jewel B. Barlow
Department of Aerospace Engineering

A systematic evaluation of one-equation near-wall turbulence models is completed and a new model is developed. The study includes five one-equation near-wall models and one two-equation model such that the performance of the one-equation models can be viewed in context of the performance of this more widely used class of models.

It is found that the majority of one-equation near-wall models do not reproduce the variation of the Reynolds shear stress near the wall, do not reproduce the dissipation at the wall, and do not predict the dissipation well in the region near the wall for a boundary layer flow. The new model is found to provide improved performance for the boundary layer and a wavy-wall channel. Specifically, it is found that the new model predicts the turbulent kinetic energy and dissipation in closer agreement with direct numerical simulation data than existing one-equation models for the boundary layer and

provides improved predictions of the shear stress distribution for the wavy-wall channel.

It is found that the one-equation near-wall models generally predict the shear stress distribution for the wavy-wall channel with greater accuracy than the two-equation model. In addition, it is shown that computations using the one-equation models are less sensitive to wall spacing than those using the two-equation model. This suggests that one-equation near-wall models, and in particular the new model, are ideal for engineering computations of practical flows where computational expense may be a significant factor entering into the choice of turbulence model.

CRITICAL EVALUATION AND DEVELOPMENT

OF ONE-EQUATION NEAR-WALL

TURBULENCE MODELS

by

Ricardo Heinrich Diaz

Dissertation submitted to the Faculty of the Graduate School of the
University of Maryland, College Park, in partial fulfillment
of the requirements for the degree of
Doctor of Philosophy
2003

Advisory Committee:

Professor Jewel B. Barlow, Chair
Professor John D. Anderson
Professor James D. Baeder
Professor Harland M. Glaz
Professor Allen E. Winkelmann

DEDICATION

To my family,

present and future.

ACKNOWLEDGMENTS

I thank Dr. J. B. Barlow for his support, advice, and guidance, without which I could not have completed this work. I learned a great deal through our many discussions over the years. I thank the National Science Foundation for providing financial support for my studies. I thank the examining committee for their support of my work. I thank my parents for their support and my father for his advice and encouragement. I thank the Xaverian Brothers for educating me in my early years. I would like to thank the Department of Aerospace Engineering for providing me with the opportunity to gain experience through teaching courses. I thank the San Diego Supercomputer Center for providing computational resources through two workshops that allowed me to extend my work. I would like to thank the staff and fellow students at the Glenn L. Martin Wind Tunnel for their support. Finally, I thank my oldest and closest friends for their support and encouragement.

TABLE OF CONTENTS

LIST OF TABLES

LIST OF FIGURES

LIST OF SYMBOLS

Latin

a_i	Coefficients for the finite volume method for node i
a_q	Coefficient of leading term of series expansion for quantity q
A_x, a_x	Modeling constant number x
B	Log-law additive constant
c_f	Skin friction coefficient defined as $c_f = 2\tau/\rho U^2$
c_{fo}	Predicted skin friction coefficient for the finest wall spacing
C_ε	Modeling constant for dissipation
C_p	Pressure coefficient defined by $C_p = 2(p-p_\infty)/\rho U^2$
C_μ	Modeling constant for the eddy viscosity for two-equation models
C_ν	Modeling constant for the eddy viscosity for one-equation models
C_1, C_2	Modeling constants for the dissipation equation
dy	Elemental length in the y direction
D_k	Viscous diffusion term for k
D_ε	Viscous diffusion term for ε
$e(c_f)$	Percent error in c_f with respect to c_f at finest wall spacing or DNS data
f_μ	Damping function for eddy viscosity
f_x	Modeling function number x
h	Channel height or step height for the backward-facing step

H	Shape factor defined as $H = \delta/\theta$ or channel height
k	turbulent kinetic energy defined by $k = \frac{1}{2}\overline{u_i' u_i'}$.
k-ε	The k-epsilon turbulence model
k^+	turbulent kinetic energy normalized by wall units given by $k^+ = k/u_\tau^2$
k-ω	The k-omega turbulence model
k-τ	The k-tau turbulence model
l	Length scale
l_μ	Length scale for eddy viscosity
l_ε	Length scale for dissipation
M	Number of grid points in the streamwise direction
N	Number of grid points in the wall-normal direction
n_{ab}	Exponent of leading term of series expansion for correlation $\overline{ab}$
p, P	Pressure or pressure normalized by dynamic pressure $\rho U^2/2$
p_o	Pressure at channel inlet
p_e	Pressure at channel exit
q	Flow quantity (u, v, p, k, or ε)
q_m	Flow quantity (u, v, p, k, or ε) predicted by the model
q_e	Flow quantity (u, v, p, k, or ε) given by DNS or experiment
P_x	Peclet number defined by $u\Delta x/\nu$ where Δx is grid spacing
P_k	Production of turbulent kinetic energy
P_ε	Production of dissipation rate
Re	Reynolds number defined as $Re = \rho Uc/\mu = Uc/\nu$

Re_b	Re based on bulk velocity given by $Re_b = U_b h/\nu$
Re_θ	Re based on momentum thickness given by $Re_\theta = U\theta/\nu$
Re_τ	Re based on friction velocity given by $Re_\tau = U_\tau h/\nu$
Re_x	Re based on distance x defined as $Re_x = Ux/\nu$
R_y	Turbulence Reynolds number defined as $R_y = k^{1/2}y/\nu$
R_T	Turbulence Reynolds number defined as $R_T = k^2/\nu\varepsilon$
s	Parameter delineating the edge of the near-wall boundary
S	Source term of a transport equation
S_x	Source term of a transport equation in direction x
S_{ij}	Fluid mean strain defined as $S_{ij} = (U_{i,j}+U_{j,i})/2$
t	Time or time-scale (also denoted by T)
T	Turbulence intensity given by $T = [(\overline{uu}+\overline{vv}+\overline{ww})/3]^{1/2}/U$
T_k	Turbulent transport term for k
T_s	Turbulence time scale
T_ε	Turbulent transport term for ε
u, U	Velocity (or normalized velocity) component in the x direction
u_τ	Friction velocity defined by $u_\tau = [\tau_w/\rho]^{1/2}$
u', u''	Fluctuating velocity in the x direction
$\overline{u}$	Time-averaged velocity in the x direction
$\tilde{u}$	Periodic fluctuation of velocity in the x direction
U^+	Velocity component in the x direction normalized by wall units

U^*	Uncorrected velocity or pseudo-velocity pertaining to projection method
U_∞	Freestream velocity
U_b	Bulk velocity
U_{max}	Maximum streamwise velocity
u_{rms}	Root mean square of fluctuating velocity in the x direction
$\overline{uu}^+$, $\overline{uu}$	Reynolds stress normalized by wall units
$\overline{uv}^+$, $\overline{uv}$	Reynolds shear stress normalized by wall units
v, V	Velocity (or normalized velocity) component in the y direction
v'	Fluctuating velocity in the y direction
v_s	Velocity scale usually taken to be $k^{1/2}$
v_{rms}	Root mean square of fluctuating velocity in the y direction
$\overline{vv}^+$, $\overline{vv}$	Reynolds stress normalized by wall units
w, W	Velocity (or normalized velocity) component in the z direction
w'	Fluctuating velocity in the z direction
w_{rms}	Root mean square of fluctuating velocity in the z direction
$\overline{ww}^+$, $\overline{ww}$	Reynolds stress normalized by wall units
x	Dimension in the streamwise direction
x^+	Dimension in the streamwise direction normalized by wall units
x_l	Laminar region of a boundary layer flow
x_s	Flow separation point
x_t	Turbulent flow region of a boundary layer flow

x_{tr}	Transition region or point of a boundary layer flow
x_r	Flow reattachment point
y	Dimension in the wall-normal direction
y^+	Dimension in the wall-normal direction normalized by wall units
z	Dimension in the spanwise direction
z^+	Dimension in the spanwise direction normalized by wall units

Greek

α	Wave amplitude for the wavy-wall channel
δ	Boundary layer thickness or wall spacing defined as $\Delta y Re$
δ^*	Boundary layer displacement thickness
δ_{ij}	Kronecker delta
$\Delta(q)$	Difference or error between predictions of q by two models
Δt	Time step
Δx	Elemental length in the x direction or grid spacing in the x direction
Δy	Elemental length in the y direction or grid spacing at the wall
ε	Dissipation rate of turbulent kinetic energy
ε^+	Dissipation rate normalized by wall units given by $\varepsilon^+ = \varepsilon\nu/u_\tau^4$
ζ	Coordinate in the spanwise direction
η	Coordinate in the wall-normal direction or $\eta = [U/(2\nu x)]^{1/2}$
θ	Boundary layer momentum thickness
κ	Kármán constant

λ	Wavelength for the wavy-wall channel
μ	Fluid viscosity coefficient
ν	Fluid kinematic viscosity defined by $\nu = \mu/\rho$
ν_t	Eddy viscosity or turbulence eddy viscosity
ξ	Coordinate in the streamwise direction
Π_k	Pressure-velocity term in turbulent kinetic energy equation
ρ	Fluid density
σ_ε	Prandtl number for dissipation equation
σ_k	Prandtl number for turbulent kinetic energy equation
τ	Time scale
Y	Destruction term for dissipation
ϕ	Transported scalar
ω	Specific dissipation

CHAPTER 1

1. Introduction

The introduction that follows is divided into five sections. The first section describes the background of analyzing fluid flows and the various levels of sophistication of solving the equations governing the flow of turbulent flows. The second section discusses previous work concerning near-wall turbulence modeling. The third section introduces the objectives of this study. The fourth section provides an overview of the methodology utilized to evaluate the near-wall turbulence models. The final section describes the organization of this document.

1.1 Background

Engineering studies of complex three-dimensional flows about aircraft, ground vehicles, and buildings that were once conducted almost exclusively by experimentation are now made routinely through computations using a variety of commercial codes. While complex potential flows and laminar flows can be solved relatively easily due to advances in numerical schemes and computational resources, complex turbulent flows resist accurate solution due primarily to the difficulties of accounting for the effects of the turbulence. The computation of such complex flows is of great value as a complement to traditional experimental studies [38]. Turbulence models tailored to match experimental results can be utilized to study the effects of perturbations of either geometry or flow

conditions. Details of the flow, that would be difficult to obtain experimentally due to either expense or the limitations of experimental measurements, can then be extracted easily from computations. What has developed in the engineering community is the simultaneous use of computational fluid dynamics and experimental studies [46]. Since the accuracy of these engineering computational studies is primarily a function of the turbulence models employed, there exits a need to continually develop new models and evaluate existing models at every level of model complexity [116]. The various methods available for the computation of turbulent flows are described briefly below.

Turbulent flows can be computed directly by solution of the Navier-Stokes, but the computational resources required to capture the finest details of the fluid motion scale with the Reynolds number cubed limiting such numerical solutions to Reynolds numbers far below those of interest to the designer [114]. Such computations are referred to as direct numerical simulations (DNS). A landmark DNS of a turbulent channel flow at a Reynolds number of 3300 required 4 million grid points and 250 hours to complete 22500 time steps on a computer that yielded a time per step per point of $1x10^{-7}$ seconds [77]. This simulation at a Reynolds number of a million would require $1x10^{14}$ grid points. To complete the simulation of this simple flow at a Reynolds number of one million in the same amount of time, a computer five orders of magnitude faster would be required. Direct numerical solution of the Navier-Stokes equations is therefore not considered feasible for the solution of practical engineering problems.

Turbulent flows may also be computed by resolving the largest scales of the turbulent motions while modeling the smaller more isotropic scales. This method is known as Large Eddy Simulations (LES). A filtering operation decomposes the velocity

into a resolved component and a residual subgrid-scale component. The filtered component is, unlike the traditional RANS methods, a function of time and represents the motions of the large scales in the flow. For this reason, LES can be expected to provide more accuracy than the RANS methods for unsteady flows that contain large scale unsteadiness such as the flow over a bluff body [116]. The equations of motion consist of the Navier-Stokes equations containing a residual stress tensor. The equations are often closed using an eddy-viscosity model [134]. Early LES simulations were carried out for various fluid flow studies in the 1960s and 1970s [134, 93, 37]. Interest in LES increased in the 1990s as computational costs decreased and new models were developed [115, 58]. The computational cost of LES is typically an order of magnitude less than DNS for wall bounded flows [114]. This computational cost therefore limits the regular use of LES for practical engineering problems.

Computational resources presently available limit engineering computations of turbulent flows of practical interest to solution of the Reynolds-averaged Navier-Stokes (RANS) equations for the mean flow, or time-averaged flow. The time-averaging of the Navier-Stokes equations, after substitution of a velocity field that is decomposed into a mean, periodic, and fluctuating component, gives rise to stress-like terms called the Reynolds stresses [22]. These stresses are due to the nonlinearity of the convective terms of the Navier-Stokes equations. To close the resulting equations, expressions for the Reynolds stresses must be provided. These expressions, generally empirical, constitute the turbulence model. One of the first practical turbulence models available for the closure of the RANS equations was the classic mixing-length model introduced in the 1920s [117]. Since the equations of motion are time averaged, RANS solutions are

typically steady state computations in which the effects of all scales of motions are modeled by the turbulence closure.

Turbulence models of various levels of sophistication have been developed over the past decades to close the Reynolds-averaged Navier-Stokes equations. A turbulence model can be classified as either an eddy viscosity model, a Reynolds stress transport model, or an intermediate model that contains elements of each of the former [54, 139]. The eddy viscosity models express the Reynolds stresses using relations similar to the stress-strain relation for a viscous fluid while the Reynolds stress transport models provide transport equations for each component of the Reynolds stresses. The eddy viscosity models require the input of a velocity scale, v, and a length scale, l. The velocity and length scales are often obtained from the turbulent kinetic energy, k, and a length scale determining quantity such as the dissipation, ε, or the specific dissipation, ω. The dissipation rate appears as a tensor quantity in the transport equations for the Reynolds stresses and therefore the intermediate models and Reynolds stress transport models require a model for the dissipation. Therefore, two distinct components to the modeling required to close the RANS equations can be identified. The first component consists of the modeling of the Reynolds stresses and the second component consists of the modeling of the scale quantities.

The hierarchy of models for the Reynolds stresses, in order of increasing sophistication, are the eddy viscosity models, algebraic stress models, and Reynolds stress transport models. The first level is broken into three groups. These groups include, in order of increasing sophistication, the Boussinesq model, the tensorial stress models, and the nonlinear models. Detailed descriptions of these models can be found in

references 22, 54, 139, and 153. The hierarchy of the models for the scale quantities can be divided into two levels. The first level consists of models based on a single time scale and the second level consists of models based on multiple time scales. The first level can be divided into three groups including the algebraic models, the one-equation models, and the two-equation models. It should be noted that these can also be formulated as models based on multiple time scales. Detailed descriptions of the models for the scale quantities can be found in references 22 and 153. The various models for the Reynolds stresses and scale quantities are described in further detail below.

Figure 1.1 below shows the hierarchy of the various models for the Reynolds stresses and provides example expressions for each level of modeling. The definitions of the many variables appearing in these expressions and the majority of the expressions can be found in references 22, 54, and 139.

The first level expresses the Reynolds stresses using the turbulent-viscosity hypothesis [17]. The turbulent-viscosity hypothesis implies that the Reynolds stresses can be expressed by a relation similar to the stress-strain relation for a viscous fluid. As stated above, this level consists of the Boussinesq model, the tensorial stress models, and the nonlinear models. The Boussinesq model is the most popular and simplest practical model for the Reynolds stresses. The tensorial stress model expresses the eddy viscosity as a tensorial quantity thereby relaxing the unjustifiable assumption of alignment between the principle axes of the Reynolds stresses and the mean strain implied by the Boussinesq model. Note that the relation shown in Figure 1.1 for the tensorial stress model expresses the Reynolds stresses in terms of a velocity and length scale rather than directly in terms of an eddy viscosity [54].

The nonlinear models include the quadratic stress models and explicit algebraic stress models [1, 92,138]. The nonlinear models express the Reynolds stresses using a nonlinear constitutive relation that can be viewed as an extension to the Boussinesq model. While these models can predict the anisotropy of the normal Reynolds stresses in simple flows such as the plane channel, they generally provide no modification of the relation used for Reynolds shear stress. These models cannot, for example, predict the nonzero Reynolds shear stress that occurs at the point of zero mean velocity gradient in the flow through a rough wall channel or the flow of a wall jet.

The second level consists of the algebraic stress models. The algebraic stress models (ASM) replace the Reynolds stress transport equations, described below, with algebraic relations that can be solved for the Reynolds stresses [120]. The usual assumption made in deriving the algebraic stress models is that the time rate of change and convection of the Reynolds stresses is proportional to the time rate of change and convection of the turbulence to the turbulent kinetic energy scaled by the ratio of the Reynolds stresses [22].

Neglecting the convection and diffusion terms results in a simplified form of the ASM [22]. The resulting algebraic relations for the Reynolds stresses are usually used with a two-equation model [22]. Unlike the Boussinesq relation, these are capable of reproducing the anisotropy of the Reynolds stresses in flows such as the plane channel, reproducing flow phenomenon such as the corner vortices in rectangular ducts [153], and can account for the effects of streamline curvature [22].

The third and highest level consists of the Reynolds stress transport models (RSM). Reynolds stress transport models, sometimes called second-order models or

simply Reynolds stress models, provide transport equations for each component of the Reynolds stresses. The Reynolds stress transport models are capable of accounting for the effects of the history of the flow upon the Reynolds stresses. Numerous Reynolds stress transport models have been introduced over the past two decades [33, 87, 120, 125]. In addition to accounting for history effects, the Reynolds stress transport models can account for streamline curvature, rotational effects, rapid distortions, strong pressure gradients, and anisotropy of the Reynolds stresses [22].

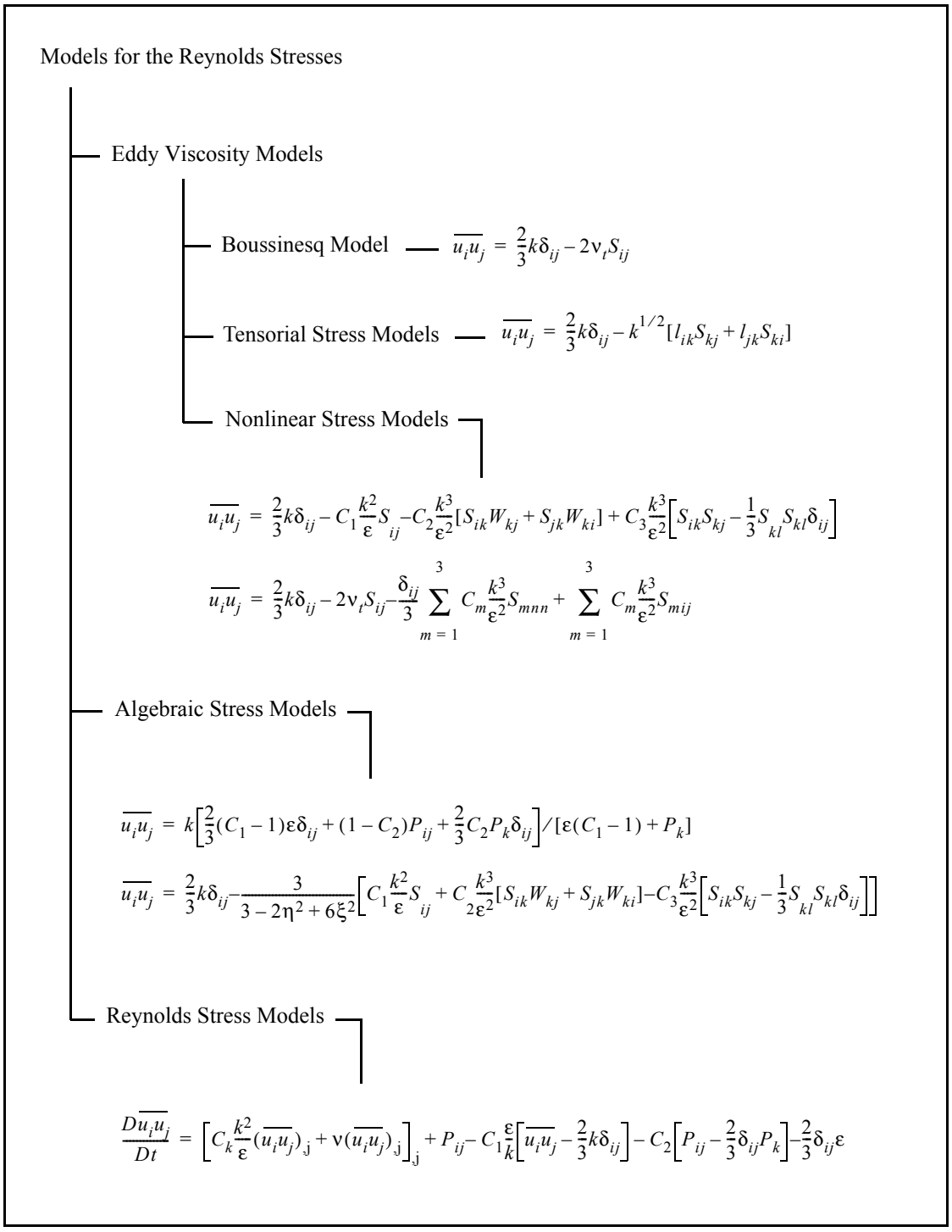

Figure 1.1: Hierarchy of models for the Reynolds stresses showing example expressions for each level of modeling.

While these models may provide improved predictions of the turbulence quantities over the less sophisticated models, the predicted skin friction and pressures are often very similar to those predicted by the simpler models [153]. In addition, the computational expense of solving the six partial differential equations needed by Reynolds stress transport models combined with the uncertainty in the modeling constants has made the Reynolds stress transport models far less popular for engineering computations than the eddy viscosity models. Even for flows two-dimensional in the mean, where only transport equations for the normal stresses and one shear stress component are required to close the RANS equations, Reynolds stress transport models have remained less popular than the eddy viscosity models. The dissipation rate, required by Reynolds stress transport models, is generally provided by the modeled dissipation equation of a two-equation model. This compounds the difficulties in justifying the use of Reynolds stress transport models for most engineering computations since the transport models currently in use for the dissipation rate contain more uncertainty in both the modeling of the individual budget terms and the associated constants than even those models in use for the transport of the Reynolds stresses [153].

Figure 1.2 shows the hierarchy of models for the scale quantities and provides example expressions for each level of modeling. The definitions of the many variables appearing in these expressions and majority of the expressions can be found in references 22 and 151.

The first level consists of models based on one time scale. As stated earlier, this level consists of the algebraic models, the one-equation models, and the two-equation

models. The algebraic models form the most basic means of obtaining a velocity and length scale. These provide an expression for an eddy viscosity using a velocity scale expressed algebraically in terms of the mean flow quantities and a length scale provided by the user or linked to geometrical considerations. The algebraic models include the classic mixing-length model [117], the Cebeci-Smith model [21], and the popular Baldwin-Lomax model [9]. The model shown in Figure 1.2 is the mixing-length model. While simple, these models are effective, efficient, and rarely cause numerical problems [151]. Furthermore, these can be easily modified to account for effects such as surface roughness and pressure gradients.

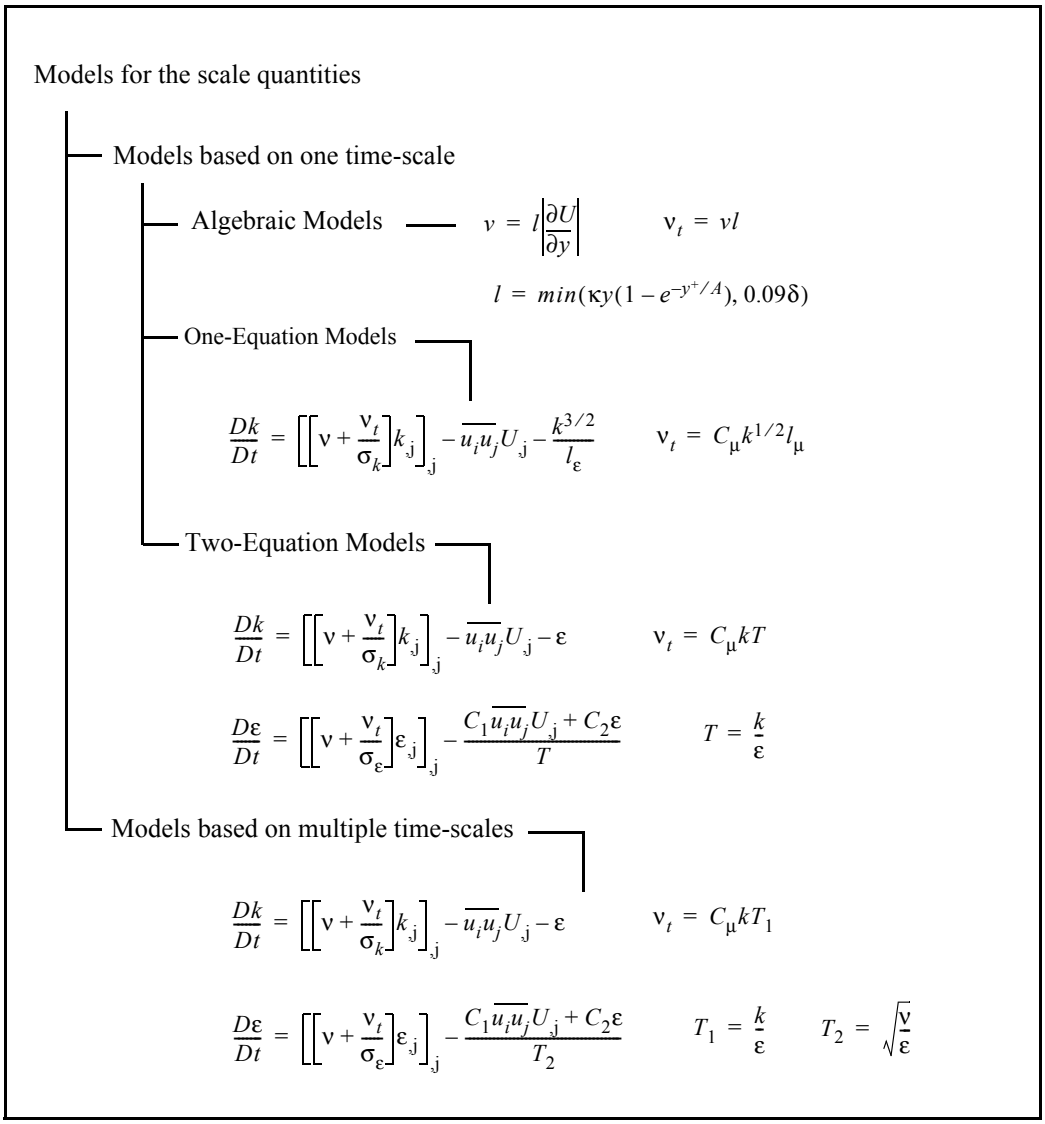

Figure 1.2: Hierarchy of models for the scale quantities showing example expressions for each level of modeling.

The second group of the first level consists of the one-equation models. These models typically provide a transport equation for the turbulent kinetic energy. The one-equation model, proposed in the 1940s, accounted for history effects on the turbulent

kinetic energy and was therefore considered an improvement over the algebraic models [118]. The first practical one-equation model and a one-equation model for the turbulent kinetic energy applicable to wall bounded flows were introduced two decades later [18, 154]. More recently, one-equation models based on transport equations for the eddy viscosity were introduced [8, 48, 101, 124, 137]. These models are considered simple to implement and rarely produce numerical difficulties [151]. Like the algebraic models, these models require that the length scale be either specified by the user or linked to geometrical considerations. The one-equation model provided in Figure 1.2 is similar to that of reference 118. The third group of the first level consists of the two-equation models. The algebraic and one-equation models are often called incomplete models since the user must specify a length scale distribution [153]. Two-equation models provide transport equations for both the turbulent kinetic energy and a length scale determining quantity, such as the dissipation, and therefore form the simplest complete models of turbulence [116]. The 1940s saw the introduction of an early two-equation model and a model based on the turbulent kinetic energy and the dissipation rate [29, 80]. The classic two-equation Jones-Launder k-ε model was introduced in the early 1970s [75, 89] . The k-ε model is considered the first practical turbulence model in which no length scale needed specification. It is the most popular turbulence model, is available in virtually all commercial CFD codes, and is considered to have the widest range of applicability of any turbulence model [116]. Two-equation models using the specific dissipation, ω, as the length-scale determining variable were also introduced [126]. The second most widely used two-equation model is the Wilcox k-ω model [152]. Recently, two-equation k-τ models based on the time scale τ have been developed [81] as well as two-equation k-ζ

models based on enstrophy ζ [4]. Being complete, the two-equation models offer the ability to predict such phenomenon as transition and relaminarization. The two-equation models used with the Boussinesq approximation cannot, however, capture the effects of streamline curvature without modification [143, 153]. These two-equation models utilize the same transport equation for the turbulent kinetic energy and differ primarily in the diffusion term appearing in the length-scale determining equation. This difference apparently becomes a significant factor affecting performance for nonhomogenous flows [116].

The second level consists of models based on more than one time scale. This level includes, for example, the two-time-scale Jaw-Chen k-ε model [72] in which the two time scales consist of the customary k/ε and the scale $\sqrt{\nu/\varepsilon}$. This model is based on the observation that the energy containing scales of motion take place at the scale k/ε and that the dissipating scales of motion take place at the scale $\sqrt{\nu/\varepsilon}$. The 1990s saw the introduction of other multi-time-scale models [22, 48, 156]. According to reference 22, a two time-scale k-ε model was capable of resolving the well known anomalous behavior of the standard k-ε model in which the predicted spreading rate of round jets is overestimated. The model shown in Figure 1.2, being based on only two time-scales, is among the simplest multi-time-scale models [22]. In general, multi-time-scale models utilize systems of transport equations representing the transport of the turbulent kinetic energy and dissipation at various scales of motion.

Engineering computations of external flows have traditionally been completed using either algebraic turbulence models such as the Baldwin-Lomax model [9] or a two-equation closure such as the k-ε model shown in Figure 1.2 above [151]. Internal flows

have traditionally been computed using the latter. In general, the eddy viscosity model for the Reynolds stresses shown in Figure 1.1, is utilized for these engineering computations. The eddy viscosity model is also refered to as the Boussinesq model [17]. Most commercial codes include several of the turbulence closures described above and thereby give the user a wide variety of models from which to choose. The models presented in Figures 1.1 and 1.2 above are formulated in a way appropriate for use far from no-slip surfaces and are therefore termed high Reynolds number models. These models must generally be modified for use near a no-slip surface. Since virtually all practical engineering problems include some no-slip surfaces, choosing a turbulence model involves not only selecting some combination of the models for the Reynolds stresses and scaling quantities, but also the selection of a near-wall model. The selection of a near wall model has often been circumvented by the use of wall functions. This, however, has fallen out of favor for engineering computations since the use of such functions may render the results grid dependent and therefore of questionable value [114, 116]. The practitioner of CFD generally has limited guidance with respect to how best to make such choices. Choosing a near-wall model has been identified as a constant source of difficulties and frustration to CFD users when attempting to predict practical flow problems [49].

1.2 Previous Work and Motivation

As mentioned above, the models described above are formulated in a way appropriate for use far from no-slip surfaces and must, in general, be modified for use near a no-slip surface. Very near a no-slip surface the molecular viscosity dominates the flow. The assumptions of isotropic dissipation and isotropic diffusion upon which most

high-Reynolds number models are based become questionable very near the wall [22]. The transport properties vary quickly near the wall requiring a relatively dense discretization to resolve the resulting gradients. The shear rate, for example, is a maximum at the wall. The no-slip surface suppresses the wall-normal component of the Reynolds shear stress such that it varies with distance to the fourth power whereas the other components vary with distance squared. The impermeability of the wall also affects the turbulence characteristics up to one integral scale away from the wall [116]. These effects require modification of the high-Reynolds number turbulence models described above. The primary problems with respect to near-wall modeling for the traditional two-equation models is that they require special treatment in the form of damping functions for application near solid walls, very fine grid spacing near the wall for grid independence [10], and are often difficult to integrate through the sublayer to the wall due to the stiffness of the dissipation equation [153]. While the basic form of the two-equation models has not changed significantly, near-wall treatments have been developed continuously as the availability of DNS data provided the needed variation of the turbulence quantites near the wall that make possible the detailed evaluation and development of near-wall turbulence models. A brief list of DNS and experimental data available for the evaluation of near-wall models is given in the section concerning methodology below. The various methods of applying the turbulence models to flows with no-slip surfaces include the wall functions mentioned earlier, two-equation near-wall models, and two-layer techniques that break the flow into regions in which various models are applied.

The development and evaluation of near-wall turbulence models often occurs in

tandem. Proposed models are evaluated to some degree by the developers. The evaluation in this case is often restricted to the standard benchmark flows including the flat plate turbulent boundary layer and the turbulent plane channel. More extensive evaluations are usually undertaken as a task separate from development [111, 128]. Such studies generally include the standard benchmarks as well as complex cases such as flow over a hill, flow past a backward facing step, or flow about an airfoil [1]. These studies also investigate the performance of the individual budget terms in the model [99] as well as the asymptotic behavior, or near-wall limiting behavior, of the model [135]. The majority of evaluations of near-wall models have concentrated on the two-equation near-wall models in which damping functions similar to the classic van Driest damping function [149] have been incorporated into the high-Reynolds number form of the transport equations to mimic the effects of the wall on the turbulence quantities. The evaluations of one-equation near-wall models have generally been made by the developers and thus extensive studies of this class of near-wall models have not been completed. Recent evaluations of a two-layer k-ε model and a two-layer k-τ model can be found in references 81 and 124. The previous work with near-wall treatments and near-wall models is described further below.

1.2.1 Wall Functions

Although rarely referred to as a near-wall model, wall functions are included here since they constitute a near-wall treatment available for the computation of wall bounded flows. Circumventing the need to resolve the near-wall flow, the outer flow has traditionally been bridged to the no-slip surface through the use of wall functions in which the turbulence statistics are expressed solely as a function of distance from the wall

and the friction velocity [151]. The use of wall functions avoids the need to solve the turbulence transport equations near the wall and eliminates the need for a fine mesh to resolve the high velocity gradients occurring in the wall layer. This method assumes that the convection and pressure gradient are negligible in the near-wall region and that flow in the near-wall region is in a state of equilibrium in which the production and dissipation of turbulent kinetic energy are in balance [151]. In many flows, such as those with strong pressure gradients, a law of the wall does not exist [3]. In a separated flow the friction velocity vanishes and is no longer an appropriate scale rendering the use of wall functions suspect. It has been suggested that wall functions can often drive the numerical solution more than the turbulence model [51] and, in cases of modest to strong pressure gradients, it may be impossible to obtain grid independent results [153]. It has also been suggested that grid independence may not be possible in general when using wall functions [116] and that the use of wall functions should be avoided even for engineering simulations [114]. Wall functions are often the only possible choice for practical engineering problems due to limits in computational resources and development of wall functions continues [7]. Wall functions based on wall-laws developed for flows with pressure gradients have been reported [66]. Wall functions can be viewed as artificial boundary conditions applied to the transport equations and will not be considered further in this work.

1.2.2 Two-Equation Near-Wall Model

The most common near-wall models currently in use include those in which the governing turbulence transport equations are modified, if necessary, so that they can be solved throughout the flow. These are referred to as two-equation near-wall models or,

more commonly, as low-Reynolds number models. These two terms are used interchangeably in this work. The most well known and first popular two-equation near-wall model is the standard Jone-Launder k-ε model mentioned earlier [75]. Others include those of references 26, 85, 88, and 57, and the Yang-Shih model used later in this work [157]. Two more recent two-equation near-wall models include those of references 68 and 112. In these models, additional modeling terms and variable constants are introduced into the transport equations for the turbulent kinetic energy and the dissipation to account for the effects of the wall and to provide asymptotic consistency as the wall is approached. The variable constants often take the form of damping functions similar to the Driest function applied to the production of dissipation and destruction of dissipation terms in the dissipation equation and to the relation for the eddy viscosity. Various expressions for these damping functions appear in the literature and a commonly referenced comprehensive review of what may be considered first generation models was completed in the mid-1980s [111]. That work demonstrated that the asymptotic behavior of the models available at the time was often inconsistent with the behavior of the damping function indicated by experimental data. Due to the lack of DNS data, the evaluation of the dissipation predicted very near the wall could not be made. A recent and comprehensive evaluation of near-wall models is provided in reference 128. There the performance was studied for several benchmark flows including the backward facing step [90]. It was concluded that models giving the correct asymptotic behavior of the turbulent kinetic energy and dissipation near the wall produced the most accurate predictions for all cases studied. The conclusion most relevent to this work was that models should be developed to give the correct near-wall limiting behavior. Those that

did not reproduce the near-wall limiting behavior did not perform as well in general [128].

The primary advantage to integration of the governing equations to the wall is that the assumptions made in deriving the law-of-the-wall, upon which wall functions are based, are removed. There is no assumption of equilibrium between the production and dissipation of turbulent kinetic energy, the effects of the pressure gradient, or the importance of turbulence transport. Two-equation near-wall models can provide a natural transition from laminar to turbulent flow and allow relaminarization The modeled budget terms of the turbulent kinetic energy equation are the turbulent diffusion, pressure diffusion, and the production of turbulent kinetic energy. These have been shown to agree well with DNS data for plane channel and boundary layer flows [99]. The dissipation equation includes eight budget terms, of which at least six require modeling, including the mixed production of dissipation, velocity gradient production, turbulent production, turbulent transport, pressure transport, and the destruction of dissipation. The modeled budget terms have been shown to be poorly predicted in the sublayer and buffer layer where y^+ is less than thirty [99].

The modeled dissipation equation of the Jones-Launder model is generally considered the weak link in the k-ε model [99, 153] and several researchers have attempted to improve it by adding additional modeling terms [135, 155, 157]. The dissipation equation is also stiff in the sublayer and integration to the wall often requires special treatment [153]. An evaluation of the Jones-Launder model using DNS data showed that the modeling of the dissipation equation near the wall was particularly poor [99]. A recent extensive evaluation of two-equation near-wall models showed that the

Wilcox k-ω model [152] and several popular k-ε models did not reproduce the trubulence quantities well near the wall [140]. Specifically, it was shown that the k-ω model did not yield the correct asymptotic variation of k near the wall for flat plate boundary layer flow, that most k-ε models yielded similarly poor results, and that the stiffness of the dissipation equation near the wall was due in part to the lack of additional terms needed to model the higher-order correlations that appear in the exact dissipation equation. Evaluations have also been completed for this class of models for flow over complex flows such as backward facing steps [144].

Newer two-equation near-wall k-ε models, such as that of reference 68, reproduce the variations of the turbulent kinetic energy, dissipation, and Reynolds shear stress well in the near-wall region. This model has also been shown to reproduce the budgets of the turbulent kinetic energy well in the near-wall region. Very recently, a two-equation near-wall model was used in conjunction with a Reynolds stress transport model forming a two-layer model [65].

1.2.3 One-Equation Near-Wall Model

An alternative to the two-equation near-wall models is the coupling of a high-Reynolds number two-equation model with a one-equation near-wall model. The flow is split into inner and outer regions delineated by, for example, the outer edge of the log-layer. The idea of using distinct expressions in the near-wall and outer regions is not new. The first such model to split the flow into two layers appears to have been the classic mixing-length model [117]. The turbulent kinetic energy equation, which has been shown to perform well near the wall, is solved throughout the flow. The dissipation is given by the standard transport equation far from the wall and algebraically as a

function of the turbulent kinetic energy and distance from the wall near the wall. In this case, the dissipation can be viewed as a modeled budget term of the turbulent kinetic energy equation. This method is commonly referred to as the two-layer technique [24, 123]. It has been shown recently that this technique can provide performance exceeding the two-equation near-wall models in flows subject to such affects as pressure gradients [22] and yet they have not been given the attention that the two-equation near-wall models have enjoyed. In addition, as shown in reference 10, one-equation models require less computational effort since they appear to require fewer grid points in the wall region in order to resolve the near-wall flow and obtain grid independent results. According to that study, a two-equation near-wall k-ε model required a wall spacing, Δy^+, of 0.5 to resolve the skin friction for flow over a flat plate to within 5% of the value given by a wall spacing approaching zero. The error in the skin friction predicted by the two-equation near-wall model approached 15% for wall spacings of 1.0. Very recently, there has been interest in developing two-equation models that do not require such fine wall spacings [120]. Computations leading to the study reported in this work indicated that the one-equation near-wall models are capable of resolving the skin friction coefficient for a flat plate to within 5% for wall spacings as great as 1.5. These computations are described in detail in Chapter 3. The ability to resolve flows with greater wall spacings makes the one-equation near-wall models particularly attractive for engineering computations. Furthermore, the two-layer method is attractive since it avoids the problematic stiffness of the dissipation equation near the wall, avoids the need to specify wall boundary conditions for the dissipation [135], circumvents near-wall budget modeling uncertainties in the dissipation equation [124], and is considered more robust

than integrating the dissipation equation to the wall [81].

The first one-equation model suitable for use as near-wall model for the dissipation was the Wolfshtein model (WS) [154]. The dissipation rate for WS was given by the standard relation for high Reynolds numbers, but modified with a Driest type damping function for application near no-slip surfaces. Other one-equation near wall models include the Norris-Reynolds model (NR) [108], used to study flows over wavy surfaces, and the Hassid-Poreh model (HP) [57]. An improved form of WS is the Chen-Patel model (CP) [24]. The Chen-Patel model provided constants that were modified to improve the asymptotic behavior, but the functional relationships of WS were maintained. It has been suggested that the correct velocity scale in the near wall layer was the wall normal Reynolds stress and not the turbulent kinetic energy [48]. A recent one-equation near wall model based on the use of the wall-normal Reynolds stress as the velocity scale is the Rodi-Mansour-Michelassi model (RM) [124]. This appears to be the first one-equation near-wall model reported to have been developed and evaluated using DNS data. A one-equation near-wall model formulated in terms of the time scale, τ, forms part of the two-layer k-τ of reference 81. Evaluations show that this model also reproduces the correct variation of τ near the wall. An evaluation of the Wolfshtein model and Norris-Reynolds model concluded that both overpredicted dissipation in the buffer layer of a boundary layer [122].

The one-equation models can be identified as traditional models and second generation models. The traditional models include those developed without DNS data. The second generation models include all those developed with the aid of DNS data. The second generation models therefore include RM and the new model presented later in this

work. The remaining are refered to as traditional models.

The chronological presentation of one-equation near-wall models given above is not intended to be a definitive registry. The number of entries of such a registry would depend upon defining the elements that constitute a distinct model. If modified constants alone constitute a new or distinct model, then the list of models would likely grow. For example, constants recommended in reference 69 for the Wolfshtein model different than those recommended in reference 24. Some consider these modified constants to constitute a distinct model [22]. As seen later, the results of the study of the one-equation near-wall models completed in this work will eliminate the need to consider models in which the constants alone have been modified.

These one-equation models are state-of-the-art and are commonly used in complex engineering simulations such as unsteady bluff body flows [82, 123], algebraic Reynolds stress model airfoil simulations [34], Reynolds stress model (RSM) airfoil simulations [35], Reynolds stress transport simulations of three dimensional boundary layers [94], simulations of flow through curved ducts [96], two-layer finite volume computations [103, 104], and other recent works [15, 23, 40, 81, 84, 158].

Despite the apparent advantages and growing popularity of these one-equation near-wall models, it does not appear that they have been studied systematically. The desire to quantify the difference between predictions made with the one-equation models in a systematic way has led to the present study.

1.3 Objectives

The objective of this study is to quantify the differences in performance of the one-equation near-wall turbulence models when utilized to compute two fundamental

benchmark flows for which direct numerical simulations and experiments exist. Several one-equation near-wall models, including a new model, are coupled with the standard k-ε model and applied using the two-layer method. The model constants of the new model are determined using DNS data. The performance of each near-wall model is evaluated by computing errors in the predicted quantities of interest with respect to the direct numerical simulation data throughout the flows and by computing metrics such as the predicted shape factor, Kármán constant, log-law additive constant, series expansion coefficients, and skin friction coefficient [10, 128]. In addition, the benchmark flows are computed using a two-equation near-wall model such that the performance of the one-equation near-wall models can be viewed in context of at least one member of this more popular class of near-wall models [128].

1.4 Evaluation Methodology

The evaluation of near-wall turbulence models can be separated into three parts consisting of the analysis of the limiting behavior of the models, the analysis of the model expressions or budget terms, and the evaluation of model predictions. The evaluation makes use of DNS data to form a baseline for comparison. A brief list of DNS and experimental data available for the evaluation of turbulence models is given in Table 1.1. Predictions of DNS are, of course, subject to numerical errors that can impact the accuracy of data derived from the simulation. It is believed, for instance, that the DNS for the boundary layer may suffer from slight numerical errors at the highest Re. This is used extensively to access model performance and is used in this work [129, 134, 165]. Differences can also be seen in the DNS of the wavy-wall channel of the two references indicated in the table. The DNS and the experiments, however, agree well in general.

Table 1.1: Benchmark flows available for the evaluation of turbulence models.

Flow	Type	Reference	Re_τ	Re_b	Comments
Channel	DNS	[77] 1986	180/395	3300/ 6875	Low Re
Channel	DNS	[85] 1999	180/395	3300/ 6990	Low Re
Channel	DNS	[106] 1999	590	10935	Moderate Re
Wavy Wall Channel	DNS	[25] 1998	171	60.4	Very low Re
Wavy Wall Channel	DNS	[99] 1996	N/A	3380	Moderate Re
Wavy Wall Channel	Exp.	[68] 1996	N/A	3380	Water tunnel experiment
Boundary Layer	DNS	[140] 1988	690-1410	N/A	Zero pressure gradient
Backward Facing Step	DNS	[92] 1992	NA	5100	Reattachment point of x/h=6

The first part of the evaluation is an analytical analysis of the limiting near-wall behavior of each model. The limiting behavior of the turbulence quantities is given by series expansions [128, 135]. In the case of one-equation near-wall models, the relevant quantities are the eddy viscosity, or Reynolds shear stress, and the dissipation. The limiting near-wall behavior of eddy viscosity and dissipation predicted by each model is determined analytically and compared to that given by the series expansions.

The second part is a comparison with the DNS data of the modeled eddy viscosity and dissipation computed using the exact turbulent kinetic energy [99]. The eddy viscosity and dissipation rate are computed for each near-wall model using the turbulent

kinetic energy given by the DNS data for a flat plate [136]. The modeled eddy viscosity and dissipation are compared to that given by the DNS data throughout the boundary layer. The variation of the Reynolds shear stress at the wall and the value of the dissipation at the wall are compared to the value given by the DNS data.

The third part of the evaluation requires computation of the benchmark flows using each turbulence model. Each model is evaluated by the computing a set of metrics that indicate the performance of the model. For the computation of the first benchmark problem, a flat plate turbulent boundary layer, the predicted values of the Kármán constant, log-law additive constant, skin friction coefficient, and shape factor are compared to those given by the DNS. The behavior of the predicted velocity, turbulent kinetic energy, dissipation rate, and turbulence shear stress in the near-wall region is compared to series expansions. Note that this provides an evaluation distinct from the second component since the turbulent kinetic energy will not, in general, match that given by the DNS. The total error is computed for each quantity and each model. For the computation of the second benchmark problem, a wavy-wall channel, the models are evaluated by computing the total error in the predicted velocity, turbulent kinetic energy, and turbulence shear stress with respect to the corresponding DNS data throughout the flow. The predicted separation point, reattachment point, and skin friction over the wavy wall, are compared to those given by the DNS. The error in the predicted skin friction coefficient is computed. In addition, for each benchmark case, the quantities of interest are compared qualitatively.

1.5 Organization of Dissertation

The transport equations for the mean flow and turbulence quantities are presented in Chapter 2. The numerical technique and validation of the projection method code are presented in Chapter 3. A description of the general characteristics of the benchmark flows and the associated performance metrics is given in Chapter 4. A brief description of the computation of each benchmark case, the results of the evaluation of the near-wall models, and the new model, are presented in Chapter 5. Concluding remarks are given in Chapter 6. In addition, an appendix provides further details and supplemental studies.

CHAPTER 2

2. Governing Equations and Formulation

The equations governing the incompressible flows investigated in this work, including the Reynolds-averaged Navier-Stokes equations, the continuity equation, the modeled transport equation for the turbulent kinetic energy, the modeled transport equation for the dissipation rate, and all associated algebraic equations, are presented in this chapter.

2.1 Governing Equations

The equations governing the flow of an incompressible fluid with constant transport properties are the Navier-Stokes equations,

$$u_{i,t} + u_j u_{i,j} = g_i - \frac{1}{\rho} p_{,i} + \nu u_{i,jj}, \tag{2.1}$$

and the continuity equation,

$$u_{i,i} = 0 . \tag{2.2}$$

The quantities u, g, ρ, p, and ν, are the fluid velocity, the acceleration due to gravity, the density, the pressure, and the kinematic coefficient of viscosity, respectively. Assuming unit density, neglecting body forces, and normalizing by U^2/c, where U is a reference velocity and c a characteristic length, the equations take the form

$$u_{i,t} + u_j u_{i,j} = -p_{,i} + \frac{1}{Re} u_{i,jj} . \tag{2.3}$$

The variables u and p are now taken to represent normalized values and Re is the Reynolds number defined as Uc/ν. If the reference velocity, U, and the characteristic length, c, are taken to be one, the quantities ν and $1/Re$ may be used interchangeably.

Exact solutions of the Navier-Stokes equations exist for only simple flows [151]. These flows have relatively simple geometries and occur at Reynolds numbers sufficiently low such that the flow remains laminar due to the suppression of unsteady fluctuations by the dissipative action of the fluid viscosity. Commonly cited exact solutions include Couette flow, Poiseulle flow, Stokes' first problem, Stokes' second problem, flow at a stagnation point, flow between concentric rotating cylinders, and flow over an infinite rotating disk [151]. At Reynolds numbers above some critical value, unsteady fluctuations in quantities such as the velocity appear due to the formation of small coherent structures in the flow called eddies. As the Reynolds number of a particular flow increases further, these turbulent fluctuations increase. Flows at sufficiently high Reynolds numbers, corresponding to those at which most practical engineering flow problems occur, are generally turbulent. As noted previously, resolution of all the scales of motion in such turbulent flows requires computational resources beyond those currently available for complex engineering analyses [114]. For this reason, the solution of practical engineering problems generally requires the solution of a filtered form of the Navier-Stokes equations coupled with a suitable model to account for the effects of the turbulence on the resolved quantities. Time-averaging of the Navier-Stokes equations is the most fundamental type of filtering and yields the classic Reynolds-averaged Navier-Stokes equations traditionally used to solve turbulent flow problems of practical interest in engineering. The Reynolds-averaged Navier-

Stokes equations are described in the section following.

2.1.1 Reynolds-averaged Navier-Stokes Equations

Seeking to resolve only the mean flow, the instantaneous flow quantities are decomposed into mean and fluctuating parts. For the velocity, this decomposition can be expressed as

$$u_i = \bar{u}_i + u'_i , \tag{2.4}$$

where the $\bar{u}$ represents the mean velocity and *u'* represents the turbulent fluctuation. The mean velocity is a time-average given by

$$\bar{u}_i = \frac{1}{T} \int_{t}^{t+T} u_i dt , \tag{2.5}$$

where T is a time period much greater than that of the turbulent fluctuations [22, 123, 151]. Substitution of the decomposed quantities into equation (2.3) and time-averaging yields the time-averaged Navier-Stokes equations,

$$U_j U_{i,j} = -P_{,i} + \frac{1}{Re} U_{i,jj} - (\overline{u_i u_j})_{,j} . \tag{2.6}$$

The overbar used to denote the averaged quantity is dropped so that the uppercase U and P now represent the mean velocity and pressure, respectively. The prime used to denote the turbulent fluctuation is dropped so that the lowercase u now represents the turbulent fluctuation. The last two terms result from the Reynolds stresses arising from the nonlinearity of the convection terms. The continuity equation remains unchanged in form so that

$$U_{i,i} = 0 . \tag{2.7}$$

For flows unsteady in the mean, such as flows about bluff bodies with large scale periodicity, a stochastic turbulent fluctuation u'' and a periodic fluctuation $\tilde{u}$ can be defined [105, 123]. A typical variation of u with time for such a flow is illustrated in Figure 2.1 below.

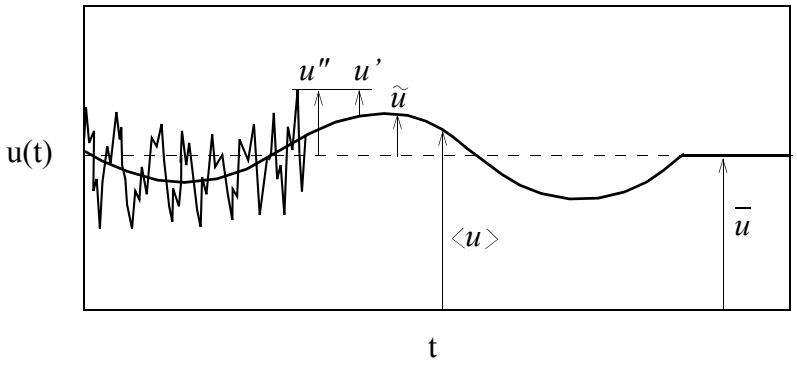

Figure 2.1: Fluctuations in a turbulent flow.

The quantity u'' represents the sum of the stochastic and periodic fluctuations. The quantity $\bar{u}$ is a long-time time-averaged value and the quantity $\langle u \rangle$ is a phase-averaged value. The relationships between the various quantities are

$$u'' = u' + \tilde{u} \tag{2.8}$$

and

$$u = \bar{u} + u'' = \bar{u} + \tilde{u} + u' = \langle u \rangle + u' . \tag{2.9}$$

Substitution of the above into the Navier-Stokes equations followed by phase averaging results in the phase-averaged form of the Navier-Stokes equations given by

$$\langle U \rangle_{i,t} + \langle U \rangle_j \langle U \rangle_{i,j} = - \langle P \rangle_{,i} + \frac{1}{Re} \langle U \rangle_{i,jj} - \langle u_i u_j \rangle_{,j} . \tag{2.10}$$

Here, the lowercase u has been replaced with an uppercase U and the primes are dropped on the turbulent fluctuation. The brackets represent the phase averaging to distinguish the phase-averaged form of the Navier-Stokes equations from the time-averaged form given earlier. The last term represents the Reynolds stresses. The phase-averaging of the Navier-Stokes equations constitutes a higher level of filtering than time-averaging and the resulting equations are commonly called the unsteady Reynolds-averaged Navier-Stokes equations (URANS) [53, 123, 151].

Note that unlike the traditional time-averaged Navier-Stokes equations, the phase-averaged Navier-Stokes equations retain a time derivative term. The time derivative is often included without making any distinction between the time-averaged and phase-averaged forms. Similarly, the term Reynolds-averaged Navier-Stokes equations is often used to describe both forms without distinction. In general, the Reynolds-averaged Navier-Stokes equations (RANS) can be written as

$$U_{i,t} + U_j U_{i,j} = -P_{,i} + \frac{1}{Re} U_{i,jj} - (\overline{u_i u_j})_{,j} \; . \tag{2.11}$$

The brackets have been dropped for convenience. Note that the brackets on the Reynolds stress terms are replaced by the overbar such that the equations take the traditional form most commonly seen in the literature [22, 116].

Equations (2.11) are not closed. An expression is required for the unknown Reynolds stress terms. Closure is obtained by introducing a model for the Reynolds stresses. Seeking such closure is the fundamental goal of turbulence modeling. Closure is traditionally achieved by expressing the Reynolds stresses in terms of mean flow quantities through the eddy viscosity model where the stresses are given in terms of an eddy viscosity [17]. The eddy viscosity is given by the a velocity scale and a length scale

determined from algebraic relations or model transport equations [75, 117]. These are described in the sections that follow.

2.1.2 Turbulence Transport Equations

A transport equation for the fluctuating velocity, obtained by subtracting the Reynolds-averaged Navier-Stokes equations from the instantaneous momentum equations [151], is given by

$$u_{i,t} + (U_j u_i)_{,j} = -p_{,i} + (\nu u_{i,j} + u_i u_j + \overline{u_i u_j})_{,j} - u_j U_{i,j} \ . \tag{2.12}$$

The continuity equation for the fluctuating velocity is given by

$$u_{i,i} = 0 . \tag{2.13}$$

Note that lowercase u represents the fluctuating velocity as in equation (2.4). Multiplication of equation (2.12) by u_j and addition with the same equation where i is replaced by j gives a transport equation for the turbulent kinetic energy

$$k_{,t} + (U_j k)_{,j} = -\overline{u_i u_j} U_{i,j} - \frac{1}{2}(\overline{u_i u_j u_k})_{,k} - (\overline{p u_k})_{,k} + \nu k_{,jj} - \nu \overline{u_{i,k} u_{j,k}} \ , \tag{2.14}$$

where k is defined as the trace of the Reynolds stresses given by

$$k = \frac{1}{2}\overline{u_i u_i} . \tag{2.15}$$

The turbulent kinetic energy equation can be written in compact form as

$$\frac{Dk}{Dt} = k_t + (U_j k)_{,j} = P_k + T_k + \Pi_k + D_k - \varepsilon \ . \tag{2.16}$$

The terms on the right hand side, referred to as budget terms, are the production term,

$$P_k = -\overline{u_i u_j} U_{i,j} , \tag{2.17}$$

the turbulent transport term,

$$T_k = -\left(\frac{1}{2}\overline{u_i u_i u_j}\right)_{,j}, \tag{2.18}$$

the viscous diffusion term,

$$D_k = \nu k_{,jj}, \tag{2.19}$$

the pressure-velocity term,

$$\Pi_k = -\left(\frac{1}{\rho}\overline{p u_j}\right)_{,j}, \tag{2.20}$$

and the dissipation rate,

$$\varepsilon = -\overline{\nu u_{i,j} u_{i,j}}. \tag{2.21}$$

Note that the pressure-velocity term vanishes for incompressible flow due to the divergence free constraint placed by the continuity equation. A concise description of each budget term shown above is provided in Table 2.1 below.

Table 2.1: Budget terms of the turbulent kinetic energy equation.

Budget Term	Symbol	Description
Production	P_k	Rate at which kinetic energy is transferred from the mean flow to the turbulence.
Turbulent transport	T_k	Rate of transport of k by turbulent fluctuations from high intensity to low intensity. Also called turbulent diffusion.
Diffusion	D_k	Rate of transport of k by molecular diffusion.
Pressure diffusion	Π_k	Rate of transport of k by pressure-velocity correlations from high intensity to low intensity. Also called pressure-velocity transport term.
Dissipation	ε	Rate at which k is converted into thermal internal energy.

Models based on the turbulent kinetic energy equation can account for nonlocal and history effects of the turbulence on the mean flow through an eddy viscosity. The turbulent kinetic energy equation eliminates the need to model the characteristic velocity scale in the classical mixing-length model [118]. The eddy viscosity is given by

$$\nu_t = C\sqrt{k}\, l, \tag{2.22}$$

where k is the turbulent kinetic energy, l is a length scale, and C is taken to be a constant of proportionality. The only budget term in the k equation requiring no modeling is the diffusion. The modeling required for the production term takes place when utilizing the model,

$$\overline{u_i u_j} = \frac{2}{3}k\delta_{ij} - 2\nu_t S_{ij}, \tag{2.23}$$

to express the Reynolds stresses [17]. The production is now a function of the mean quantities k, U, and ν_t. The eddy viscosity and Boussinesq approximation are described further in the section that follows.

A model of the dissipation can be developed by idealizing a turbulent eddy as a cylindrical structure moving through the turbulent flow at a known velocity of V [151]. The units of dissipation are work per unit time per unit mass, m, or equivalently, power per unit mass. The dissipation can therefore be expressed as

$$\varepsilon = \frac{F \cdot V}{m} = c\frac{k^{3/2}}{l}, \tag{2.24}$$

where F is the drag force on the eddy, k is the characteristic velocity, and l is the characteristic length. The constant of proportionality c results from the drag coefficient

of the idealized turbulent eddy. The dissipation can then be written as

$$\varepsilon = C_D \frac{k^{3/2}}{l}. \tag{2.25}$$

This form can also be derived by considering purely dimensional arguments [116]. The modeling constant C_D is approximately 0.8 in regions of the flow where the production of turbulent kinetic energy and corresponding dissipation rate are in dynamic equilibrium [151]. It is clear from the relation above that the dissipation increases as the length scale characterizing the turbulence decreases. This is consistent with the observation that the majority of the dissipation occurs at the high wave-numbers corresponding to the smallest scales of motion [62]. Using this relation, the eddy viscosity can be rewritten as

$$\nu_t = C_\mu \frac{k^2}{\varepsilon}, \tag{2.26}$$

where C_μ is taken to be a constant of 0.09 in regions of the flow where the production of turbulent kinetic energy and corresponding dissipation rate are in dynamic equilibrium [151].

To develop a model for turbulent diffusion, it is useful to consider the forms of expressing the diffusion of momentum, mass, and heat. For momentum diffusion in the Navier-Stokes equations, the shear stress is given by the gradient of the velocity or $\tau_{ij} \sim \mu \nabla U_i$. Fluids for which this linear gradient-diffusion hypothesis holds are called Newtonian fluids. For mass diffusion, the mass flux is a function of the gradient of concentration or $m_i \sim \alpha \nabla C$. For heat diffusion, the heat flux is given by the gradient of the temperature or $q_i \sim k \nabla T$. Considering the above, it seems reasonable to assume that for quantity q, the turbulent diffusion term in equation (2.18) can be written as [22]

$$-\overline{u_i q'} \sim \nu_e \nabla q \sim (C_k k^2/\varepsilon)\nabla q \ , \tag{2.27}$$

where ν_e is an eddy viscosity relating turbulent momentum diffusion to gradients of the turbulent kinetic energy k. The turbulent transport term can therefore be modeled as

$$T_k = -\left(\frac{1}{2}\overline{u_i u_i u_j}\right)_{,j} = \left(\frac{1}{2}\overline{k' u_j}\right)_{,j} = [\nu_e k_{,j}]_{,j} = \left[\frac{\nu_t}{\sigma_k} k_{,j}\right]_{,j} = \left[C_k \frac{k^2}{\varepsilon} k_{,j}\right]_{,j} \ , \tag{2.28}$$

where σ_k is a Prandtl number relating the eddy viscosity, ν_t, to the eddy viscosity, ν_e. This expression for the turbulent transport term is therefore consistent with the gradient-diffusion hypothesis and models the flow as locally isotropic. A model of anisotropic diffusion can be expressed as [22]

$$T_k = -\left(\frac{1}{2}\overline{u_i u_i u_j}\right)_{,j} = \left[C_k \overline{u_i^2} \frac{k}{\varepsilon} k_{,i}\right]_{,i} . \tag{2.29}$$

Since the pressure diffusion is generally very small for boundary layers and channel flows, it is often neglected in the modeling or lumped together with the turbulent transport and assumed to only affect the value of the Prandtl number σ_k [22]. The turbulent kinetic energy equation now takes the form

$$\frac{Dk}{Dt} = -\overline{u_i u_j} U_{i,j} + ((\nu + \nu_t/\sigma_k) k_{,j})_{,j} - \varepsilon \ . \tag{2.30}$$

This equation is used in virtually all turbulent kinetic energy models. Since all velocities, including the fluctuating velocities, are zero at a stationary wall, the turbulent kinetic energy vanishes at the wall giving a boundary condition of zero. The assumptions underlying the turbulent kinetic energy equation given in equation (2.30) are given in Table 2.2 below. Note that the first entry does not apply to incompressible flows since the pressure diffusion term vanishes due to the divergence free constraint.

Table 2.2: Modeling assumptions for the turbulent kinetic energy equation.

Modeling Assumptions
1. Pressure diffusion negligent or can be modeled with turbulent transport term.
2. Locally isotropic turbulence for turbulent transport term.
3. Turbulent transport behaves as a gradient-diffusion process.

The dissipation rate appears explicitly in the turbulent kinetic energy equation and was modeled algebraically above. Alternatively, a transport equation for the dissipation can be derived from the Navier-Stokes equation in a manner similar to that done for the turbulent kinetic energy equation. The exact equation is given by

$$\varepsilon_t + (U_j \varepsilon)_{,j} = P_\varepsilon + T_\varepsilon + \Pi_\varepsilon + D_\varepsilon - \Upsilon \, . \tag{2.31}$$

The first budget term is the production of dissipation given by

$$P_\varepsilon = -2\nu(\overline{u_{i,j}u_{k,j}} + \overline{u_{j,i}u_{j,k}})S_{ik} - 2\overline{\nu u_k u_{i,j}}U_{i,kj} \, , \tag{2.32}$$

where the first term is the production due to mean strain, the second is the production due to the velocity gradient, and the last is the turbulent production. The other budget terms are the turbulent transport (a turbulent diffusion term),

$$T_\varepsilon = -(\overline{u_i}\varepsilon)_{,i} \, , \tag{2.33}$$

the pressure transport (also a turbulent diffusion term),

$$\Pi_\varepsilon = -\frac{2\nu}{\rho}(\overline{p_{,j}u_{i,j}})_{,i} \, , \tag{2.34}$$

the viscous diffusion,

$$D_\varepsilon = \nu\varepsilon_{,jj}, \tag{2.35}$$

and the destruction of dissipation term,

$$\Upsilon = \overline{2\nu u_{i,jk}u_{i,jk}} + 2\nu\overline{u_{i,k}u_{i,j}u_{k,j}}. \tag{2.36}$$

The budget terms are described in the table below.

Table 2.3: Budget terms of the dissipation rate equation.

Budget Term	Symbol	Description
Production	P_ε	Rate of production of dissipation by the mean strain, velocity gradient, and turbulent fluctuations.
Turbulent Transport	T_ε	Rate of transport of dissipation by the turbulent fluctuations. Also called the turbulent diffusion.
Pressure Transport	Π_ε	Rate of transport of dissipation due to pressure-velocity correlations. Also called pressure diffusion.
Viscous Diffusion	D_ε	Rate of transport of dissipation due to molecular diffusion.
Destruction Term	Υ	Rate of destruction of dissipation or dissipation of dissipation.

The budget terms are modeled in a fashion similar to those of k. The turbulent transport and pressure transport terms are modeled together giving [22]

$$T = T_\varepsilon + \Pi_\varepsilon = \left[C_k\frac{k^2}{\varepsilon}\varepsilon_{,j}\right]_{,j} = \left[\frac{\nu_t}{\sigma_k}\varepsilon_{,j}\right]_{,j}. \tag{2.37}$$

This relation implies that the flow can be modeled as locally isotropic. For anisotropic flow, a more appropriate model might be given by [22]

$$T = \left[C_k\frac{k}{\varepsilon}\overline{u_ju_j}\varepsilon_{,j}\right]_{,j}. \tag{2.38}$$

The production term is

$$P_\varepsilon = -2\nu(\overline{u_{i,j}u_{k,j}} + \overline{u_{j,i}u_{j,k}})S_{ik} - 2\overline{\nu u_k u_{i,m}}U_{i,km} - 2\nu\overline{u_{i,k}u_{i,m}u_{k,m}} \,. \tag{2.39}$$

If it is assumed that the velocity fluctuation and the gradient of the fluctuation are not as well correlated as the correlation of the gradients of the fluctuations themselves, then the last term is very small. This assumption is considered valid in flows such as the boundary layer and plane channel [22]. The production then becomes

$$\begin{aligned} P_\varepsilon = & -2\nu(\overline{u_{i,j}u_{k,j}} + \overline{u_{j,i}u_{j,k}})S_{ik} - 2\nu\overline{u_{i,k}u_{i,m}u_{k,m}} = \\ & -2\nu(\overline{u_{k,i}u_{k,j}} + \overline{u_{i,k}u_{j,k}})U_{i,j} - 2\nu\overline{u_{i,k}u_{i,m}u_{k,m}} \end{aligned} \,. \tag{2.40}$$

For incompressible flow, the first term vanishes if i equals j. On the other hand, if i is not equal to j, then the term in brackets vanishes since the dissipation is, by definition as a scalar, implicitly assumed to be isotropic. Then only the last term contributes to the production of dissipation. The turbulent production term is then assumed to be proportional to the production of k divided by the appropriate time scale giving

$$P_\varepsilon = -2\nu\overline{u_{i,k}u_{i,m}u_{k,m}} = -C_1\frac{P_k}{T} = -C_1\frac{\overline{u_i u_j}U_{i,j}}{T}, \tag{2.41}$$

where C_1 is a constant taken to be 1.44. If the time scale of dissipation is taken to be the k-ε scale k/ε then

$$P_\varepsilon = -C_1\overline{u_i u_j}U_{i,j}\frac{\varepsilon}{k}. \tag{2.42}$$

The destruction term is the dissipation of dissipation. It should be noted that the ratio k/ε is generally considered to be the time scale of the large scale motions. Since the dissipation occurs mostly at high wave-numbers, it has been suggested that the time-scale $(\nu/\varepsilon)^{1/2}$ should be used in modeling the production of dissipation [22]. If the time scale of dissipation is small, then the destruction will be greater. If the time scale is large, then

the destruction will be smaller. Therefore, the destruction can be modeled as being proportional to the dissipation divided by the time scale giving

$$\Upsilon = -\overline{2\nu u_{i,jk} u_{i,jk}} = -C_2 \frac{\varepsilon}{T}. \tag{2.43}$$

If the time scale is again taken to be k/ε then

$$\Upsilon = -C_2 \frac{\varepsilon^2}{k}. \tag{2.44}$$

The modeled equation is then given by

$$\frac{D\varepsilon}{Dt} = -C_1 \overline{u_i u_j} U_{i,j} \frac{\varepsilon}{k} + ((\nu + \nu_t / \sigma_\varepsilon)\varepsilon_{,j})_{,j} - C_2 \frac{\varepsilon^2}{k}. \tag{2.45}$$

Despite the term-by-term modeling above, the relationship between the exact dissipation equation and its modeled form is considered very distant [152]. For example, some claim that the production due to the mean strain is not zero, but should be modeled as [55]

$$P_s = (-2\nu(\overline{u_{i,j} u_{k,j}} - \overline{u_{j,i} u_{j,k}}) S_{ik}) = -C_1 \frac{\varepsilon}{k} \overline{u_i u_j} + C_1^* \varepsilon \delta_{ij} U_{i,j} = -C_1 \frac{\varepsilon}{k} \overline{u_i u_j} U_{i,j} \tag{2.46}$$

and that the triple correlation and destruction can be modeled together giving

$$P_t + \Upsilon = -2\nu[\overline{u_{i,k} u_{i,m} u_{k,m}} + \overline{u_{i,jk} u_{i,jk}}] = -C_2 \frac{\varepsilon^2}{k}. \tag{2.47}$$

Yet another argument assumes that since dissipation must be conserved if the production and dissipation of k are in local equilibrium, then if there is any nonequilibrium effect, the influence should be proportional to the difference between the production and destruction. The turbulent production and the destruction can therefore be modeled together leading to both of the modeled terms for the production and destruction. Regardless of the modeling assumptions made above, the final form of the dissipation

equation does not change.

The assumptions underlying the dissipation rate equation are given in Table 2.4 below. Note that the first entry does not apply to incompressible flows since the pressure diffusion term vanishes due to the divergence free constraint.

Table 2.4: Modeling assumptions for the dissipation rate equation.

Modeling Assumptions
1. Pressure diffusion negligent or can be modeled with turbulent transport term.
2. Locally isotropic turbulence for turbulent transport term.
3. Turbulent transport behaves as a gradient-diffusion process.
4. The time scale for the desctruction is k/ε.
5. Turbulent production term is proportional to the production of k divided by the time scale k/ε.
6. Turbulent transport and pressure transport can be modeled together.

The modeled dissipation equation remains only distantly related to its exact form. For this reason, the dissipation model is not considered reliable, especially near the wall, and is often called the weak link in the two-equation models [152]. It is in part for this reason that there has been renewed interest in replacing the dissipation equation with one-equation models for application near walls [15, 34, 35, 40, 81, 82, 94, 96, 103, 123, 158].

In summary, the turbulent kinetic energy equation is modeled by

$$\frac{Dk}{Dt} = ((\nu + \frac{\nu_t}{\sigma_k})k_{,j})_{,j} - \overline{u_i u_j} U_{,j} - \varepsilon \quad . \tag{2.48}$$

The modeled dissipation equation is given by

$$\frac{D\varepsilon}{Dt} = ((\nu + \frac{\nu_t}{\sigma_\varepsilon})\varepsilon_{,j})_{,j} - \frac{C_1 \overline{u_i u_j} U_{,j} + C_2 \varepsilon}{T} \quad . \tag{2.49}$$

The constants σ_k and σ_ε are taken to be 1.0 and 1.3, respectively [75]. The time scale T is k/ε for this standard model. The dissipation equation is the length scale determining equation which, along with the turbulent kinetic energy equation, forms the simplest complete model of the turbulence [116, 153]. Equations (2.48) and (2.49) form the classic high-Reynolds number k-ε model.

2.1.3 Reynolds Stresses and Eddy Viscosity

The Reynolds stresses are traditionally modeled by the eddy viscosity model first presented in the section above. This eddy viscosity model, also called the Boussinesq model, was given by

$$\overline{u_i u_j} = \frac{2}{3}k\delta_{ij} - 2\nu_t S_{ij} \tag{2.50}$$

where k is the turbulent kinetic energy, δ_{ij} is the Kronecker delta function, ν_t is the eddy viscosity, and S_{ij} is the mean rate of shear given by

$$S_{ij} = \frac{1}{2}(U_{i,j} + U_{j,i}) \ . \tag{2.51}$$

The eddy viscosity model implies that the transfer of momentum due to turbulent fluctuations is analogous to the transfer of momentum by molecular motions. There is no clear physical basis for this assumption. The time scale of the turbulent motions is too great in general for such a direct relationship between the Reynolds stresses and the mean flow to be valid [116]. The Reynolds stresses cannot generally adapt to the mean flow sufficiently quickly for this model to hold. This is in direct contrast to the transfer of momentum by molecular motions where the time scale of the molecular motions is far less than that of the mean flow motions in all but cases involving rarified gases where the

mean free path of the molecules is very large. It is important to note that the molecular viscosity is a property of the fluid whereas the eddy viscosity is a property of the flow such that it will generally vary in space and time and may be a vectorial quantity in a flow that is three dimensional in the mean. The *2/3k* in equation (2.50) is required such that, in the absence of mean shear, the sum of the normal stresses is consistent with the definition of the turbulent kinetic energy and given by $2k$. The expression for the eddy viscosity depends on the closure chosen.

Examples of relatively simple flows in which the eddy viscosity model is known to produce erroneous results include the wall jet and the rough wall channel. In the former case, the model predicts a vanishing of the Reynolds shear stress where the mean flow has no velocity gradient in direct contrast to experimental observations. In the latter, the model fails to predict the non-zero Reynolds shear stress in a region of the flow where the mean flow velocity gradient is zero. A more complex case illustrating the shortcomings of the eddy viscosity model include the flow though a duct with a quadrilateral cross section. The model fails to predict the secondary flows arising in the corners of such a channel [138]. Never-the-less, despite the development of the implicit and explicit algebraic stress models [139, 1, 55] described in the first chapter, the eddy viscosity model remains the most common model used to express the Reynolds stresses and is utilized in most two-equation computations [22, 151].

A relation for the eddy viscosity was presented earlier as

$$\nu_t = C\sqrt{k}l \tag{2.52}$$

where C is a constant of proportionality and l is a length scale. This relation is utilized in one-equation models such as the turbulent kinetic energy model [118], and forms the

basis of most one-equation near-wall models. Substituting the relation for the dissipation given in the previous section, the eddy viscosity can be written as

$$\nu_t = C_\mu \frac{k^2}{\varepsilon} \tag{2.53}$$

where C_μ is 0.09. This relation is used by the standard k-ε model [75] and is utilized in this work for application far from no-slip surfaces.

This work, like the majority of work concerning turbulence modeling, is concerned with incompressible flows. For flows in which the effects of compressibility are significant, the equations of motion are generally written in terms of mass-weighted variables and an equation for the conservation of energy is added to the system [104]. The density naturally varies and, accordingly, the eddy viscosity model is written as

$$\bar{\rho}\widetilde{u_i u_j} = \frac{2}{3}(\mu_t U_{j,j} + \bar{\rho}k)\delta_{ij} - 2\mu_t S_{ij} \tag{2.54}$$

where $\bar{\rho}$ is the time-averaged density, μ is the fluid viscosity, and S_{ij} is the mean strain rate. The ε relation given by equation (2.25) remains unchanged in form and ν_t would be written as $\mu_t = C_\nu \bar{\rho} k^{1/2} l_\mu$. The eddy viscosity relation used by the two-equation model would be written as $\mu_t = C_\mu \bar{\rho} k^2/\varepsilon$. Further discussions concerning turbulence modeling for compressible flows can be found in references 74 and 156. The use of a one-equation near-wall model for computations of compressible flows can be found in reference 104.

2.1.4 Near-Wall Models

Turbulence models have traditionally been developed for high-Reynolds number flows which are, by definition, free of the effects of no-slip surfaces. Very near a no-slip surface the molecular viscosity dominates the flow. The assumptions of isotropic

dissipation and isotropic diffusion upon which most high-Reynolds number models are based become questionable very near the wall [22]. The transport properties vary quickly near the wall requiring a relatively dense discretization to resolve the resulting gradients. The shear rate, for example, is a maximum at the wall. The no-slip surface suppresses the wall-normal component of the Reynolds stress such that it varies with distance to the fourth power whereas the streamwise and spanwise components vary with distance squared. The impermeability of the wall also affects the turbulence characteristics up to one integral scale away from the wall [116]. These effects require modification of the high-Reynolds number k-ε model described above.

These effects of the no-slip surface are traditionally modeled by the introduction of van Driest like damping functions into the transport equations and the expression for the eddy viscosity. These modifications take two general forms for the k-ε models. If the k-ε equations are modified for application to the wall, the resulting model is called a two-equation near-wall model. If the dissipation equation is replaced by an algebraic relation near the wall, the resulting model is called a one-equation near-wall model. In this case, the k-ε equations are solved far from the wall and the k equation coupled with the algebraic relation for dissipation is solved near the wall. This is known as the two-layer approach [123]. These are described in detail below.

Before continuing with the discussion of near-wall models, it is important to define the regions of the boundary layer. The turbulent boundary layer, described in detail in Chapter 4, is a typically thin shear-layer made up of four distinct regions known as the sublayer, the buffer layer, the log-layer, and the outer layer. Viscosity dominates the motion in the sublayer closest to the wall while the Reynolds shear stress dominates

the motion in the log-layer far from the wall. The effects of the viscosity and Reynolds shear stress are of similar magnitude in the buffer layer. The sublayer is considered the region from the wall to y^+ of 5, the buffer layer is the region between y^+ of 5 and about 30, and the log-layer is the region between y^+ of 30 and 100, where y^+ is the wall unit given by

$$y^+ = y\frac{u_\tau}{\nu} \tag{2.55}$$

The friction velocity, u_τ, is given by the square root of the product of the density and the wall shear stress. The outer region beyond y^+ of 100 follows a velocity-defect law [151]. Near-wall modeling is generally concerned with the region where y^+ is less than 100. Beyond this value, the direct effects of the wall, such as the damping of the wall-normal Reynolds stress, diminish and the turbulence tends to become isotropic.

2.1.4.1 Two-Equation Near-Wall Models

As mentioned above, the modeled transport equation for the dissipation and the relations for the eddy viscosity given above cannot be applied near a no-slip surface. The time scale in the dissipation equation vanishes near the wall so that the production and destruction of dissipation terms do not vary correctly near the wall. The classic remedy is to introduce damping functions similar to the Driest function [149]. The dissipation equation becomes

$$\frac{D\varepsilon}{Dt} = ((\nu + \frac{\nu_t}{\sigma_\varepsilon})\varepsilon_{,j})_{,j} - f_{\varepsilon_1} C_1 \overline{u_i u_j} U_{,j} \frac{\varepsilon}{k} - f_{\varepsilon_2} C_2 \frac{\varepsilon^2}{k} \ . \tag{2.56}$$

Along with modeled turbulent kinetic energy equation, equation (2.48), this form constitutes a two-equation near-wall model. The prescription of the damping functions

vary according to specific model and can be found for several common two-equation near-wall models in [153]. A review and evaluation of the various damping functions can be found in reference 111.

A relatively recent two-equation near-wall model is the Yang-Shih model [157]. The dissipation equation for this two-equation near-wall model is given as

$$\frac{D\varepsilon}{Dt} = ((\nu + \frac{\nu_t}{\sigma_\varepsilon})\varepsilon_{,j})_{,j} - \frac{C_1\overline{u_i u_j}U_{,j} + C_2\varepsilon}{T} + 2\nu\nu_t U_{i,ij}^2 \,, \tag{2.57}$$

where

$$T = \frac{k}{\varepsilon} + \sqrt{\frac{\nu}{\varepsilon}} \tag{2.58}$$

is a composite time scale that incorporates the time scale of the highest wave-numbers given by the time scale $\sqrt{\nu/\varepsilon}$. The evaluation of reference 128 suggests that the Yang-Shih model is one of the best performing of the two-equation near-wall models. For this reason, this is the two-equation near-wall model chosen as a baseline with which to compare the performance of the one-equation near-wall models investigated in this work. An evaluation and review of related two-equation models can be found in reference 128.

The eddy viscosity predicted by equation (2.53) is too great near the wall. A damping function, f_μ, is introduced such that

$$\nu_t = C_\mu f_\mu \frac{k^2}{\varepsilon}. \tag{2.59}$$

Various expressions have been provided for the damping function f_μ [111, 128]. The proper variation of the damping functions is not independent of Reynolds number. It has been shown [99] that the damping functions calculated from the DNS data for the flat

plate [136] is different from that for the plane channel [77].

In addition to the weak relationship between the modeled and exact dissipation equation [153], the dissipation equation is stiff near the wall and thus difficult to integrate through the sublayer. This has prompted many to use a different set of transport equations for the length scale determining equation. The most common alternative is the k-ω model [153]. A less popular alternative is the two-equation the k-τ model [81]. The k-ω model has been shown to provide improved performance in adverse pressure gradients [153], but suffers from sensitivity to the value of the freestream length scale [10]. This limits the applicability and testing of the k-ω model for practical flows since the freestream length scale is often unknown even when detailed experimental studies have been completed. An increasingly popular approach is to avoid the integration of the dissipation equation to the wall by replacing the dissipation equation with an algebraic model in the near-wall region. This approach leads to the one-equation near-wall models described further below. Limitations of the k-ε model are given in Table 2.5 below.

Table 2.5: Limitations of the two-equation near-wall k-ε model.

Limitation
Damping functions are dependent on Reynolds number and flow type.
Difficult to integrate through sublayer due to stiffness of dissipation equation.
Dissipation equation requires ad-hoc modifications for application near the wall.

Due to the great variation among k-ε turbulence models, the advantages and limitations listed above are not universal. They are given as a general guide subject to

the particular formulation of the models. For example, the problematic near-wall stiffness of the dissipation equation can be eliminated by the choice of a time scale other than the k-ε scale. The two-equation near-wall Yang-Shih model [157] presented above alleviates the effects of the near-wall stiffness of the dissipation equation by utilizing a modified time scale for the modeled production and destruction terms of the dissipation equation.

2.1.4.2 One-Equation Near-Wall Models

The two-equation near-wall k-ε model, presented above, is included in this study since this class of near-wall models has remained the most popular currently in use [116]. An alternative to the use of the two-equation near-wall models is the coupling of a high-Reynolds number two-equation model such as the standard k-ε model presented in Section 2.1.2 with a one-equation model. The flow is split into inner and outer regions delineated by, for example, the outer edge of the log-layer. The idea of using distinct expressions in the near-wall and outer regions to form a multi-layer model is not new. The first practical turbulence model, the mixing-length model used in conjunction with the Driest dampng function [151], is essentially a two-layer model. For the one-equation near-wall models, the turbulent kinetic energy equation, that has been shown to perform well near the wall for simple flows [99], is solved throughout the flow. The dissipation is given by the standard transport equation, equation (2.45), far from the wall and algebraically as a function of the turbulent kinetic energy and distance from the no-slip surface near the wall. This relation, presented earlier, takes the form

$$\varepsilon = C_D \frac{k^{3/2}}{l_\varepsilon}. \tag{2.60}$$

Expressed as above, the dissipation can be viewed as a modeled budget term of the turbulent kinetic energy equation. This method of splitting the flow into two distinct layers is commonly referred to as the two-layer technique [24, 123]. It has been shown recently that the two-layer technique can provide performance exceeding that of the two-equation near-wall models in flows subject to such affects as pressure gradients [22] and yet the one-equation near-wall models used by the two-layer technique have not been given the attention that the two-equation models have enjoyed. In addition, as shown in reference 10, and verified in this work, one-equation models require less computational effort since they may require fewer grid points in the wall region in order to resolve the near-wall flow and obtain grid independent results. This makes the one-equation near-wall models particularly attractive for engineering computations that are often poorly resolved near the wall due to the taxing of computational resourses. This approach is further attractive since it avoids the problematic stiffness of the dissipation equation near the wall, avoids the need to specify conditions for the dissipation at the wall [135], circumvents near-wall budget modeling uncertainties in the dissipation equation, and is generally more robust than integrating the dissipation equation to the wall [81].

The first practical one-equation model suitable for use as a near-wall model for the dissipation was the Wolfshtein model [154]. The dissipation rate given by $C_D k^{3/2}/l$ was modified with a Driest type damping function for application near no-slip surfaces. The Wolfshtein model gives

$$\varepsilon = C_\varepsilon k^{3/2} / (y(1 - \exp(-A_\varepsilon R_y))) \tag{2.61}$$

where y is the distance from the no-slip surface and R_y is the turbulence Reynolds number defined by

$$R_y = \frac{\sqrt{k}y}{\nu}. \tag{2.62}$$

Once the dissipation is known, the eddy viscosity can be given by

$$\nu_t = C\sqrt{k}l \tag{2.63}$$

where l is a length scale. The Wolfshtein model gives

$$\nu_t = C_\nu \sqrt{k}y(1 - \exp(-A_\nu R_y)) \ . \tag{2.64}$$

The model constants, listed in Table 2.6, were chosen from experimental data. Note that, unlike damping functions utilizing wall units, such as the Driest function, this formulation is applicable to flows involving separation since the turbulence Reynolds number, unlike wall units, remains well defined in regions of flow reversal.

The one-equation near wall models investigated in this work include the Norris-Reynolds model used originally to study flows over wavy surfaces [108], the Hassid-Poreh model used to study drag reduction [57], the Chen-Patel model used to study flows over bodies of revolution [24], and the more recent Rodi-Mansour-Michelassi model [124]. The Chen-Patel model utilized the functional relationships of the Wolfshtein model, but used modified constants to give the correct asymptotic behavior. It has been suggested that the correct velocity scale in the near-wall region is the wall-normal Reynolds stress and not the turbulent kinetic energy [48]. The Rodi-Mansour-Michelassi model was apparently developed along these lines and seems to have been the first one-equation near-wall model to be developed using DNS data. For two-equation models using the eddy viscosity model, such as the standard k-ε model, a model for the wall-normal Reynolds stress must be provided since the variation of the Reynolds stresses given by the eddy viscosity model provides no anisotropy of the normal Reynolds

stresses in plane flow and thus gives a poor prediction of the wall-normal Reynolds stress. Therefore, within the frame-work of the two-equation models using the eddy viscosity model, replacing the turbulent kinetic energy with the wall-normal Reynolds stress in the relation for the dissipation reduces to a formality. The model is, however, well suited for use with Reynolds stress models provided that they reproduce the wall-normal Reynolds stress correctly. One-equation models have also been cast in terms of variables other than the quantities of k and ε. A one-equation near-wall model based on the transport equation for the time scale, τ, is the two-layer k-τ model of reference 81. Evaluation apparently showed that this model reproduces the correct variation of τ near the wall. A comparison of near-wall models was made for the Wolfshtein model and Norris-Reynolds model in reference 122. This study concluded that both models overpredicted dissipation in the buffer layer of a boundary layer. The listing of models here is not meant to serve as a definitive registry. The difficulty in compiling such a registry depends in part in the difficulty in defining the parameters that constitute a distinct model. If modified constants are sufficient to consititute a model, then the number of one-equation near-wall models may be greater than those listed here. For example, constants recommended in reference 69 for the Wolfshtein model are different from those recommended in reference 24 for the Chen-Patel model. Some consider this use of modified constants to constitute a distinct model.

These one-equation near-wall models are state-of-the-art and are commonly used in practical engineering simulations such as unsteady bluff body flows of reference 82 using the Chen-Patel model, the study of flow over a square cylinder using the Norris-Reynolds model of reference 123, Reynolds stress model (RSM) airfoil simulations [35],

algebraic Reynolds stress model (ARM) airfoil simulations [34], the implicit solution method of reference 81, RSM simulations of three dimensional boundary layers [94], RSM simulations of flow through curved ducts using the Chen-Patel model [96], two-layer finite volume computations for compressible flows using the Chen-Patel model [103, 104], and other very recent works [15, 40, 158].

The models for the dissipation and eddy viscosity utilized in this work are summarized in the table below. If used to close the turbulent kinetic energy equation and applied throughout the flow, they would form one-equation models. The models include those of Wolfshtein (WS), Norris-Reynolds (NR), Hassid-Poreh (HP), Chen-Patel (CP), and Rodi-Mansour-Michelassi (RM).

Table 2.6: Models for the dissipation and eddy viscosity.

Model	Relations	C_ε	C_ν	A_ε	A_ν
WS	$\varepsilon = C_\varepsilon k^{3/2}/(y(1-\exp(-A_\varepsilon R_y)))$ $\nu_t = C_\nu \sqrt{k} y(1-\exp(-A_\nu R_y))$	0.416	0.22	0.263	0.016
NR	$\varepsilon = C_\varepsilon \frac{k^{3/2}}{y}(1+A_\varepsilon/R_y)$ $\nu_t = C_\nu \sqrt{k} y(1-\exp(-A_\nu R_y))$	$\frac{C_\mu^{3/4}}{\kappa}$	$\kappa C_\mu^{1/4}$	5.3	0.0198
HP	$\varepsilon = 2(\nu + C_\varepsilon \nu_t)k/y^2$ $\nu_t = C_\nu \sqrt{k} y(1-\exp(-A_\nu R_y))$	0.945	0.22	NA	0.012
CP	$\varepsilon = C_\varepsilon k^{3/2}/(y(1-\exp(-A_\varepsilon R_y)))$ $\nu_t = C_\nu \sqrt{k} y(1-\exp(-A_\nu R_y))$	$\frac{C_\mu^{3/4}}{\kappa}$	$\kappa C_\mu^{1/4}$	$C_\varepsilon/2 =$ 0.1966	0.0143
RM	$\varepsilon = C_\varepsilon \frac{v_r k}{y}\left(1+2.12\frac{\nu}{v_r y}\right)$ $\nu_t = C_\nu v_r y \; v_r^2 = k(A_\varepsilon R_y + A_\nu R_y^2)$	0.769	0.33	$4\text{x}10^{-4}$	$4.65\text{x}10^{-5}$

The advantages and limitations of the one-equation near-wall models are listed in the tables below. The primary advantage of these models is that they encourage stable solutions with grid densities lower than those required for the two-equationnear-wall models. The primary limitation is that they apparently cannot model transition or relaminarization since the dissipation is determined directly by the magnitude of the turbulent kinetic energy.

Table 2.7: Advantages of the one-equation near-wall models.

Advantage
Provides grid-independent results with moderate grid density
Circumvents uncertainty of modeled dissipation equation

Table 2.8: Limitations of the one-equation near-wall models.

Limitation
No capability to model transition or relaminarization
Length scale damping functions show dependence on Reynolds number and flow type

The limitations and advantages above are given as a general guide subject to the particular formulation of the models.

The two-layer models can be summarized as follows. Define a quantity s that varies with distance from the wall. If $s > s_o$ the equations to be solved are

$$\frac{Dk}{Dt} = ((\nu + \frac{\nu_t}{\sigma_k})k_{,j})_{,j} - \overline{u_i u_j} U_{,j} - \varepsilon \ , \tag{2.65}$$

$$\frac{D\varepsilon}{Dt} = ((\nu + \frac{\nu_t}{\sigma_\varepsilon})\varepsilon_{,j})_{,j} - \frac{C_1 \overline{u_i u_j} U_{,j} + C_2 \varepsilon}{T} \ , \tag{2.66}$$

$$\nu_t = C_\mu k^2 / \varepsilon \, , \tag{2.67}$$

and

$$\overline{u_i u_j} = \frac{2}{3} k \delta_{ij} - 2\nu_t S_{ij} \tag{2.68}$$

These are the standard k-ε high Reynolds number turbulence transport equations [75]. If $s < s_o$ then the equations to be solved include equation (2.65) and equation (2.68) along with

$$\varepsilon = f(k, y) \tag{2.69}$$

and

$$\nu_t = g(k, y) \tag{2.70}$$

where f and g depend on the particular model given in Table 2.6.

For the majority of models investigated in this work, s is the turbulence Reynolds number,

$$R_y = \sqrt{k}y/\nu, \tag{2.71}$$

and the value of s_o is usually taken to be 250 [24, 122]. The turbulence Reynolds number typically rises monotonically throughout the log-layer of a boundary layer or plane channel flow. The point delineating the two regions must be chosen sufficiently far from the surface such that the eddy viscosity given by equation (70) is nearly equal to that given by equation (2.67) used in the outer region. This point corresponds to that at which the length scale is no longer damped and is given by a y^+ of approximately 100 or an R_y of approximately 250 [24, 122]. Of the models given in the table, only RM uses a lower value of s_o.

2.2 Concise Formulation

The set of equations to be solved in this work include the Reynolds-averaged Navier-Stokes equations,

$$U_{i,t} + U_j U_{i,j} = -P_{,i} + \frac{1}{Re} U_{i,jj} - (\overline{u_i u_j})_{,j} \,, \tag{2.72}$$

and the continuity equation,

$$U_{i,i} = 0 \,, \tag{2.73}$$

for all computations.

2.2.1 Two-Layer Models

For the two-layer computations the equations to be solved include the turbulent kinetic energy equation,

$$\frac{Dk}{Dt} = ((\nu + \frac{\nu_t}{\sigma_k})k_{,j})_{,j} - \overline{u_i u_j} U_{,j} - \varepsilon \,, \tag{2.74}$$

the dissipation equation in regions where $s > s_o$,

$$\frac{D\varepsilon}{Dt} = ((\nu + \frac{\nu_t}{\sigma_\varepsilon})\varepsilon_{,j})_{,j} - \frac{C_1 \overline{u_i u_j} U_{,j} + C_2 \varepsilon}{T} \,, \tag{2.75}$$

the algebraic relation for dissipation in regions where $s < s_o$,

$$\varepsilon = f(k, y) \,, \tag{2.76}$$

the relation in regions where $s > s_o$,

$$\nu_t = C_\mu \frac{k^2}{\varepsilon} \,, \tag{2.77}$$

the one-equation eddy viscosity relation in regions where $s < s_o$,

$$\nu_t = g(k, y) \,, \tag{2.78}$$

and the eddy viscosity model $\overline{u_i u_j} = \frac{2}{3} k \delta_{ij} - 2\nu_t S_{ij}$. The time scale T is set to the k-ε scale. The constants C_1 and C_2 are 1.45 and 1.92, respectively. The two constants, σ_k

and $\sigma_{\varepsilon,}$ are 1.0 and 1.3, respectively. The constant C_μ is 0.09. The value s_o is the parameter delineating the near-wall and outer regions of the flow. For RM, s_o is set to the ratio ν_t/ν. The one-equation model is used from the wall to the point where s_o=16 [124]. For all other one-equation models, s_o is set to the turbulence Reynolds number, R_y. For these models, the one-equation model is used from the wall to the point where s_o=250 [24, 122]. The ratio ν_t/ν is 16 when R_y is about 90 for a turbulent boundary layer indicating that RM switches to the standard k-ε model closer to the wall than the traditional one-equation models.

2.2.2 Two-Equation Near-Wall Models

For the two-equation near-wall model, the set of equations includes the turbulent kinetic energy equation,

$$\frac{Dk}{Dt} = ((\nu + \frac{\nu_t}{\sigma_k})k_{,j})_{,j} - \overline{u_i u_j} U_{,j} - \varepsilon \ , \tag{2.79}$$

the dissipation equation [157],

$$\frac{D\varepsilon}{Dt} = ((\nu + \frac{\nu_t}{\sigma_\varepsilon})\varepsilon_{,j})_{,j} - \frac{C_1 \overline{u_i u_j} U_{,j} + C_2 \varepsilon}{T} + 2\nu\nu_t U_{i,ij}^2 \ , \tag{2.80}$$

the relation $\nu_t = f_\mu C_\mu \frac{k^2}{\varepsilon}$ and the eddy viscosity model $\overline{u_i u_j} = \frac{2}{3} k\delta_{ij} - 2\nu_t S_{ij}$. The damping function is given by,

$$f_\mu = (1 - \exp(1.5x10^{-4} R_y + 5x10^{-7} R_y^3 + 1x10^{-10} R_y^5))^{1/2} \ . \tag{2.81}$$

The constants are the same as those of the standard k-ε model and the time scale T is a composite of the k-ε time scale and the time scale of the smallest motions given by

$T_s = \frac{k}{\varepsilon} + \sqrt{\frac{\nu}{\varepsilon}}$. The partial differential equations presented above are subject to appropriate boundary conditions. The specific boundary conditions completing the problem formulation are described in the sections concerning the computations.

2.3 Summary

The governing equations for the incompressible flows investigated in this work include the Reynolds-averaged Navier-Stokes equations, the continuity equation, the modeled transport equation for the turbulent kinetic energy, and in the case of the two-equation near-wall model, a modeled transport equation for the dissipation rate of the turbulent kinetic energy. For the one-equation near-wall models, the modeled transport equation for the dissipation is replaced by an algebraic relation in the near-wall region. The Reynolds-averaged Navier-Stokes equations are closed using the eddy viscosity model that forms the basis of the linear relationship between the mean flow quantities and the Reynolds stresses.

CHAPTER 3

3. Numerical Technique and Code Validation

The numerical technique for the code used for this work is summarized in the first section below. Since the development of the code does not form the objective of this work, the details of the method used to solve the transport equations are presented in an appendix. The validation of the code, through the prediction of the flows for a laminar boundary layer, a turbulent boundary layer, a turbulent plane channel, a lid-driven cavity, a laminar backward facing step, and between concentric rotating cylinders, is presented in the second section below. In this chapter, customary superscript '+' denotes normalization by the friction velocity and kinematic viscosity, and variables without superscript '+' are appropriately normalized by a reference velocity and length.

3.1 Numerical Method

The solution of the Reynolds-averaged Navier-Stokes equations and accompanying turbulence transport equations, described in the previous chapter, requires an iterative scheme in which the equations are discretized over the region of space and interval of time of interest. The variables describing an incompressible flow with constant transport properties and without heat transfer or body forces include the velocity and pressure. These variables are referred to as primitive variables. The variables representing the turbulence quantities needed to close the Reynolds-averaged Navier-

Stokes equations include the turbulent kinetic energy and a length scale determining variable such as the dissipation rate of the turbulent kinetic energy. The mathematical form of the transport equations for the quantities representing the turbulence quantities is typically similar to that of the Navier-Stokes equations. Schemes developed for the solution of the Navier-Stokes equations can therefore generally be utilized to solve the modeled turbulence transport equations provided that the source terms are modified appropriately.

The Navier-Stokes equations are a closed set of the partial differential equations governing the flow of incompressible fluids. Much work pertaining to the numerical solution of the Navier-Stokes equations has been concerned with accuracy and convergence characteristics [12, 44]. The majority of computations made for engineering studies have used finite difference and finite volume techniques [20, 31, 44, 63, 64, 104, 109, 150]. Other methods for solving the RANS equations include the finite element and finite analytic techniques [22, 63].

Solutions to the set of equations governing incompressible flows are generally considered more difficult to obtain than those of the compressible set due to the lack of an explicit equation for the pressure [151]. The pressure and velocity fields that develop in an incompressible flow computation may, for example, become decoupled due to the central differencing of a pressure field in which the value of the pressure is equal at every other grid point [151]. This decoupling of the pressure and velocity fields can be eliminated by use of a staggered grid as implemented in the classic marker-and-cell (MAC) method of [56]. However, a staggered grid may not be practical for the body-fitted coordinates utilized for the geometries of practical importance. Experience gained

with the code developed for this work indicates that the decoupling of the velocity and pressure may be less problematic for computations made using nonuniform grids. The final numerical difficulty commonly encountered when solving the algebraic equations resulting from the discretization of the Navier-Stokes equations is due to the nonlinearity of the convective terms. As the cell Reynolds numbers increase, the central differences, commonly used to compute the first derivatives when implementing the finite difference technique, become increasingly inaccurate estimations of the gradient of the quantities of interest at the central node of the discretization stencil. A simple solution would consist of one-sided differencing of the convective terms to first or second order. A more elegant solution consists of the exponential convection method [109]. In this method, an exact solution to the one-dimensional convection-diffusion equation is utilized to develop a computational algorithm for the solution of the Navier-Stokes equations. This method can be made more efficient by use of a power law estimate of the exponential convection relations or by use of a hybrid scheme [109].

One technique of circumventing the lack of coupling between the pressure and velocity fields arising from the formulation of the equations governing incompressible flows is to cast the equations in terms of vorticity and a stream-function. This reformulation leads to the classic stream-function vorticity method [146] in which the pressure gradient is eliminated by taking the curl of the transport equations [151]. In addition to eliminating the pressure, this approach removes the numerical difficulties associated with the nonlinear convection terms making the method ideal for two dimensional computations of internal flows. Recent work using the stream function-vorticity method includes that of reference 142. When extended to three dimensions

however, much of the advantage of the stream-function vorticity method is lost due to the appearance if two additional partial differential equations not present in the primitive variable formulation. For this reason the primitive variable formulation is most often utilized for three dimensional computations [151]. The tendency to favor primitive variables for two-dimensional computations stems from the desire that a two-dimensional code be easily extended to three dimensions.

The classic approach to solving the primitive variable formulation is the MAC method mentioned above [56]. For the MAC method, a Poisson equation for the pressure is derived by differentiating and adding the momentum equations. The computations are carried out on a staggered grid to prevent pressure-velocity decoupling. In addition to requiring one more boundary condition than the original Navier-Stokes equations, this method is considered inefficient due to slow convergence of the Poisson equation [151].

Another popular technique is the method of artificial compressibility [28]. This method introduces a time derivative for the pressure into the continuity equation and thereby couples the pressure with the velocity. As a steady state is approached the time derivatives vanish leaving a solution of the steady form of the Navier-Stokes equations. Techniques used for compressible flows can be applied to this method making it an efficient method [63]. One research-oriented code utilizing this method is that described in reference 20. This method is traditionally limited to steady computations since the solution must converge so that the time derivative of the pressure vanishes.

A technique particularly well suited to the computation of incompressible flows is the projection method [12, 27, 102, 144]. The projection method solves the momentum

equations without the pressure to obtain a so-called pseudo-velocity field. To recover the Navier-Stokes equations, the velocity must then be written in terms of this pseudo-velocity and the pressure gradient. Since the incompressible flow is divergence free, the relation linking the velocity, pseudo-velocity, and pressure gradient, leads to a Poisson equation for the pressure with the divergence of the pseudo-velocity as the forcing term. The pressure, obtained from the solution of this Poisson equation, is then used to update the velocity giving a divergence free flowfield which simultaneously satisfies the momentum equations and the continuity equation. The projection method is also known by names such as the splitting scheme [42] and the fractional step method [76]. Given sufficient convergence of the Poisson equation, this method can provide a time-accurate solution to the transport equations. This method is easily extended to three-dimensional flow and has been formulated to be second-order accurate in both space and time [12, 13, 102] and there has been interest recently in the use of the projection method for the direct numerical simulation of viscous incompressible flows [42, 119]. The projection method forms the basis of the code utilized for this work and is described further below and in detail in an appendix.

3.1.1 Projection Method

The transport equations for the momentum can be solved without the pressure gradient term. Using vector notation, a first-order-in-time method can be written as

$$U^* = U - \Delta t(U \cdot \nabla)U + \Delta t \frac{1}{Re}\nabla^2 U + \Delta t S \quad , \tag{3.1}$$

where S is a source term containing terms such as those arising from the Reynolds stresses. All terms on the right-hand side are at time level k and all variables are

nondimensional. To recover the Navier-Stokes equations from equation (3.1), the pseudo-velocity must be related to the velocity through

$$U^* = U^{k+1} + \Delta t \nabla p . \tag{3.2}$$

Since the incompressible flow is divergence free, application of the divergence operator to the relation above gives a Poisson equation for the pressure

$$\nabla^2 p = \frac{1}{\Delta t} \nabla \cdot U^* . \tag{3.3}$$

The pseudo-velocity along the boundary, required to solve the discretized form of equation (3.3), is obtained at each time step by solving the discretized form of equation (3.2) along the boundaries using the boundary conditions for the velocity or, in the case of a pressure driven flow, the specified pressure gradient. Pressure along the boundaries is obtained from the Navier-Stokes equations directly or, in the case of a pressure driven flow, from the specified pressure gradient. Once the pressure has been obtained throughout the flowfield by solving the Poisson equation, the velocity is projected onto the space of divergence free vectors by

$$U^{k+1} = U^* - \Delta t \nabla p , \tag{3.4}$$

giving a velocity field that is divergence free to satisfy the continuity equation.

For the code developed for this work, the equations of motion are discretized using either finite differences or the finite volume technique [150]. For the computations completed for this work, the equations of motion are solved using either direct finite differences or the hybrid scheme [109] adapted for curvilinear coordinates [64]. The hybrid scheme approximates the exponential convection scheme and circumvents the instability due to central-differencing of the convection terms by switching to an up-wind

scheme when the Peclet number exceeds the value two [109]. Although the schemes based on exponential convection may lead to poor resolution for flows in which the velocity vectors are not closely aligned with the grid, the hybrid scheme works well as shown by the computation of flow in the lid-driven cavity presented later. An illustration of the discretization of the domain for the computation of the classic lid-driven cavity is shown in Figure 3.1 below. For two-dimensional computations, the flow domain is discretized into quadrilateral elements forming a nine point stencil. For uniform orthogonal grids, only the points indicated by the solid symbol contribute. The points indicated by the open symbol contribute when the grid is non-orthogonal. For a uniform orthogonal grid, the discretized form of equation (3.1) can be expressed as

$$u_a^{*k+1} = u_a^k + \Delta t[c_0 u_a^k + c_1 u_b^k + c_2 u_c^k + c_3 u_d^k + c_4 u_e^k + c_5 u_f^k + c_6 u_g^k + s_x] \quad , \qquad (3.5)$$

where Δt is the time step, k denotes the time level, s_x is a source term that may contain terms such as the Reynolds stresses, and the coefficients c_i are influence coefficients that are determined using the hybrid scheme described above [109]. The field of u^* given by equation (3.5) is used to determine the right hand side of equation (3.3) for solution of the pressure field. The pressure is then used to update the velocity by equation (3.4).

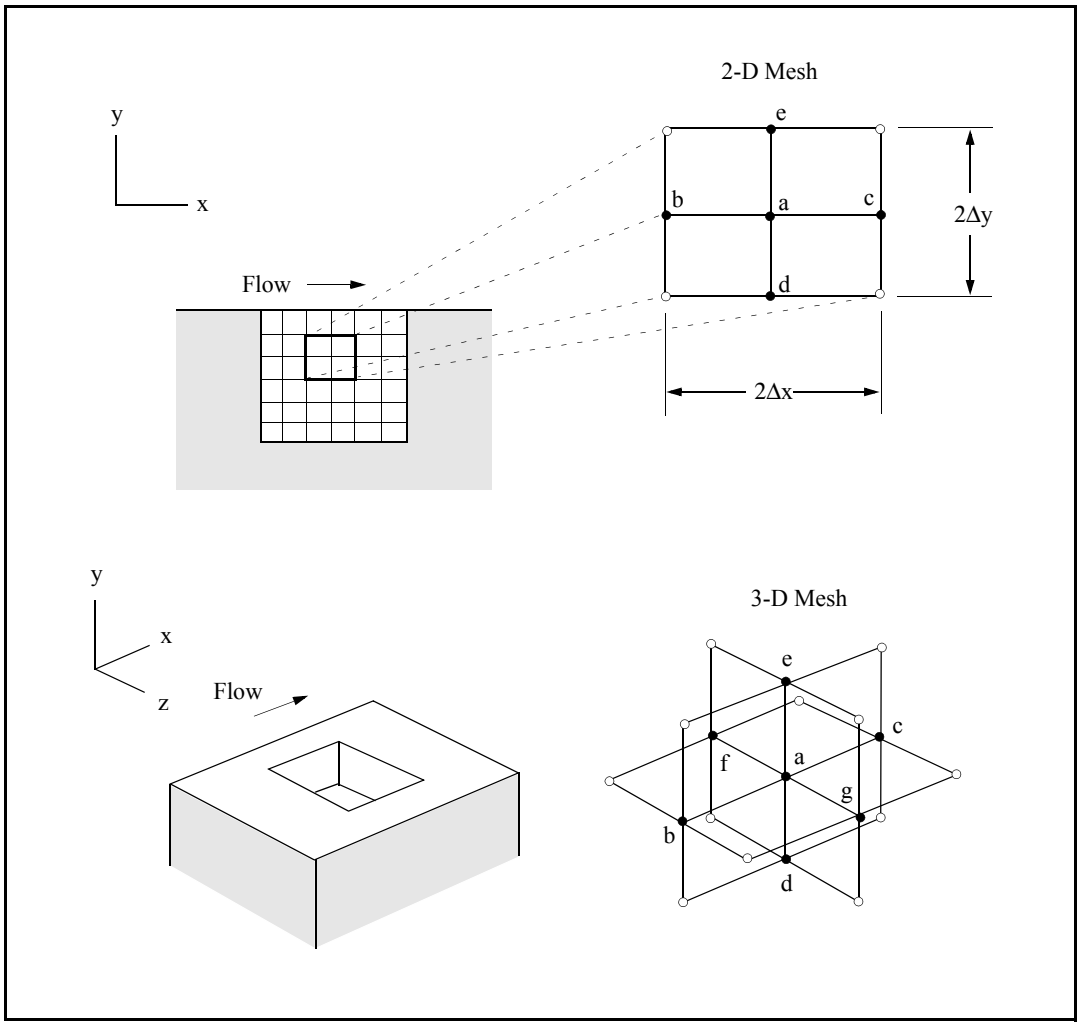

Figure 3.1: Discretization of the domain for the computation of flow in a lid-driven cavity.

Since the development of the code is not the subject of this work, further description of the method is left to an appendix. Surveys of projection methods can be found in references 52 and 113. A comprehensive analysis of projection methods can be found in reference 42. Recent applications of similar methods, formulated within the framework of the finite volume technique, include the computations of unsteady transitional flow over oscillating airfoils [78] and the simulations of vortex shedding past

triangular cylinders [74]. Both applications utilize one of the many existing variations of the k-ε turbulence model to close the RANS equations.

3.1.2 Implementation of Boundary Conditions

The boundary conditions naturally vary depending on the flow investigated and are described in detail in the following chapter discussing the benchmark flows and performance metrics. There are four types of boundaries encountered in the flows investigated in this work. The first boundary condition is a no-slip condition where the velocity is specified to be zero, the turbulent kinetic energy is zero, the pressure is obtained from the NS or RANS equations, and the dissipation is determined by the turbulent kinetic energy equation. The surface of a flat plate placed in a freestream is an example of a boundary where the no-slip boundary condition applies. The second type of boundary condition pertains to the inlet and outlet for a pressure driven periodic internal flow. In this case, the pressure gradient is specified and the velocity, turbulent kinetic energy, and dissipation rate are determined by the periodicity of the flow. The plane channel and wavy-wall channel are examples of pressure driven flows. The third type of boundary condition is the freestream boundary for external flows. In this case the velocity and turbulence quantities are prescribed and the pressure is obtained from the NS or RANS equations. The boundary layer flow is an example of an external flow having a freestream boundary. The fourth type of boundary condition is the farfield condition. In this case zero-gradient conditions are generally applied to the flow variables. Note that specified and gradient conditions are formally referred to as Dirichlet and Neumann conditions, respectively.

As mentioned above, the pressure at a no-slip surface is determined from the

governing transport equation. The momentum equation in the wall-normal direction for a steady flow for an orthogonal mesh is

$$u_t + uv_x + vv_y = -p_y + \nu(v_{xx} + v_{yy}) - \langle \overline{vv} \rangle_y - \langle \overline{uv} \rangle_x \quad . \tag{3.6}$$

Here, x is parallel to the wall and y is normal to the wall. The left hand side, first quantity in the diffusion term, and the Reynolds shear stress term vanish due to the no-slip condition. Since the instantaneous wall-normal velocity v' varies as y^2, the wall-normal Reynolds stress varies as y^4. The second to last term therefore vanishes when equation (3.6) is evaluated at the wall. If the eddy viscosity model is used to express the Reynolds stresses, then the modeled wall-normal Reynolds stress will vary not as y^4, but as y^2. In this case, the second to last term will still vanish when equation (3.6) is evaluated at the wall. Therefore, equation (3.6) becomes

$$p_y = \nu v_{yy}, \tag{3.7}$$

when evaluated at the wall [44]. The second derivative on the right-hand-side can be evaluated with a one-sided difference formula to first-order using the first point away from the surface. Since the velocity is zero at the wall, the second derivative can be written as

$$v_{yy_{wall}} = 2\left(\frac{\partial}{\partial y}\sqrt{v}\right)^2_{wall} \tag{3.8}$$

by using the product rule of differentiation. Differencing to first order gives

$$v_{yy_{wall}} = \frac{2v_2}{\Delta y^2}, \tag{3.9}$$

where v_2 is the value of the velocity at the first point away from the surface. Using the first two points away from the surface, this could be evaluated to second-order with a

one-sided difference. The pressure at the surface when using the first order accurate difference becomes

$$p_1 = p_2 - 2\nu\frac{v_2}{\Delta y}. \tag{3.10}$$

For body-fitted coordinates, v_2 would represent the velocity in the direction of the wall normal coordinate. A zero-normal gradient condition approximates equation (3.10). The solutions completed for this work appear insensitive to the use of either equation (3.10) or a zero-normal-gradient condition. Since the pressure at the surface is a function of a dependent variable, it is clear that there is no boundary condition for pressure at a no-slip surface. In general, at boundaries where conditions for the velocity are prescribed, the pressure is determined by the RANS equations. Equation (3.10) is an approximation of the RANS equations at the wall. In this work, the RANS equations are used to determine the pressure at each point where the velocity is prescribed including no-slip surfaces.

The turbulent kinetic energy is zero at no-slip surfaces. Setting the turbulent kinetic energy at the freestream boundaries to zero to represent the absence of turbulence in the freestream is problematic since the time scale, k/ε, must be nonzero throughout the flow domain in which the turbulence transport equations are solved in order to avoid the singularity that arises in the budget terms of the modeled dissipation equation. Therefore, the turbulence intensity is often set to a small value in the freestream. The turbulent kinetic energy on the freestream boundary can be expressed as

$$k = \frac{3}{2}T^2, \tag{3.11}$$

where T is the turbulence intensity defined as $T = \frac{1}{U}\left[\frac{1}{3}(u^2 + v^2 + w^2)\right]^{1/2}$. Since k is

normalized by the square of the freestream velocity, U does not appear explicitly in equation (3.11). A freestream turbulent kinetic energy of $1x10^{-8}$, corresponding to a freestream turbulence intensity of about 0.01%, is chosen for the computations described in this work. This corresponds to the value that may be seen in a low turbulence wind tunnel [11].

For the one-equation near-wall models, no other boundary conditions are required. For the two-equation near-wall models, the dissipation at the wall must be determined. The dissipation at the wall is determined by evaluating the turbulent kinetic energy equation,

$$\frac{Dk}{Dt} = ((\nu + \frac{\nu_t}{\sigma_k})k_{,j})_{,j} - \overline{u_i u_j} U_{,j} - \varepsilon \quad , \tag{3.12}$$

at the wall. Using the product rule of differentiation together with the condition that k vanishes at a no-slip surface, the dissipation at the wall becomes

$$\varepsilon_{wall} = \nu k_{yy_{wall}} = 2\nu\left(\frac{\partial}{\partial y}\sqrt{k}\right)^2_{wall} \quad . \tag{3.13}$$

This can be discretized as was equation (3.8). This relation for the dissipation at the wall is commonly used and provides the value of dissipation at the wall needed to solve the discretized form of the dissipation equation [128, 157].

The sections above complete the description of the formulation of the method used to complete the computations described in this work. Details of the projection method are given in an appendix. The precise boundary conditions for each flow case computed in this work are given in the section discussing that specific flow. A description of the validation of the projection method code is given in the following section.

3.2 Code Validation

The projection method code used in this work was written in FORTRAN and is capable of solving three-dimensional internal and external incompressible flows. The problem geometry and domain discretization are generated internally. The code is validated by computing the laminar and turbulent flow over a flat plate, turbulent flow through a plane channel, flow in a lid-driven cavity at two Reynolds numbers, flow over a laminar backward facing step at various Reynolds numbers, and flow between concentric rotating cylinders. Table 3.1 below lists the criteria for validation.

Table 3.1: Validation criteria for the projection method code.

	Criteria	Flows
1	Resolution of flow for grids with high aspect ratio cells	Laminar boundary layer at high Re / Turbulent boundary layer
2	Resolution of skewed flows and separated flows	Lid-driven cavity at high Re / Backward facing step
3	Correct implementation of the grid metric transformations	Counter-rotating cylinders / Laminar boundary layer
4	Capture of Reynolds number effects (minimal numerical diffusion)	Laminar Backward facing step / Lid-driven cavity
5	Solution of turbulence transport equations	Turbulent channel / Turbulent boundary layer
6	Resolution of near-wall turbulence quantities	Turbulent channel / Turbulent boundary layer

Before proceeding with the discussion of code validation, it is necessary to discuss the grid spacing parameters. For turbulent flows, the wall-normal coordinate is often normalized as

$$y^+ = \frac{u_\tau}{\nu} y \,, \tag{3.14}$$

where y is the coordinate normal to the wall, ν is the fluid kinematic viscosity, and u_τ is the friction velocity given by

$$u_\tau = \sqrt{\tau_w / \rho} \,, \tag{3.15}$$

where τ_w is the shear stress at the wall and ρ is the fluid density taken to be one for the incompressible flows investigated here. This is a convenient unit for turbulent computations since it is generally agreed that the wall spacing must be at most one wall unit (y^+=1) to resolve the viscous sublayer of a turbulent flow for computational algorithms commonly used to solve the RANS equations. Wall spacings of y^+=0.1 are needed to resolve the flow for certain models including, according to reference 10, the standard k-ε model [75]. Being flow dependent, the value of u_τ is not known precisely until the computation is completed. For example, u_τ may be greater for the impinging flow near the leading edge of a bluff body or airfoil than for the flow over a flat plate. The wall spacing can be specified by

$$\Delta y = \frac{\delta}{Re} \,. \tag{3.16}$$

Setting δ to 2 gives a wall spacing that, for a turbulent boundary layer or channel flow, corresponds to roughly y^+=0.1. In general, $y^+ = u_\tau \delta \sim 0.05\delta$ for turbulent boundary layers and channel flows. For the computations described subsequently in this work, all grid spacings at the wall will be given in terms of δ unless otherwise specified. The computations of the boundary layer, the plane channel, the lid-driven cavity, the laminar backward facing step, and the concentric rotating cylinders are described in detail in the

sections that follow. For the computations described in this work, all nonuniform grids utilize geometric spacings where the differences in the dimensions of adjoining sides of adjacent cells are no greater than 10%.

3.2.1 Laminar and Turbulent Boundary Layer

The velocity profile of a laminar boundary layer is obtained through the solution of an ordinary differential equation and is thus considered an exact solution providing an excellent test case for code validation [14, 151]. Furthermore, this test case validates the ability of the code to resolve flows using grids with cells having large aspect ratios. This use of cells of high aspect ratio is required for the efficient solution of problems at the high Reynolds numbers of practical importance in engineering applications. The geometry chosen for this code validation case is a rectangle of one unit in length and half a unit in height. The boundary conditions for velocity are freestream at the inlet, no-slip at the lower boundary or wall, and zero-gradient at both the upper boundary and exit. Since the boundary layer grows with distance downstream of the leading edge of the flat plate, the grid spacing is necessarily finer at the leading edge. The grid utilized for the computation of the boundary layer flow is illustrated in the figure below.

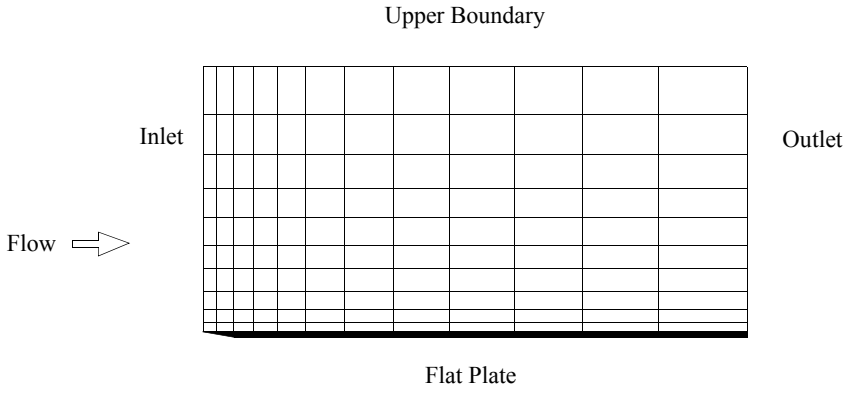

Figure 3.2: Illustration of the grid for the computation of the boundary layer flow over a flat plate.

The domain is discretized into 63 nodes in the streamwise direction and 127 nodes in the wall-normal direction. The grid spacing, δ, is $5\text{x}10^{3}$ at the leading edge, corresponding to 0.005 dimensional units, and five at the wall. The Reynolds number based on unit plate length is one million and the time step is $1\text{x}10^{-3}$. The computation yields the velocity profile shown in Figure 3.3. The velocity profile compares well with the exact solution. The abscissa is given by the usual similarity variable

$$\eta = \sqrt{\frac{U}{2\nu x}}, \tag{3.17}$$

where U is the freestream velocity, and x is the distance from the leading edge of the plate. Lowercase u in Figure 3.3 is the streamwise velocity. Plotting the results against the similarity variable indicates that the boundary layer growth is captured.

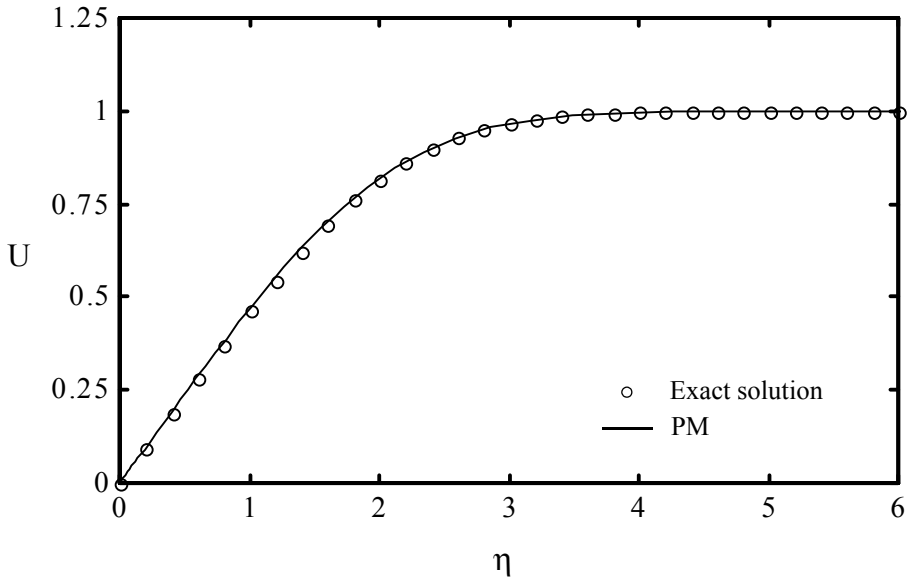

Figure 3.3: Predicted *U* for the laminar boundary layer.

The turbulent boundary layer is solved over a similar domain. The most important grid parameter upon which the accuracy of the solution depends is the wall-spacing [10]. Here, δ=2 corresponding to the value $2\text{x}10^{-6}$. Using δ=5 is found to yield indistinguishable results. The boundary conditions for the velocity are the same as those of the laminar computation. The boundary conditions for the turbulent kinetic energy are zero at the wall, freestream at the inlet and upper boundary, and zero-gradient at the exit.

Since the solution depends on the choice of model, the code cannot be validated by comparing to the DNS. The solution must be computed using a particular turbulence model and compared to results from the open literature in which the same model is utilized. Here, the turbulence model utilized is the Yang-Shih two-equation near-wall *k*-ε model (YS) [157]. The resulting profiles of the velocity, the Reynolds shear stress, the

turbulent kinetic energy, and the dissipation, are compared to the results of the model developers in Figure 3.4 to 3.7 below. These profiles are taken at a streamwise position where the Reynolds number based on the momentum thickness, Re_θ, defined later, is approximately 1416. Also shown in those figures are the DNS results [136] such that any differences between the results of the computation using the projection method code with model YS and the solution taken from reference 157 can be put into perspective. Figure 3.5 shows that the computation using model YS and the results of reference 157 both indicate a maximum k of about 4.5. To further put any slight differences into perspective, a computation using the Norris-Reynolds model (model NR) gives a maximum k of only about 3.2. Slight differences between the solutions are expected due to unavoidable small differences in the value of Re_θ at which the profiles are taken, the choice of outlet boundary conditions, and differences in numerical condition for dissipation at the wall.

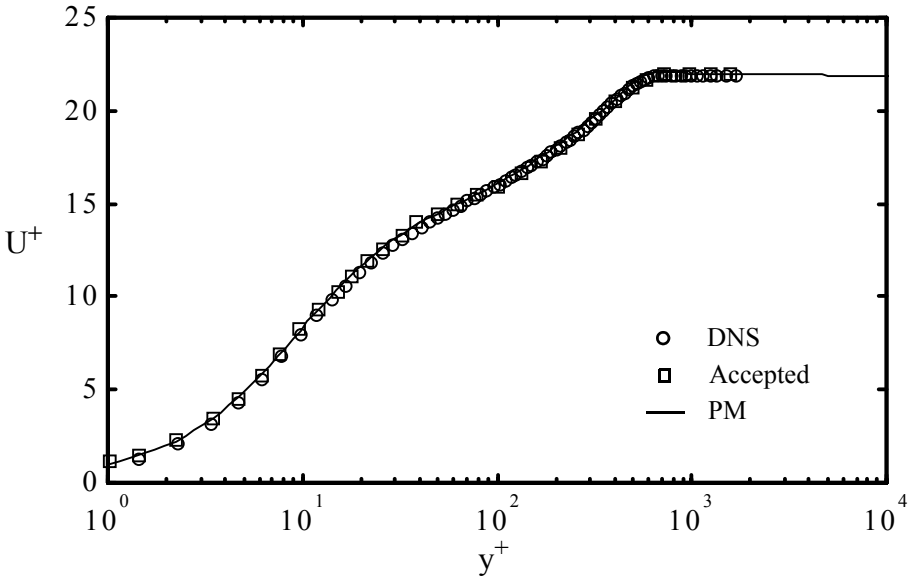

Figure 3.4: Predicted U by the projection method shown with accepted results and DNS data.

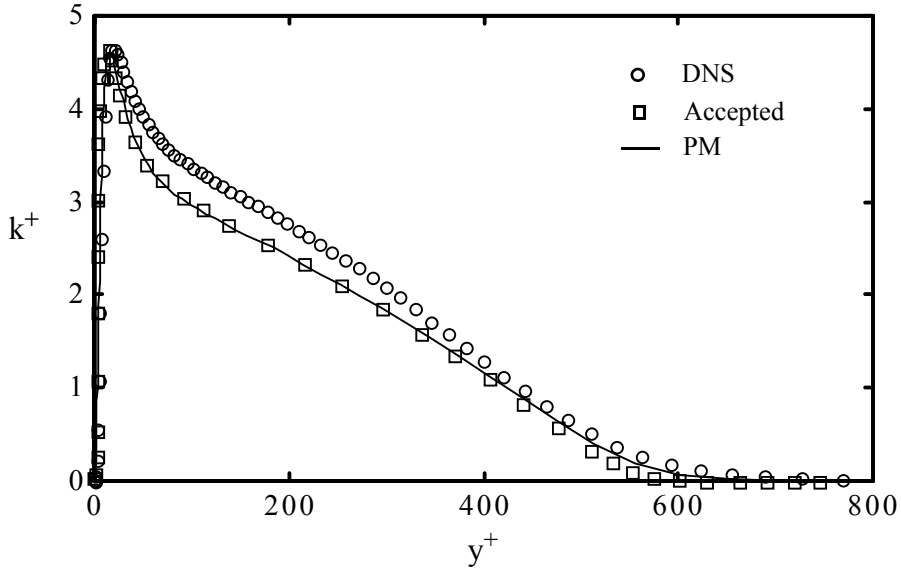

Figure 3.5: Predicted *k* by the projection method shown with accepted results and DNS data.

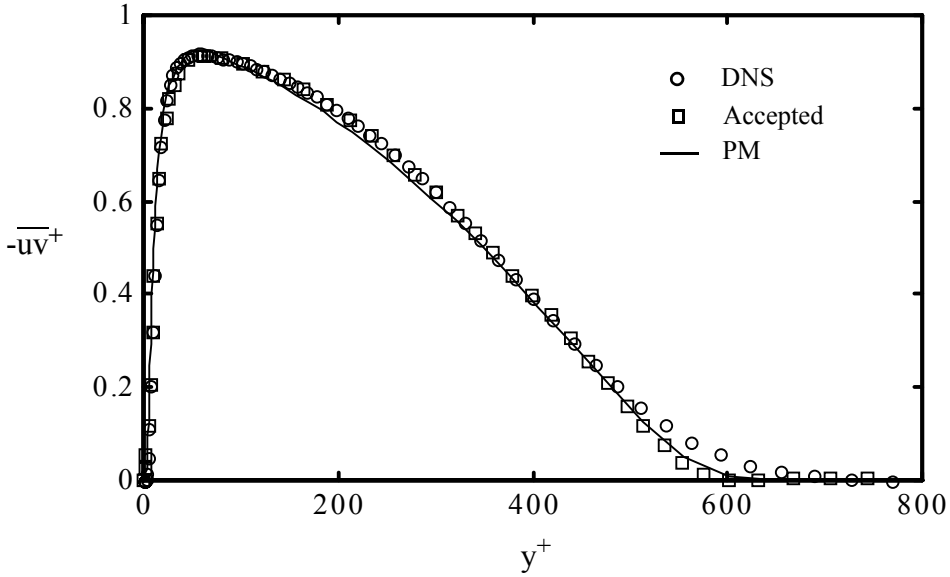

Figure 3.6: Predicted $-\overline{uv}$ by the projection method shown with accepted results and DNS data.

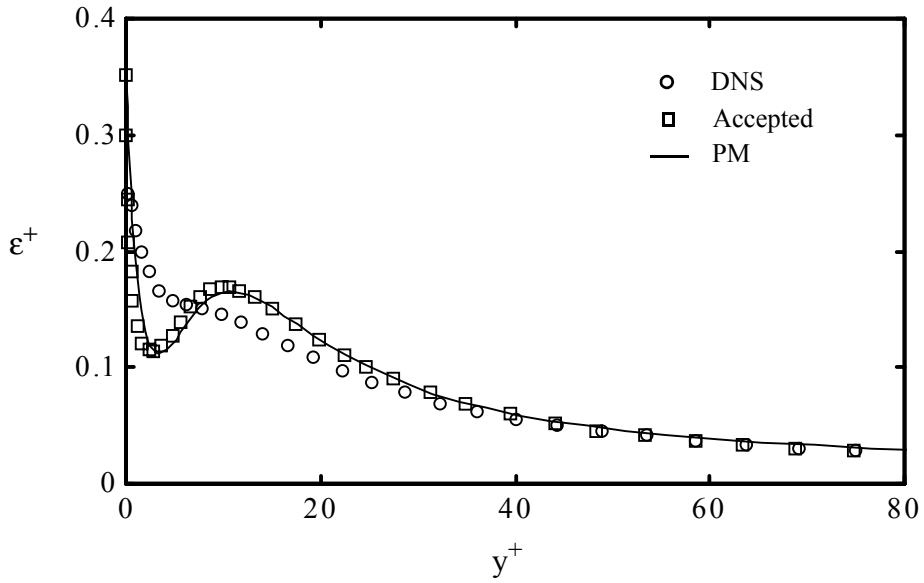

Figure 3.7: Predicted ε by the projection method shown with accepted results and DNS data.

The very close match of the predictions of the projection method code and those of the model developers indicates that the code implements the turbulence transport equations into the algorithm correctly and solves the turbulence transport equations.

Comparing the predicted skin friction coefficient of various models is one component of the critical evaluation of near-wall turbulence models. To verify that the projection method code can resolve the skin friction coefficient, the predictions of the projection method code using model YS for various wall spacings. The predicted skin friction coefficient is also compared to the value given in reference 128.

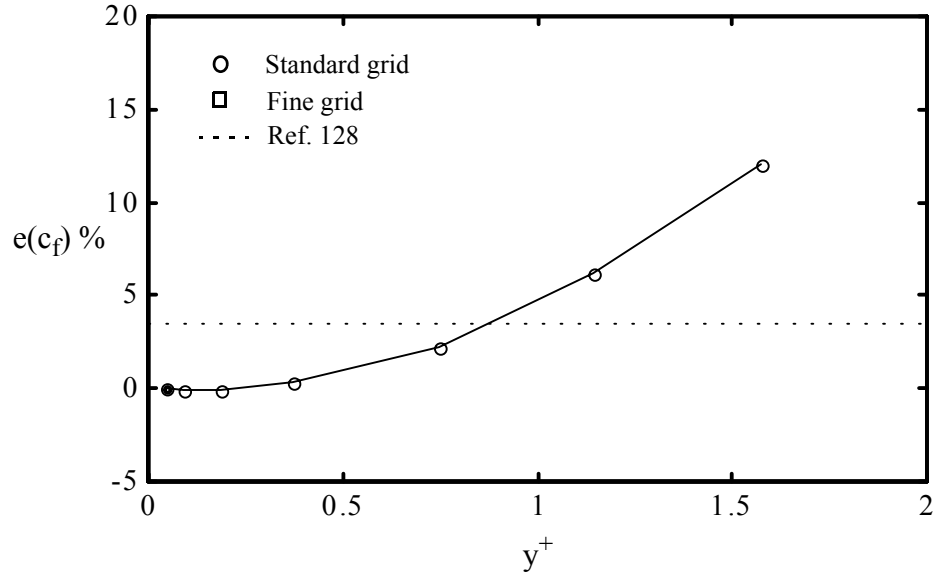

Figure 3.8: Percent error in predicted skin friction coefficient as a function of wall spacing.

Figure 3.8 shows the percent error in the skin friction coefficient with respect to the skin friction coefficient computed for a wall spacing of $\delta = 1$ using a fine grid with 63 streamwise node points and 255 wall-normal node points. The wall spacings corresponding to each symbol are $\delta = 1, 2, 4, 8, 16, 24$, and 32. Figure 3.8 shows that the error for the 'standard' grid, with 63 streamwise points, 127 wall-normal points, and $\delta = 1$, gives a skin friction coefficient equal to that of the fine grid. This indicates grid independence of the solution computed with the standard grid. The error increases with wall spacing and reaches 5% when $y^+ \sim 1$. This indicates that a wall spacing of $\delta = 8$, corresponding to $y^+ \sim 0.5$, is sufficiently fine to resolve the skin friction coefficient. Figure 3.8 also shows that the prediction of the projection method code with the finest

wall spacing is within 5% of those of reference 128. Since it has been shown that the two-equation near-wall model of Jones and Launder is more sensitve to wall-spacing that one-equation models [10], this spacing should also be sufficient to resolve the near-wall flow for the one-equation near wall models. Figure 3.9 below shows explicitly that the one-equation near-wall model NR resolves the skin friction coefficient for y^+ up to 1.5 whereas the two-equation near wall model of Yang and Shih (model YS) requires much finer wall spacings to resolve the flow to the same level.

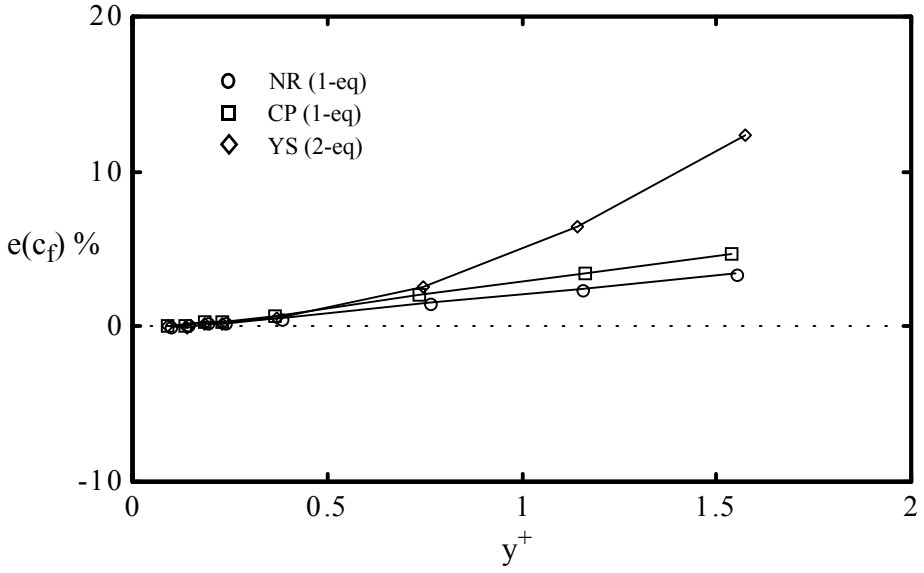

Figure 3.9: Percent error in predicted skin friction coefficient as a function of wall spacing for NR, CP, and YS.

Comparing the predicted series expansion coefficients of the turbulence quantities to the known or accepted values is one component of the critical evaluation of near-wall

turbulence models. The series expansion coefficients, a_k , a_{uv}, and a_ε, are described in Chapter 4. The computation of the boundary layer is repeated using various wall spacings to determine sensitivity of the series expansion coefficients and skin friction coefficients to the wall spacing. Figure 3.10 shows the error in a_k with respect to the value at a wall spacing of δ=2 corresponding to y^+=0.05.

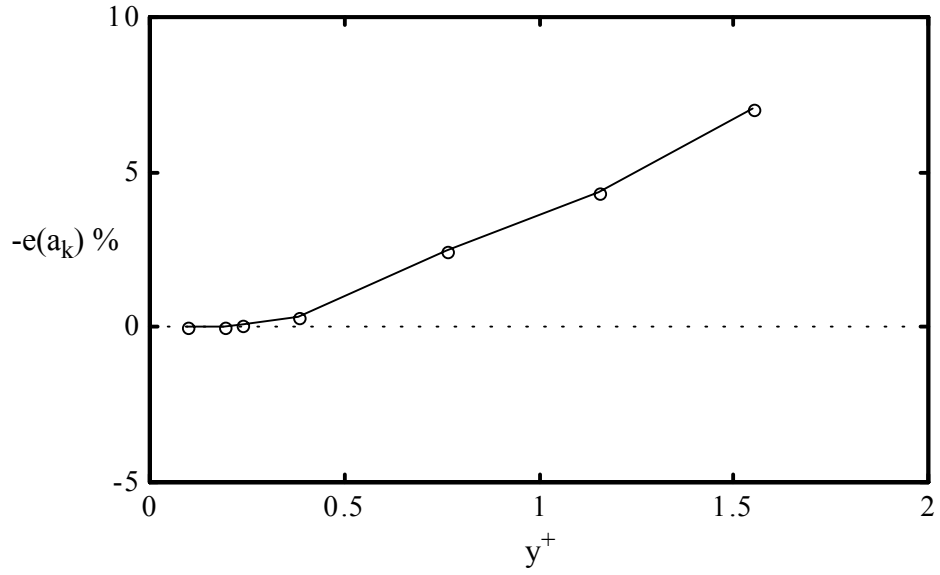

Figure 3.10: Percent error in series expansion coefficient a_k as a function of wall spacing for YS.

The figure shows that wall spacings δ of up to 16 are sufficient to resolve the coefficients to within 5%.

3.2.2 Turbulent Plane Channel

The plane channel is the most common flow utilized to evaluate turbulence models. The flow is one-dimensional with no-slip boundary conditions on the walls. If the flow is solved using a two-dimensional domain, periodic boundary conditions apply on the remaining boundaries. The grid used for the computation uses 5 node points in the streamwise direction and 127 points in the wall normal direction. The Re_b is 6875 and Re_τ is 395. The wall spacing is $2/Re_b$. The computation yields an Re_τ within 1% of the DNS value indicating that the pressure and drag forces are in balance. Figures 3.11 through 3.14 show the mean velocity, turbulent kinetic energy, Reynolds shear stress, and dissipation for the computation using the projection method, the computation of the model developers [157], and the DNS data.

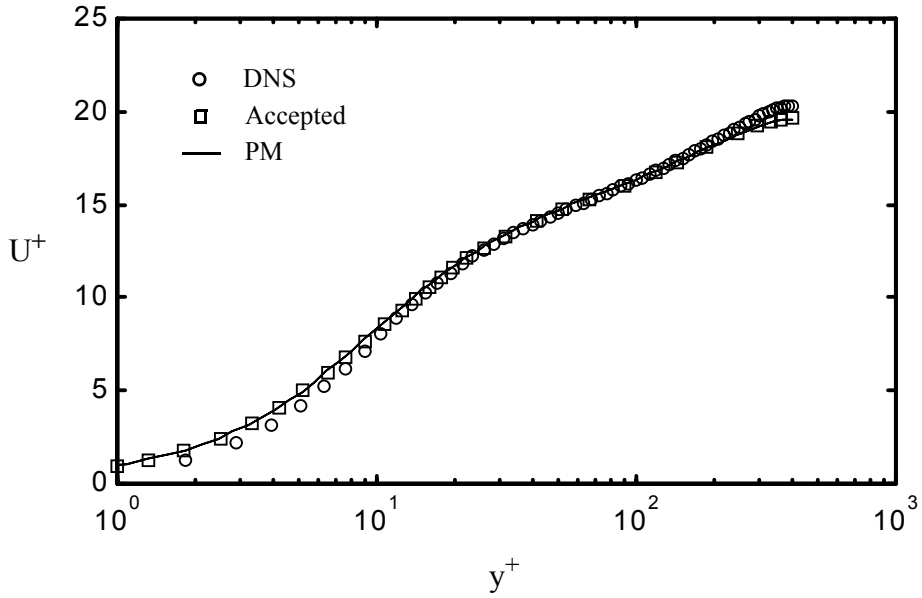

Figure 3.11: Predicted *U* by the projection method shown with accepted results and DNS data.

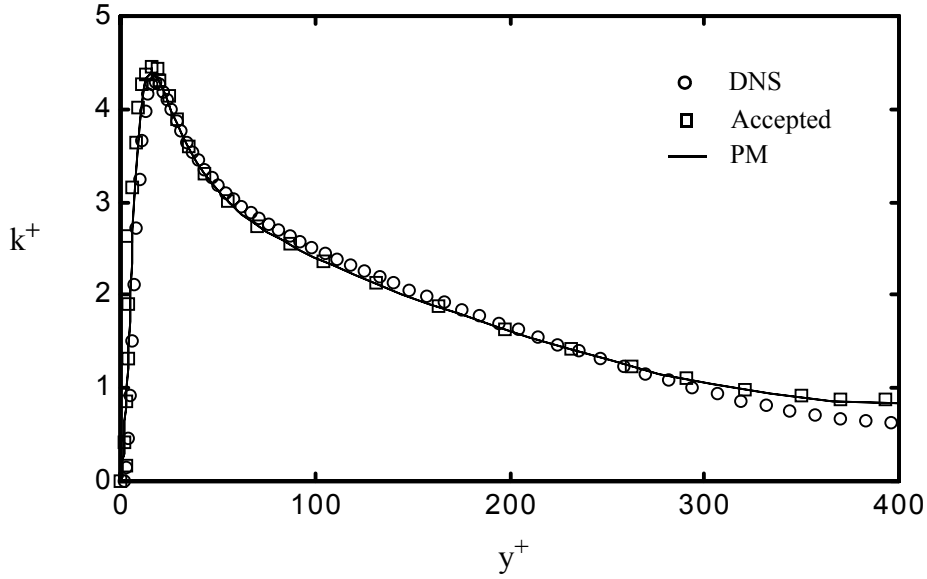

Figure 3.12: Predicted *k* by the projection method shown with accepted results and DNS data.

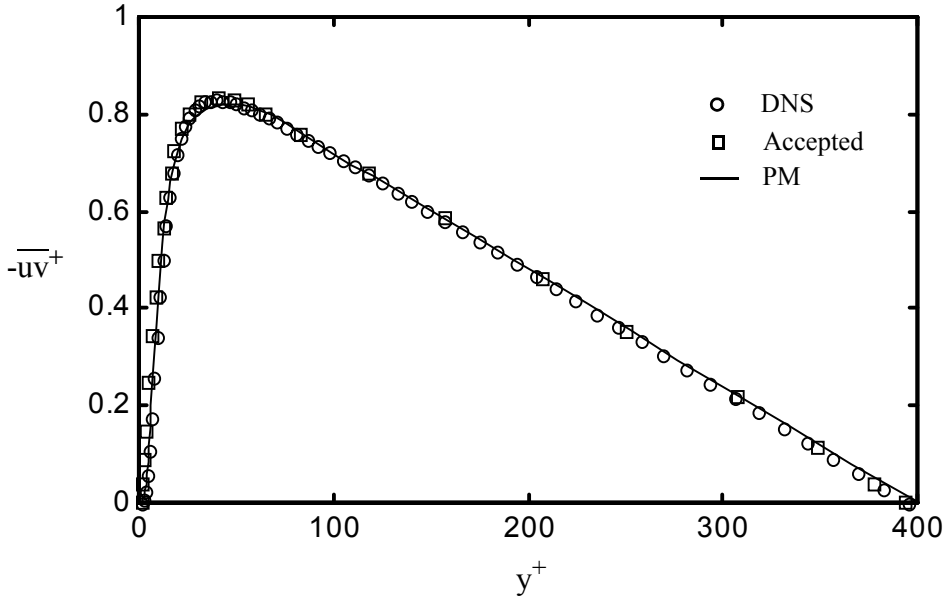

Figure 3.13: Predicted $\overline{uv}$ by the projection method shown with accepted results and DNS data.

.

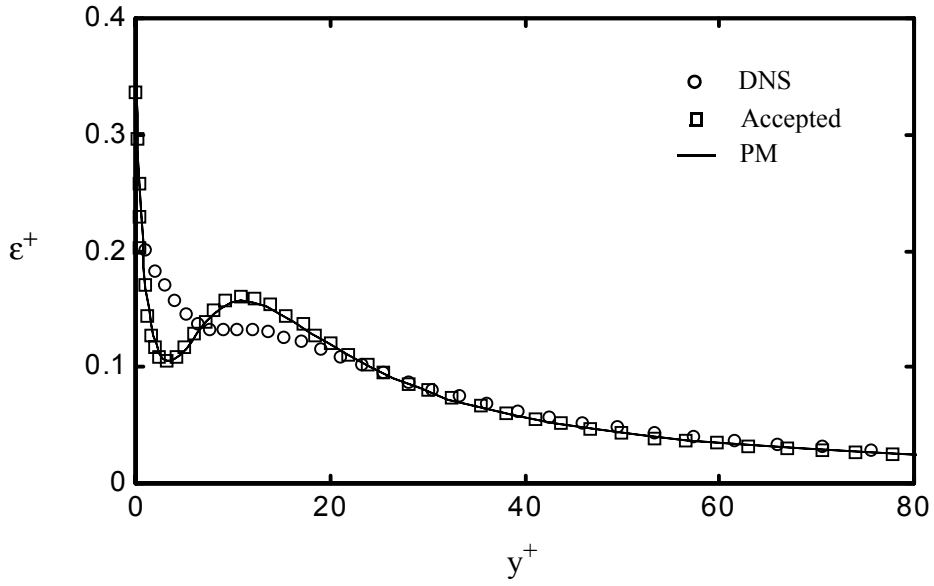

Figure 3.14: Predicted ε by the projection method shown with accepted results and DNS data.

Clearly the computations using the projection method code match those of the model developers very closely further indicating that the projection method code solves the turbulence transport equations.

As mentioned above, comparing the predicted series expansion coefficients of the turbulence quantities to the accepted values is one component of the critical evaluation of near-wall turbulence models. For the channel computation above, the projection method code gives values of 0.176 and 0.352 for a_k and a_ε, respectively. These can be compared to the corresponding values of 0.167 and 0.330 given in reference 128. To place the differences between these two sets into perspective, the DNS data gives a value of 0.122 for a_k and 0.251 for a_ε. The close match between the computed results and those given in

reference 128 suggests that the projection method code resolves the near-wall flow.

3.2.3 Lid-Driven Cavity

The resolution of the laminar flow in a lid-driven cavity is considered to be among the most challenging test cases for code validation [43, 44, 131]. The geometry consists of a square cavity with boundary conditions of zero velocity on the three walls and a unit horizontal velocity on the upper boundary called the lid. The lid-driven cavity is illustrated in Figure 3.15. The corresponding experiment would consist of a cavity of effectively infinite dimension in the spanwise direction providing a two-dimensional flow at sufficiently low Reynolds numbers. The flow in the experiment would naturally transition to turbulence at sufficiently high Reynolds numbers. Since the computations are two-dimensional, the computed flow remains laminar regardless of Reynolds number.

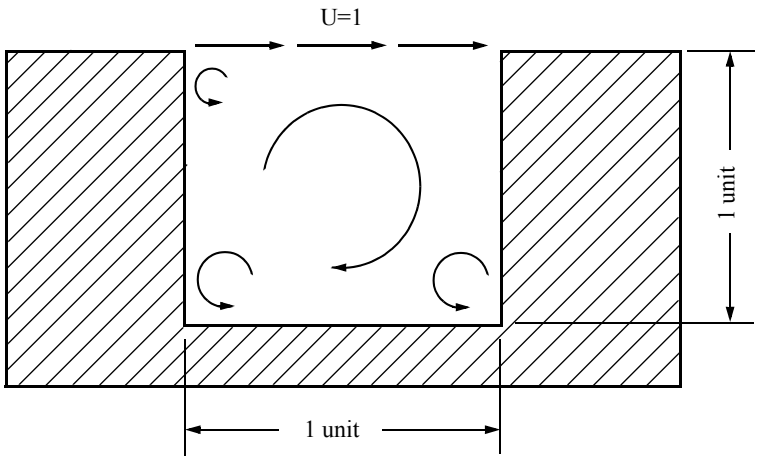

Figure 3.15: Illustration of the lid-driven cavity flow.

The solution is typically steady at Reynolds numbers, based on unit depth and height, below seven thousand [43]. At a Reynolds number of ten thousand, the solution may not be steady depending on the characteristics of the numerical scheme. This flow is the most common test case used to study the characteristics of CFD codes and numerical algorithms [43]. The lid-driven cavity flow tests the capability of the code to resolve flows that are highly skewed with respect to the mesh. Furthermore, since the solution depends highly upon the Reynolds number of the flow, this case indicates whether the numerical scheme suffers from excessive numerical diffusion. Figure 3.16 below shows the streamlines for a cavity at a Reynolds number of 10^3 computed using the projection method (pm) code on a uniform grid of 127^2 mesh points. The velocity profile along the centerline is compared to that obtained using a code based on the stream-function vorticity method (svm) on a uniform grid of 255^2 mesh points. The stearmline pattern and velocity profile for the Reynolds number of 10^3 compare well to those obtained in the literature [44].

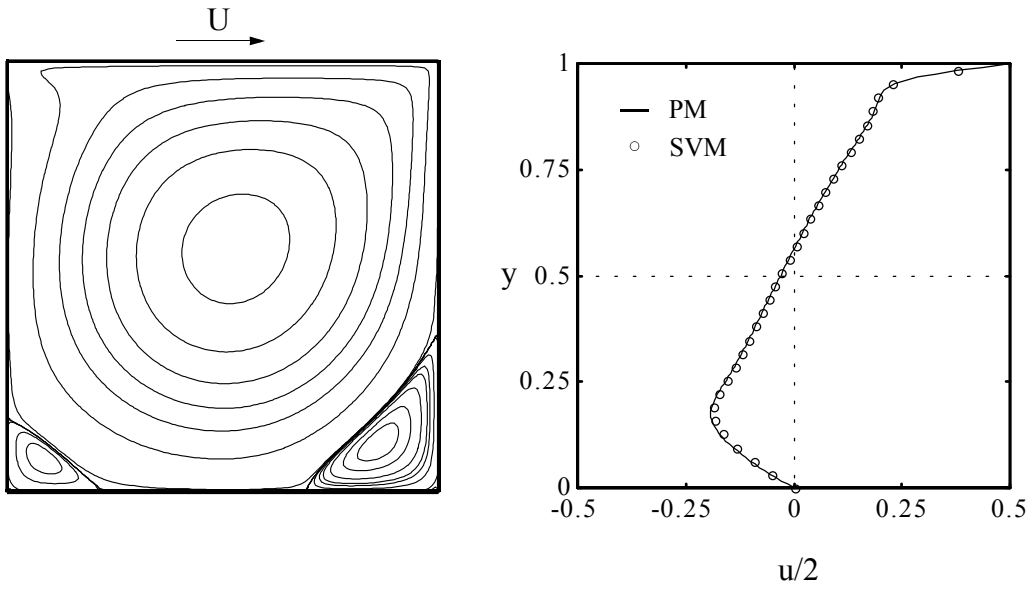

Figure 3.16: Streamlines for the lid-driven cavity at Re=10^3 by the projection method and the velocity profile along the vertical centerline.

The streamline pattern for the Reynolds number of 10^4 shown in Figure 3.17 compares well with the frequently referenced classic solution [47] as well as more recent results [41, 43].

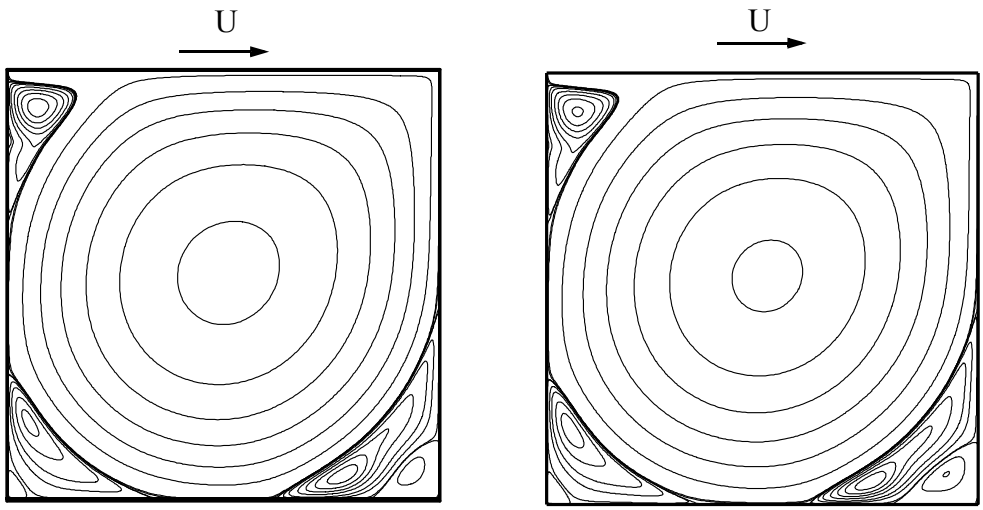

Figure 3.17: Streamlines for the lid-driven cavity at Re=10^4 using uniform and nonuniform grids.

At a Reynolds number of 10^4, a steady solution may not exist [43]. Many solutions in the open literature appear to have been obtained with a steady-state formulation in which the time derivative appearing in the Navier-Stokes equations has been effectively removed from the computation. The solution at Re=10^4 computed here using the first-order-in-time projection method exhibits a slight unsteady nature and small variations in the size and form of the vortices in the upper corner ans lower left corner can be seen as the computation proceeds. The streamlines shown in Figure 3.17 represent the time-averaged flow. Further details concerning the computation of this flow are provided in an appendix discussing the projection method code.

The figures above indicate that the code resolves the flow in the lid-driven cavity.

The solution of the lid-driven cavity flow indicates that the code can resolve flows that are highly skewed with respect to the computational grid.

3.2.4 Laminar Backward Facing Step

The reattachment distance for the laminar backward-facing step depends clearly on the Reynolds number in the range from 50 to 400. If the numerical method cannot reproduce the Reynolds number dependence of the reattachment length, the method may suffer from excessive numerical diffusion [76]. For this reason, the laminar backward facing step is an excellent test case for numerical schemes. The geometry consists of a channel with a length generally at least 25 times the half-width. The step size is equal to the channel half-width. The Reynolds number reported here is based on step height while that of some studies [76] are based on channel height. The values above therefore correspond to a range from 100 to 800 when based on channel height. The computation is completed on a 127^2 uniform grid with an outlet boundary at 25 step heights downstream as generally recommended [76, 144]. The time step is 10^{-3} or 10^{-2} with the lower time step being used for higher Reynolds numbers. The inlet velocity profile is specified as that of a laminar channel flow with a bulk velocity of one. The Navier-Stokes equation for a plane channel simplify to $p_x + \mu u_{yy} = 0$. Since the pressure gradient is constant, integration twice gives

$$u(y) = \frac{p_x}{2\mu} y^2 + Ay + B \quad . \tag{3.18}$$

The boundary conditions are $u(0)= u(1)= 0$ giving

$$u(y) = \frac{p_x}{2\mu} y(1-y) \quad . \tag{3.19}$$

Integration over y from y=0 to y=1 gives the bulk velocity. Setting the bulk velocity to one gives

$$u(y) = 6y(1-y) \quad . \tag{3.20}$$

This gives the velocity at the inlet of the backward facing step. Zero-gradient conditions are applied at the exit for velocity. Alternatively, the exit velocity could be specified as a laminar channel giving the same mass flow as the inlet profile. The former method is preferred, however, because it permits the verification of mass and momentum conservation over the domain. The conditions along the walls are no-slip. Before the computations proceed, the inlet velocity and the zero velocity along the back face of the step are extended downstream forming a divergence free initial velocity field.

The results for the projection method code match well with experimental values [6, 50, 133] and computations [44, 76] as shown in Figure 3.18. The streamline pattern for an intermediate Reynolds number case is shown in Figure 3.19.

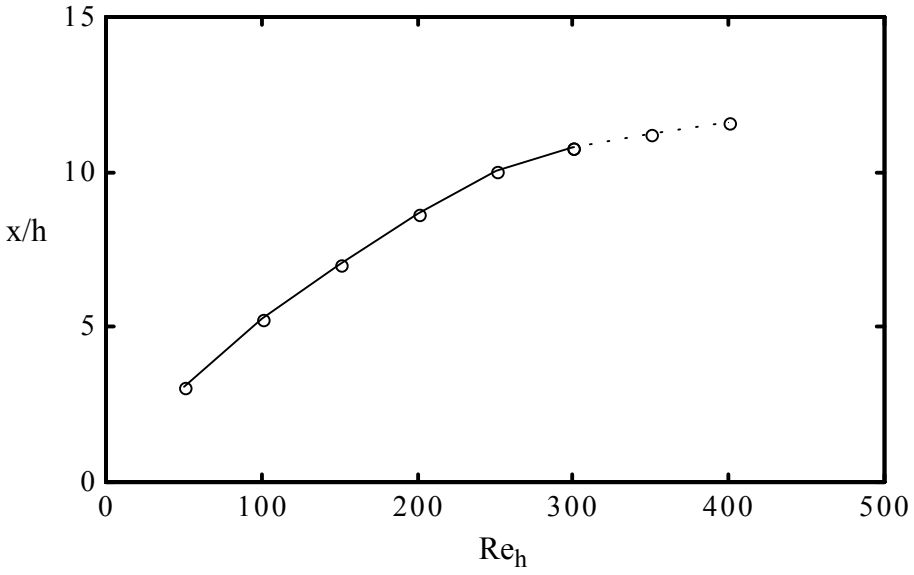

Figure 3.18: Reattachment length as a function of Re_h for the computation by the projection method.

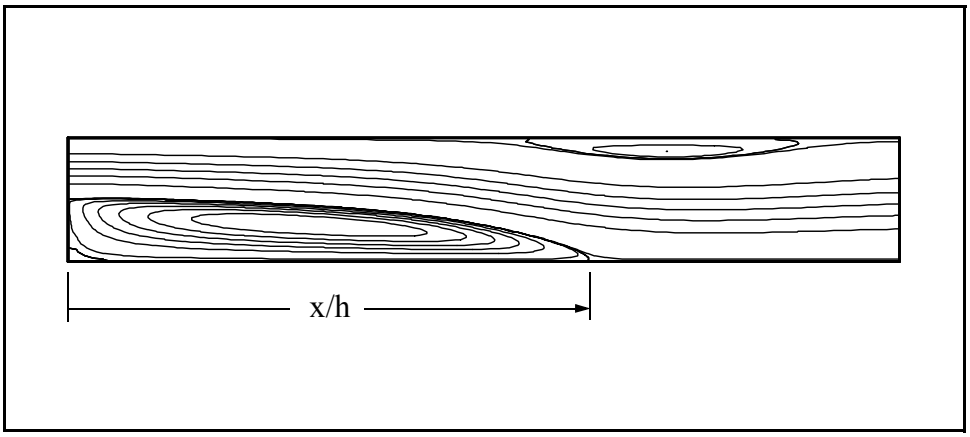

Figure 3.19: Streamlines for the backward facing step at Re_h of 250.

The lack of matching between simulated and experimental results at higher Reynolds numbers is attributed to the development of three dimensional effects in the flow [76].

The reattachment length predicted by the projection method for Reynolds numbers 350 and higher fluctuates by as much as 10%. At this Reynolds number, spots of low pressure indicating shed vortices can be seen just downstream of the upper corner of the step. A steady solution could not be attained at this Reynolds number using zero-gradient outlet boundary conditions without elimination of the unsteady terms in the Navier-Stokes equations when using the first-order-in-time method.

The solution of the laminar backward facing step indicates that the code can resolve the flow with numerical diffusion sufficiently low to capture the effect of the Reynolds number upon the reattachment length.

3.2.5 Rotating Concentric Cylinders

Flow between rotating concentric cylinders at a Reynolds number sufficiently low to ensure laminar flow is among the few flows for which exact solutions to the Navier-Stokes equations exist [151]. The flow domain consists of an annulus of fluid between two counter-rotating tubes of effectively infinite length. This flow is chosen as a validation case since, in addition to the existence of an exact solution with which to make comparisons, the flow tests the implementation of the grid transformation metrics. All previous test cases involved orthogonal grids which include at most nonuniform meshes. The flow geometry is illustrated in Figure 3.20 below.

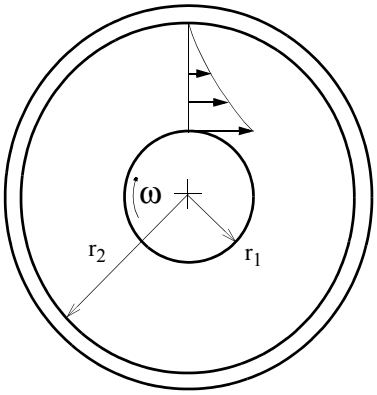

Figure 3.20: Geometry of the rotating concentric cylinders illustrating the velocity profile.

The flow domain for the rotating concentric cylinders consists of the space between an inner cylinder of radius 1 unit and outer tube of radius 3 units. The outer tube is fixed and the inner cylinder rotates at an angular velocity such that the tangential velocity at the surface of the cylinder is one. The resulting fluid motion is illustrated by the velocity profile along a radial line shown in Figure 3.20. The domain is discretized into 61 radial and 61 circumferential nodes with uniform spacing. The Reynolds number is set arbitrarily to 100 and the time step utilized is 0.001. The analytic solution is given by

$$u = \frac{r_2/r - r/r_2}{r_2/r_1 - r_1/r_2} \quad , \tag{3.21}$$

where r_1 is the radius of the inner cylinder and r_2 is the radius of the outer tube. Note

that there is no direct dependence of the solution upon the Reynolds number. Comparison of the computed results and the analytic solution is shown in Figure 3.21 below.

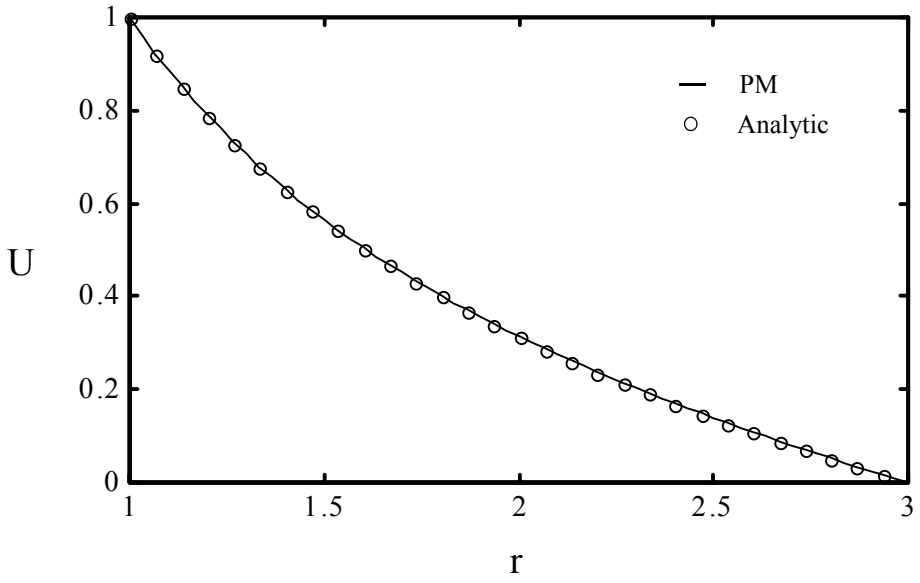

Figure 3.21: Velocity profile for flow between concentric rotating cylinders.

Clearly the code predicts the velocity profile correctly. This indicates that the code implements the grid metric transformations correctly and can therefore resolve flows using meshes with curvilinear coordinates.

3.3 Summary

The numerical technique upon which the projection method code is based was presented. The projection method code was validated through the prediction of the flows for a laminar and turbulent boundary layer, a lid-driven cavity at a Reynolds number of

1000 and 10,000, a laminar backward facing step at various Reynolds numbers, and flow between concentric rotating cylinders. The solution of the laminar boundary layer indicates that the code can resolve flows on grids with cells of high aspect ratio at high Reynolds numbers. The solution of the turbulent boundary layer indicates that the code implements the turbulence transport equations into the algorithm correctly. The solution of the challenging canonical test case of the high Reynolds number lid-driven cavity indicates that the code can resolve flows that are highly skewed with respect to the computational grid. The solution of the laminar backward facing step indicates that the code can resolve the flow with numerical diffusion sufficiently low to capture the effect of the Reynolds number upon the reattachment length. The solution of the flow between concentric rotating cylinders indicates that the code implements the grid metric transformations correctly and can therefore resolve flows using meshes with curvilinear coordinates.

CHAPTER 4

4. Benchmark Flows and Performance Metrics

Two flows are chosen to evaluate the performance of the one-equation near-wall turbulence models. The first benchmark is a zero-pressure-gradient turbulent boundary layer flow corresponding to a direct numerical simulation of a boundary layer flow at a Reynolds number based on momentum thickness of 1410. The second benchmark is a wavy-wall turbulent channel flow corresponding to an experiment and a direct numerical simulation of a wavy-wall channel at a Reynolds numbers based on bulk velocity and channel height of 6760. The characteristics of the benchmark flows and the associated performance metrics by which the near-wall turbulence models are evaluated are described in the sections that follow.

4.1 Turbulent Boundary Layer

The turbulent boundary layer is, along with the plane channel, one of the most common benchmark flows for the testing and evaluation of tubulence models. A boundary layer is a typically thin region of fluid in which the flow velocity is rapidly brought from the freestream value to zero relative velocity at the surface of the object immersed in the fluid [5]. An extensive discussion of boundary layer theory can be found in Ref. 129. At the Reynolds numbers of practical interest, the boundary layer thickness, defined as the distance from the surface of the plate at which the mean velocity reaches a

magnitude of $0.99U_\infty$, is small compared to the characteristic length of the body immersed in the fluid. The boundary layer thickness for a laminar flow over a flat plate varies as $5x/Re_x^{1/2}$, where x is the distance measured from the leading edge of the flat plate and Re_x is the Reynolds number based on distance x [5]. This indicates that for air flowing at 3.3 m/s over a flat plate, the thickness of the boundary layer one meter from the leading edge would be 10 mm. At this height above the flat plate, the velocity is expected to have reached within a few percent of the freestream value. The velocity profile of the laminar boundary layer is self-similar and is obtained by reducing the governing Navier-Stokes equations to an ordinary differential equation [14]. Experiments [79, 91], have verified the Blasius solution. The computation of the laminar boundary layer is useful as a code validation benchmark and was utilized for that purpose in the previous chapter.

The majority of flows occurring in practice are turbulent. A laminar boundary layer flow developing over an object will typically transition to turbulence within some distance from the leading edge of the object. For a flow at 3.3 m/s over a flat plate, transition to fully turbulent flow may occur where the boundary layer is 40 mm thick at about 1 meter from the leading edge. In this case, the transition may take place over a distance of 0.3 meters [116]. An exaggerated illustration of the boundary layer growth and transition from laminar to turbulent flow is shown in the left of the figure below. The position and extent of the transition region, x_{tr}, depends on various parameters including surface roughness, freestream turbulence levels, and acoustic disturbances [151]. In the figure, x_l is the extent of the laminar flow and x_t is the turbulent flow region.

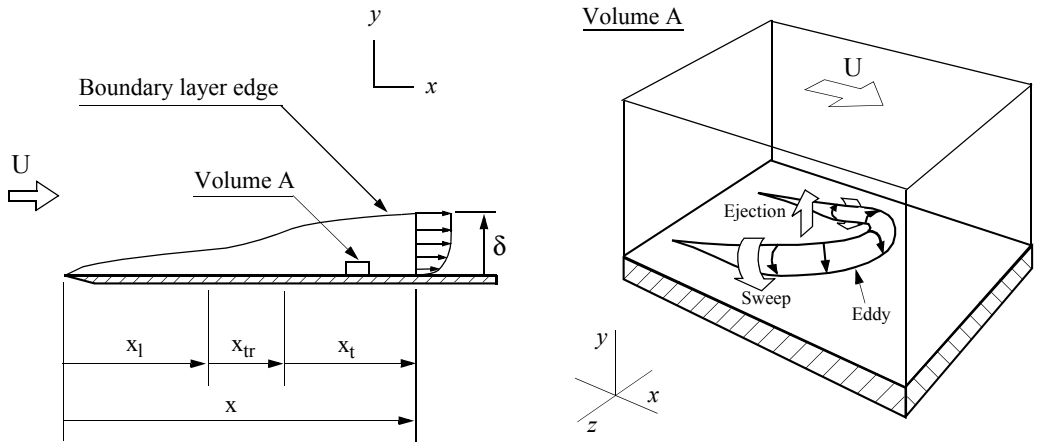

Figure 4.1: Illustration of a boundary layer flow over a flat plate showing the formation of eddies near the wall.

The thickness of the turbulent boundary layer is generally greater than that of the corresponding laminar boundary layer and the skin friction coefficient due to a turbulent boundary layer may be nearly an order of magnitude greater than that of the corresponding laminar flow at high Reynolds numbers. An estimate of the thickness of a turbulent boundary layer over a flat plate suggests a variation with $Re_x^{-1/5}$ [151]. While the thickness of the turbulent boundary layer based on this relation is the most often quoted in the literature, the relation based on the 1/7 power-law velocity profile given by

$$\delta = \frac{0.16x}{Re_x^{1/7}} \quad . \tag{4.1}$$

is considered the most accurate estimate [151]. The parameters here are interpreted as for the laminar boundary layer. The increased skin friction of the turbulent boundary layer is associated with a greater mean velocity gradient near the wall that is, in turn, associated with the actions of streamwise eddies that cause higher speed fluid flowing further from

the wall to move inwards towards the wall and slower speed fluid near the wall to move outwards in a cycle of motions called sweeps and ejections [116]. This process is illustrated in the right of the figure. The eddy of exaggerated size in the illustration is a horseshoe shaped vortical structure that exists near the outer edge of the near-wall region [59]. Below these structures, in the near-wall region, pairs of counter-rotating vortices have been identified [116]. These structures, stretching axially in the streamwise direction, form the streamwise eddies that are associated with the sweeps and ejections. The size of the eddies may range from the Kolmogorov scale of 0.05 mm to the boundary layer thickness of 40 mm for the flow at 3.3 m/s mentioned above [151].

The boundary layer is typically characterized by either the Reynolds number based on distance from the leading edge, defined above, or by the Reynolds number based on the momentum thickness, θ, given by

$$Re_\theta = \frac{U_\infty \theta}{\nu} = \frac{1}{\nu}\int_0^\infty U\left(1 - \frac{U}{U_\infty}\right)dy \quad , \tag{4.2}$$

where U_∞ is the freestream velocity, U is the mean velocity, y is the wall-normal coordinate, and . The definition of Re_θ above allows one to eliminate the effects of the uncertainty of the predicted transition upon the solution. Generally, when evaluating the performance of a turbulence model, the position along the plate at which the quantities of interest are compared to the known solution is that having an Re_θ equal to that of the known solution [157]. Alternately, the Reynolds number based on the friction velocity, Re_τ, could be used to indicate the position along the plate at which solutions are to be compared. Choosing the position according to the value of Re_τ, however, would set the value of the skin friction coefficient. In the absence of pressure drag, it is the skin

friction that determines the power required to propel an object through a fluid. It is therefore the predicted skin friction that is of concern in the majority of engineering studies, not the boundary layer thickness. Using Re_θ to indicate points of comparison therefore permits variations in the predicted skin friction coefficient that, as indicated later, provides a metric of practical consequence by which the performance of the models may be evaluated.

Before continuing with the discussion of the turbulent boundary layer, it is important to define the regions of the boundary layer. As mentioned in Chapter 2, four regions, known as the sublayer, the buffer layer, the log-layer, and the outer layer, can be identified in the boundary layer. Viscosity dominates the motion in the sublayer closest to the wall while the Reynolds shear stress dominates the motion in the log-layer away from the wall. The effects of the viscosity and Reynolds shear stress are of similar magnitude in the buffer layer. The sublayer is considered the region from the wall to y^+ of 5, the buffer layer is the region between y^+ of 5 and about 30, and the log-layer is the region between y^+ of 30 and 100, where y^+ is the wall unit,

$$y^+ = y\frac{u_\tau}{\nu}, \tag{4.3}$$

first defined in Chapter 2. The friction velocity, u_τ, is given by the square root of the wall shear stress divided by the density. In the region beyond y^+ of 100 to 200, corresponding roughly to y/δ of 0.2, the velocity exceeds that predicted by the log-law. The velocity in this region follows a velocity-defect law or law of the wake [151]. Near-wall modeling is generally concerned with the region in which y^+ is less than 100. Beyond this value, the direct effects of the wall, such as the damping of the wall-normal Reynolds stress,

diminish and the turbulence tends to become isotropic. From a modeling point of view, beyond y^+ of 100, the damping functions required for application of the standard k-ε model in the near-wall region presented in Chapter 2 are no longer required.

4.1.1 Turbulence Measurements

Landmark experiments provided measurements of the fluctuating streamwise velocity u, the wall-normal velocity v, and the spanwise velocity w, in a turbulent flat plate boundary layer at an Re_x of 10^7 [79]. For a freestream velocity U, the maximum magnitudes of the rms values of the fluctuations of u, v, and w, were found to be $0.1U$, $0.06U$, and $0.04U$, respectively. The flow is clearly three-dimensional despite the two-dimensionality of the mean flow. The fluctuations were found to persist very close to the wall where, even at distances from the wall of 0.01δ, the magnitude of u_{rms} is near its maximum of $0.1U$ [151]. Measurements have shown significant fluctuations even at distances of 0.0001δ. The fluctuations were found to extend up to 0.2δ beyond the boundary layer edge. The fluctuations were also found to be intermittent in nature with periods of alternating turbulent and laminar flow in the region of 0.4δ to 1.2δ. Another important finding with significance to near-wall turbulence modeling is that the fluctuations, nearly equal in magnitude for distances greater than 0.8δ, are highly anisotropic near the wall. In the region far from the wall, the assumption of isotropic flow made during the development of the turbulence transport equations is therefore considered valid. Near the wall, however, this assumption does not hold. It is in this region that the production and dissipation of turbulence is greatest and that the model transport equations, specifically that for the dissipation rate, become most suspect [153].

Measurements close to the wall provided little guidance of the variation of quantities such as the dissipation since these measurements, made using traditional instruments such as hot-wire probes, are often subject to effects such thermal conduction that may render the data suspect [151]. This uncertainty in the variation of dissipation is clearly evident in an extensive review of early two-equation near-wall models where the presentation of a plot of the dissipation provides no data points in the region closest to the wall [111]. Experimental studies confirm the validity of the results of direct numerical simulations described in the section that follows.

4.1.2 Turbulence Computations

The common direct numerical simulation (DNS) of a turbulent boundary layer reported in the open literature was that of a flat plate at a Reynolds number based on momentum thickness of about 1410 [136]. This computation solved the Navier-Stokes equations over a domain of extent sufficient to contain the largest turbulent structures and used inlet and outlet boundary conditions that effectively resulted in the computation of the flow in a fully turbulent region downstream of the leading edge of the flat plate. Complete solutions of the boundary layer flow including the laminar flow near the leading edge, the transition region, and the fully turbulent boundary layer are still considered beyond the limits of current computational resources [114]. The DNS solution provided a means of computing the budget terms of the turbulent kinetic energy near the wall, including the dissipation rate of particular interest in this work. These quantities could not be obtained with sufficient precision by experimental means in the region closest to the wall. The variation of the mean velocity, turbulent kinetic energy, dissipation, and Reynolds shear stress is shown in Figures 4.3 and 4.2. The quantities are

plotted against wall units and U and ε are scaled by 1/5 and 10, respectively

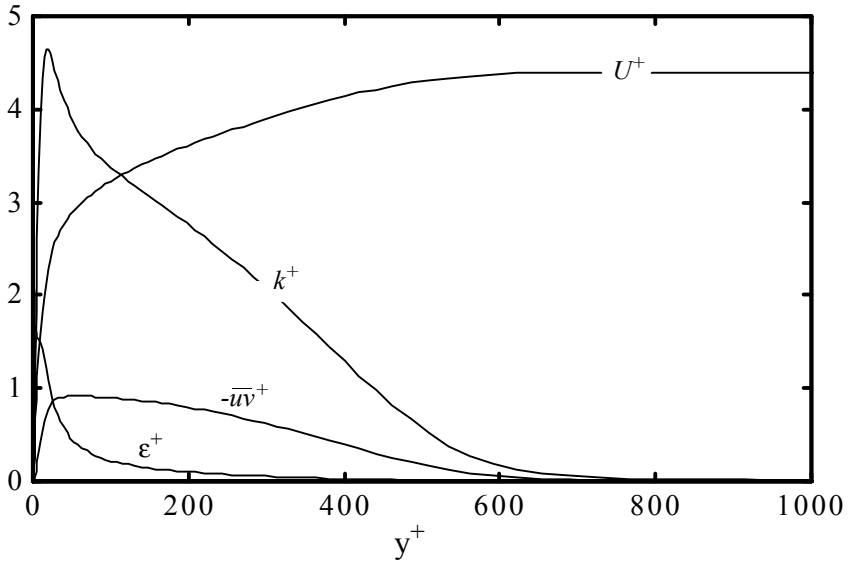

Figure 4.2: Variation of U and the turbulence quantities provided by the DNS for the boundary layer.

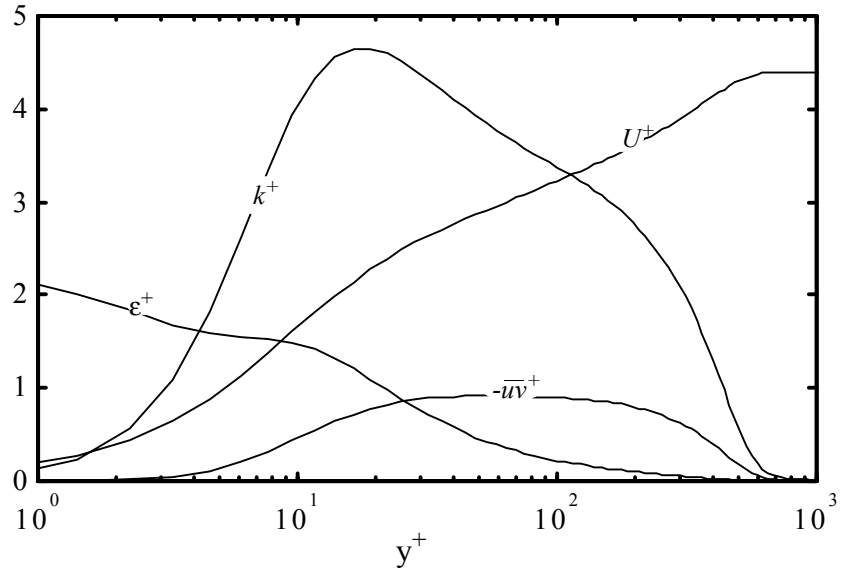

Figure 4.3: Variation of U and turbulence quantities provided by the DNS for the boundary layer near the wall.

The variation of the turbulence statistics compare well with experimental results [79]. This simulation, along with the landmark DNS of a turbulent channel flow [77], has led to detailed analyses of near-wall turbulence modeling in which the predicted budget terms of the standard k-ε model were compared with those given by the DNS results. The boundary layer flow corresponding to a direct numerical simulation of a boundary layer flow at Reynolds number based on momentum thickness of up to 1410 [136] is among the most common test cases for the evaluation of turbulence models [128] and the development of new models [68, 124]. The data available, and of interest in this work, includes the wall-normal distance, the mean velocity, the Reynolds stresses, the dissipation, and the skin friction coefficient. The turbulent kinetic energy is one-half the trace of the Reynolds stresses and is therefore obtained directly from the Reynolds stresses. This data set is shown in the table below. Note that wall unit normalization is implied for this data.

Table 4.1: DNS data set for the turbulent boundary layer.

Parameter	Description
y	Wall-normal coordinate
U	Mean velocity
$\overline{uu}$	Streamwise normal Reynolds stress
$\overline{vv}$	Wall-normal Reynolds stress
$\overline{ww}$	Spanwise normal Reynolds stress
$\overline{uv}$	Reynolds shear stress
ε	Dissipation
c_f	Skin friction coefficient

The data shown in the table above is available for three streamwise locations in the boundary layer where Re_θ is 300, 670, and 1410. Of the three solutions, the highest Re_θ is the most commonly used for evaluations. It should be noted that the higher turbulence statistics for the position corresponding to the highest Re_θ are not considered as reliable as those for the upstream positions [73]. The series expansion coefficients for the turbulence quantities should be considered nominal values. The mean velocity, turbulent kinetic energy, dissipation rate, and Reynolds stresses at the highest Re_θ position are, however, considered reliable and this solution has often been used for model evaluation [128, 157, 68]. The solution corresponding to the Re_θ of 1410 is utilized in this work.

The grid used for the RANS computations completed for this benchmark flow expands geometrically with distance from the inlet and wall. The spacing in the streamwise direction is 0.0025 at the inlet and the wall-normal spacing is 2 grid units. The grid, shown in Figure 4.4 below, contains 63 node points in the streamwise direction and 127 node points in the wall-normal direction. The flow is from left to right. The grid utilized for the grid-independence computation has double the number of points in both directions and a wall-normal spacing of 1 grid unit.

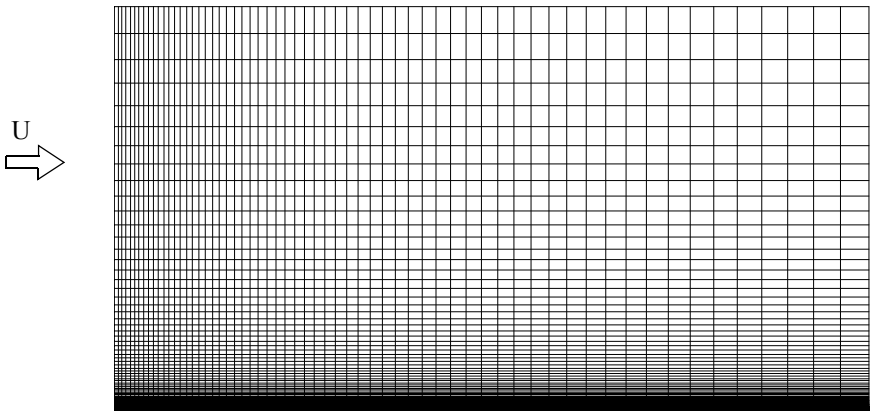

Figure 4.4: Grid for the boundary layer computations.

The boundary conditions are as outlined in Chapter 3 for the validation computations. The results of the computation are described in Chapter 5.

4.1.3 Performance Metrics

The evaluation of near-wall turbulence models requires the comparison of quantities computed using the near-wall turbulence models with the accepted or benchmark values of those quantities provided by DNS or experimental data. These parameters, first mentioned when discussing the evaluation methodology in the first chapter, form the metrics that are utilized to evaluate the performance of the near-wall models for the boundary layer flow. Before continuing with the description of the performance metrics, the elements of the evaluation as applied to the boundary layer flow

are presented in Figure 4.5 below.

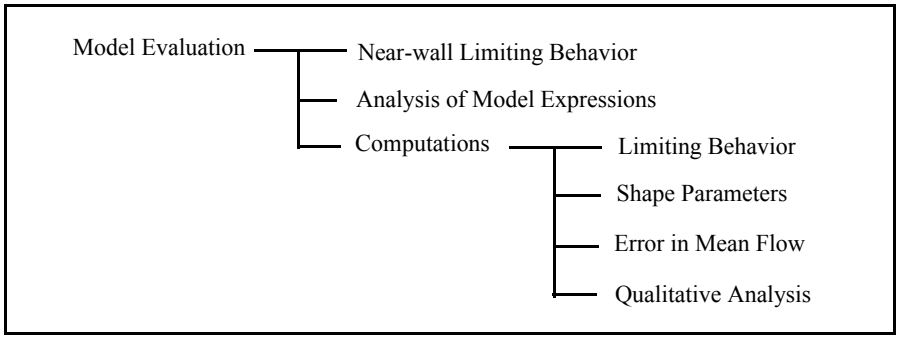

Figure 4.5: Elements of the model evaluation for a turbulent boundary layer.

As indicated in Figure 4.5 above, the model evaluation completed for this study is divided into three components. The first part is the near-wall limiting behavior in which the asymptotic behavior of the models is analyzed. The second part is the analysis of the model expressions or budget anaylsis in which the modeled budget terms of the turbulent kinetic energy equation are evaluated against the DNS data. The last part is the computation in which the predicted results of a numerical computation of the flow are evaluated against the DNS data. This part is further broken into four additional parts. The first consists of an evaluation of the predicted asymptotic behavior. The second consists of an evaluation of the predicted shape function, log-law parameters, and skin friction coefficient. The third and fourth parts include an error analysis and a qualitative analysis. Each of the metrics presented below can be associated with one of the three components shown in the second level of the chart shown in Figure 4.5.

The boundary layer is characterized by the thickness, the displacement thickness,

the momentum thickness, and the shape factor given by

$$\delta = y(U = 0.99U_\infty) \quad , \tag{4.4}$$

$$\delta^* = \int_0^\delta \left(1 - \frac{U}{U_\infty}\right) dy \quad , \tag{4.5}$$

$$\theta = \int_0^\delta \frac{U}{U}\left(1 - \frac{U}{U_\infty}\right) dy \quad , \tag{4.6}$$

and

$$H = \delta^* / \theta \quad . \tag{4.7}$$

respectively. Evaluations of the performance of turbulence models typically include the comparison of the predicted values of these parameters to the accepted values [10]. The position along the flat plate at which the computed profile is evaluated against the DNS is that where the Reynolds number based on momentum thickness is equal to that of the DNS. This is necessary in order to decouple the evaluation of the near-wall modeling from any transition characteristics of the model as indicated earlier. In this work, the shape factor, *H*, will form the first metric by which the models are evaluated. The benchmark value of *H* was computed in this work using the DNS for the boundary layer and is given in Chapter 5. Note that the boundary layer thickness is not used as a metric since it relies upon an arbitrary definition of when the velocity is sufficiently close to the freestream value to indicate the edge of the boundary layer.

Since the boundary layer flow is nearly one-dimensional, the elimination of the pressure gradient from the Navier-Stokes equations, and the assumption that the effect of the molecular viscosity is negligeable beyond the viscous sublayer, allows the derivation of the log law [151]

$$U^+ = \frac{1}{\kappa}\log y^+ + B \ . \tag{4.8}$$

The Kármán constant, κ, was first computed to be 0.40 [107]. The present value usually quoted is 0.41 [30, 151]. The Kármán constant may be calculated by $\kappa = (\log y_2^+ - \log y_1^+)/(U_2^+ - U_1^+)$ using points beyond the buffer layer such as $y_1^+ \sim 60$ and $y_2^+ \sim 65$ [10]. The additive constant B can then be obtained by $B = U_2^+ - \frac{1}{\kappa}\log y_2^+$. This provides two additional performance metrics. Viewing the log-law as a curve fit indicates the importance of specifying which points are used in computing the Kármán constant and additive constant.

The skin friction is calculated using the friction velocity that is required for normalization. The friction velocity is defined as

$$u_\tau = \sqrt{\tau_w/\rho} = \sqrt{\nu S_{12}} \quad , \tag{4.9}$$

where S_{12} is the fluid strain rate, $(u_{i,j} + u_{j,i})/2$, evaluated at the wall. For unit freestream velocity, the skin friction coefficient is $c_f = 2u_\tau^2$. Since the velocity is normalized by the friction velocity, $U^+ = U/u_\tau$, the skin friction coefficient can be rewritten as

$$c_f = \frac{2}{U^{+2}}, \tag{4.10}$$

for unit freestream velocity. The value of c_f obtained by the computation is evaluated against the value given by the DNS data. Since the computation of drag is central to many engineering problems, for the reasons indicated earlier, the skin friction coefficient

may be considered among the most important performance metrics for the boundary layer flow.

The three turbulence quantities of importance to the evaluation of two-equation and one-equation near-wall turbulence models based on the Boussinesq approximation are the turbulent kinetic energy, the dissipation rate, and the Reynolds shear stress. Near the wall, the instantaneous fluctuating streamwise, wall-normal, and spanwise velocities are given by [22]

$$u = a_u y + b_u y^2 + \dots , \tag{4.11}$$

$$v = a_v y^2 + b_v y^3 + \dots , \tag{4.12}$$

and

$$w = a_w y + b_w y^2 + \dots , \tag{4.13}$$

respectively. Note that the '+' superscript customarily used to denote normalization using the friction velocity, u_τ, and the kinematic viscosity, ν, is implied for the variables above and all series expansions that follow. The turbulent kinetic energy and dissipation rate are defined as

$$k = \frac{1}{2}\overline{u_i u_i} \tag{4.14}$$

and

$$\varepsilon = \overline{u_{i,j} u_{i,j}} \quad , \tag{4.15}$$

respectively. Note that the turbulent kinetic energy and dissipation rate are per unit mass and that both are normalized. Substituting the relations for the instantaneous velocities into the definitions above, the series expansions for the turbulent kinetic energy,

dissipation, and shear stress near the wall can be written as

$$k = a_k y^2 + b_k y^3 + \ldots , \tag{4.16}$$

$$\varepsilon = 2a_k + 4b_k y + \ldots , \tag{4.17}$$

and

$$-\overline{uv} = a_{uv} y^3 + b_{uv} y^4 + \ldots . \tag{4.18}$$

The constants a_k and a_{uv} are on the order of 0.08 and 0.0007 respectively [135]. It is the one of the goals of near-wall modeling to reproduce this asymptotic behavior. Evaluations of near-wall turbulence models list the values of a_k and a_{uv} predicted by several popular two-equation near-wall (low-Reynolds number) models [128]. To evaluate the asymptotic consistency of the models, a computation is completed and the values of k, ε, and $\overline{uv}$ near the wall are utilized to compute the coefficients of equations (4.16) and (4.18). The difference between the accepted values and the computed values is an indication of the asymptotic consistency of the model. The series expansions can be rewritten as

$$k = a_k y^{n_k} + \ldots , \tag{4.19}$$

$$\varepsilon = a_\varepsilon + \ldots , \tag{4.20}$$

and

$$-\overline{uv} = a_{uv} y^{n_{uv}} + \ldots . \tag{4.21}$$

By taking the logarithms of the equations (4.19) and (4.21), the values of the exponents can be calculated using the first two points away from the surface. The constants of proportionality can then be computed using the first point away from the surface. This

provides an additional five metrics for the evaluation of near-wall models. Equations (4.16) and (4.17) both provide a method of computing the constant a_k. As stated in the previous chapter, the dissipation at the wall is determined by evaluating the modeled turbulent kinetic energy transport equation,

$$\frac{Dk}{Dt} = ((\nu + \frac{\nu_t}{\sigma_k})k_{,j})_{,j} - \overline{u_i u_j} U_{,j} - \varepsilon, \tag{4.22}$$

at the wall. The dissipation at the wall becomes

$$\varepsilon_{wall} = \nu k_{yy_{wall}} . \tag{4.23}$$

During each iteration of the code used to solve the discretized form of the modeled turbulence transport equations, the value of the dissipation at the wall is updated using the discretized form of the relation above, $2k_2/\Delta y^2$. This update enforces the equality of a_k given by equations (4.16) and (4.17) to within the order of accuracy of the discretization of equation (4.23) assuming that the exponent n_k is equal to 2. If the exponent n_k is different from 2 by as little as a few percent, a_k computed by each equation may be different by nearly 15%. Therefore, the difference in the values of a_k computed by both equations indicates that the exponent n_k is not precisely 2. As an indication of the acceptable level of difference in the two values, the values of a_k predicted by the DNS of a channel flow are 0.106, computed by equation (4.16), and 0.110, computed by equation (4.17) [128].

The metrics presented above are useful for the evaluation of the performance of a turbulence model when utilized to compute the flat plate boundary layer flow. For complex flows, that may be defined as those where the rates of strain exist in more than

one dimension, such distinct metrics may not be well defined. It is therefore useful to define a difference or error between the computed and accepted solution as

$$\delta(q) = \left| q_m - q_e \right|, \tag{4.24}$$

where q_m is the quantity of interest predicted by the model and q_e is the accepted value taken to be an experimental or DNS result. Since the computational grid will not generally coincide with the distribution of DNS data points, the computational results are interpolated linearly onto the implied grid of the DNS data. The error defined above is an absolute error. Normalization by the accepted value would cause the error to be unbounded when the accepted value approaches zero and the model prediction is finite. For example, in the flow through a rough-wall channel, there exits a position where the mean velocity gradient is non-zero and the Reynolds shear stress is nearly zero due to a change in sign. Computations of this flow using the eddy viscosity model would predict a finite Reynolds shear stress at this point due to the mean velocity gradient. An error normalized by the accepted value at this point would be of no value in evaluating the performance of the model.

The maximum error in quantitiy q can be determined as

$$\Delta_{max} = max(\delta(q)) \tag{2.85}$$

where $\delta(q)$ ranges over the entire flow domain. This error would indicate the region in the flow in which the model performs most poorly. The total difference or error in quantitiy q is defined as

$$\Delta(q) = \sum_{j=1}^{N} \delta(q) \Delta y_j, \tag{4.25}$$

where N is the number of points in the wall normal direction and Δy_j is the grid spacing at point j. This is normalized by the area under the curve defined by q_e. The evaluation of the boundary layer flow takes place at only one position along the flat plate so this provides the total error. This provides one additional metric by which the models are evaluated. The metrics are summarized in Table 4.2.

Table 4.2: Turbulence modeling metrics for the boundary layer.

Number	Metric	Description
1	a_k	Series expansion coefficient for k
2	a_ε	Series expansion coefficient for ε
3	a_{uv}	Series expansion coefficient for $\overline{uv}$
4	n_{uv}	Series expansion exponent for $\overline{uv}$
5	ε	Dissipation model compared to DNS
6	ν_t	Eddy viscosity model compared to DNS
7	a_k	Predicted series expansion coefficient for k
8	a_ε	Predicted series expansion coefficient for ε
9	a_{uv}	Predicted series expansion coefficient for $\overline{uv}$
10	n_k	Predicted series expansion exponent for k
11	n_{uv}	Predicted series expansion exponent for $\overline{uv}$
12	H	Shape function
13	c_f	Skin friction coefficient
14	$\Delta(q)$	Total error in q with respect to DNS

In addition to the computation of these metrics, the profiles of u, k, ε, and $\overline{uv}$ are compared to the DNS results such that the ability of each model to predict certain

features of the flow, such as the plateau of ε in the buffer layer, can be evaluated qualitatively.

4.2 Turbulent Wavy-Wall Channel

Flows over wavy surfaces are of interest in the study of water waves generated by wind, the creation of sand dunes in deserts, sediment dunes in river beds, melting of ice on rivers, drag reduction, and enhanced mass and heat transfer [110]. The flow over a wavy boundary is naturally more complex than that over a flat boundary due to the effects of flow curvature and the alternating favorable and adverse pressure gradients. The wavy-wall channel consists of a two-dimensional duct of effectively infinite depth with a plane upper wall and a sinusoidal lower wall. The primary parameters characterizing the geometry are the wave aspect ratio, $2\alpha/\lambda$, and the channel half-height h. The wavy wall is specified by

$$y = \alpha \cos(2\pi x/\lambda) \tag{4.26}$$

The geometry is illustrated along with the regions of recirculating flow in Figure 4.6.

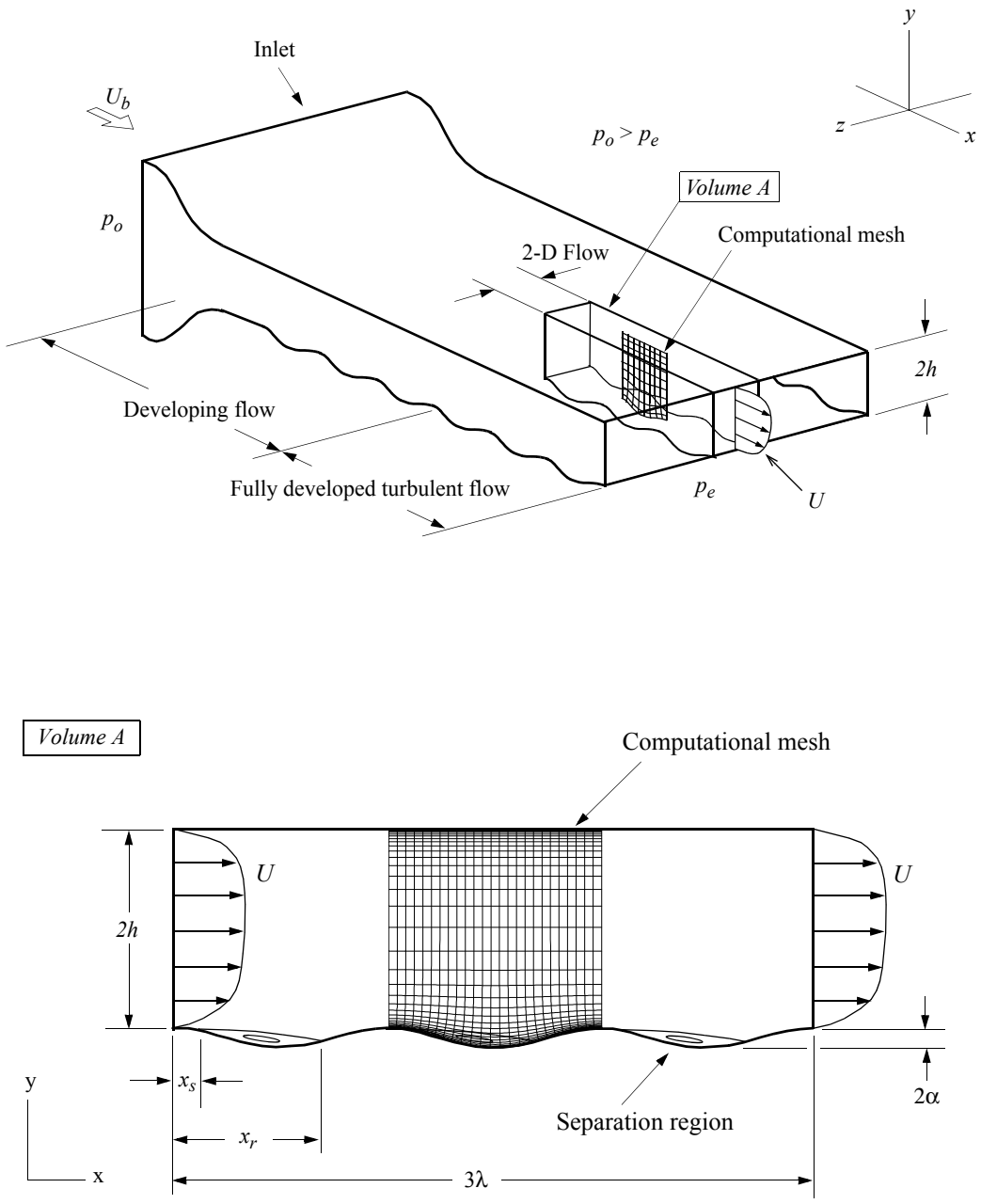

Figure 4.6: Wavy-wall channel illustrating geometry, mean velocity profile, regions of recirculating flow, and the computational mesh.

The flow curvature and varying pressure gradient along the wavy wall modify the turbulence quantities. There is also the possibility of self-induced unsteady flow with vortex shedding [110]. The transverse turbulent fluctuations are increased on the wave up-slope [60] and a double peak in the turbulent kinetic energy has been observed near the wave crest [97]. For small aspect ratios the flow remains attached and the shear stress response is linear. At an aspect ratio of 0.05 instantaneous flow reversal occurs. For an aspect ratio of 0.1, well defined separation and reattachment points appear and a recirculating region of fluid forms in the forward section of the trough. Such a recirculating region is illustrated in Figure 4.6 above. The precise values of the aspect ratios at which these phenomena occur depend on the Reynolds number [60]. The values quoted above apply to a channel with a Reynolds number based on bulk velocity, defined below, on the order of a few thousand.

The aspect ratio introduced above is defined as

$$a = \frac{2\alpha}{\lambda}, \tag{4.27}$$

where α is the wave amplitude and λ is the wavelength. The wavy-wall channel flow is also characterized by the Reynolds number based on bulk velocity given by

$$Re_b = \frac{U_b h}{\nu}, \tag{4.28}$$

where h is the channel half-height and U_b is the bulk velocity given by

$$U_b = \frac{1}{2h}\int_{-h}^{h} U dy \quad . \tag{4.29}$$

Note that some authors use the full channel height to define the Reynolds number [67]. The convention used here corresponds to that used for the plane channel where Reynolds

number is based on half the channel height. This definition was used for the wavy-wall computations of reference 60. The bulk velocity must be obtained by integration over the full height of the wavy-wall channel since, unlike the plane channel, the mean flow is asymmetric. Alternately, the flow can be characterized by the Reynolds number based of the friction velocity, Re_τ, given by integrating the shear stress over both walls.

Like the plane channel, the pressure gradient existing across the wavy-wall channel is specified for the computation. The development of the flow field depends on the choice of turbulence model. Therefore, for a given pressure gradient, a series of computations utilizing various turbulence models will generally result in different values of Re_b and Re_τ. For example, two distinct turbulence models may predict separation regions of differing extents resulting in differing shear stress distributions and therefore different values of Re_τ. The pressure gradient is the parameter characterizing the flow through the wavy-wall channel. Aternatively, Re_τ can be based on the total drag which, in the case of separated flow, would include pressure drag. This total drag is, of course, equal to the force due to the mean pressure gradient in the streamwise direction. For the wavy-wall flow investigated in this work, the parameters are given in Table 4.3. All parameters are normalized appropriately by the kinematic viscosity, bulk velocity, and wavelength.

Table 4.3: Parameters for the wavy-wall channel.

Parameter	Value
$2\alpha/\lambda$	0.1
$2h$	1.0
λ	1.0
Re_b	~ 3380
p_x	- 0.0157

The pressure gradient, p_x, was computed from the total drag provided by the source of the DNS data. The value Re_b given in Table 4.3 is model dependent, as stated above, and therefore not strictly a parameter defining the flow. Often Re_b is based on the full channel height [60]. In that case, Re_b would be 6760 for the flow above.

4.2.1 Turbulence Measurements

Several well documented experimental studies of flows over wavy surfaces have been conducted over the last three decades [2, 19, 45, 67, 83, 108, 127, 132, 147, 160]. The Norris-Reynolds one-equation near-wall model was utilized to study the turbulent flow in a channel with a flexible wavy wall driven in a time dependent manner [108]. Studies such as those of references 2 and 147 presented measurements of the shear stress perturbations at the surface of small-amplitude solid waves. It is generally agreed that experiments require at least eight wavelengths to ensure that the flow becomes effectively periodic [110]. A listing of the various experiments is given in Table 4.4 below.

Table 4.4: Experiments of the wavy-wall channel.

Reference	$2\alpha/\lambda$	Re	Measurements	Comments
[68] 1996	0.1	6760	Wall pressure, skin friction, mean velocity, fluctuating velocities	Separated flow Data obtained at ten stations along wavelength Separation and reattachment at x/λ= 0.22, 0.58
[131] 1993	0.095	-	-	-
[45] 1986	0.03125	12800	Mean and fluctuating velocities	Linear shear stress response
	0.05	77600		nonlinear shear stress response
[2] 1986, 1981	0.014	11940-24500	Mean and fluctuating wall shear stress	Linear shear stress response
[85] 1986	0.125 0.05 0.20	9600 1700 8160	Wall pressure, mean and fluctuating velocities, flow visualization	Instantaneous flow reversal separated flow
[19] 1984	0.2	24000	Wall pressure, mean and fluctuating velocities	Separated flow
[164] 1979	0.125 0.2	6000-64000	Mean velocity, turbulent velocity, flow visualization	Separated flow
[152] 1978	0.0125	11000-64000	-	Linear shear stress response
[164] 1977	0.0125 0.03125	6000-64000	Wall pressure and shear	Linear shear stress response
[110] 1975	-	-	-	-
[136] 1971	-	-	-	-

The experimental work of reference 67 and the DNS of references 97 and 25, described shortly, are complementary and used in this work as benchmark flows for the evaluation of the performance of the near-wall models. The data available from the experiment include the mean velocities u and v, the Reynolds stresses $\overline{uu}$, $\overline{vv}$, and $\overline{uv}$, the

wall pressure and shear stress at ten stations through the channel. The data available is reviewed in Table 4.5 below. All quantities are normalized appropriately using the bulk velocity and kinematic viscosity. The subscripts and superscripts often used to denote this normalization are dropped for convenience.

Table 4.5: Data available for the wavy-wall channel experiment.

Flow	Description
x	Streamwise position
y	Wall-normal position
U	Streamwise mean velocity
V	Wall-normal mean velocity
$\overline{uu}$	Streamwise normal Reynolds stress
$\overline{vv}$	Wall-normal Reynolds stress
$\overline{uv}$	Reynolds shear stress
c_p	Surface pressure coefficient
c_f	Skin friction coefficient

4.2.2 Turbulence Computations

The variation of the mean velocity, turbulent kinetic energy, and Reynolds shear stress close to the separation point is shown in Figure 4.7 for a computation using NR The variation is similar to the DNS. All quantities are normalized appropriately by the kinematic viscosity and bulk velocity. Clearly the flow is asymmetric.

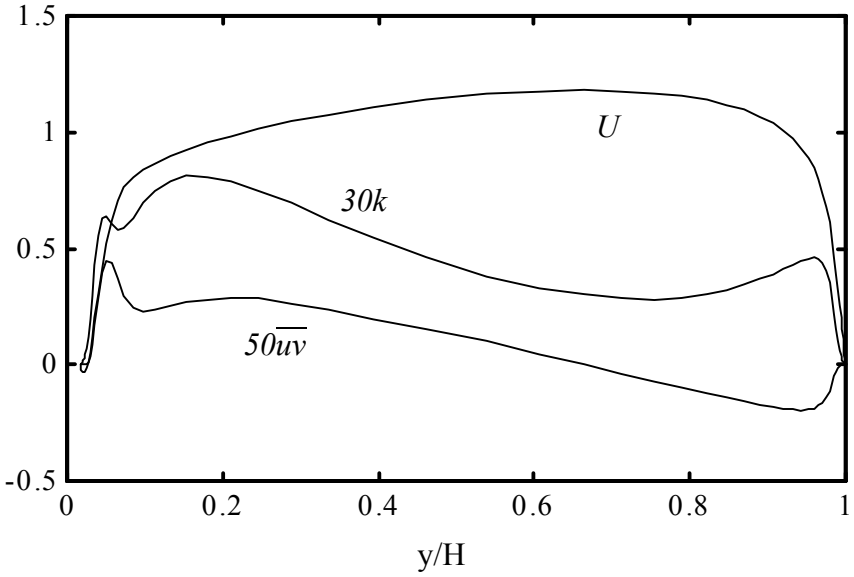

Figure 4.7: Variation of the U, k, and $\overline{uv}$ at $x/\lambda = 0.2$.

Figure 4.8 shows the mean velocity thoughout the wavy-wall channel at five locations. The variation of the turbulent kinetic energy and Reynolds shear stress is shown in Figures 4.9 and 4.10.

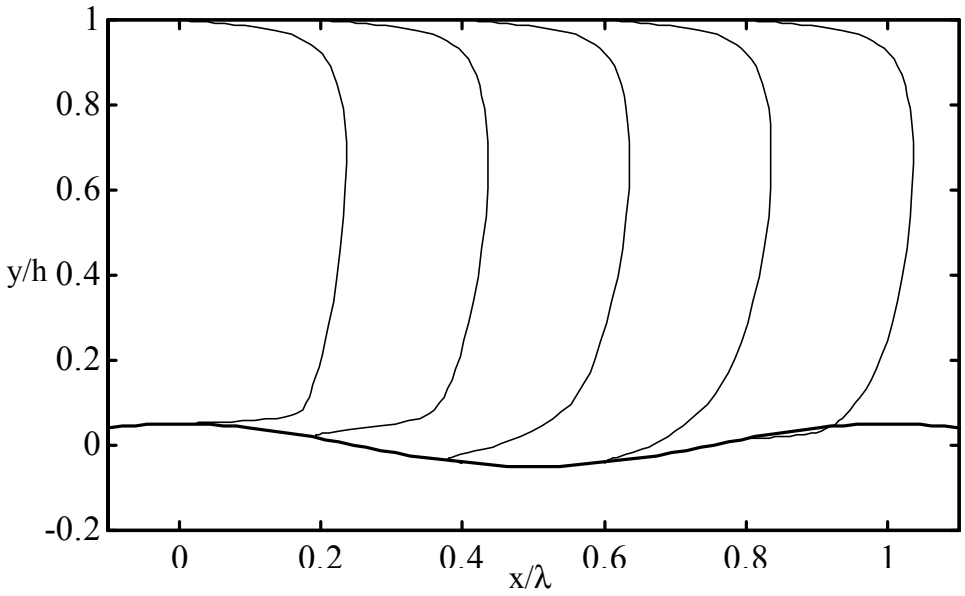

Figure 4.8: Profiles of *U* throughout the channel.

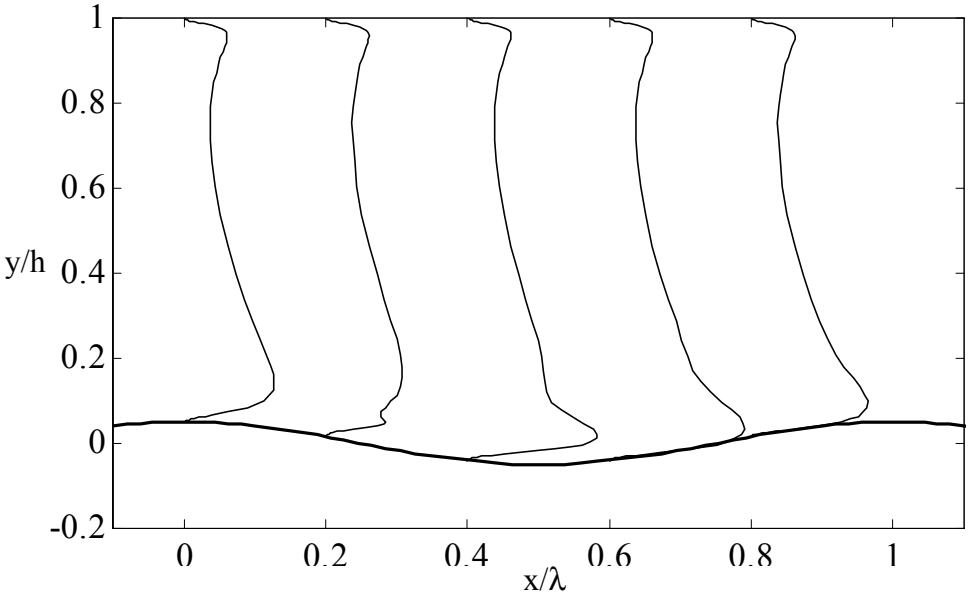

Figure 4.9: Profiles of *k* throughout the channel.

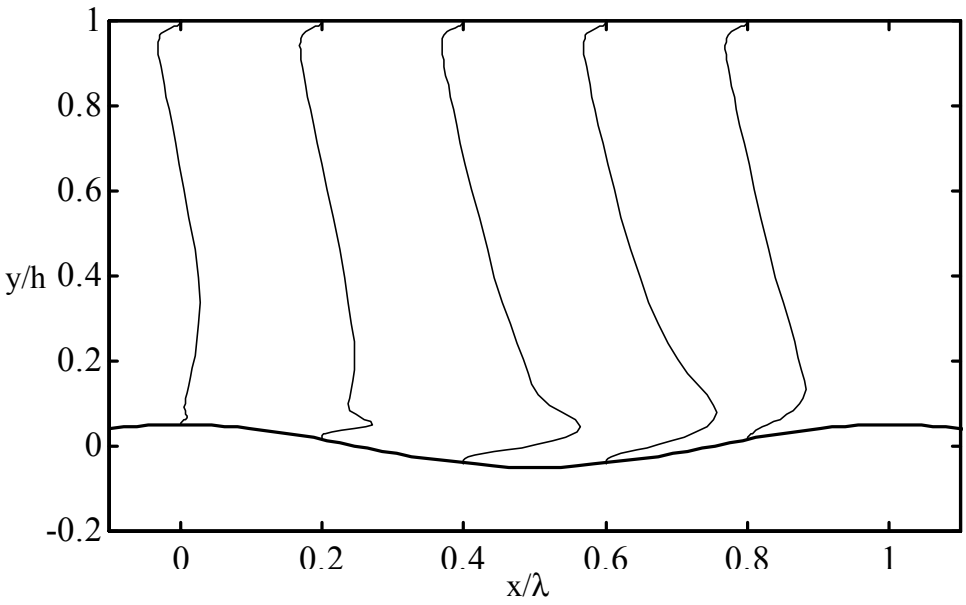

Figure 4.10: Profiles of $\overline{uv}$ throughout the channel.

A distinctive double peak in k and $-\overline{uv}$ near the wavy-wall surface can be seen on the left side of Figure 4.7. These quantities resemble those of the plane channel on the flat surface of the channel on the right of Figure 4.7. The DNS of reference 25 demonstrates the sensitivity of the turbulence quantities to grid density and shows that, in contrast to reference 97, the Reynolds shear stress on the plane wall increases beyond that of a plane channel as the grid density is increased. The overall similarity of the results of the DNS of references 25 and 97 can be considered an indication of the validity of both sets of data for the model evaluation completed in this work. The various wavy-wall computations reported in the literature are reviewed in Table 4.6 below.

Table 4.6: Computations of the wavy-wall channel.

Reference	$2\alpha/\lambda$	Re	Grid	Comments
[61] 1999	0.031 0.200	10600	48x48x71	LES, linear stress response LES, separated flow, x/λ= 0.1, 0.7
[25] 1998	0.100	6920	36x21x64 48x21x64	DNS, separated flow, x/λ= 0.14, 0.59
[36] 1997	0.050 0.100	1000	128x64x65	DNS, linear stress response DNS, separated flow
[Present] 2003	0.100	6790	101x127	RANS, separated flow
[99] 1996	0.100	6760	256x128x96	DNS, separated flow
[97] 1993	-	-	-	-
[113] 1991	0.03125 0.200	12800 8160	328x99 (50 nodes per wavelength, 6 waves)	RANS, linear stress response RANS, separated flow, x/λ= 0.08, 0.73
[134] 1985	-	-	-	RANS

Flow through a fully developed plane channel is two dimensional in the mean with all variables except the pressure being a function of only the wall-normal dimension. The flow in a wavy-wall channel is two-dimensional and periodic in the mean. This allows computation over a single wavelength for RANS computations. The DNS and LES generally require several wavelengths to permit large scale turbulent motions [60]. The data available for the DNS is shown in Table 4.7.

Table 4.7: Data available for the DNS of the wavy-wall channel.

Flow	Description
x	Streamwise position
y	Wall-normal position
U	Steamwise mean velocity
V	Wall-normal mean velocity
$\overline{uv}$	Reynolds shear stress
c_p	Surface pressure coefficient
c_f	Skin friction coefficient

The discretization of the flow domain was illustrated by the computational mesh shown in Figure 4.6 above. The grid used for the RANS computations completed for this work is body-fitted and expands geometrically with distance from the walls. The grid, shown in Figure 4.11 below, contains 102 node points in the streamwise direction with one cell overlap and 127 node points in the wall-normal direction. The spacing in the streamwise direction is 0.005 and the nominal wall-normal spacing is 2 grid units or y^+= 0.05. The overlap allows simple implementation of the periodic boundary conditions.

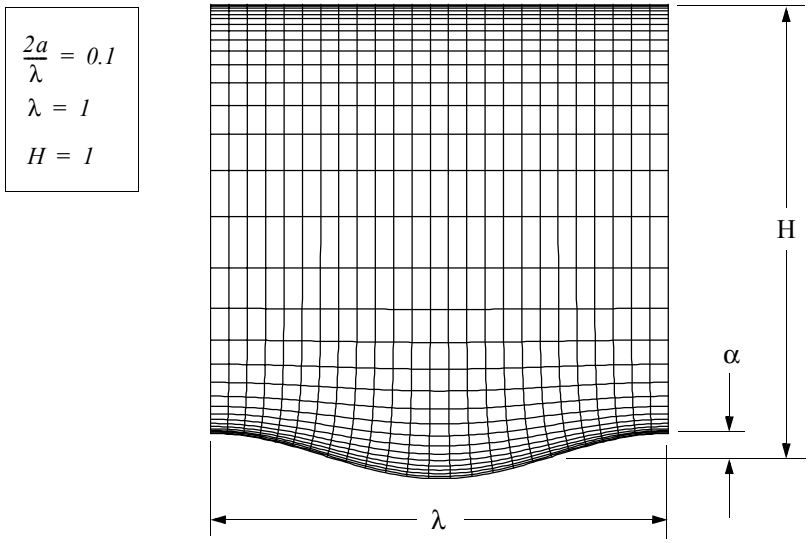

Figure 4.11: Grid for the wavy-wall computation showing every fourth grid line.

The boundary conditions at the upper and lower walls are no-slip. The results of the computation are described in the following chapter.

4.2.3 Performance Metrics

The performance metrics by which the computations of the wavy-wall channel flow are to be evaluated were first mentioned when discussing the evaluation methodology in Chapter 1. The elements composing the evaluation of the models completed in this work are shown in Figure 4.12.

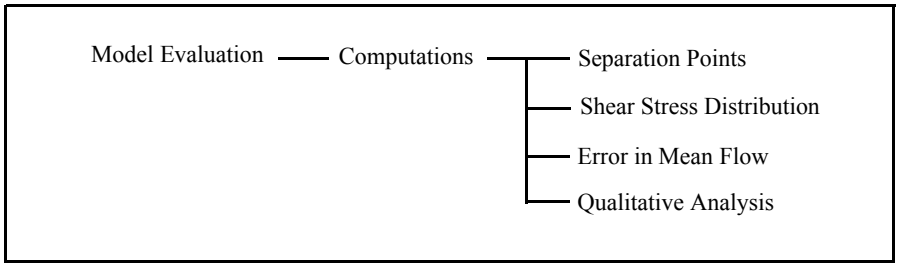

Figure 4.12: Elements of the model evaluation for the wavy-wall channel.

The most pronounced characteristic of the wavy-wall flow, for waves with sufficiently high aspect ratios, is the separation and reattachment of the fluid. The flow typically separates shortly behind the crest of the wave and reattaches some distance before the crest of the following wave. The separation and reattachment points for the DNS and LES of references 25, 60, 97, and the experiment of reference 67 are given in Table 4.8. The quantities x_s/λ and x_r/λ are the separation and reattachment points, respectively. Since the wavelength is one unit, all references to x can be interpreted as x/λ.

Table 4.8: Separation and reattachment points for the wavy-wall channel.

Reference	x_s	x_r
DNS [25]	0.14	0.59
LES [60]	0.10	0.70
Experiment [67]	0.22	0.58

The separation and reattachment points for the DNS can be estimated from the velocity data using linear interpolation $x_s = x_1 - u_1 / u_2 (x_2 - x_1)$, where x_1 and x_2 correspond to

the points where the velocity in the streamwise direction nearest the wall changes sign. The separation and reattachment points for the DNS of reference 25 were noted in the reference. Note that the results of both DNS match well. The DNS predicts an earlier separation than that observed in the experiment, but predicts a reattachment very close to the experimentally observed value.

The error in the predicted separation and reattachment points will be defined as $e_s = (x_{s_m} - x_{s_e})/x_{s_e}$ and $e_r = (x_{r_m} - x_{r_e})/x_{r_e}$, respectively. Subscript m denotes the prediction of the model and e denotes DNS or experimental data. The extent of the separation region can be defined as $e_e = (\Delta x_m - \Delta x_e)/\Delta x_e$, where $\Delta x = x_r - x_s$. The sign of the error will indicate whether the model predicts an early or late separation, early or late reattachment, or an expanded or contracted separation region. For the k-ε model, an early separation may indicate that the turbulence model predicts excessive ε while late separation may indicate that the model predicts excessive k. Historically, the standard k-ε model has been associated with the production of excessive k that tends to promote attached flows [86, 148, 153]. The separation and reattachment points or errors provide three metrics for the evaluation of the models.

The ability of the models to predict the skin friction distribution is an important measure of performance. It is known that the standard k-ε models fails to predict the skin friction correctly over curved surfaces while other two-equation models, such as the k-ω model, tend to fair better in such cases [153]. An error is defined as

$$\Delta(c_f) = \sum_{i=1}^{M} \left| c_{f_m} - c_{f_e} \right|, \tag{4.30}$$

where M is the number of points along the surface. This is normalized by the area under the curve defined by c_{fe}. The skin friction is given by

$$c_f = \frac{2\nu S_{ij}}{U_b^2}\ , \tag{4.31}$$

where S_{ij} is the mean strain rate and U_b is the bulk velocity.

The availability of data throughout the channel at several streamwise locations provides a means of computing an overall error in U, k, and $-\overline{uv}$. As was done for the computations of the boundary layer, the computed results are interpolated onto the implied DNS grid. The total error in quantity q is given by

$$\Delta(q) = \sum_{i=1}^{M} \sum_{j=1}^{N} |q_m - q_e| \Delta y_j , \tag{4.32}$$

where Δy_j is the grid spacing at point j, q_m and q_e are the quantities given by the computations being compared, N is the number of points in the wall-normal direction, and M is the number of locations in the streamwise direction. This is normalized by the area under the curve defined by q_e.

Table 4.9: Turbulence modeling metrics for the wavy-wall channel.

Number	Metric	Description
1	x_s	Separation point
2	x_r	Reattachment point
3	x_e	Extent of the recirculating region
4	$\Delta(c_f)$	Error in c_f with respect to the DNS
5	$\Delta(q)$	Error in q (= U, k, $\overline{uv}$) with respect to the DNS

In addition to these metrics, the predicted profiles of U, k, and $-\overline{uv}$ are plotted for qualitative comparison.

4.3 Summary

The turbulent boundary layer is among the most common benchmark cases for the evaluation of turbulence models. The DNS provides the velocity, turbulent kinetic energy, dissipation, and Reynolds shear stress required to evaluate two-equation turbulence models. The metrics by which the models are evaluated for the boundary layer include the series expansion coefficients and exponents, the shape factor, the Kármán constant, the log-law additive constant, the skin friction coefficient, and the total errors in the quantities of interest. The wavy-wall channel provides a flow with a well defined separation region and thus presents a challenging case by which the performance of turbulence models can be evaluated. The DNS provides the velocity, turbulent kinetic energy, and Reynolds stresses at several locations along the sinusoidal wave. The metrics utilized to evaluate the performance of the turbulence models include the predicted separation and reattachment points, the extent of the separation region, and the total errors in the quantities of interest.

CHAPTER 5

5. Results and Discussion

This chapter is divided into four sections. The first two sections present the analysis of the near-wall limiting behavior and the analysis of the model expressions. The third section presents a new one-equation near-wall model. The fourth section presents the results of the computations of the benchmark flows. In general, data used for baselines for comparison or benchmark values are represented by symbols in the figures while computed results are represented by solid lines with and without symbols.

5.1 Asymptotic Behavior

The three parameters of interest to the evaluation of near-wall models for two-equation closures are k, ε, and $-\overline{uv}$. The series expansions showed that k varies as the square of distance from the wall, ε is constant at the wall, and $-\overline{uv}$ varies as the cube of the distance from the wall. The leading terms in the expansions for k, ε, and $\overline{uv}$ are $k = a_k y^2$, $\varepsilon = a_\varepsilon = 2a_k$, and $-\overline{uv} = a_{uv} y^3$, respectively. Note that these variables are normalized by the friction velocity and kinematic viscosity. The accompanying '+' superscript customarily used to denote normalization is dropped for convenience. The constants for the turbulent boundary layer DNS and turbulent channel flow DNS are given in the table below. Note that the values for the lower Reynolds number boundary layer flow indicate that the constants are not independent of the Reynolds number. These

contants are, however, less dependent on the Reynolds number than quantities such as the skin friction coefficient. The values of the constants given in the last row is evaluated using the DNS for the boundary layer. The ratio $k/\varepsilon y^2$ is 0.5 regardless of the Reynolds number and could be used in place of the constant a_ε to evaluate the asymptotic consistency [135]. The modeled k equation provides the correct variation of k provided that the variation of ε and $-\overline{uv}$ are correct. Therefore, only the analysis of the variations of ε and $-\overline{uv}$ with distance from the wall is required for the analysis of each one-equation near-wall model.

Table 5.1: Series expansion constants.

Data	a_k	n_k	a_{uv}x10^3	n_{uv}	a_ε
TCH Re_τ=185 [128]	0.106	-	1.10	-	0.220
TCH Re_τ=395 [128]	0.080	-	0.70	-	0.166
TBL Re_θ=1410 [128]	-	2	-	3	0.260
TBL Re_θ=1410	0.128	2	1.32	3	0.251

The models for ε and ν_t, first given in Chapter 2, are reviewed in Table 5.2 below. The order of listing follows the reported date of development.

Table 5.2: Models for the dissipation and eddy viscosity.

Model	Relations	C_ε	C_ν	A_ε	A_ν
WS	$\varepsilon = C_\varepsilon k^{3/2}/(y(1-e^{-A_\varepsilon R_y}))$ $\nu_t = C_\nu \sqrt{k} y (1-e^{-A_\nu R_y})$	0.416	0.22	0.263	0.016
NR	$\varepsilon = C_\varepsilon \frac{k^{3/2}}{y}(1+A_\varepsilon/R_y)$ $\nu_t = C_\nu \sqrt{k} y (1-e^{-A_\nu R_y})$	$\frac{C_\mu^{3/4}}{\kappa}$	$\kappa C_\mu^{1/4}$	5.3	0.0198
HP	$\varepsilon = 2(\nu + C_\varepsilon \nu_t)k/y^2$ $\nu_t = C_\nu \sqrt{k} y (1-e^{-A_\nu R_y})$	0.945	0.22	NA	0.012
CP	$\varepsilon = C_\varepsilon k^{3/2}/(y(1-e^{-A_\varepsilon R_y}))$ $\nu_t = C_\nu \sqrt{k} y (1-e^{-A_\nu R_y})$	$\frac{C_\mu^{3/4}}{\kappa}$	$\kappa C_\mu^{1/4}$	$C_\varepsilon/2$	0.0143
RM	$\varepsilon = C_\varepsilon \frac{v_r k}{y}\left(1+2.12\frac{\nu}{v_r y}\right)$ $\nu_t = C_\nu v_r y$ $v_r^2 = k(A_\varepsilon R_y + A_\nu R_y^2)$	0.769	0.33	$4\text{x}10^{-4}$	$4.65\text{x}10^{-5}$

The first near-wall model under consideration is that of Wolfshtein. Replacing the exponential in the damping function used for ε with the series expansion gives $1-e^{-A_\varepsilon R_y} = A_\varepsilon R_y - \frac{1}{2}(A_\varepsilon R_y)^2 + \ldots$. The turbulence Reynolds number, R_y, was defined in Chapter 2 as $R_y = \sqrt{k} y/\nu$. When k and y are normalized by the friction velocity and viscosity, R_y is given by $R_y = \sqrt{k} y$. Note that the customary '+' superscript

denoting normalization by wall units is dropped for convenience. The leading term is therefore $A_\varepsilon R_y = A_\varepsilon \sqrt{k} y$. In the limit as y approaches zero, WS therefore gives

$$\varepsilon_0 = \lim_y \left[\frac{C_\varepsilon k^{3/2}}{y(1 - e^{-A_\varepsilon R_y})} \right] \sim \frac{C_\varepsilon k}{A_\varepsilon y^2} \sim \frac{C_\varepsilon a_k}{A_\varepsilon} = 1.58 a_k . \tag{5.1}$$

Due to the choice of constants in the model, the value dos not agree precisely with the series expansion.

Replacing the exponential in the damping function with the series expansion, ν_t for WS at the wall becomes

$$\nu_t = C_\nu \sqrt{k} y A_\nu R_y \sim y^4 \tag{5.2}$$

since k and R_y vary as y^2. Note that ν_t given by the model, and in all relations following, has been normalized by the kinematic viscosity ν. Since the mean velocity near the wall varies as y, the first derivative of the mean velocity is constant. The Reynolds shear stress then varies as ν_t near the wall. The Reynolds shear stress given by WS therefore varies as $-\overline{uv} \sim y^4$. WS therefore does not reproduce the behavior of the Reynolds shear stress at the wall.

In the limit as the wall is approached, CP gives

$$\varepsilon_0 = \lim_y \left[\frac{C_\varepsilon k^{3/2}}{y(1 - e^{-A_\varepsilon R_y})} \right] \sim \frac{C_\varepsilon k}{A_\varepsilon y^2} \sim \frac{C_\varepsilon a_k}{A_\varepsilon} = 2 a_k \tag{5.3}$$

The constants for CP were chosen by the developers such that $A_\varepsilon = C_\varepsilon / 2$ to provide the correct value of ε at the wall [24]. Therefore, CP may be expected to reproduce ε at

the wall provided that the variation of k is correct. The Reynolds shear stress given by CP is different than that given by WS only in the values of the constants. Therefore, like WS, CP does not reproduce the behavior of $-\overline{uv}$ at the wall.

In the limit as the wall is approached, NR gives

$$\varepsilon_0 = \lim_y \left[C_\varepsilon \frac{k^{3/2}}{y} \left(1 + \frac{A_\varepsilon}{\sqrt{k} y} \right) \right] \sim C_\varepsilon A_\varepsilon a_k = 5.3 \frac{C_\mu^{3/4}}{\kappa} a_k = 2.12 a_k . \tag{5.4}$$

Therefore, NR may be expected to reproduce ε at the wall. The expression for ν_t of NR differs from that of WS and CP only in the values of the constants. Therefore, like WS and CP, NR does not reproduce the behavior of $-\overline{uv}$ at the wall.

In the limit as the wall is approached, HP gives

$$\varepsilon_0 = \lim_y \left[2(1 + C_\varepsilon \nu_t) \frac{k}{y^2} \right] \sim 2 \frac{k}{y^2} \sim 2 a_k . \tag{5.5}$$

Therefore, HP may be expected to reproduce the correct asymptotic value of ε at the wall provided that the variation of k is correct. The expression used for ν_t differs from the previous models only in the values of the constants. HP therefore does not reproduce the behavior of $-\overline{uv}$ at the wall.

In the limit as the wall is approached, RM gives

$$\varepsilon_0 = \lim_y \left[C_\varepsilon \frac{\nu_r k}{y} \left(1 + 2.12 \frac{1}{\nu_r y} \right) \right] \sim 2.12 C_\varepsilon a_k . \tag{5.6}$$

RM does not appear to reproduce ε at the wall. In the limit as the wall is approached ν_t becomes

$$\nu_t = C_\nu y[a_k y^2 (A_\varepsilon a_k^{1/2} y^2 + A_\nu a_k y^4)]^{1/2} \sim y^3 . \tag{5.7}$$

RM therefore reproduces the cubic behavior of ν_t and is therefore the only model listed in Table 5.2 that provides a cubic variation of $-\overline{uv}$ near the wall.

Before continuing the evaluation, the two-equation near-wall model, YS, is investigated. YS provides a benchmark of performance for the more popular two-equation near-wall models in current use [128]. As shown in Chapter 3, ε at the wall is determined by the *k*-equation and thus all two-equation near-wall models using the *k*-equation should be capable of providing the correct value of ε at the wall. The ν_t is given by the relation

$$\nu_t = C_\mu f_\mu k T , \tag{5.8}$$

where $T = k/\varepsilon + \sqrt{\nu/\varepsilon}$. The damping function is

$$f_\mu = (1 - e^{-(a_1 R_y + a_2 R_y^3 + a_3 R_y^5)})^{1/2} , \tag{5.9}$$

where the coefficients, a_1, a_2, and a_3, are the model constants given in Chapter 2. In the limit as the wall is approached, the damping function in wall units gives

$$f_\mu \sim (a_1(\sqrt{k}y))^{1/2} \sim (a_1(a_k^{1/2} y^2))^{1/2} \sim y . \tag{5.10}$$

Since ε approaches a constant at the wall and *k* varies as y^2, the time-scale *T* approaches time-scale $(\nu/\varepsilon)^{1/2}$ at the wall. Therefore,

$$\nu_t = C_\mu f_\mu k T \sim y^3 . \tag{5.11}$$

YS therefore reproduces the variation of $-\overline{uv}$ at the wall. This result is consistent with those in the literature [128].

In summary, WS provides a value of ε at the wall and a variation of $-\overline{uv}$ at the wall that do not agree with the series expansions. CP, NR, and HP reproduce ε at the wall, but do not reproduce the behavior of $-\overline{uv}$. RM does not appear to reproduce ε at the wall precisely, but does reproduce the behavior of $-\overline{uv}$. YS, the benchmark two-equation near-wall model, reproduces the behavior of $-\overline{uv}$ and, do to the form of ε equation, may reproduce ε at the wall. These results are summarized for each model in Table 5.3 below. Recall that, from the series expansions, a_ε/a_k and n_{uv} are 2 and 3, respectively.

Table 5.3: Results of the near-wall asymptotic analysis.

Model	YS	WS	NR	HP	CP	RM
a_ε/a_k	2	1.58	2.12	2	2	1.63
n_{uv}	3	4	4	4	4	3

For the computations, presented in section 5.4, the predicted variation of k naturally depends on the near-wall models of ε and ν_t. Therefore, with respect to the analysis presented above, a choice of model constants providing the correct asymptotic value of ε is not sufficient to guarantee that the predicted ε at the wall will match the known value.

5.2 Analysis of Model Expressions

The budget terms of the k equation of interest in this work include the dissipation rate, ε, and the production, P_k. The production is a function only of $-\overline{uv}$ and mean velocity gradient for nearly one-dimensional flows such as the boundary layer. In turn, $-\overline{uv}$ is a function of ν_t. Therefore, the analysis here includes only a comparison of the predicted ε and ν_t for each one-equation near-wall model to the DNS data. The ε and ν_t are computed for each model using the exact k and velocity given by the DNS data.

The variation of ε and ν_t is shown for each model in Figures 5.1 through 5.5. The symbols show the DNS data for the boundary layer [136].

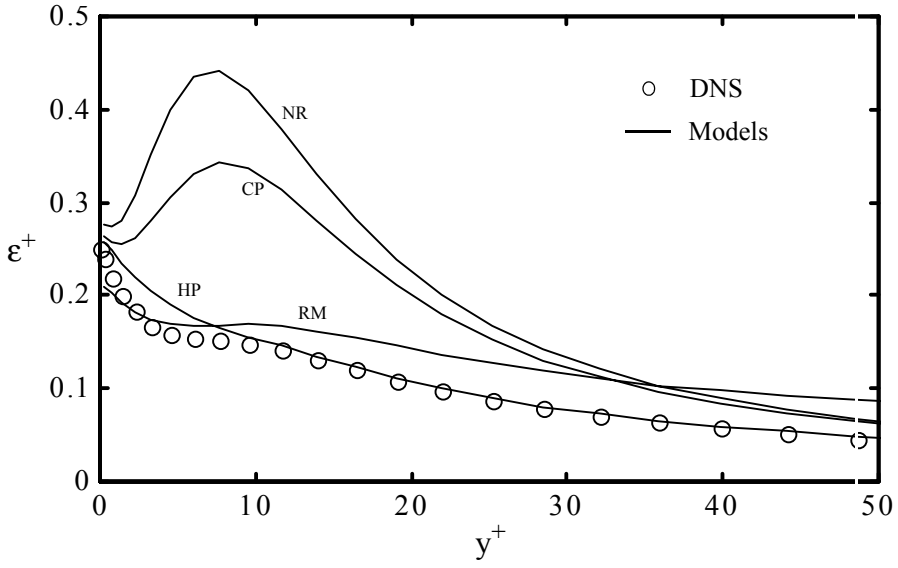

Figure 5.1: Modeled ε compared to DNS data.

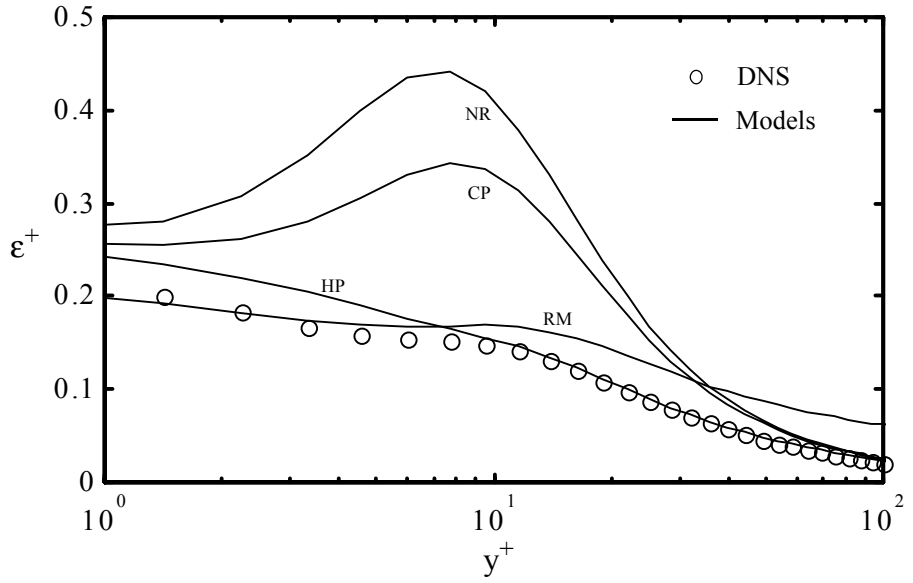

Figure 5.2: Modeled ε near the wall compared to DNS data.

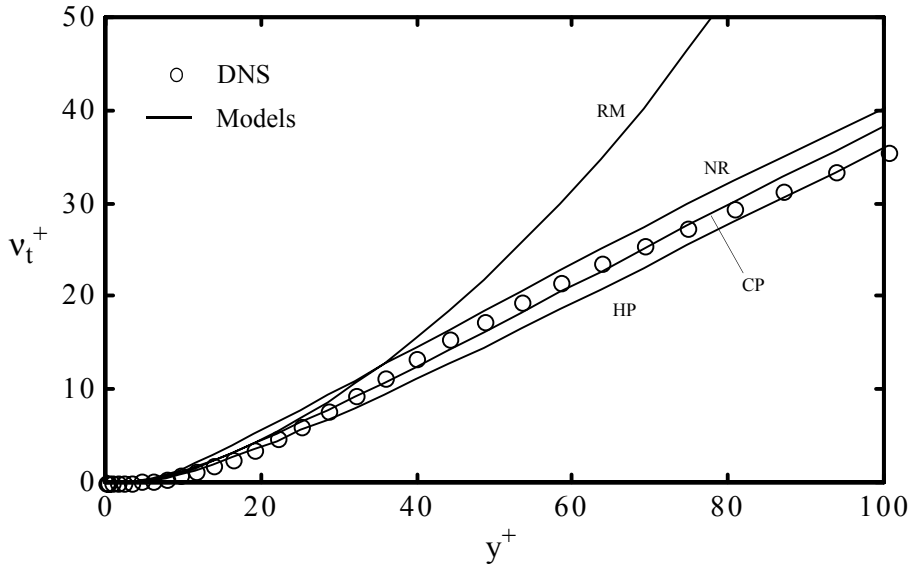

Figure 5.3: Modeled ν_t compared to DNS data.

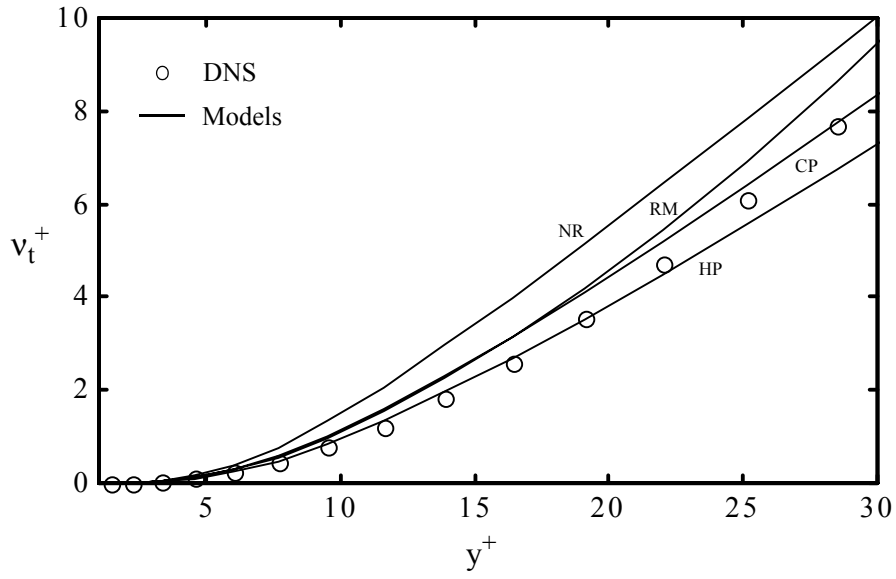

Figure 5.4: Modeled ν_t near the wall compared to DNS data.

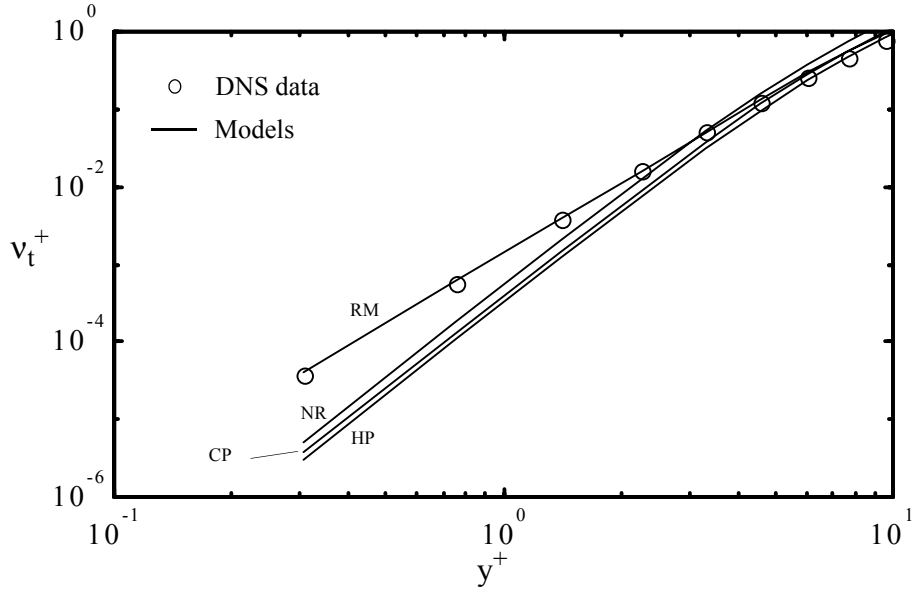

Figure 5.5: Asymptotic behavior of the modeled ν_t compared to DNS data.

WS appears almost indistinguishable from CP and is therefore not included of the figures above. CP is simply WS with modified constants and therefore WS is not included in further analyses. Figure 5.2 shows that NR and CP share the characteristic of producing excessive ε in the buffer layer where y^+ is about 30. This was apparently first noted in reference 122. HP nearly reproduces ε at the wall and appears to follow the DNS data closely. RM follows the DNS data near the wall, but diverges and predicts excessive ε beyond y^+ of about 10. In general, the one-equation model must be applied in the region near the wall, where the standard k-ε model requires modification, such that the predicted values of $-\overline{uv}$ are essentially continuous across the boundary separating the regions in which the one-equation model and the two-equation model are applied. As formulated here, the one-equation models must then be applied in the region from the wall to the point where y^+ is about 100. RM may therefore be expected to yield a discontinuity in some or all predicted quantities. This behavior can be seen clearly in the results of the computations performed by the developers where $-\overline{uv}$ is discontinuous at the boundary between the inner and outer regions [124].

Figure 5.3 shows that RM greatly overestimates ν_t beyond the point y^+ of about 40. Figure 5.4 shows that NR, CP, and RM appear to overestimate ν_t near the wall. HP reproduces ν_t most closely throughout the near-wall region, but underestimates it in the region where y^+ is between 30 and 100. Figure 5.5 shows that only RM reproduces the cubic variation of the ν_t very near the wall. NR, HP, and CP give an ν_t that varies with y^+ to the fourth power. These results are consistent with the analysis above.

Finally, the excessive ε seen in the curves for CP and NR in Figure 5.2, corresponding to the underestimation of the ε lengthscale, suggests that these models may

provide poor predictions of k near the wall.

5.3 New One-Equation Model

The analysis above indicates that one of the near-wall models reproduces the near-wall behavior of $-\overline{uv}$, but yields an ε and ν_t that vary greatly from the DNS in regions beyond the buffer layer where effects of the wall remain significant. Another reproduces ε fairly well in the near-wall region, but does not reproduce the behavior of $-\overline{uv}$ near the wall. Still others yield an ε that varies greatly from the DNS near the wall. In view of these results, a new model is proposed. The new model should reproduce the behavior of the $-\overline{uv}$ at the wall, reproduce the value of ε at the wall, and predict the correct variation of ε near the wall. It should be noted that studies suggest that velocity scales other than k, such as the wall-normal Reynolds stress, may provide better choices for expressing the ε and ν_t [124]. When used with models such as the standard k-ε model, these near-wall models require a relation for the wall-normal Reynolds stress since the eddy viscosity model predicts isotropic normal Reynolds stresses for plane flows and therefore fails to reproduce the wall-normal Reynolds stress well. The new model will therefore express the velocity scale in terms of k in a manner similar to the traditional models.

For the new model, ε is expressed using a k-l model similar to the traditional models. The ν_t can be expressed using a variation of the relation $\nu_t = C_\mu f_\mu k^2/\varepsilon$ or $\nu_t = C_\mu f_\mu kT$ used by the two-equation near-wall models, or by a variation of $\nu_t = \sqrt{k} l_\mu$ used by the traditional one-equation near-wall models. The benefit of the former relation for ν_t is that it is guaranteed to be continuous throughout the near-wall

region. This is not the case if the latter relation is used unless the constants are chosen such that the inner and outer relations for ν_t match at the near-wall boundary.

The new model expresses ν_t as

$$\nu_t = \sqrt{k} l_\mu = C_\nu \sqrt{k} y f_1 \tag{5.12}$$

The value of C_ν is $\kappa C_\mu^{1/4}$. The new model expresses ε as two components given by

$$\varepsilon = 2\nu \frac{k}{y^2} f_2 + C_\varepsilon \frac{k^{3/2}}{y} f_3 \quad . \tag{5.13}$$

The value of C_ε can be determined to be approximately 0.4 using DNS data for the boundary layer sufficiently far from the wall. The value of C_ε is $C_\mu^{3/4}/\kappa$ in this region of the flow. The modeling functions are $f_1 = (1 - e^{-a_1 R_y^{1/2} - a_2 R_y^{3/2}})$, $f_2 = e^{-a_3 R_y^{1/2}}$, and $f_3 = (1 - e^{-a_4 R_y})$. Baseline modeling constants are determined by minimizing errors between ν_t and ε and the corresponding values given by DNS data. These are then modified by computing the flow and minimizing the difference between the predicted U, k, $-\overline{uv}$, and ε and the DNS data. The recommended model constants are a_1=0.028, a_2=0.0012, a_3=0.15, a_4=0.02, C_ν=0.23, and C_ε=0.38. The model may also be optimized using the tradtional values for the last two constants. The development of the new model is described further in an appendix. Figures 5.6 and 5.7 compare the new model using the baseline constants to DNS data for the boundary layer flow.

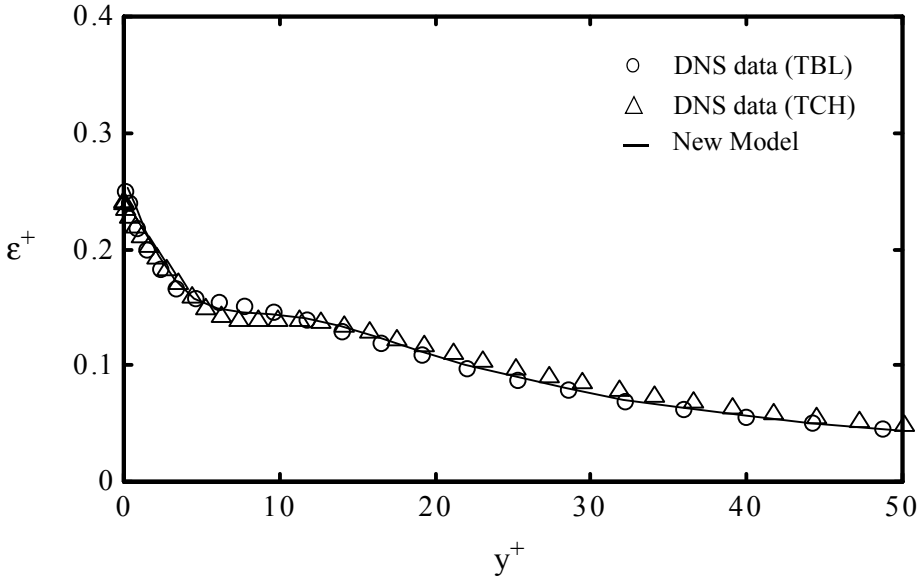

Figure 5.6: Modeled ε for the new model compared with DNS data for the boundary layer and plane channel.

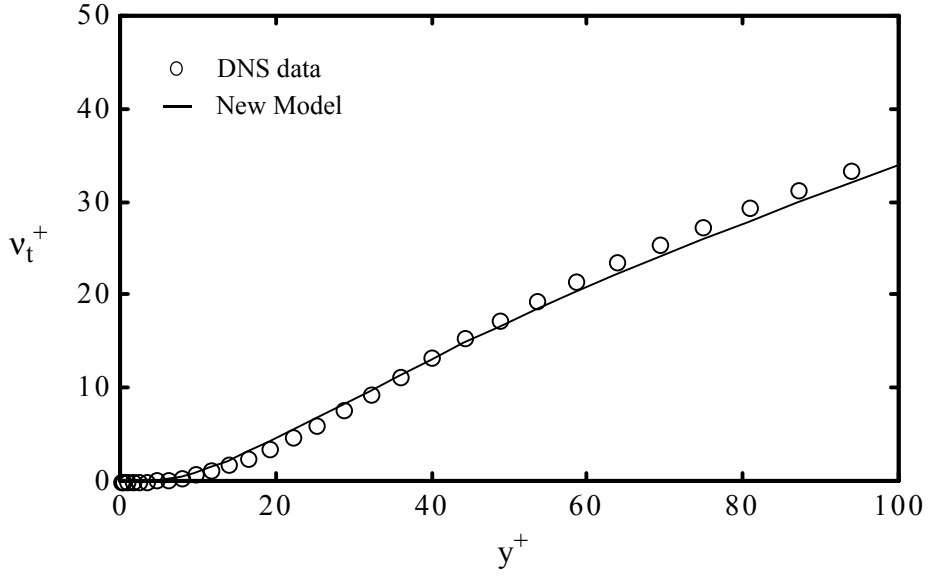

Figure 5.7: Modeled ν_t for the new model compared with DNS data.

The only choice remaining to complete the formulation of the new model is to choose a parameter delineating the point beyond which the standard k-ε model is to be applied. The boundary between the near-wall region and the outer region is called the near-wall boundary. The majority of the models listed in Table 5.2 use the turbulence Reynolds number, $R_y = \sqrt{k}y/\nu$, while RM uses the ratio of ν_t to the kinematic viscosity, $s = \nu_t/\nu$. Since $\nu_t = C_\nu \sqrt{k} y f_1$, R_y and s differ only by a constant far from the wall and thus either can be used to determine the edge of the near-wall boundary. For the majority of the models, the near-wall boundary is placed at R_y=250 [24, 122]. For RM, the near-wall boundary is at s=16 [124]. The near-wall boundary must be sufficiently far such that the relation $\nu_t = C_\mu k^2/\varepsilon$ is valid. For high Reynolds numbers, this is the point where R_y=250 or s=50. The parameter used for the new model is s. This model is applied when $s < 10$. This value of s corresponds to the point at which y^+ is approximately 30 for the benchmark turbulent boundary layer DNS [136]. For $s > 10$, ε is given by solution of the standard ε transport equation and ν_t is given by

$$\nu_t = C_\mu f_\mu \frac{k^2}{\varepsilon} \tag{5.14}$$

where $f_\mu = (f_1 + 2f_2/(C_\varepsilon R_y))f_3 \approx f_1 f_3$. This last relation is derived by equating the inner and outer relations for ν_t and substituting for ε. Using this relation, equation (5.15) could be used throughout the flow. The baseline constants determined using the DNS data are further optimized by the computation of a turbulent boundary layer flow such

that the error between the U, k, $-\overline{uv}$, and ε predicted by the computation and that given by the DNS data is minimized in a qualitative manner. Further details are left to an appendix.

Before proceeding, the modeling assumptions upon which the new model relies are reviewed. The new model implicitly includes all the assumptions upon which the modeled k equation and ε equation rely. The primary assumptions upon which the one-equation near wall model relies directly are that ν_t and ε can be expressed solely in terms of k and the normal distance from the no-slip surface throughout the near-wall region.

The analysis of the near-wall limiting behavior and model expressions can be applied to the new model. The table below shows the results of the near-wall analysis for the new model with the results from earlier. The new model is designated M1.

Table 5.4: Results of the near-wall analysis including the new model.

Model	YS	WS	NR	HP	CP	RM	M1
a_ε/a_k	2	1.58	2.12	2	2	1.63	2
n_{uv}	3	4	4	4	4	3	3

Figures 5.8 through 5.12 show that ε and ν_t predicted by the new model match the DNS well. Note that these figures show the model as optimized by a computation and therefore agreement with the DNS data is not identical to that shown in Figures 5.6 and 5.7.

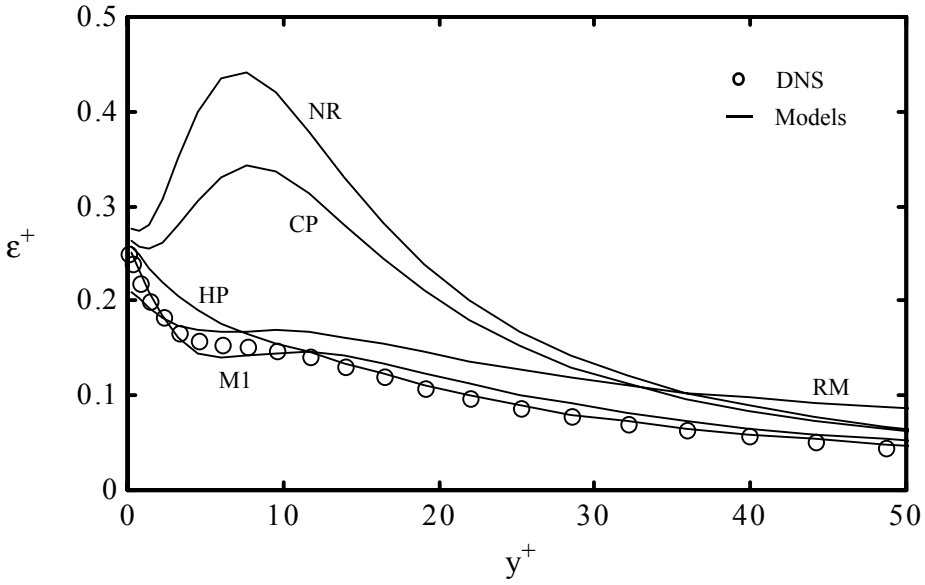

Figure 5.8: Modeled ε for the new model compared with DNS data.

Figure 5.8 above and Figure 5.9 below show that the new model predicts a dip in ε near the wall that is similar to that given by model RM and, unlike models NR and CP, the new model predicts a decreasing ε length scale in the sublayer in accord with the DNS data. At the wall, ε appears to be reproduced. Unlike model RM, the new model does not appear to predict excessive ε beyond the buffer layer.

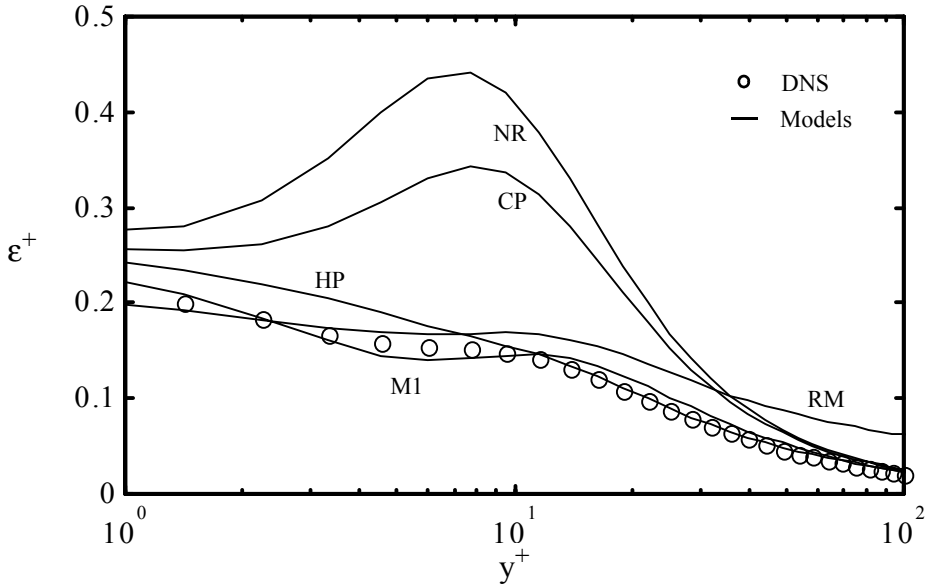

Figure 5.9: Modeled ε near the wall for the new model compared with DNS data.

Figures 5.10 through 5.12 below show that ν_t given by the new model matches the DNS well throughout the near-wall region. The model can be applied up to the point $y^+=100$, although it is developed such that the outer turbulence model can applied closer to the wall.

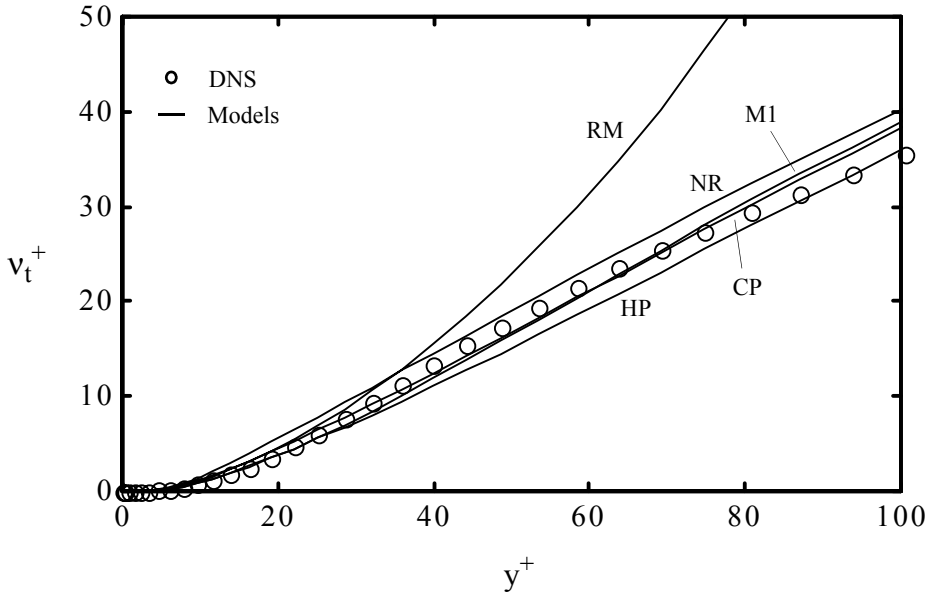

Figure 5.10: Modeled ν_t for the new model compared with DNS data.

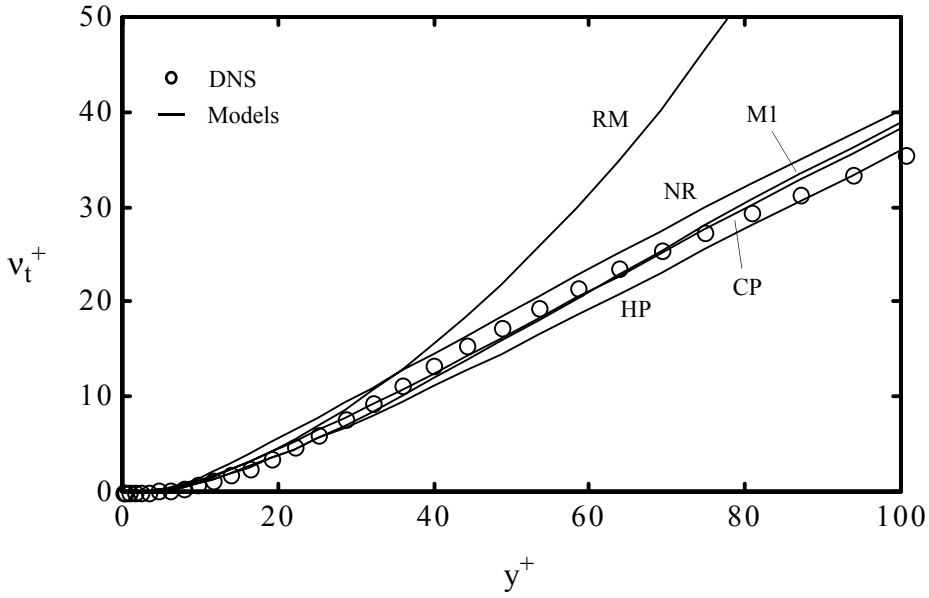

Figure 5.11: Modeled ν_t near the wall for the new model compared with DNS data.

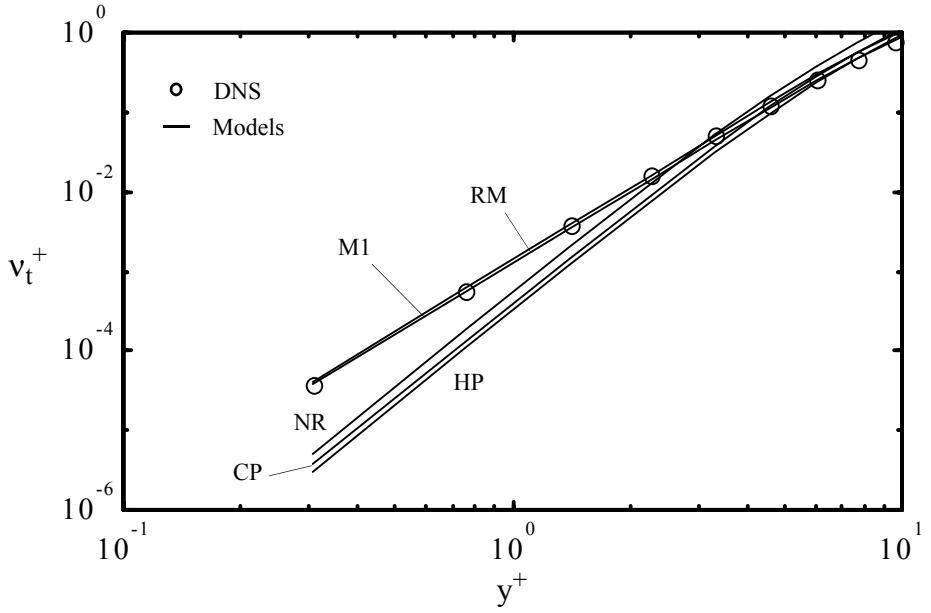

Figure 5.12: Asymptotic behavior of ν_t for the new model compared with DNS data.

Figure 5.12 clearly suggests that the new model reproduces the cubic variation of ν_t as the wall is approached. The new model therefore reproduces the cubic variation of the Reynolds shear stress correctly. The new model is included in the computations that follow.

5.4 Computations of Benchmark Flows

The benchmark flows are computed using the projection method code described in Chapter 3 with each of the near-wall models. The primary utility of the analyses of the preceding sections is in indicating deficiencies of the models in particular areas. For example, it is clear that only RM and M1 are capable of providing the correct variation of $-\overline{uv}$ near the wall. It is also clear that the variation of $-\overline{uv}$ predicted by the other one-equation near-wall models is due to the formulation and not the choice of modeling constants. The performance of the models with respect to the ability to predict a particular flow is shown by the computation of the flow and comparison with experimental data or DNS data.

Before continuing, it should be noted that the DNS data used in this work should not be considered as strict benchmarks of performance. For the boundary layer, the DNS data for the point where Re_θ is 1416 is utilized. The DNS data for the boundary layer at this Reynolds number is believed to suffer from slight numerical errors. Therefore, the DNS data is viewed in this work as a baseline for comparison rather than a strict benchmark of performance. Likewise, the work of reference 25 suggests that the turbulence quantities near the plane wall of the wavy-wall channel increase beyond those of a plane channel as grid resolution increases. The work of reference 97 may not have addressed this issue. The DNS data for the wavy-wall is therefore also viewed as a baseline for comparison rather than a strict benchmark of performance. The results of the computations of the benchmark flows are presented below.

5.4.1 Turbulent Boundary Layer

The turbulent boundary layer over a flat plate with zero pressure gradient is, along with the plane channel, among the most common benchmark flows for the evaluation of near-wall turbulence models [99, 111, 128, 135, 157]. The general characteristics of boundary layer flow and the metrics by which the models are evaluated were presented in Chapter 4. For the boundary layer, the computational analysis is broken into four parts. The first part consists of an evaluation of the predicted near-wall behavior. The second consists of an evaluation of the predicted shape function, log-law parameters, and skin friction coefficient. The third and fourth parts include computation of the errors in the predicted flow and a qualitative analysis. Before proceeding with the evaluation, the computation is described briefly.

The computation of the turbulent flat-plate boundary layer is completed using the projection method code described in Chapter 3. The boundary conditions are as specified for the turbulent boundary layer validation case, also presented in Chapter 3. The convergence criteria is that the solution become stationary and that the divergence in the flow is less than 10^{-5} at each node point [61]. The grid spacing at the wall, δ, is set to 5 corresponding to y^+ in the range of 0.2 to 0.25. Figure 5.13 below shows the variation in predicted skin friction coefficient with wall spacing for three models. For wall spacings of δ greater than or equal to 2, the grid consists of 63 points in the streamwise direction and 127 in the wall-normal direction. For the finest spacing of δ=1, the grid consists of 255 points in the streamwise direction and 511 in the wall-normal direction. The solution on the finest grid, shown by the solid symbol in Figure 5.13, suggests that the solutions at the finer wall spacings are grid independent.

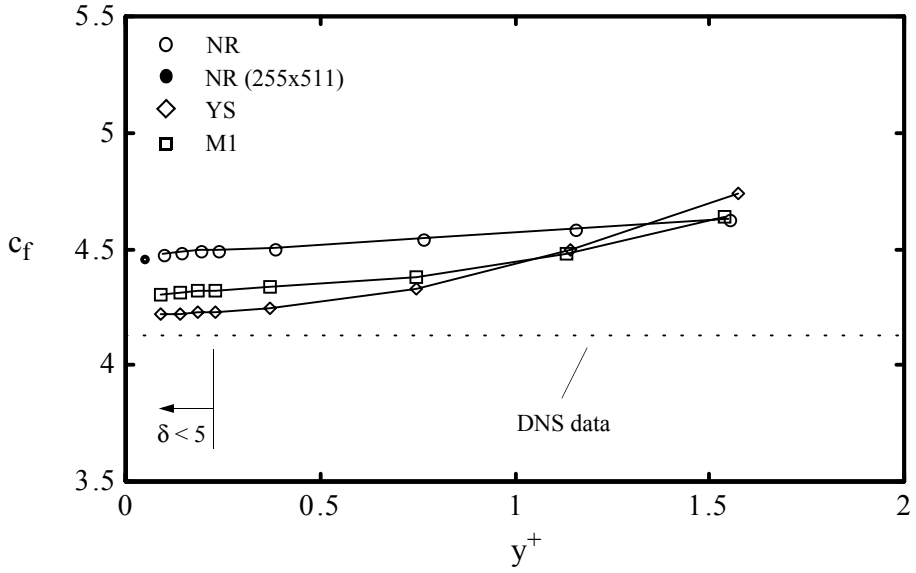

Figure 5.13: Variation of c_f with wall spacing for NR and M1 and two-equation near-wall model YS.

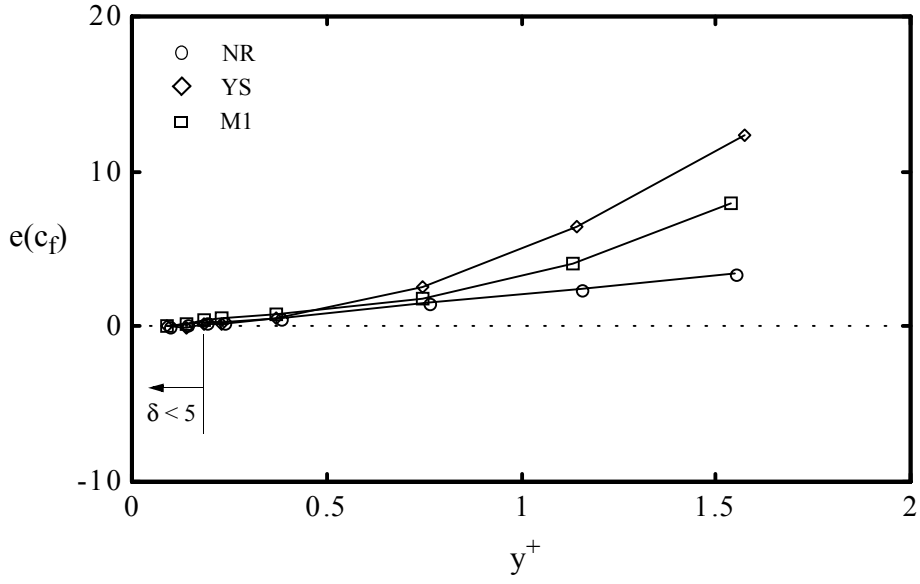

Figure 5.14: Variation of the error of c_f with wall spacing for NR and M1 and two-equation near-wall model YS.

Figure 5.14 shows the variation in error in the predicted skin friction coefficient, $e(c_f) = (c_f - c_{f_o})/c_{f_o}$ [10]. The value c_{f_o} is the skin friction coefficient at the finest wall-spacing. The figures show that a spacing of δ=5 is sufficient to resolve the flow near the wall for one-equation and two-equation near-wall models. Grid independence of the solutions is addressed in detail in an appendix.

5.4.1.1 Predicted Near-Wall Behavior

The values of the coefficients and exponents of the series expansions of k, $-\overline{uv}$, and ε are obtained from the computation as described in Chapter 4. The results for each model are given in the table below. The values shown in the first row are computed using the DNS data for the boundary layer at Re_θ = 1416. It should be noted that, as mentioned above, the DNS data for the boundary layer at this Reynolds number is believed to suffer from slight numerical errors. For this reason, the values given for the DNS data in the table should be considered baselines for comparison rather than strict benchmark values.

The computed values vary slightly during computation and may be sensitive to the order of accuracy of boundary conditions. Certain models, such as NR and HP, yield very steady computations. Others, such as CP and the two-equation near-wall model, yield quantities that fluctuate by a few percent. The position along the flat plate at which these quantities are evaluated for the computations is the point where Re_θ most closely matches the DNS value of 1416. The difference between the Re_θ at which the profile is taken and the DNS value can also affect the computed coefficients. Each of these factors

may contribute to variability in the computed coefficients.

Table 5.5: Predicted series expansion coefficients for the boundary layer.

Model	DNS	YS	NR	HP	CP	RM	M1
a_k	0.13	0.16	0.032	0.079	0.040	0.10	0.11
n_k	2.0	1.9	2.0	2.0	2.0	1.9	2.0
a_{uv}x10^3	1.3	0.23	0.14	0.21	0.13	1.2	1.2
n_{uv}	3.0	3.0	4.0	4.0	4.0	2.9	3.0
a_ε	0.25	0.38	0.057	0.16	0.077	0.29	0.22
$2a_k/a_\varepsilon$	1.0	0.84	1.1	1.0	1.0	0.69	1.0

The computations indicate that the reproduction of the various metrics varies greatly between the one-equation near-wall models. M1, RM, and the two-equation near-wall model predict a value for a_k that is most similar to the DNS value. The traditional one-equation near-wall models predict values for a_k substantially lower. M1 and RM predict values of a_{uv} and a_ε similar to the DNS value. RM, however, does not appear to reproduce the ratio $2a_k/a_\varepsilon$. This is consistent with the results of the near-wall analysis in which it was found that RM does not reproduce a_ε at the wall. The two-equation near-wall model predicts a value for a_ε higher than the DNS, consistent with the results indicated in reference 128. The computations verify the quartic behavior of $-\overline{uv}$ for NR, HP, and CP indicated by the near-wall analysis presented earlier. The models developed using DNS data, M1 and RM, reproduce the proper behavior of $-\overline{uv}$ near the wall.

It should be noted that the computations indicate that CP and NR do not reproduce a_ε correctly in contrast to the results of the near-wall analysis. The failure of these models to reproduce a_ε may be due to the tendency of both models to produce excessive ε in the buffer layer of the boundary layer and therefore predict a distribution of k that varies significantly from the DNS data. The tendency to predict excessive ε in the buffer layer shown here is consistent with the findings of reference 122.

5.4.1.2 Log-law, Shape Function, and Skin Friction

The log-law was given in Chapter 4. The first estimates for the Kármán constant, κ, and additive constant, B, were κ=0.40 and B=5.5 [107]. The values most often quoted are κ=0.41 and B=5.0 [30]. The values of the Kármán constant, κ, and additive constant, B, may be determined from the DNS data by fitting a line to the plot of the mean velocity [135]. Here, the Kármán constant and additive constant are determined to be κ=0.409 and B=4.85 by evaluating the data for the velocity profile at the positions y^+=58.3 and y^+=63.5 using the formulas presented in Chapter 4 and the DNS data. This method is similar to that suggested in reference 10. These values are comparable to the accepted values given above. Figure 5.15 below shows the log-law determined using the values κ=0.409 and B=4.85.

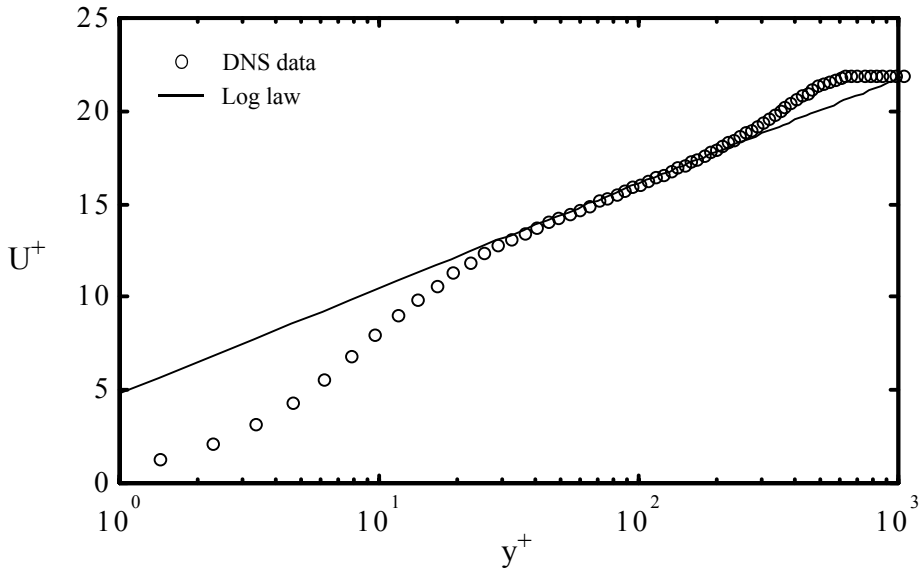

Figure 5.15: The log-law determined using κ=0.409 and B=4.85 for the boundary layer.

The shape factor was presented in Chapter 4. The value computed here using the DNS data is H=1.41. The skin friction coefficient was also given in Chapter 4 and the value computed here using the DNS data is 4.128×10^{-3}. The values for the log-law parameters, the shape function, and the skin friction coefficient predicted by the computations of the boundary layer using each of the one-equation near-wall models are presented in the table below. Slight fluctuations in these parameters occur during computation. The log-law parameters will depend on the choice of points to which the log-law is fit. These factors contribute to variability in the parameters given in the table.

Table 5.6: Predicted shape parameters and skin friction for the boundary layer.

Model	DNS	YS	NR	HP	CP	RM	M1
κ	0.41	0.46	0.39	0.36	0.37	0.35	0.41
B	4.9	5.9	4.3	3.7	4.6	2.9	4.8
U_m^+	22.0	22.0	21.3	21.5	22.1	22.1	21.8
c_f x 10^3	4.13	4.22	4.49	4.42	4.17	4.21	4.29
$\Delta(\kappa)$	-	12.2	-4.8	-12.2	-9.8	-14.6	0.0
$\Delta(B)$	-	20.4	-12.2	-24.5	-6.1	-40.8	-2.0
$\Delta(c_f)$	-	2.2	8.7	7.0	0.97	1.9	3.9

The table above shows that all models predict κ to within about 15%. The new model reproduces the traditional value of κ. There is wide variation in the predicted value of B with the new model predicting a value most close to the DNS and experimental data. All models reproduce the shape function H and predict c_f well.

5.4.1.3 Error of the Predicted Mean Flow

The errors are listed for each model in the table below. The errors are, as defined in Chapter 4, the differences between the predicted values and DNS data at each node point, summed over all node points, and normalized. Since the flow quantities are normalized, these errors are dimensionless.

Table 5.7: Error of the predicted mean flow for the boundary layer.

Model	YS	NR	HP	CP	RM	M1
$\Delta(U)$	0.00262	0.0300	0.0250	0.0165	0.0130	0.0124
$\Delta(k)$	0.115	0.188	0.106	0.157	0.159	0.0630
$\Delta(-\overline{uv})$	0.0328	0.0895	0.0939	0.0908	0.0778	0.0342
$\Delta(\varepsilon)$	0.126	0.206	0.109	0.213	0.156	0.102

The results suggest that M1 predicts U most similar to the DNS. Only the benchmark two-equation near-wall model predicts U in better agreement with the DNS. The predictions of k by NR, CP, and RM agree least with the DNS while M1 and HP appear to be the most accurate. M1 and HP predict ε in closest agreement with the DNS.

5.4.1.4 Qualitative Analysis

Errors are rarely presented in the literature concerning the evaluation of turbulence models. In general, the predicted values are plotted along side the DNS or experimental data and conclusions concerning the performance of the models are made qualitatively. This qualitative analysis is beneficial in that it allows the evaluation of the capability of the models to capture salient features of the flow such as the peak in k or the plateau in ε that occurs near the wall in the boundary layer flow.

Figures 5.16 to 5.19 below show the mean velocity, U, k, $-\overline{uv}$, and ε, for each model. Figures 5.20 through 5.23 present ε in an alternate format with three models

shown in each figure for a more direct comparison.

All models predict U well. CP, however, overestimates U in the log layer while NR and HP underestimate U in the outer wake region. NR and CP clearly fail to capture the peak in k near the wall. This result is consistent with previous studies [122]. HP, RM, and the benchmark two-equation near-wall model capture the peak in k. M1 overestimates the peak in k slightly, but follows the DNS well beyond the buffer layer. NR, HP, and CP, underestimate $-\overline{uv}$ slightly and exhibit a clear discontinuity at the near-wall boundary where the two-layer method switches from the inner one-equation model to the standard k-ε model. RM shows a significant discontinuity in $-\overline{uv}$, consistent with results reported in the literature [124]. The reproduction of $-\overline{uv}$ by the new model is greater than that of any other one-equation model and similar to the benchmark two-equation near-wall model. In addition, the new model displays no discontinuity at the near-wall boundary. Consistent with previous work [122], NR and CP overestimate ε in the buffer layer leading to the underestimation of k near the wall. HP fairs better, predicting ε well beyond the buffer layer, but clearly fails to predict the value of ε at the wall. RM predicts the correct behavior near the wall, but also appears to underestimate the value of ε in the sublayer and at the wall. M1 predicts ε throughout the sublayer, buffer layer, and log-layer well.

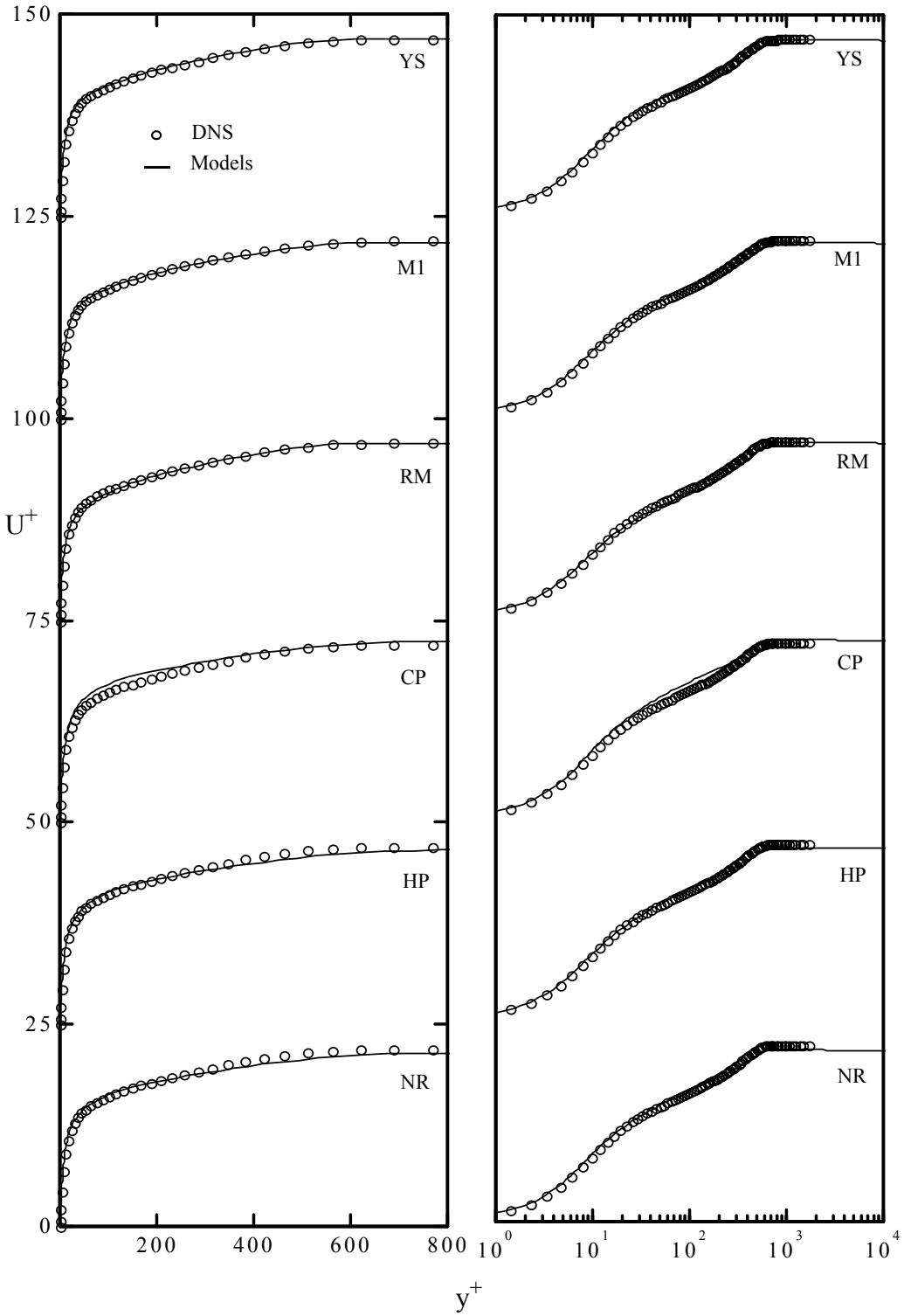

Figure 5.16: Predicted *U* for the boundary layer.

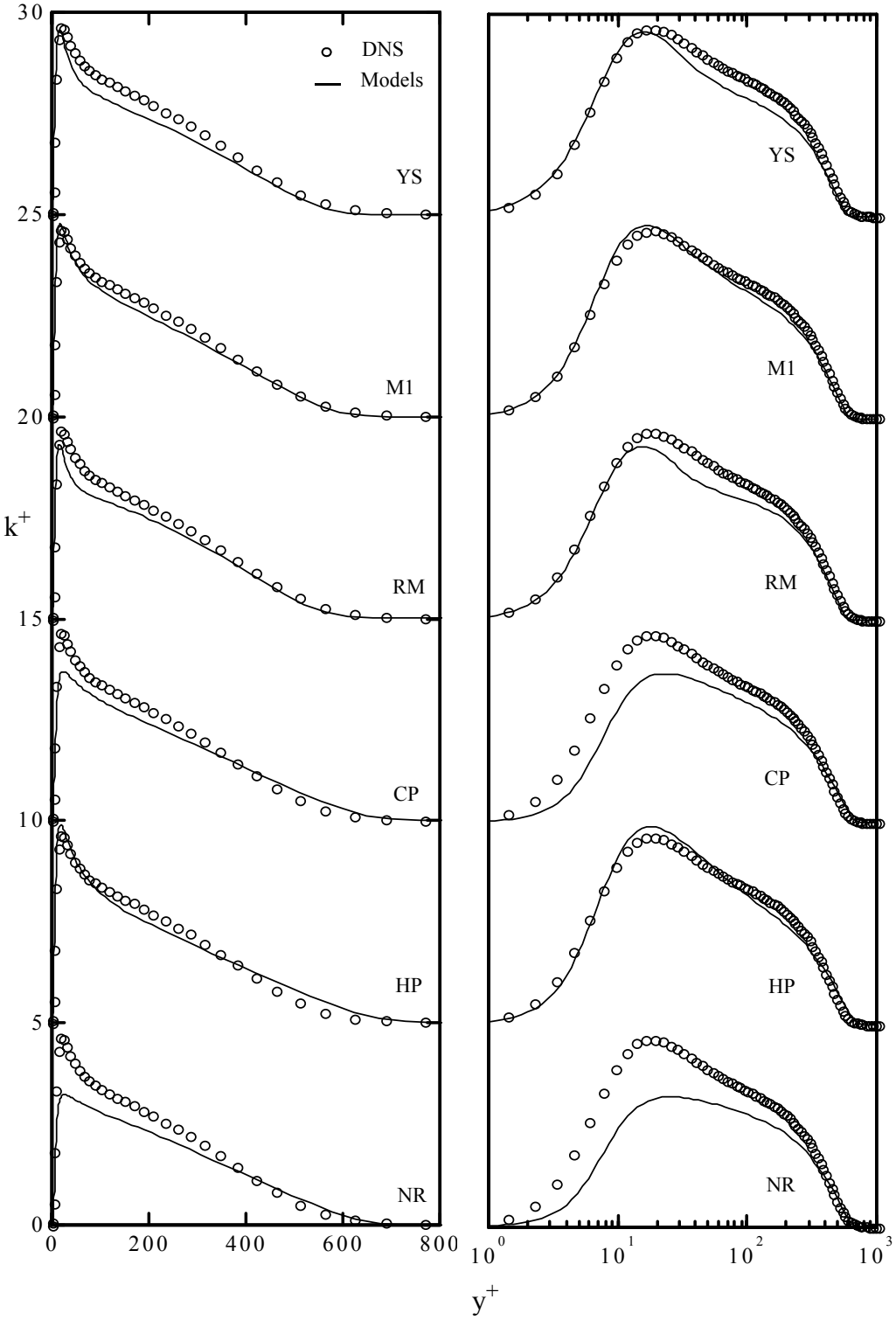

Figure 5.17: Predicted *k* for the boundary layer.

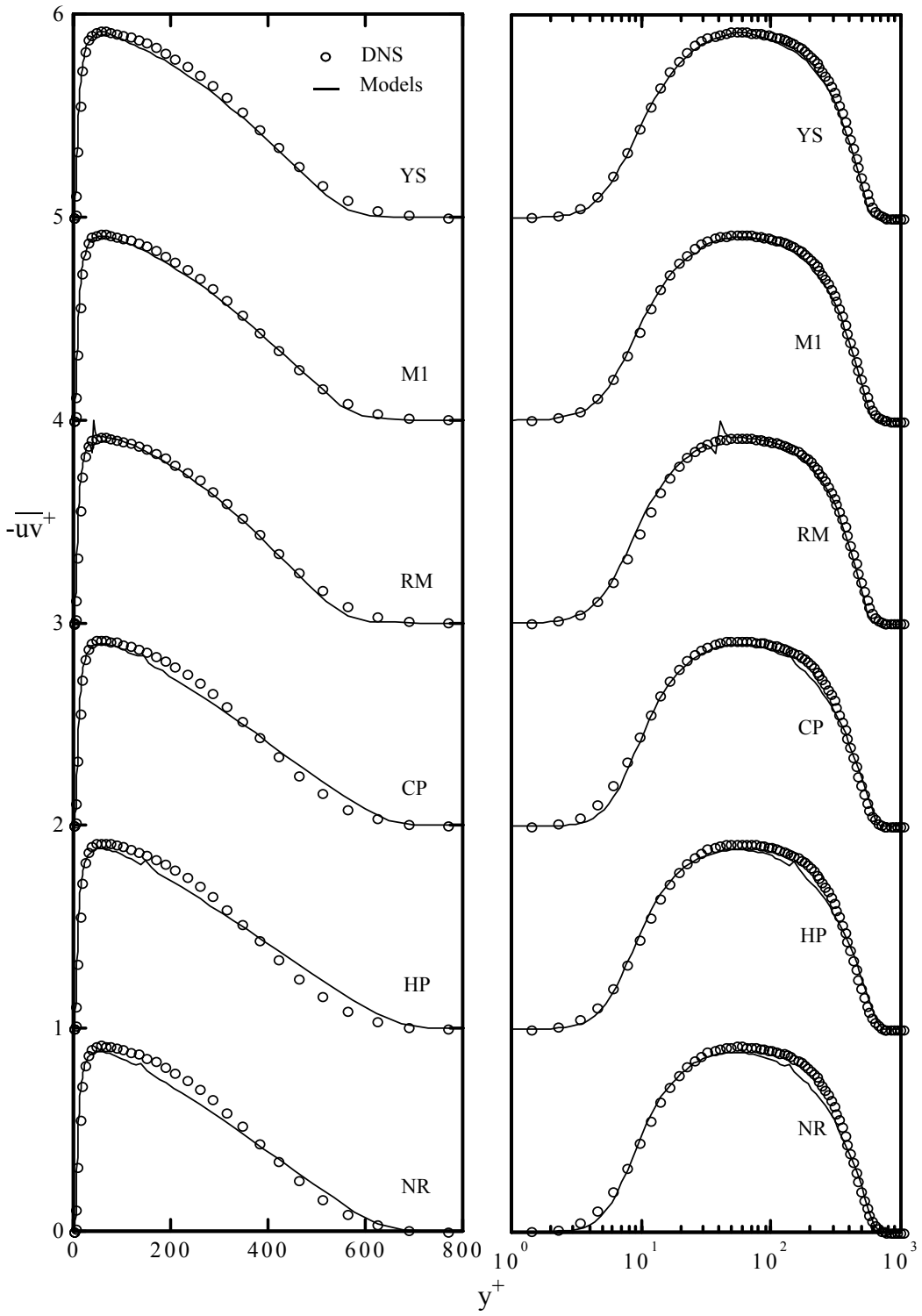

Figure 5.18: Predicted $\overline{uv}$ for the boundary layer.

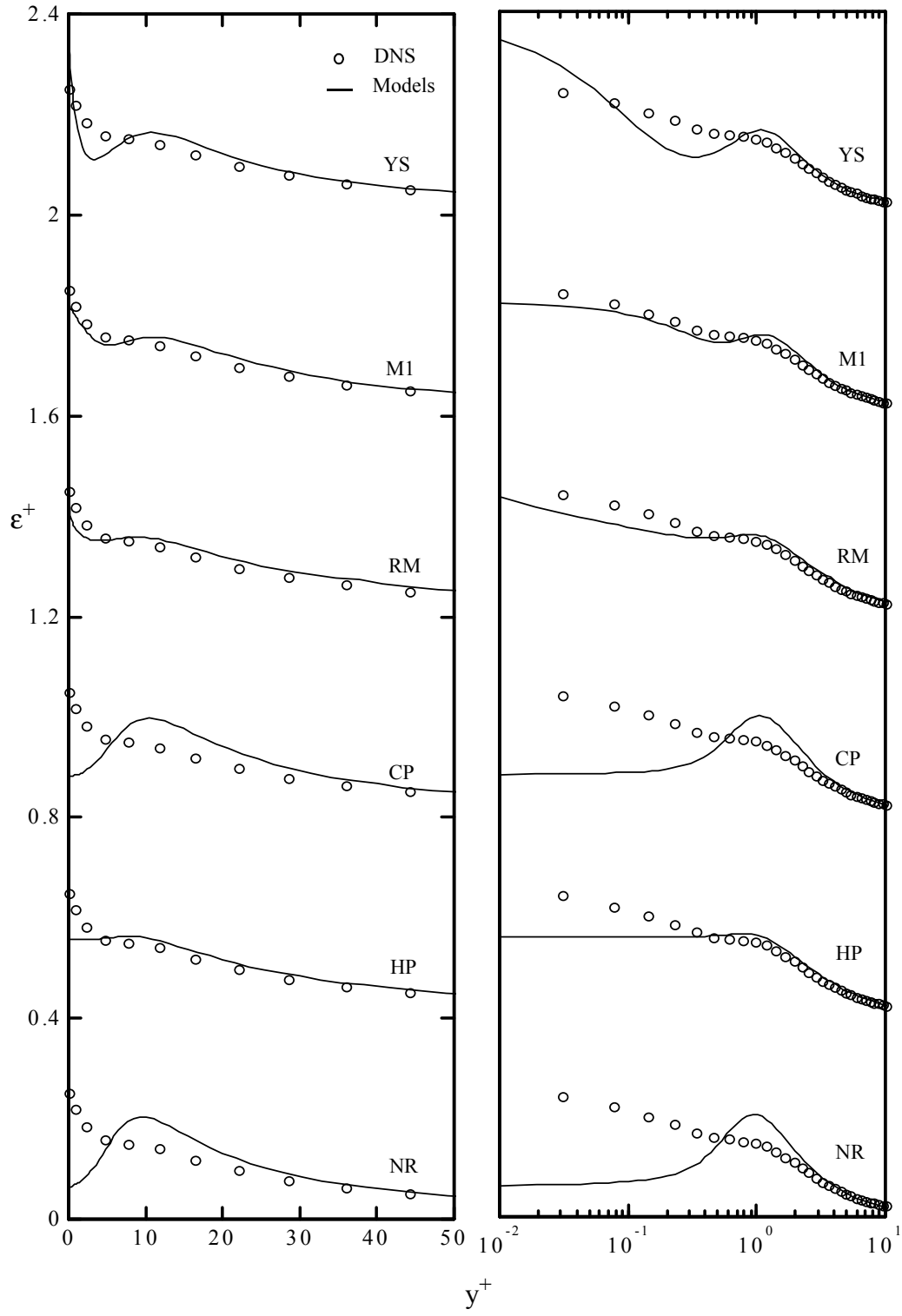

Figure 5.19: Predicted ε for the boundary layer.

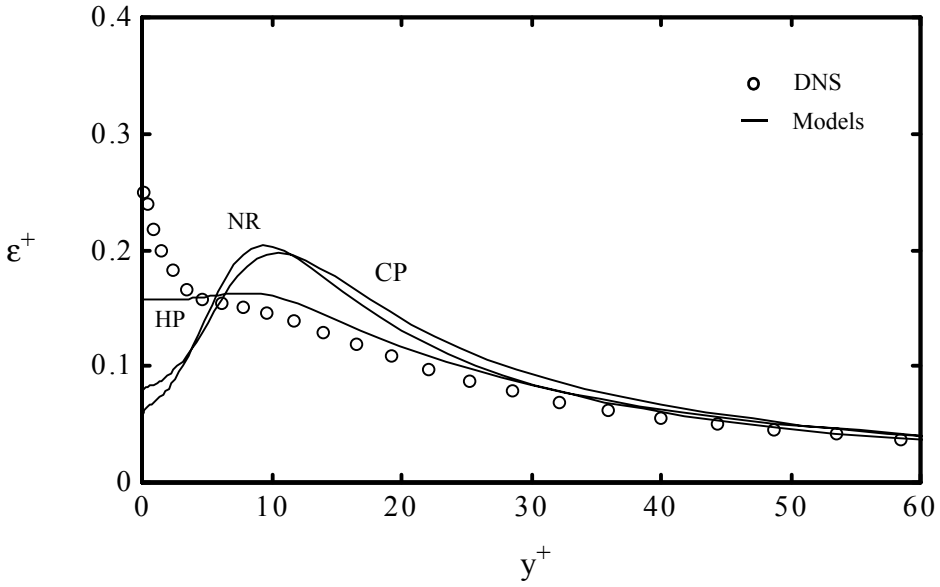

Figure 5.20: Predicted ε for the boundary layer for NR, HP, and CP.

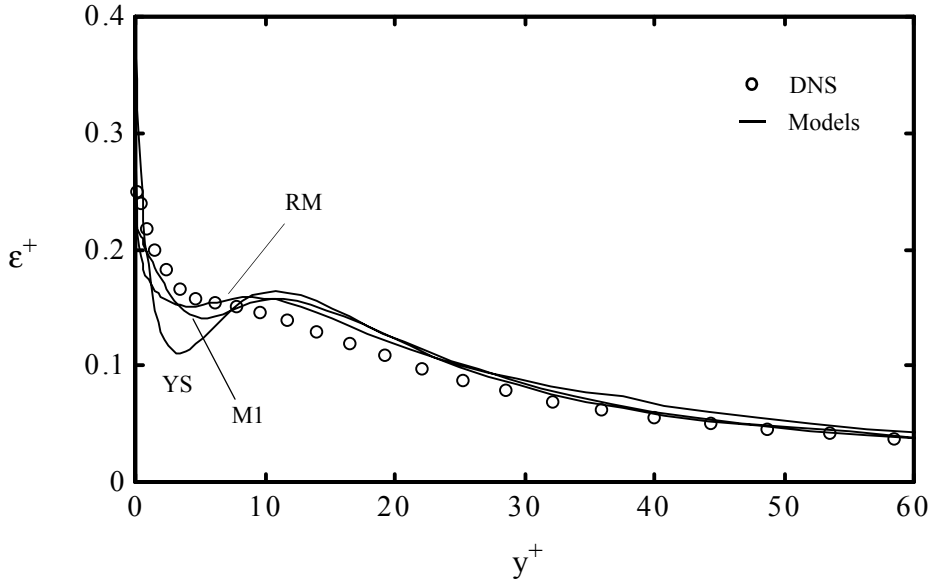

Figure 5.21: Predicted ε for the boundary layer for RM, M1, and YS.

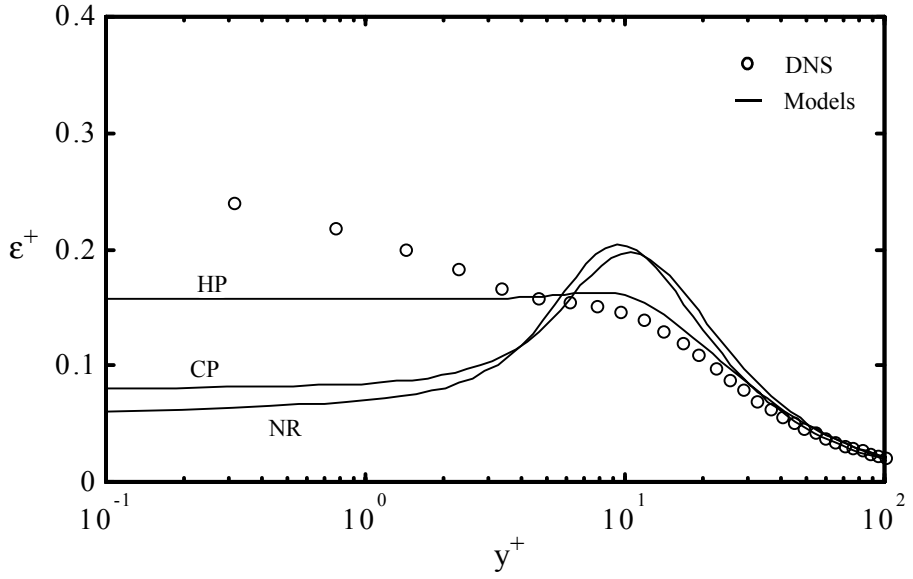

Figure 5.22: Predicted ε near the wall for the boundary layer for NR, HP, and CP.

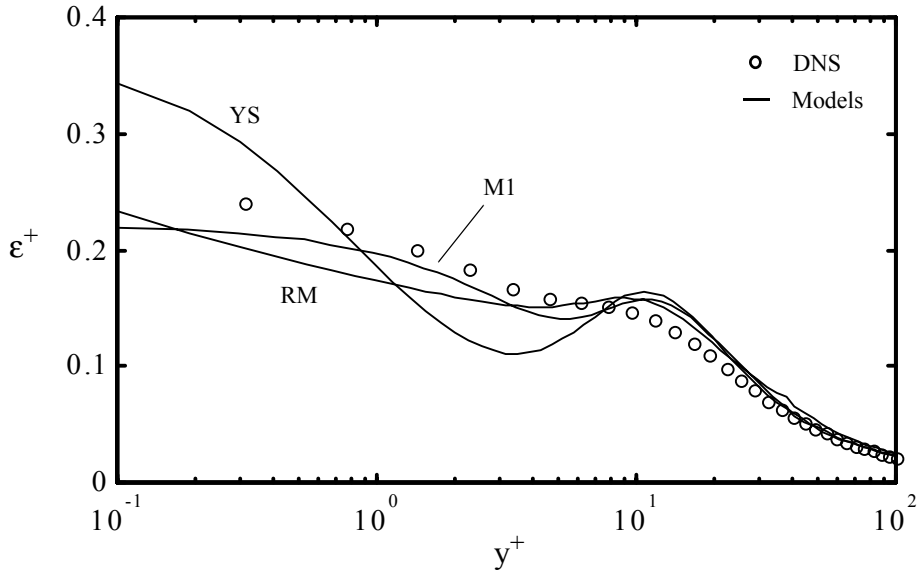

Figure 5.23: Predicted ε near the wall for the boundary layer for RM, M1, and YS.

It was found in the section concerning the near-wall analysis, and verified in the section discussing the predicted near-wall behavior, that only RM and M1 are capable of reproducing the behavior of $-\overline{uv}$ near the wall.

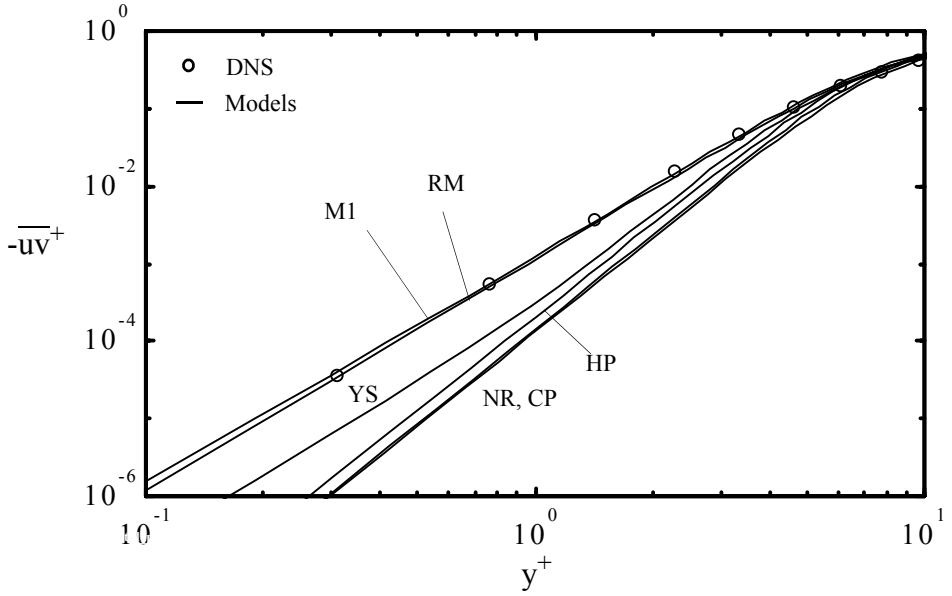

Figure 5.24: Predicted $-\overline{uv}$ near the wall for the boundary layer for all models.

This behavior can be seen clearly in Figure 5.24 above where only M1 and RM predict a variation of $-\overline{uv}$ matching the DNS data. For comparison, the benchmark two-equation model predicts a cubic behavior of $-\overline{uv}$, but, due to the predicted value of a_{uv}, does not agree with the DNS data.

5.4.2 Turbulent Wavy-Wall Channel

The turbulent wavy-wall channel provides a benchmark flow having a mild separation region. The general characteristics of wavy-wall channel flow and the metrics by which the models are evaluated were presented in Chapter 4. Unlike the boundary layer, the wavy-wall channel is not a common benchmark flow for the testing of turbulence models. The computation of the turbulent wavy-wall channel flow is completed using the projection method code described in Chapter 3. The boundary conditions are no-slip on the upper plane wall, no-slip on the lower wavy wall, and periodic on the remaining boundaries. The grid is body-fitted, expands from the walls geometrically, and is generated algebraically. The dimensionless pressure gradient imposed on the flow, computed from the total drag provided with the DNS data [97], is -0.0157. This pressure gradient is normalized using the square of the bulk velocity and the wavelength of the wavy wall. The convergence criteria is that, like the boundary layer, the solution become stationary. The divergence in the flow is less than 10^{-3} at each node point throughout the domain. Typically, $1x10^{5}$ iterations yield a converged solution with a time step of $1x10^{-4}$. Conservation of momentum is checked by computing the force on the wavy wall and plane wall. The force on the lower wall naturally includes significant pressure drag since the flow is separated. The pressure force on the control volume is equal to the pressure gradient of -0.0157 since the wavy-wall channel height is nominally one. The drag for a typical computation is 0.0151. This is within a few percent of the pressure force. The grid spacing at the wall is δ=2 or δ=5 which corresponds to y^+ of nominally 0.02 or 0.05 at the wave crest, wave trough, and upper plane wall. The grid for the wavy-wall computation showing every fourth grid line

for a grid with δ=5 is illustrated in Figure 5.25.

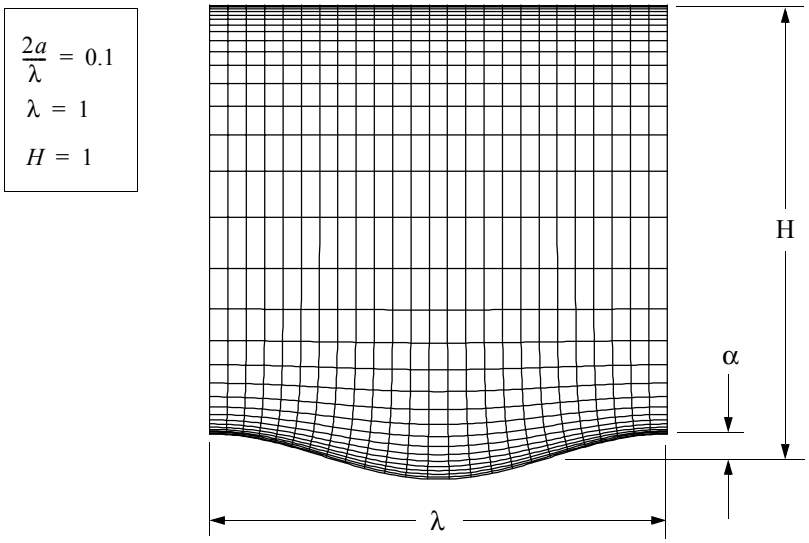

Figure 5.25: Grid for the wavy-wall computation showing every fourth grid line.

The computations are repeated using a domain of two wave-lengths in the streamwise direction verifying that the solution in each region is indistinguishable from the other and indistinguishable from the solution using a single wave-length.

Grid independence of the solutions is verified by the doubling of the number of grid points in each direction. Figures 5.27 and 5.27 below show the shear stress distribution for the standard and fine grids. The standard grid has a wall spacing of δ=5 with 102 points in the streamwise direction and 127 points in the wall-normal direction. The fine grid has a wall spacing of δ=2 with 202 points in the streamwise direction and 255 points in the wall-normal direction.

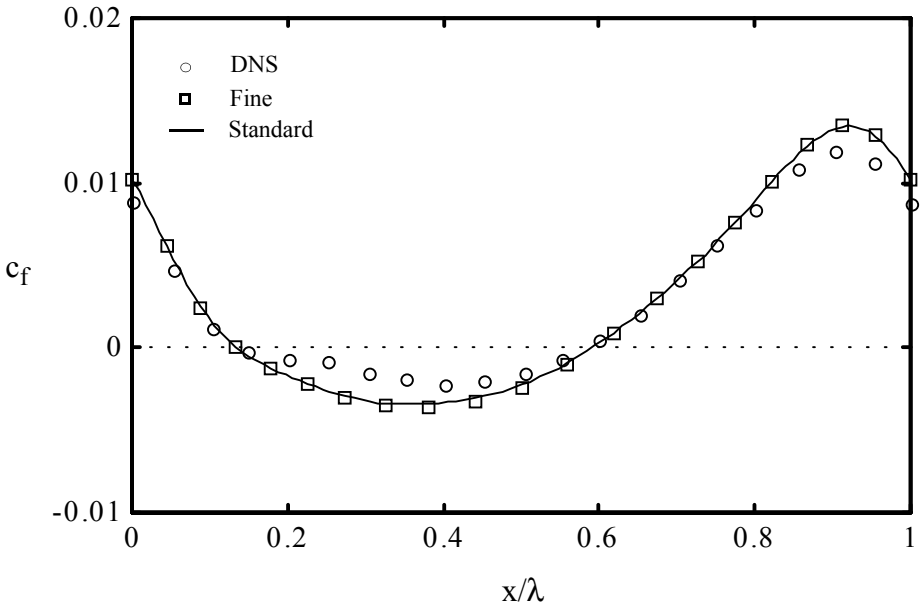

Figure 5.26: Shear stress distribution over the wavy-wall predicted by NR using the standard and fine grid densities.

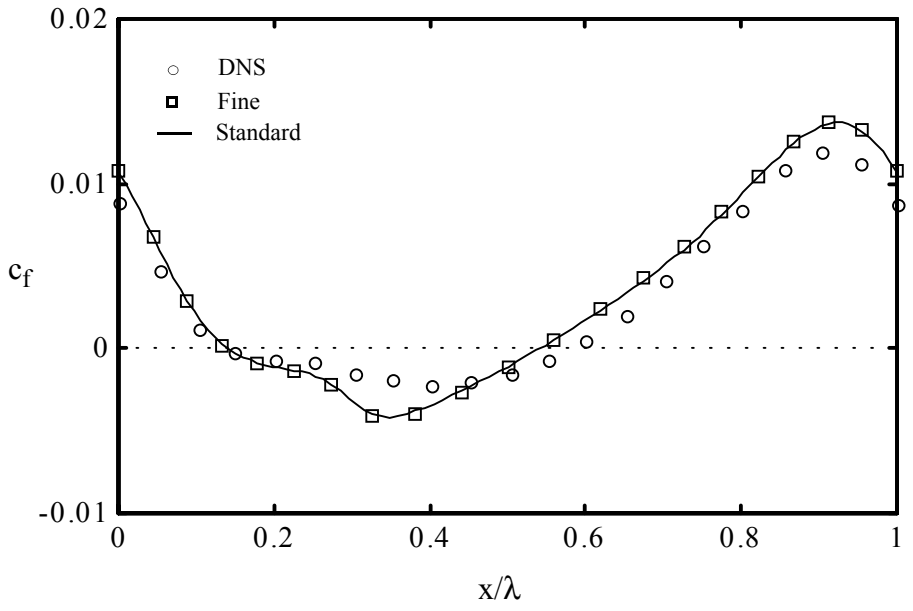

Figure 5.27: Shear stress distribution over the wavy-wall predicted by two-equation model YS using the standard and fine grid densities.

The figures show that the shear stress distribution over the wavy-wall is essentially unchanged by the doubling of the grid points for both one-equation model NR and two-equation model YS. Furhter details are provided in an appendix.

5.4.2.1 Predicted Separation and Reattachment Points

The flow for a wave aspect ratio of 0.1 separates near the wave crest and reattaches downstream of the trough. The inset of Figure 5.28 shows the wavy-wall channel. The streamline pattern for the flow in the highlighted region of the inset is shown in Figure 5.28 for the computation using NR and a wall spacing of δ=5.

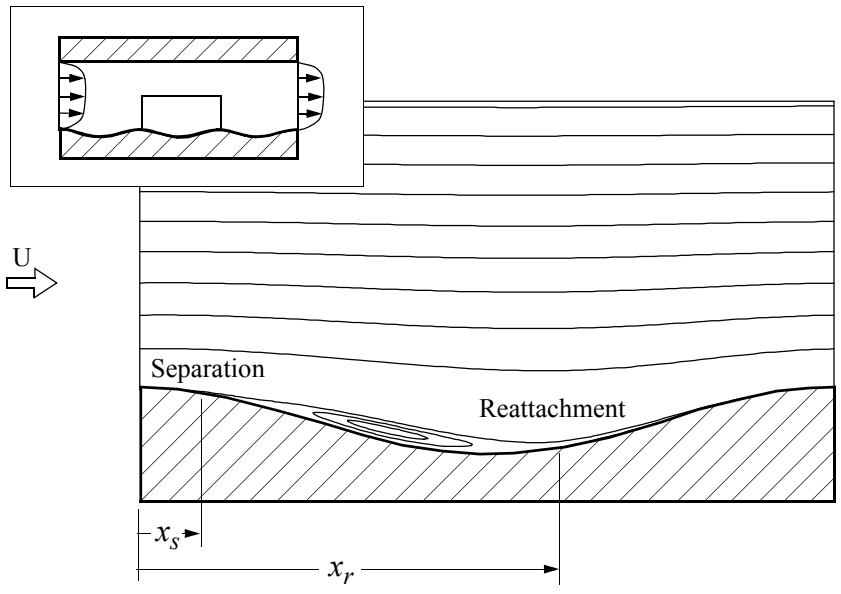

Figure 5.28: Streamlines for the wavy-wall showing the recirculation region.

The predicted separation point, reattachment point, and extent of the separation region are

provided in the table below. A positive error indicates that the predicted separation or reattachment occurs later than the DNS. A positive error in the extent indicates that the separation region is greater in extent than the DNS. The separation and reattachment points are constant to three places. Both quantities fluctuate sinusoidally with an amplitude that depends on the turbulence model. A typical fluctuation is on the order of $1x10^{-4}$.

All the models appear to predict errors within about 10% for the separation and reattachment points. All the models tend to predict separation somewhat earlier than the DNS. Only the two-equation near-wall model predicts an early reattachment and a separation region smaller than that indicated by the DNS data. It should be noted that underestimation of separation regions is generally associated with the excessive production of k and has often been associated with the k-ε model [86]. The difference in performance between the one-equation near-wall models and the two-equation near-wall model indicates that the predictions are highly dependent on the choice of near-wall model.

Table 5.8: Separation and reattachment points for the wavy-wall channel.

Model	DNS	YS	NR	HP	CP	RM	M1
x_s	0.142	0.140	0.135	0.134	0.131	0.134	0.134
x_r	0.603	0.539	0.591	0.600	0.610	0.582	0.594
x_e	0.461	0.399	0.475	0.474	0.478	0.448	0.460
Δx_s	-	-1.4	-4.9	-5.6	-7.7	-5.6	-5.6
Δx_r	-	-10.6	-2.0	-0.5	1.2	-3.5	-1.5
Δx_e	-	-13.4	-1.1	1.1	3.7	-2.8	-0.22

5.4.2.2 Predicted Shear Stress Distribution

It is commonly held that the k-ε model using the eddy viscosity model cannot predict the shear stress well for flows with streamline curvature [22, 153]. It is believed that the predictions of the k-ε model can be improved by using an algebraic stress model or a Reynolds stress model suggesting that the inability is due at least in part to the eddy viscosity model [22]. The shear stress distribution over the lower wall of the wavy-wall channel is presented for each near-wall model in Figure 5.29. Figures 5.30 and 5.31 present the shear stress distribution in an alternate format with three models shown in each figure for a more direct comparison.

The two-equation near-wall model appears to predict a minimum shear stress in the trough of the wave that is much less than that indicated by the DNS data. The k-ε model is often sighted as predicting smaller separation regions than those observed experimentally [51, 138]. This is generally attributed to the excessive production of k [86]. The one-equation near-wall models appear to fair better and predict more realistic shear stress distributions. This suggests that the near-wall model has a noticeable effect on overall performance as stated in reference 128.

The traditional one-equation near-wall models appear to give similar results. All seem to underestimate the shear stress in the trough and overestimate the shear stress in at the crest. Model RM does not appear to capture the trend in the shear stress distribution predicting a minimum forward of that indicated by the DNS data. Model RM seems to underestimate the shear stress over the rising slope behind the separation region. The new model appears to predict the shear stress well over the wave crest and along the rising slope directly behind the separation region.

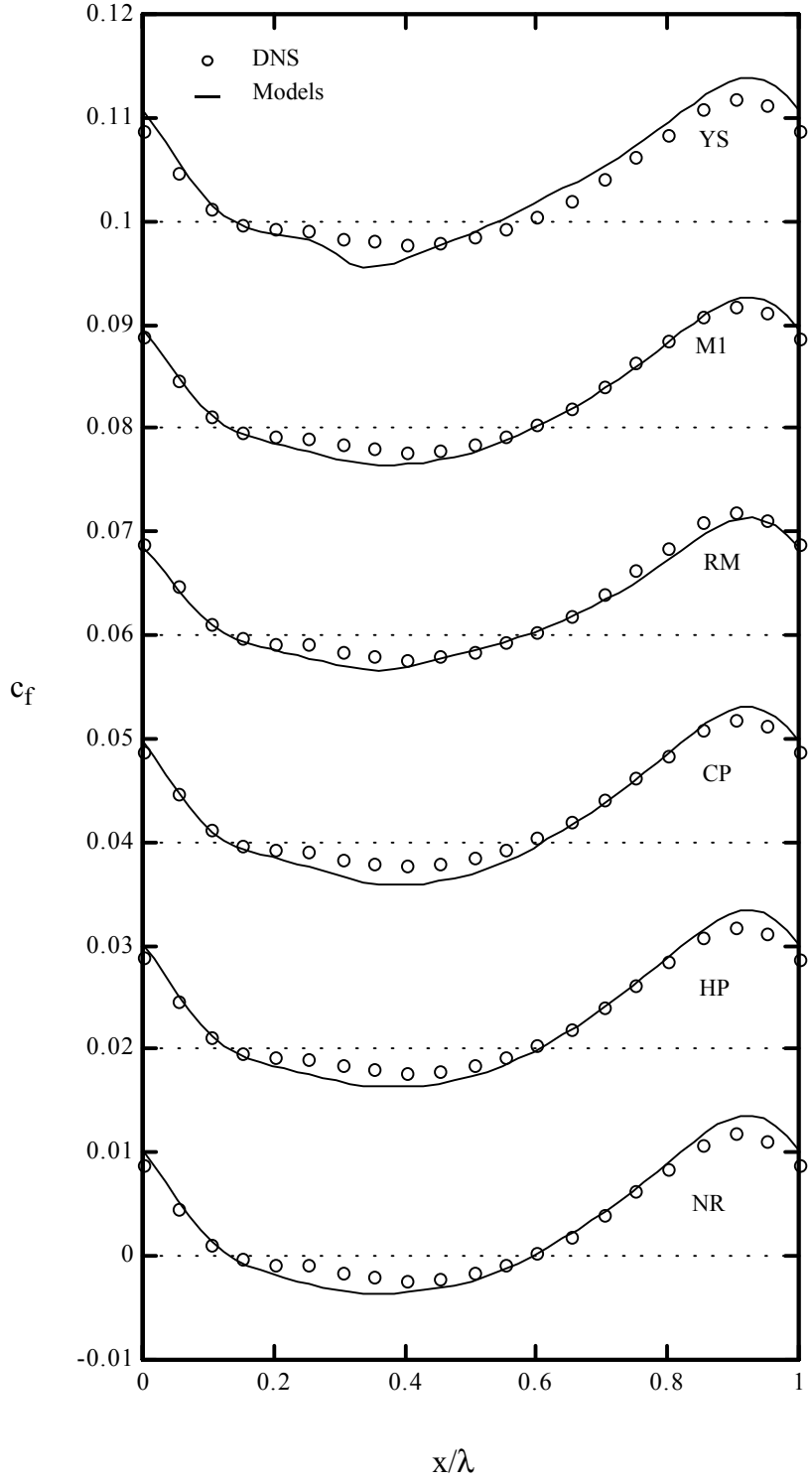

Figure 5.29: Predicted shear stress distribution over the wavy wall shown with DNS data.

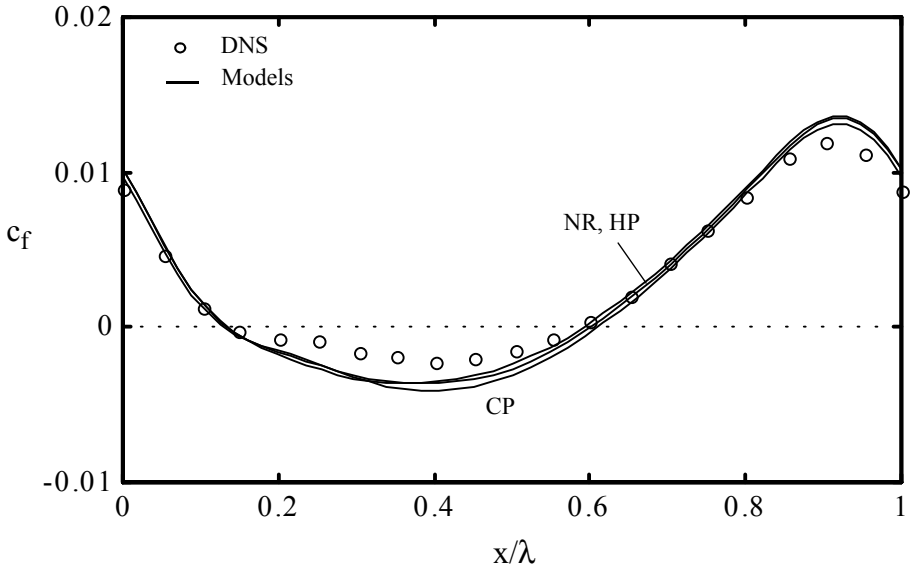

Figure 5.30: Predicted shear stress distribution over the wavy wall for models NR, HP, and CP.

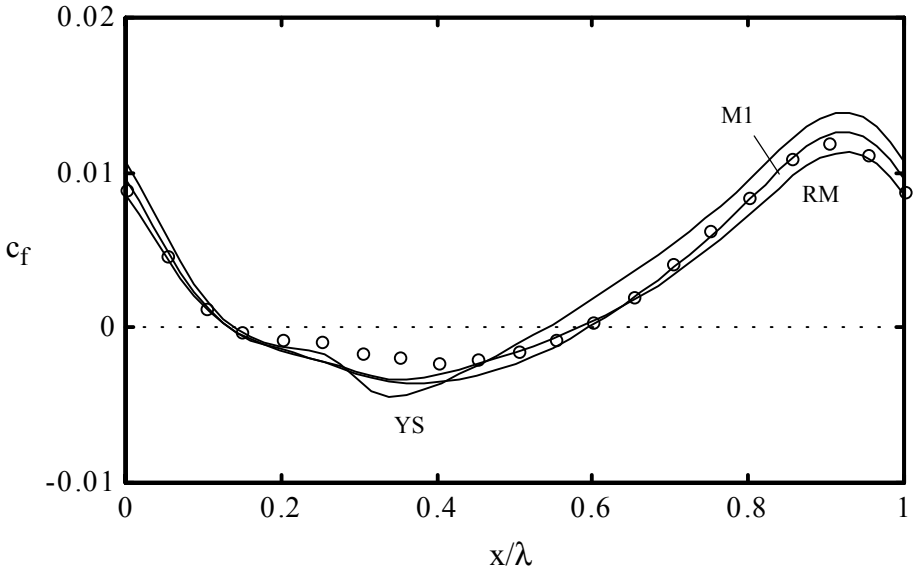

Figure 5.31: Predicted shear stress distribution over the wavy wall for model RM, M1, and the two-equation model.

The error in the shear stress distribution is reported in the table below. The error is defined in Chapter 4 and is scaled by a factor of 10^3. The errors in the skin friction coefficient suggest that the one-equation near-wall models agree more closely with the DNS than the two-equation near-wall model. Note that no general conclusion concerning the performance of one-equation models versus two-equation near-wall models is implied here since a wider sampling of two-equation near-wall models would clearly be necessary. The performance of the traditional one-equation models appears relatively consistent with errors in the predicted skin friction on the order of 9×10^{-4}. RM and M1 appear to provide improved predictions of the shear stress distribution over the wavy wall with errors one third less than those predicted by the traditional models.

Table 5.9: Error of the predicted skin friction for the wavy-wall channel.

Model	YS	NR	HP	CP	RM	M1
$\Delta(c_f)$	1.164	0.917	0.905	0.923	0.613	0.641

The computations are repeated using δ=5 with the same number of node points. The error in the shear stress distribution for these cases were within a few percent of those shown above. A formal grid dependence study for the wavy-wall channel is reported in an appendix.

5.4.2.3 Error of Predicted Mean Flow

The errors for U, k, and $-\overline{uv}$ are reported in the table below. This error is, as

defined in Chapter 4, the error at each point summed up throughout the flow and normalized using the DNS data.

Table 5.10: Error of the predicted mean flow for the wavy-wall channel.

Model	YS	NR	HP	CP	RM	M1
$\Delta(U)$	0.030	0.041	0.038	0.027	0.037	0.020
$\Delta(k)$	0.005	0.003	0.004	0.003	0.005	0.003
$\Delta(-\overline{uv})$	0.0013	0.0014	0.0015	0.0014	0.0017	0.0012

The errors in the predicted mean quantities indicate that all models provide comparable performance. CP and M1 provide slightly better predictions of U than the other models. NR, CP, and M1 appear to provide the best prediction of the k throughout the flow. For NR and CP, this result may be unexpected in view of the performance of these models for the boundary layer where it was found that k was underestimated. All models produce comparable errors in the predicted $-\overline{uv}$. The results of the computations are analyzed qualitatively below.

5.4.2.4 Qualitative Analysis

The profiles of U, k, and $-\overline{uv}$ are provided in Figures 5.32 to 5.34. Each figure shows the predictions of two models.

Figure 5.32 shows the profiles for NR and HP. The predicted U is very similar for both models and the trends in k appear to be captured by both models. NR predicts a lower k in general while HP tends to overestimate k throughout the flow. Both models

predict a double peak in k close to the separation point near x/λ=0.2. Although not shown, HP predicts a variation of k that is significantly greater than the DNS at the plane wall. Both models predict the general trend in $-\overline{uv}$, but do not predict the peak in $-\overline{uv}$ at the wave crest. At this location in the flow, the mean strain in the streamwise direction and the mean strain in the wall-normal direction are of opposite sign leading to cancellation of the two contributing terms to the Reynolds shear stress in the eddy viscosity model. It is possible that an algebraic stress model used with the k-ε model would fair better at predicting the Reynolds shear stress than the eddy viscosity model at this point in the flow due to the ability of the algebraic stress models to capture the effects of streamline curvature [22]. Both models overestimate $-\overline{uv}$ in the region behind the separation zone.

Figure 5.33 shows the profiles for CP and RM. Once again, the predicted U appears comparable for both models. RM predicts a lower k in general while model CP overestimates k near the wavy wall. Both models predict a double peak in k close to the separation point near x/λ=0.2. Both models predict the general trend in $-\overline{uv}$, but do not predict the peak in $-\overline{uv}$ at the wave crest for reasons given above. RM predicts a variation of $-\overline{uv}$ closer to that of the DNS as evidenced by the errors presented earlier. CP tends to overestimate $-\overline{uv}$ behind the separation zone as do closely related models NR and HP.

Figure 5.34 shows the profiles for M1 and YS, the benchmark two-equation near-wall model. YS over-estimates k throughout the flow and does not predict a double peak in k near x/λ=0.2. The new model predicts a distribution of k more similar to the DNS near the wavy wall, but predicts a k exceeding the DNS near the plane wall. YS tends to predict a $-\overline{uv}$ that exceeds the DNS downstream of the separation zone. The new model

predicts a distribution of $-\overline{uv}$ near the wavy wall that more closely follows the DNS data than YS. The figures clearly show that the near-wall models affect the predictions of the various quantities even far from the wall.

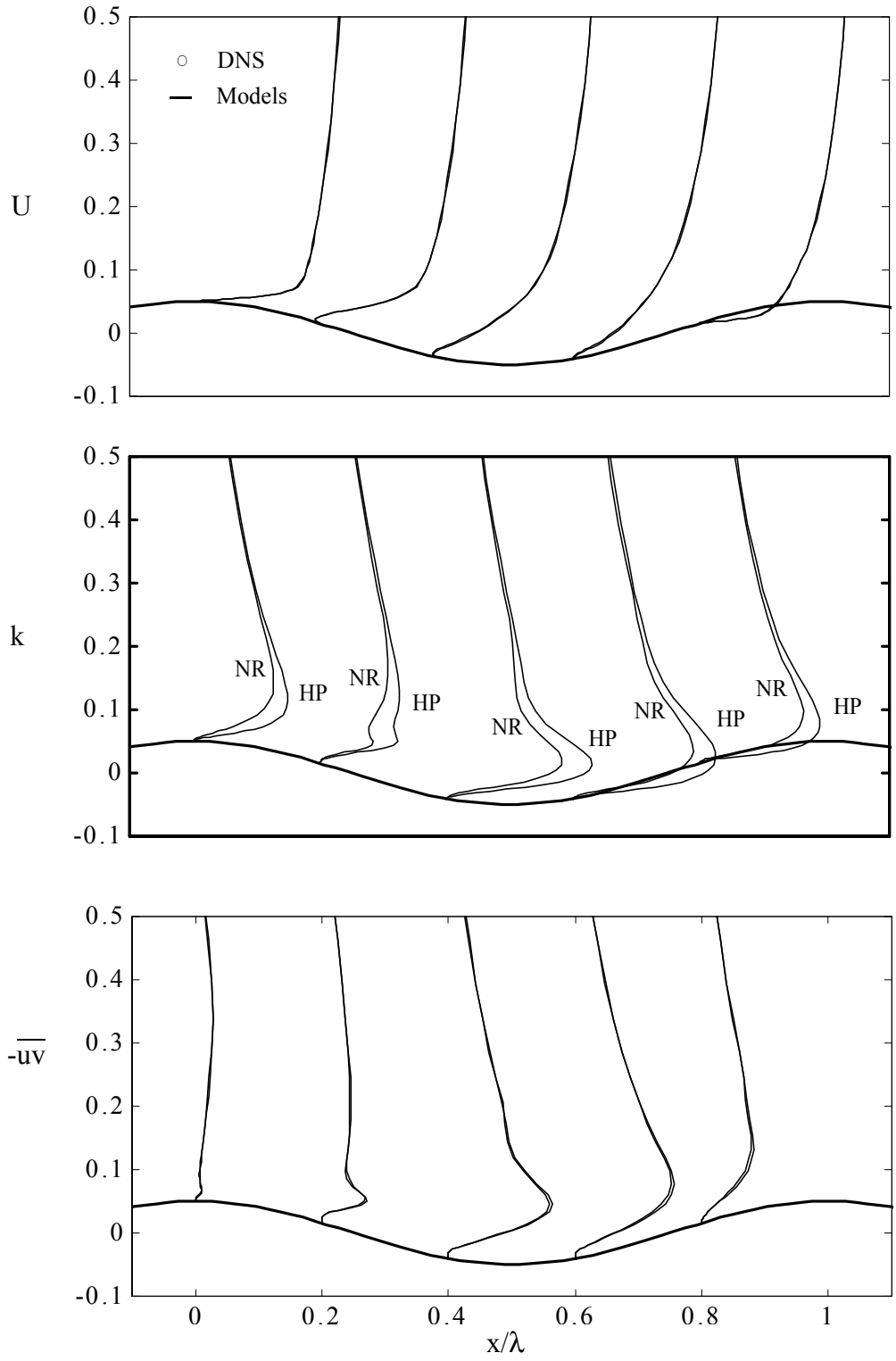

Figure 5.32: Predicted profiles of U, k, and $-\overline{uv}$ for the wavy-wall channel for NR and HP.

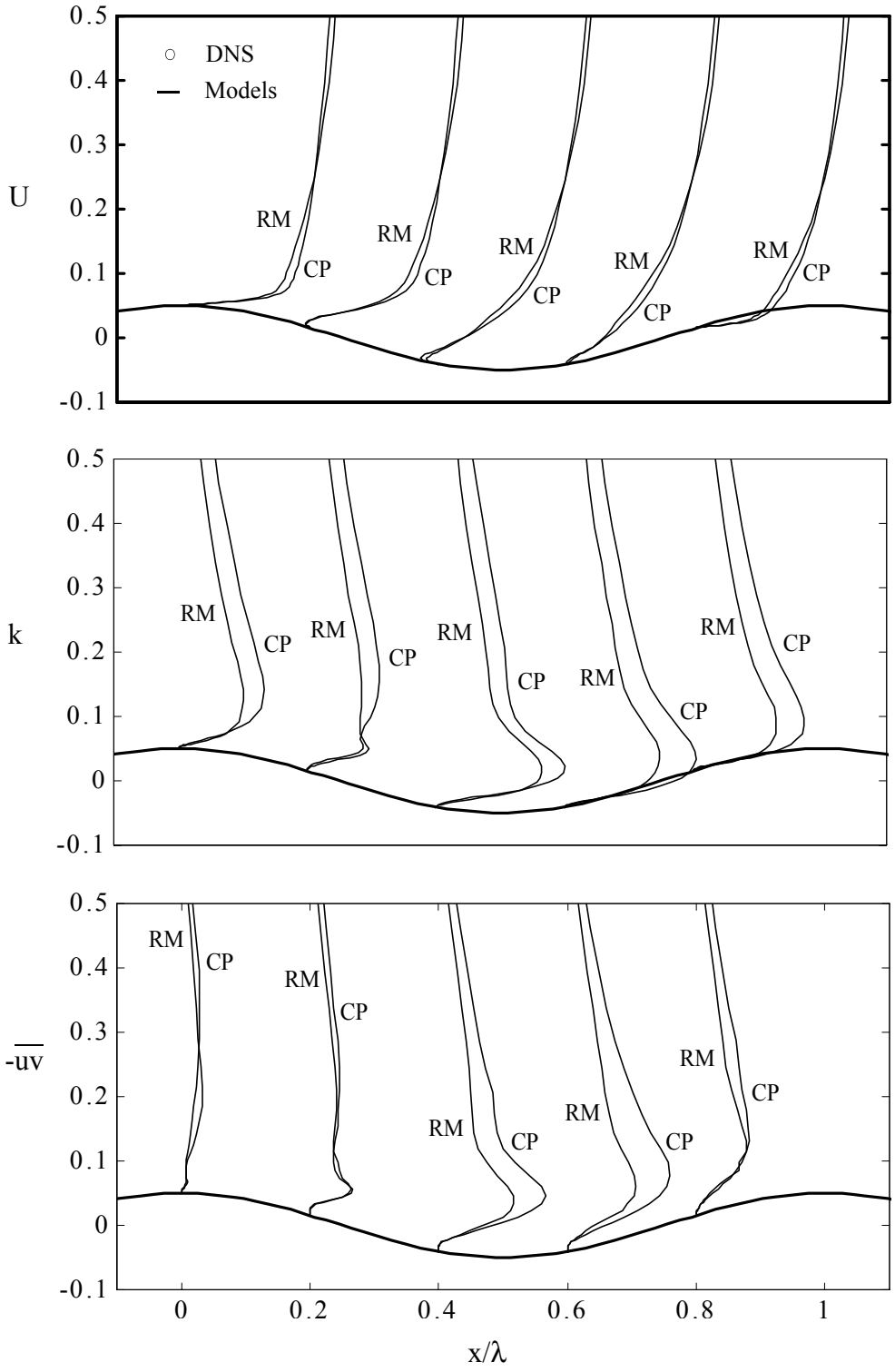

Figure 5.33: Predicted profiles of U, k, and $-\overline{uv}$ for the wavy-wall channel for CP and RM.

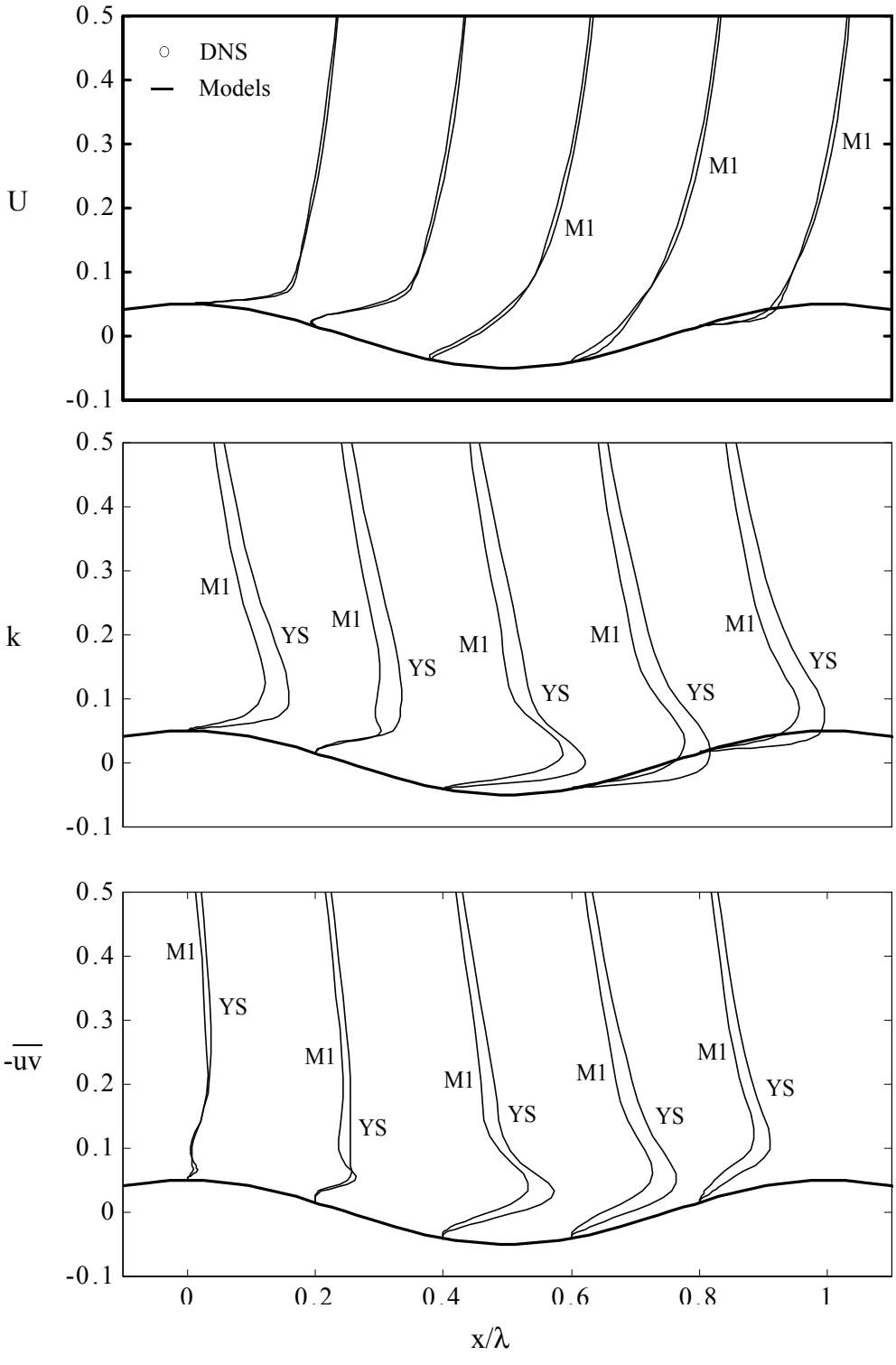

Figure 5.34: Predicted profiles of U, k, and $-\overline{uv}$ for the wavy-wall channel for M1 and YS.

5.5 Summary

The results of the asymptotic analysis showed that only two one-equation models are capable of reproducing the behavior of $-\overline{uv}$ near the wall. The asymptotic analysis suggested that the majority of models could reproduce ε at the wall. The results of the analysis of the model expressions indicated that only HP, RM, and M1 predict ε near the wall well. Consistent with previously reported results, NR and CP were found to predict an ε exceeding that indicated by the DNS data throughout the near-wall region. RM, HP, and M1 were found to predict ε well throughout the near-wall region. All models predicted $-\overline{uv}$ sufficiently well in the region near the wall, despite the inability of NR, CP, and HP to predict the behavior at the wall.

The computations of the boundary layer showed clearly that only the benchmark two-equation near-wall model, RM, and M1 were able to predict series coefficients in agreement with the DNS. The computations verified that NR, CP, and HP do not predict the cubic variation of $-\overline{uv}$ at the wall. All models predicted the Kármán constant, shape factor, and skin friction well. The errors in the predicted mean flow indicated that all models predict U and $-\overline{uv}$ well. The error in predicted k and ε are greatest for NR and CP. Due to the excessive predicted ε in the near-wall region, NR and CP do not predict ε at the wall and do not capture the peak in k near the wall. HP, RM, and M1 do capture the peak in k at the wall and predict ε well throughout the near-wall region. Consistent with the results of the asymptotic analysis, only RM and M1 predict the behavior of $-\overline{uv}$ at the wall.

The computation of the wavy-wall channel indicated all one-equation models predict the separation and reattachment points well while the two-equation near-wall

model predicted a smaller separation region than the DNS. The two-equation model predicts the wall shear stress distribution most poorly while RM and M1 predict the shear stress most similar to the DNS. The remaining models fall between these two extremes. The predicted U, $-\overline{uv}$, and k show variations throughout the wavy-wall channel similar to the DNS data for the one-equation models. The two-equation near-wall model predicts U and $-\overline{uv}$ well, but k exceeds that indicated by the DNS throughout the channel.

CHAPTER 6

6. Conclusions

This chapter is divided into two sections. The first section consists of concluding remarks and summarizes the most important findings of this work. The second section consists of recommendations for future work and describes several ways in which this work may be extended.

6.1 Concluding Remarks

The evaluation of near-wall turbulence models consists of an asymptotic analysis, an analysis of model expressions, and the computation of fundamental benchmark flows. The study of the one-equation near-wall models indicates several model characteristics not previously reported. Based on the findings of the asymptotic analysis and analysis of model expressions, a new model is developed and evaluated.

Based on the asymptotic analysis, it is found that only one of the previously existing models reproduces the behavior of $-\overline{uv}$ at the wall. The traditional models do not reproduce the variation of $-\overline{uv}$ at the wall. Specifically, only RM and the new model reproduce the cubic variation at the wall. The traditional models predict a quartic variation at the wall that is not consistent with the behavior indicated by series expansions for the boundary layer. It is further found that all but one model appear to reproduce ε at the wall. Specifically, only the traditional models and the new model yield

an ε at the wall consistent with the value indicated by the series expansions.

The analysis of the model expressions indicates that all models reproduce ν_t well throughout the near-wall region, but that only one of the previously existing models reproduces ε well throughout the near-wall region. Specifically, HP and the new model yield a distribution of ε that agrees with DNS data well throughout the near-wall region. NR and CP yield a distribution that greatly exceeds that indicated by the DNS data in the buffer layer, consistent with previous studies. RM yields an ε that agrees with the DNS data well very near the wall, but exceeds that indicated by the DNS beyond the buffer layer.

The computations of the turbulent boundary layer indicate that only three models predict ε at the wall and well throughout the near-wall region. Specifically, only HP, RM, and the new model appear to predict ε correctly throughout the near-wall region. Consistent with the findings of the analysis of model expressions, NR and CP predict excessive ε in the buffer layer. Due to the excessive ε in the buffer layer, both underestimate k in the near-wall region. Consequently, in contrast to the results of the analysis of model expressions, neither appears to predict ε at the wall. Furthermore, consistent with the findings of the asymptotic analysis, only RM and the new model are found to reproduce the behavior of $-\overline{uv}$ at the wall for the boundary layer. The traditional models predict a quartic variation at the wall. With respect to reproduction of the log law, it is found that, while all models reproduce κ well, only the new model predicts the log-law additive constant well for the boundary layer flow. Only RM and the new model predict series expansion coefficients for k and $-\overline{uv}$ consistent with the DNS data. In addition, it is shown that only the new model predicts $-\overline{uv}$ without any discontinuity

across the boundary between the near-wall and outer models.

The computations of the wavy-wall channel indicate that all the models predict the general characteristics of the mean flow including the separation region. The one-equation models predict separation and reattachment points within a few percent of the DNS data. While the one-equation models provide fairly consistent predictions, the two-equation near-wall model predicts an early reattachment. It is found that the one-equation near-wall models predict the shear stress distribution over the wavy wall in closer agreement with the DNS than the two-equation near-wall model. The error in the predicted shear stress distribution is greatest for the two-equation near-wall model and least for RM and the new model.

In addition to the findings resulting directly from the evaluation of the models, it is found that the one-equation near-wall models require grids less fine than the two-equation near-wall model to obtain grid independent results for the boundary layer flow. This suggests that the one-equation models are an ideal choice for engineering computations of practical flows where computational expense may be a significant factor influencing the choice of turbulence model.

6.2 Future Work

The evaluation of the near-wall turbulence models described in this work can be extended by including a greater sample of two-equation models such that a more general comparison between the performance of one-equation near-wall models and two-equation near-wall models can be made. Alternate formulations of the one-equation near-wall models studied in this work are utilized by various commercial codes. Rather than express the eddy viscosity directly in terms of the turbulence kinetic energy and distance

from the no-slip surface, these alternate formulations express the eddy viscosity using an expression similar to that used by the two-equation models. This work could be further extended by incorporating such alternate formulations into the analysis.

This work can also be extended by the inclusion of more benchmark flows. For example, evaluations of turbulence models often include the backward facing step, airfoil flows, and flows about various obstacles. It has been shown that the near-wall model greatly affects the predictions for the backward facing step. Incorporating these benchmark flows into the analysis would allow more general conclusions to be made concerning the performance of the one-equation models.

In this work, the metrics by which the models are judged concern the extent to which the predictions of the benchmark flows agree with known behavior and DNS data. In addition to this metric of performance, the computational expense of using various models could be considered as a metric of performance since computational expense may be a significant factor influencing the choice of a model for practical engineering computations. This work clearly indicated that one-equation models require less fine grids to obtain grid independent results for the boundary layer flow. Further investigation could serve to indicate whether this is the case for more complex flows.

Finally, alternate expressions for the new model proposed in this work could be investigated. The new model could, for example, be based on velocity scales other than those used by the traditional models. The new model could also use simpler modeling functions or functions similar to those used by two-equation models. The investigation of such alternate expressions would clearly extend this work.

APPENDIX

New One-Equation Near-Wall Turbulence Model

The dissipation, ε, for the new model is expressed using a *k-l* model similar to existing one-equation near-wall models. The new model expresses the eddy viscosity, ν_t, as

$$\nu_t = \sqrt{k} l_\mu \tag{A.1}$$

The choice for l_μ made by the majority of the existing models is such that $\nu_t = C_\nu k^{1/2} y(1-\exp(-A_\nu R_y))$. As shown in Chapter 5, this relation does not provide the correct variation of the Reynolds shear stress, $-\overline{uv}$, near the wall. To provide the correct variation of $-\overline{uv}$ near the wall, ν_t is be given by

$$\nu_t = C_\nu \sqrt{k} y f_1 \ , \tag{A.2}$$

where $f_1 = (1 - e^{-a_1 R_y^{n_1} - a_2 R_y^{n_2}})$. In the limit as the wall is approached it can be shown that, for the proper choice of n_1 and n_2, ν_t, and therefore $-\overline{uv}$, varies as y^3. The new model is therefore capable of reproducing the cubic behavior of $-\overline{uv}$ at the wall. The value of C_ν is $\kappa C_\mu^{1/4}$.

The new model expresses ε in the form $\varepsilon_1 + \varepsilon_2$ as

$$\varepsilon = 2\nu \frac{k}{y^2} f_2 + C_\varepsilon \frac{k^{3/2}}{y} f_3 . \tag{A.3}$$

The value of C_ε can be determined to be approximately 0.4 using DNS data for the boundary layer sufficiently far from the wall. It can be shown that C_ε is $C_\mu^{3/4}/\kappa$ in this region of the flow.

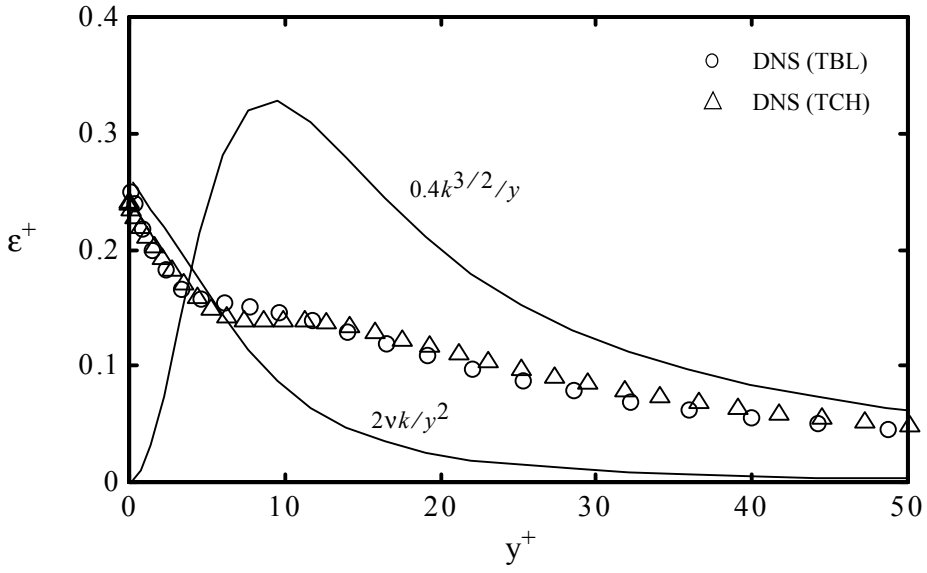

Figure A.1: Variation of ε_1 and ε_2 shown with the DNS data for the boundary layer and plane channel.

Figure A.1 shows the variation of the two terms of expression for ε in the near-wall region when the functions f_2 and f_3 are one. The DNS data is that for the boundary layer and plane channel. Figure A.1 suggests that the first term of equation (A.3) does not reproduce the rapid decrease in ε at the wall and that the second term exceeds the DNS data in the buffer layer. To reproduce ε near the wall, f_2 can be chosen to be $e^{-a_3 R_y}$. To reproduce ε in the buffer layer, f_3 can be chosen to be $(1 - e^{-a_4 R_y})$. There are two

unknown modeling constants for ν_t and two for the ε for a total of four constants that must be determined. The function f_3 could also be chosen to be equal to f_1. This would allow the new model to be written compactly as $\varepsilon = (2\nu f_2 + (C_\nu/C_\varepsilon)\nu_t)k/y^2$, reducing the number of unknown modeling constants for ε. Figure A.2 below shows the variation of the two functions f_1 and f_3 using DNS data for the boundary layer. Figure A.2 indicates that the two functions are clearly different in region in which the one-equation models are to be utilized.

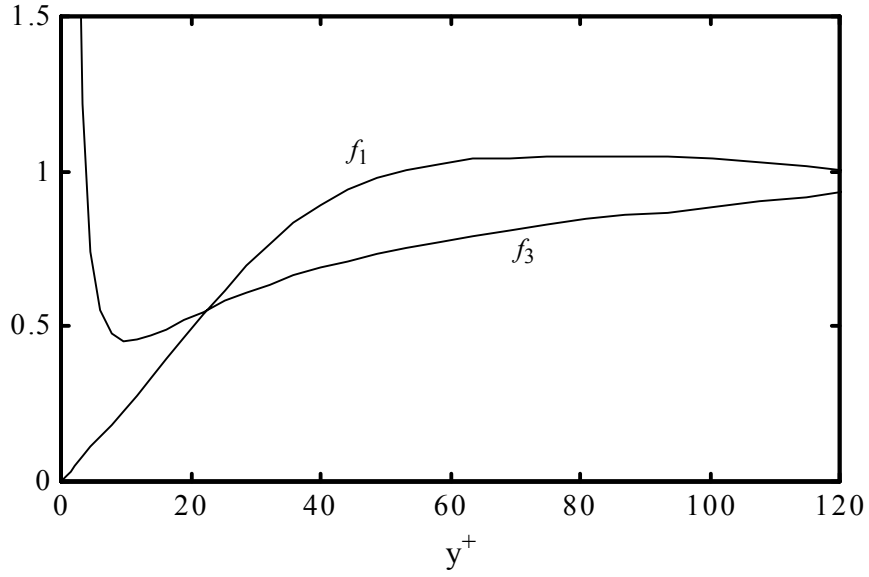

Figure A.2: Functions f_1 and f_3 determined using DNS data for the boundary layer.

Therefore, the models for ν_t and ε are kept separate by choosing f_3 independently of f_1. Since the leading term of the series expansion of f_2 is one, the new model given by equation (A.3) reproduces the value of $2a_k$ for ε at the wall.

Before continuing, it is important to identify the two steps to determining the modeling constants. The new model requires the determination of six modeling constants, two of which, C_ε and C_ν, are essentially known. The first step is to determine the constants by fitting the functions above to the DNS data for the boundary layer or channel flow. This provides the baseline constants and is described further directly below. The second step is to compute the flow and adjust the baseline constants to obtain a satisfactory prediction of the relevant quantities. This provides the recommended model constants to be used for computations. This is described further later.

The modeling constants for the new model are determined using an optimization code. Each of the modeling constants are varied one at a time to minimize the error between the model and the DNS data, $\Delta\varepsilon = |\varepsilon - \varepsilon_{DNS}|$. This is completed over a predetermined interval such as that comprising the region from the wall to the point where $y^+ = 50$. The modeled ε is given by equation (A.3) evaluated using the data for the turbulent kinetic energy, k, given by the DNS. The baseline constants are a_3=0.1, a_4=0.023, and C_ε=0.307. The model fits the DNS data well as indicated in Figure A.3.

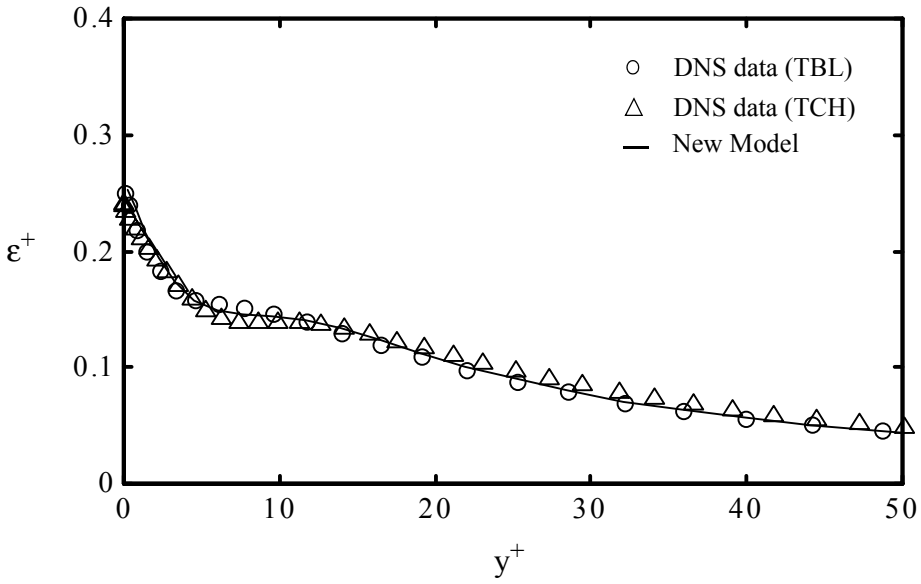

Figure A.3: The new model for ε compared to DNS data for the boundary layer and plane channel.

Baseline constants can be determined for the eddy viscosity in a similar fashion. The exponents n_1 and n_2 for f_1 are chosen to be 1/2 and 3/2, respectively. The value of n_1 is chosen such that the model reproduces the cubic variation of $-\overline{uv}$ at the wall. The fit of the eddy viscosity to the DNS is shown in Figure A.4. The baseline constants are a_1=0.01, a_2=0.00272, and C_ν=0.185.

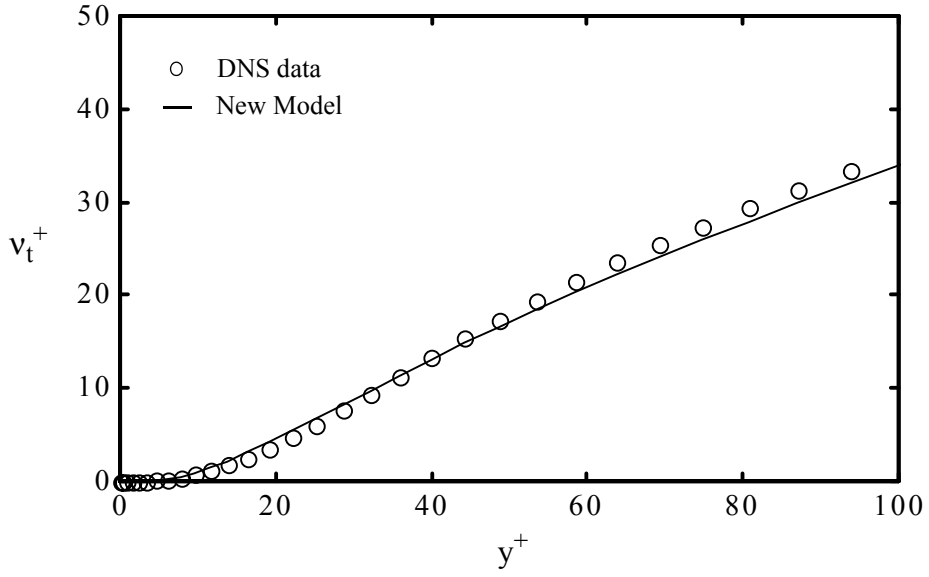

Figure A.4: The new model for ν_t compared to DNS data.

The only choice remaining to complete the formulation of the new model is to identify the point beyond the wall at which the two-equation model is to be applied. The boundary between the near-wall region and the outer region is called the near-wall boundary. Most models utilize the turbulence Reynolds number, $R_y = \sqrt{k}y/\nu$, to delineate the near-wall boundary. Others uses the ratio of ν_t to the kinematic viscosity, ν_t/ν, to delineate the near-wall boundary. Since $\nu_t = C_\nu \sqrt{k} y f_1$, R_y and ν_t/ν differ only by a constant far from the wall and therefore either can be used to determine the edge of the near-wall boundary. For the majority of the models, the near-wall boundary is placed at R_y=250. The near-wall boundary must be sufficiently far such that the relation

$\nu_t = C_\mu k^2/\varepsilon$ is valid. For high Reynolds numbers, this is the point where R_y=250 or ν_t/ν=50. The parameter used for the new model is ν_t/ν. There may be an advantage to moving the near-wall boundary closer to the wall. If the near-wall boundary is closer to the wall, the region of the flow in which the two-equation model is applied is increased. Since the two-equation model is a complete model, it is reasonable to expect that the computations would benefit from moving the near-wall boundary closer to the wall. This can be accomplished by using the two-equation near-wall relation

$$\nu_t = C_\mu f_\mu \frac{k^2}{\varepsilon} \quad . \tag{A.4}$$

with $f_\mu = (f_1 + 2f_2/(C_\varepsilon R_y))f_3 \approx f_1 f_3$. The last relation is derived by equating the inner and outer relations for ν_t. The near-wall boundary for the new model can now be set close to the wall.

In summary, the new one-equation near-wall model is given by the k equation

$$\frac{Dk}{Dt} = ((\nu + \nu_t/\sigma_k)k_{,j})_{,j} - \overline{u_i u_j} U_{,j} - \varepsilon \tag{A.5}$$

with

$$\nu_t = C_\nu \sqrt{k} y f_1 \tag{A.6}$$

and

$$\varepsilon = 2\nu \frac{k}{y^2} f_2 + C_\varepsilon \frac{k^{3/2}}{y} f_3 . \tag{A.7}$$

The functions f_1, f_2, and f_3 were given above. This model is applied when $\nu_t/\nu < 10$. This value of ν_t/ν corresponds to the point at which y^+ is approximately 30 for the benchmark turbulent boundary layer DNS. With the k energy equation and eddy viscosity model, the

model above is used to close the RANS equations for the region near the wall. For $\nu_t/\nu >$ 10, ε is given by solution of the standard ε equation and the eddy viscosity is given by

$$\nu_t = C_\mu f_\mu \frac{k^2}{\varepsilon}. \tag{A.8}$$

where $f_\mu = (f_1 + 2f_2/(C_\varepsilon R_y))f_3 \approx f_1 f_3$. Therefore, in regions far from the wall, the RANS equations are closed using the k equation, the ε equation, the eddy viscosity model, and equation (A.8). It should be noted that, since the functions f_1 and f_3 asymptote to one far from the wall, equation (A.8) is equivalent to the relation used by the standard k-ε model far from the wall.

The six baseline constants determined by fitting to the DNS data are further optimized by the computation of a turbulent boundary layer flow such that the errors between U, k, $-\overline{uv}$, and ε predicted by the computation and the DNS data are minimized. This can be done by calculating total errors as described in Chapter 4 or the predicted quantities can be plotted against the DNS data and judged qualitatively. The constants are then adjusted appropriately and the computation is repeated until the errors are considered acceptable. For example, decreasing a_1 or a_2 will tend to increase the maximum U^+ indicating a decrease in c_f. Increasing C_ε will tend to decrease the peak in k that occurs near the wall.

The recommended model constants are a_1=0.028, a_2=0.0012, a_3=0.15, a_4=0.02, C_ν=0.23, and C_ε=0.38. It should be noted that this model can be optimized using f_1 in place of f_3 in the ε relation despite the apparent difference of the functions indicated by Figure A.2. Also, neglecting the first exponential in the new model for ε yields an acceptable model.

Figures A.6 through A.12 show the various quantities predicted by the new model for the computation of the boundary layer flow. Clearly, all quantities are predicted well. Figure A.7 shows that the peak in k is captured. Figure A.8 shows that the growth of k is captured near the wall. Figure A.9 indicates no discontinuity in $-\overline{uv}$ and Figure A.10 shows that the correct behavior of $-\overline{uv}$ near the wall is reproduced. Figure A.11 and A.12 show that ε is predicted well. Specifically, the correct behavior of ε near the wall is reproduced and the value of ε at the wall is very close to the DNS data. The new model is compared to existing one-equation near-wall models in Chapter 5.

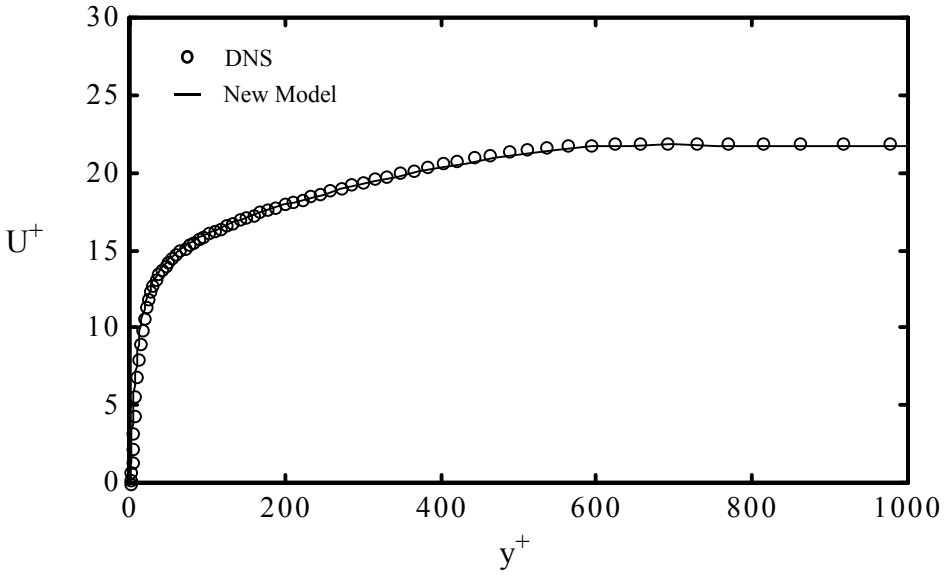

Figure A.5: Predicted U for the new model.

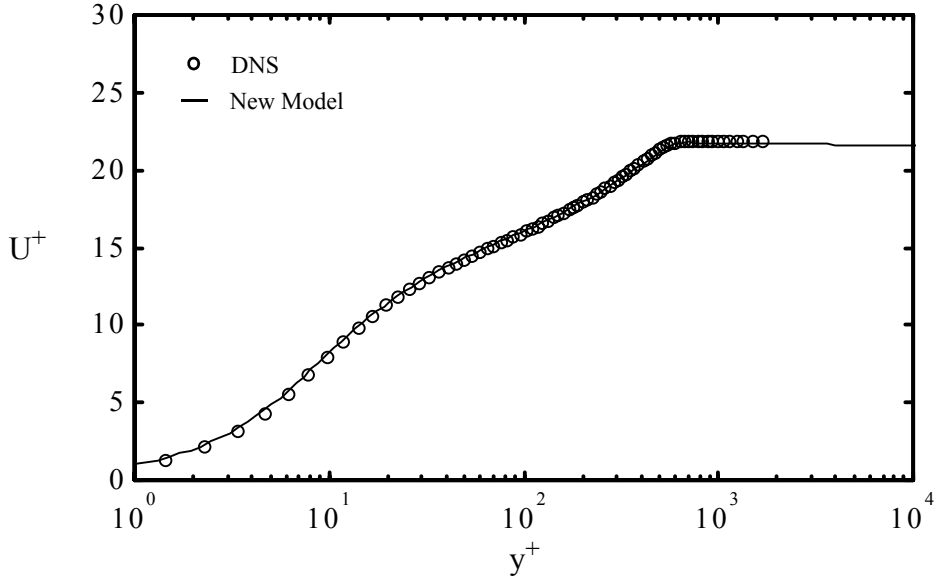

Figure A.6: Predicted *U* near the wall for the new model.

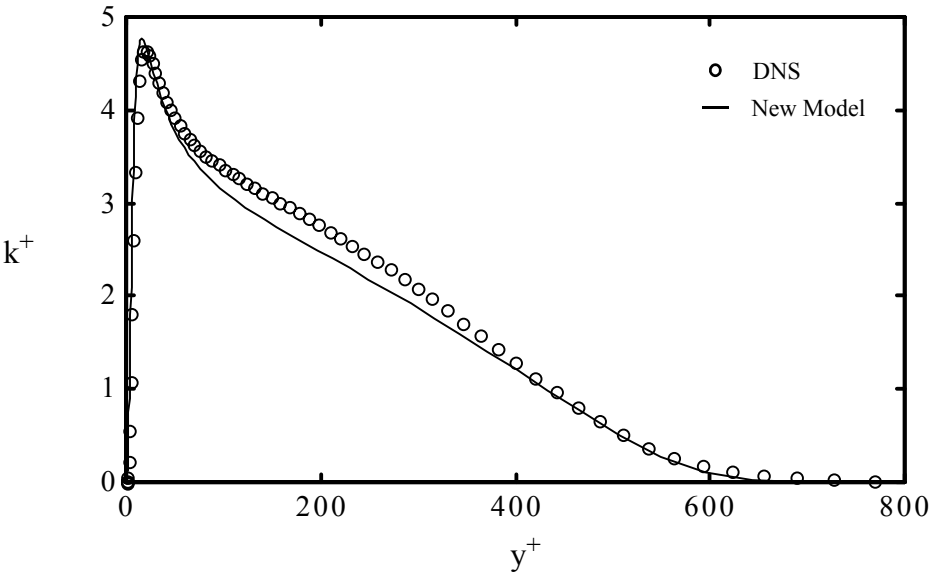

Figure A.7: Predicted *k* for the new model.

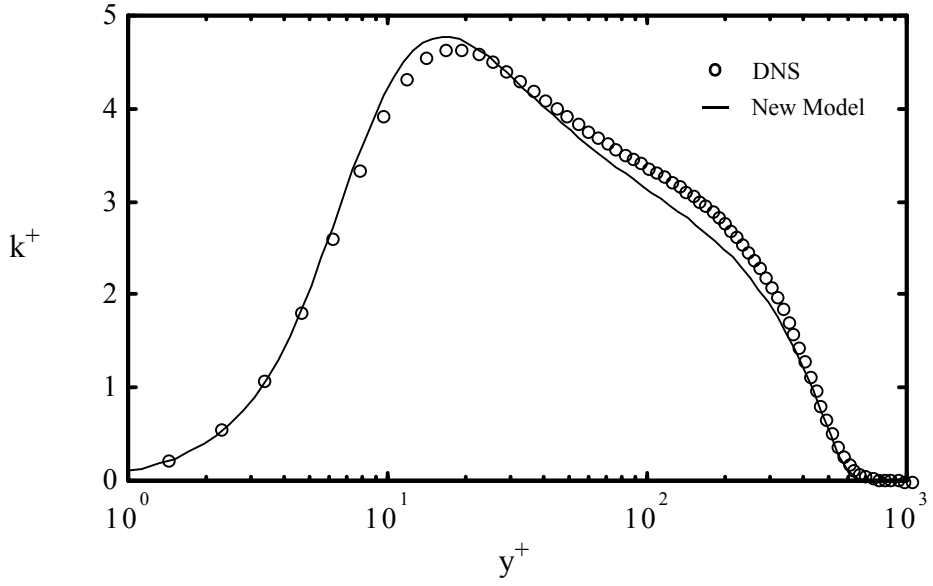

Figure A.8: Predicted *k* near the wall for the new model.

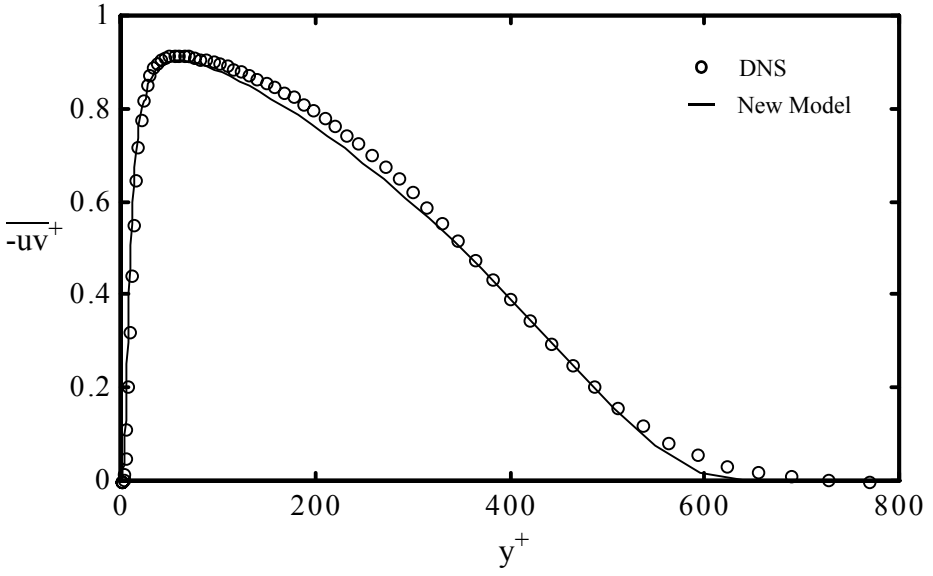

Figure A.9: Predicted $-\overline{uv}$ for the new model.

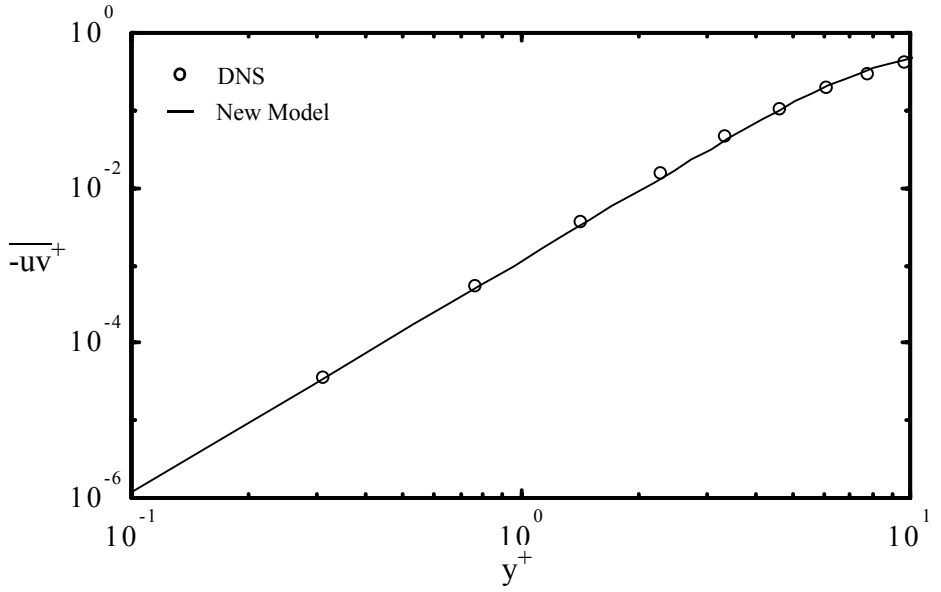

Figure A.10: Asymptotic behavior of predicted $-\overline{uv}$ for the new model.

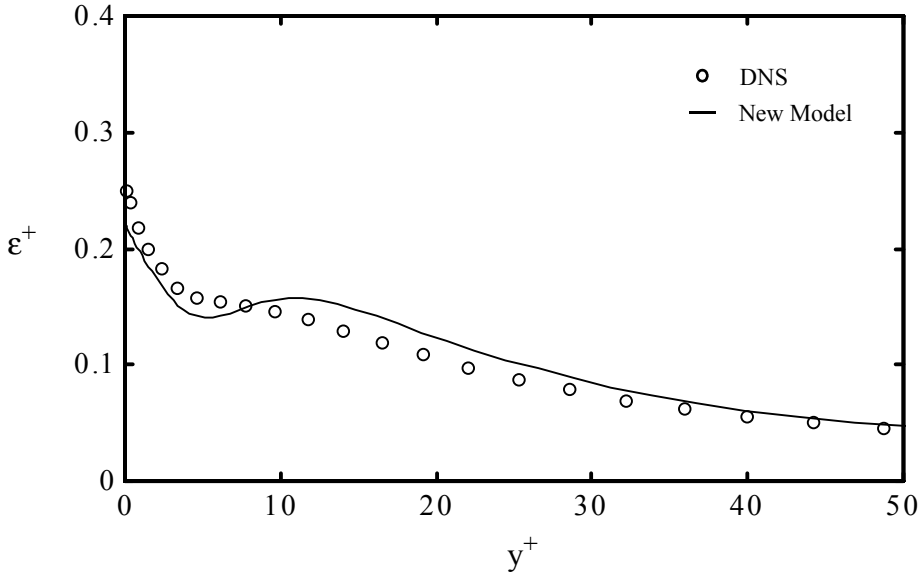

Figure A.11: Predicted ε for the new model.

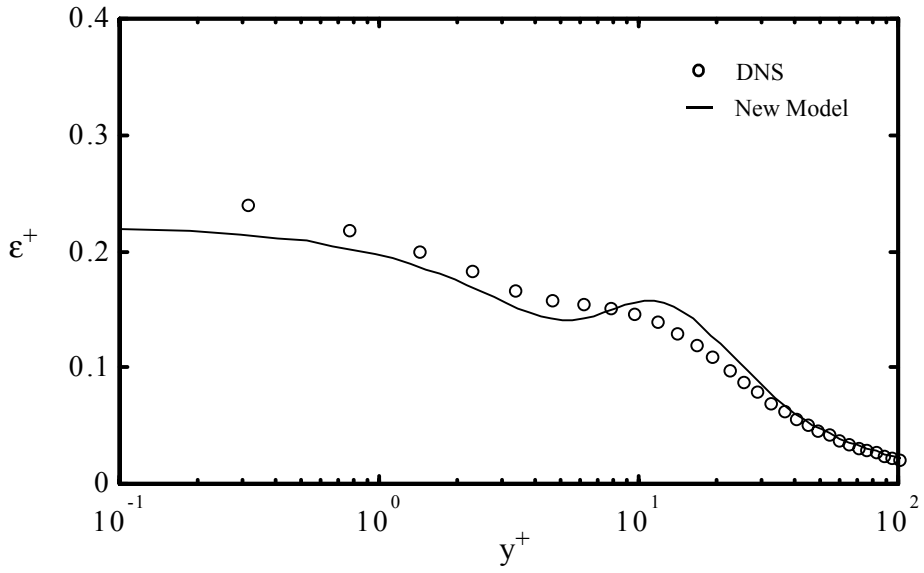

Figure A.12: Predicted ε near the wall for the new model.

Grid Dependence Study

To verify that the solutions computed using the projection method code are grid independent, the number of grid points for the boundary layer and wavy-wall channel are doubled in each direction. Doubling of the grid points is uniform such that the wall spacing is halved. For the boundary layer, the standard grid consists of 63 points in the streamwise direction and 127 in the wall-normal direction while the fine grid consists of 127 points in the streamwise direction and 255 points in the wall-normal direction. The wall spacings for the standard and fine grids at the position where Re_θ is 1416 are y^+= 0.05 and y^+= 0.1, respectively. For the second benchmark flow, the wavy-wall channel, the standard grid consists of 101 points in the streamwise direction and 127 in the wall-

normal direction while the fine grid consists of 201 points in the streamwise direction and 255 points in the wall-normal direction. The extra grid point in the streamwise direction for the wavy-wall channel grids allows simple implementation of the periodic boundary conditions and ensures continuity of all derivatives. The nominal wall spacings for the standard and fine grids are $y^+ = 0.05$ and $y^+ = 0.1$, respectively.

The boundary layer flow is computed with the standard and fine grids using the one-equation near-wall model NR coupled, as throughout this work, with the standard k-ε model. The details of the implementation of the model are provided in Chapter 5. The boundary conditions used for the computation are described in Chapter 3. Table A.1 below lists the predicted series expansion coefficients and skin friction coefficient for the boundary layer flow for both cases. As shown in Table A.1, the predicted coefficients and skin friction change little for the fine grid suggesting that the standard grid is sufficiently fine.

Table A.1: Predicted series expansion coefficients and c_f for the boundary layer.

Grid	a_k	$a_{uv} \times 10^3$	a_ε	$c_f \times 10^3$
Standard	0.0317	0.140	0.057	4.49
Fine	0.0321	0.146	0.056	4.45

Figures A.13 through A.21 below show the mean velocity and turbulence quantities for the boundary layer. The solution in each case is effectively unchanged by the doubling of the number of grid points indicating that the standard grid is sufficiently fine to resolve the flow.

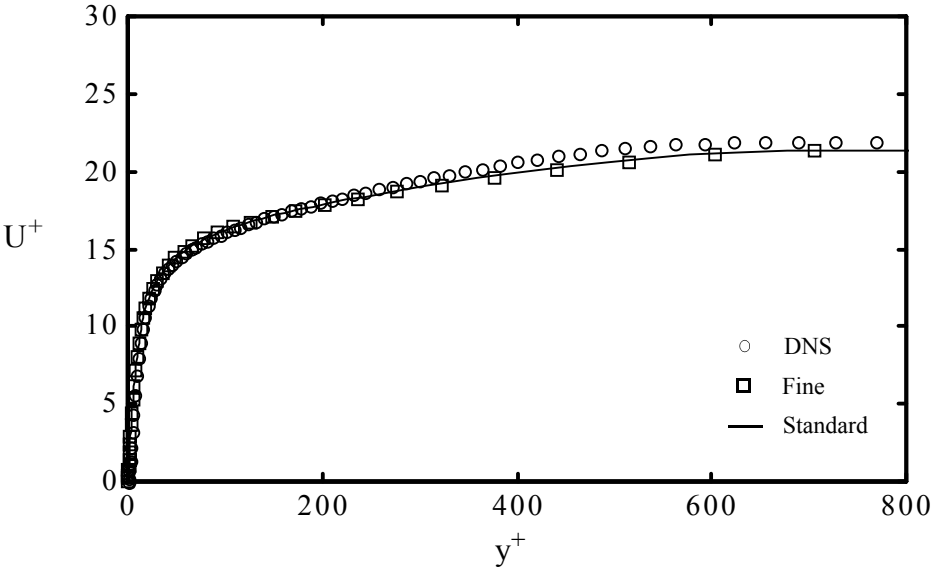

Figure A.13: Predicted *U* for the boundary layer for the standard and fine grids.

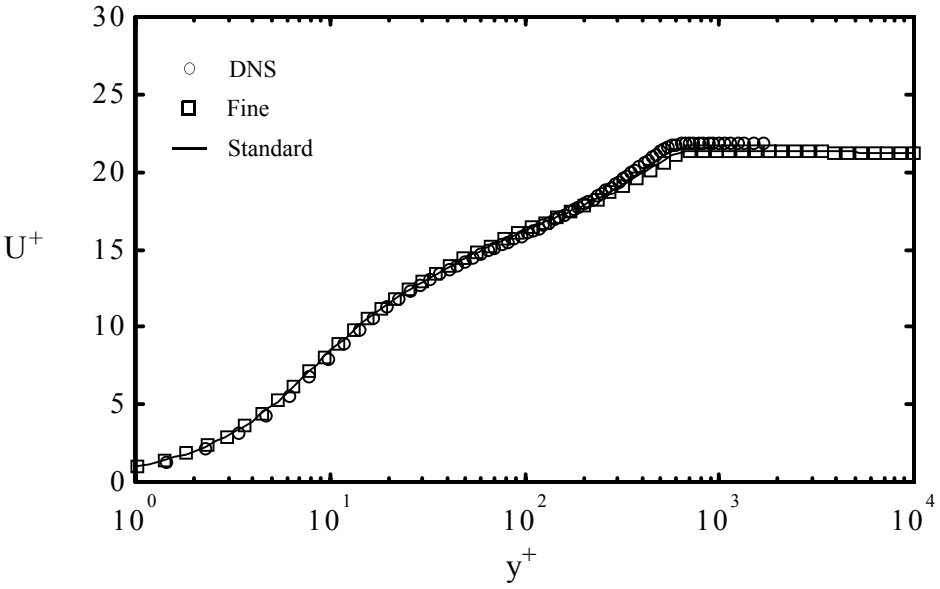

Figure A.14: Predicted *U* near the wall for the boundary layer for the standard and fine grids.

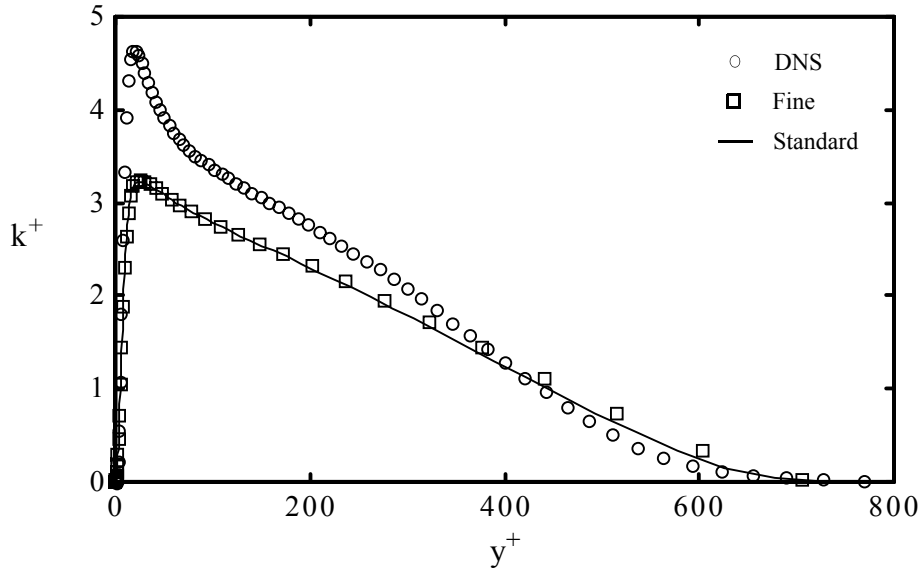

Figure A.15: Predicted *k* for the boundary layer for the standard and fine grids.

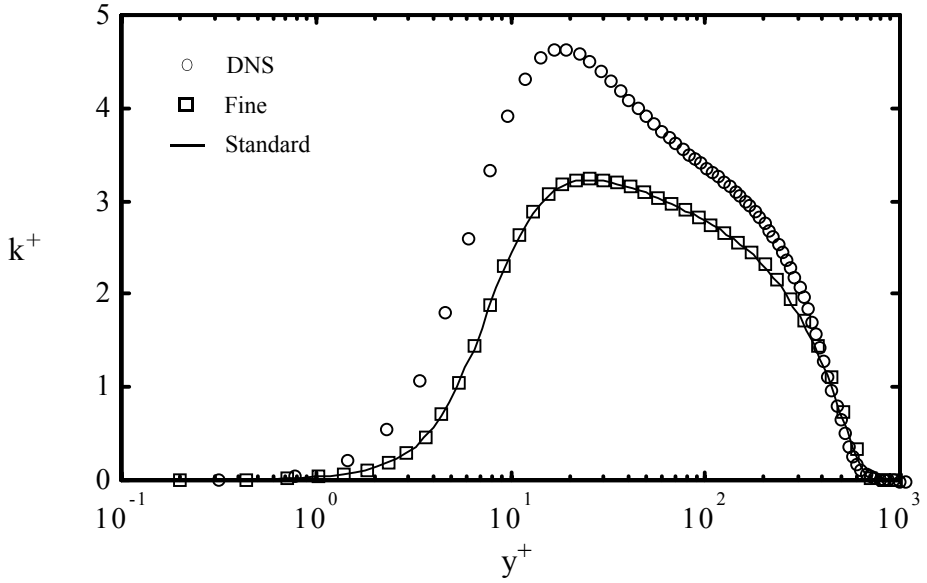

Figure A.16: Predicted *k* near the wall for the boundary layer for the standard and fine grids.

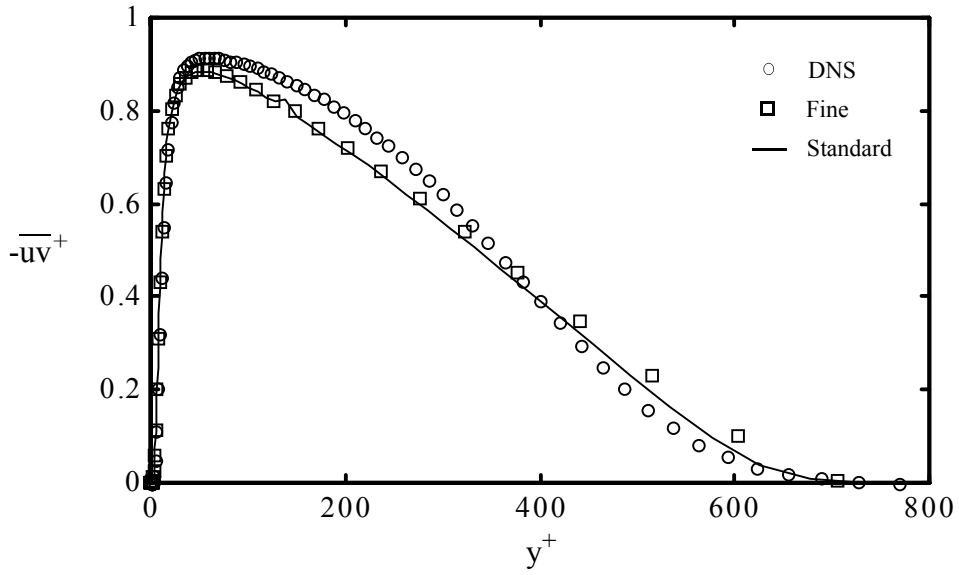

Figure A.17: Predicted -$\overline{uv}$ for the boundary layer for the standard and fine grids.

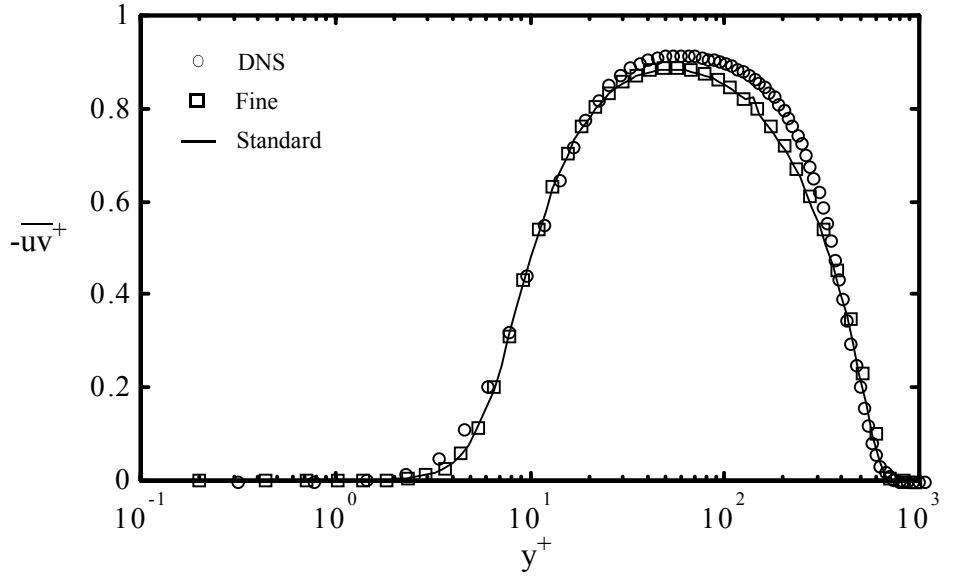

Figure A.18: Predicted -$\overline{uv}$near the wall for the boundary layer for the standard and fine grids.

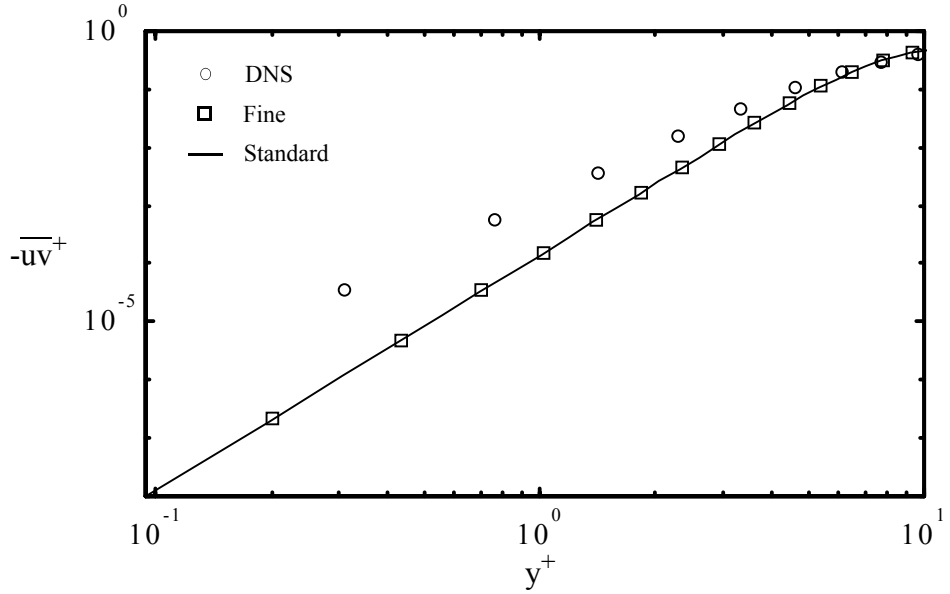

Figure A.19: Predicted -$\overline{uv}$ closest to the wall for the boundary layer for the standard and fine grids.

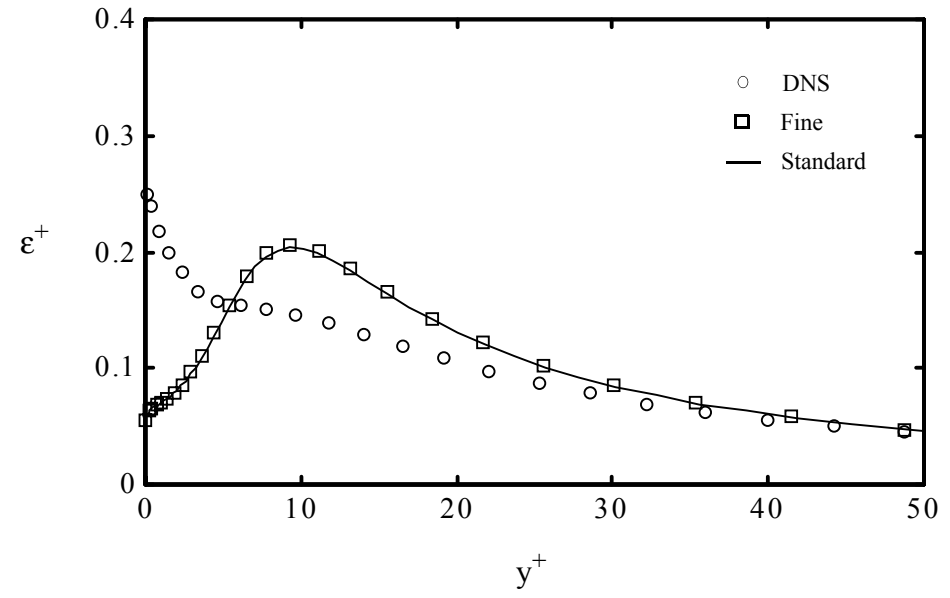

Figure A.20: Predicted ε for the boundary layer for the standard and fine grids.

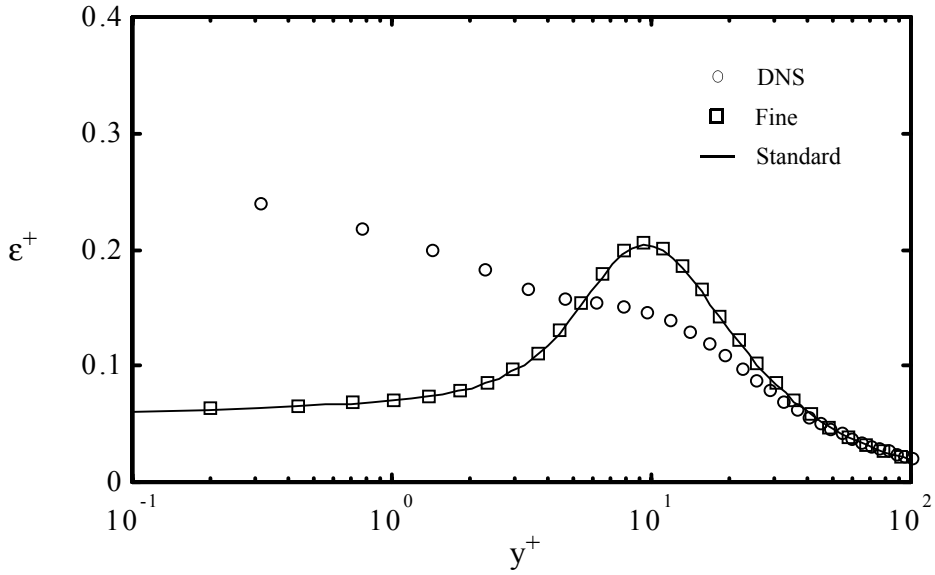

Figure A.21: Predicted ε near the wall for the boundary layer for the standard and fine grids.

Figures A.22, A.23, and A.24 show the predicted *U*, *k, and* $-\overline{uv}$ for the wavy-wall channel using NR scaled by 1/5, 4, and 8 respectively. The boundary conditions and geometry for the wavy-wall flow are described in Chapter 4. It is clear from the figures that the solution in each case is effectively unchanged by the doubling of the number of grid points indicating that standard grid is sufficiently fine to resolve the flow.

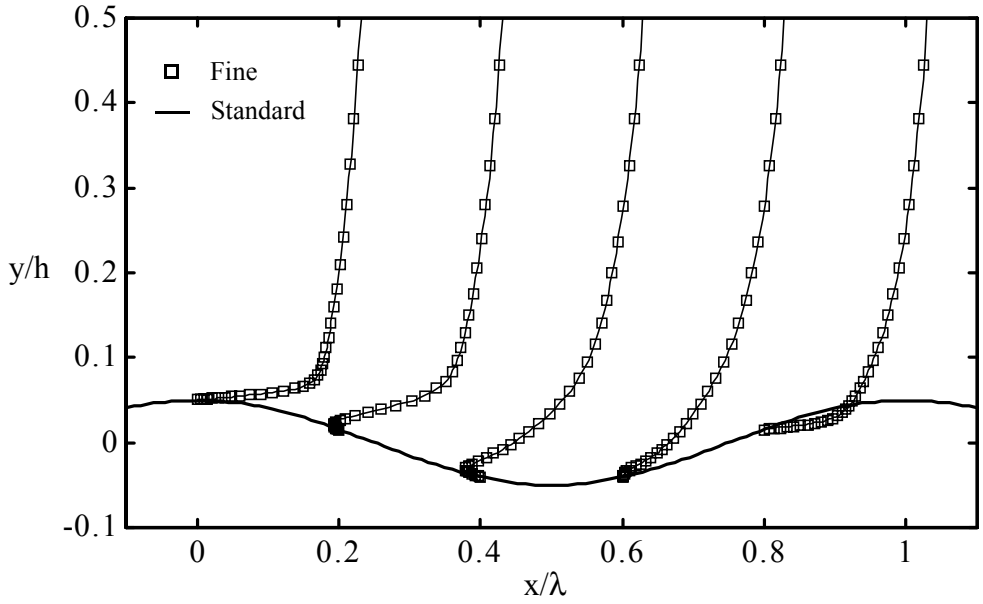

Figure A.22: Predicted *U* for the wavy-wall channel for the standard and fine grids.

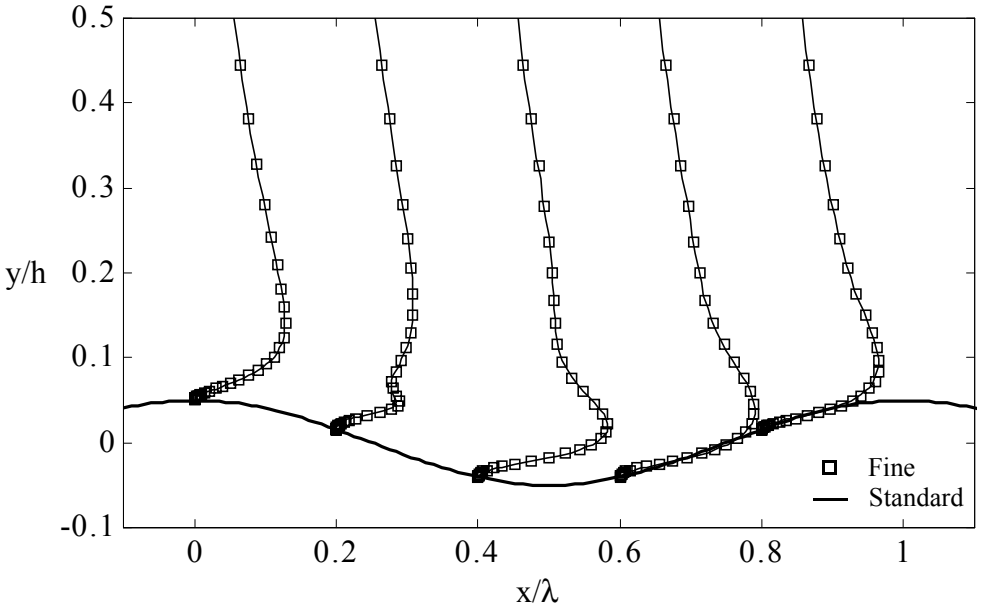

Figure A.23: Predicted *k* for the wavy-wall channel for the standard and fine grids.

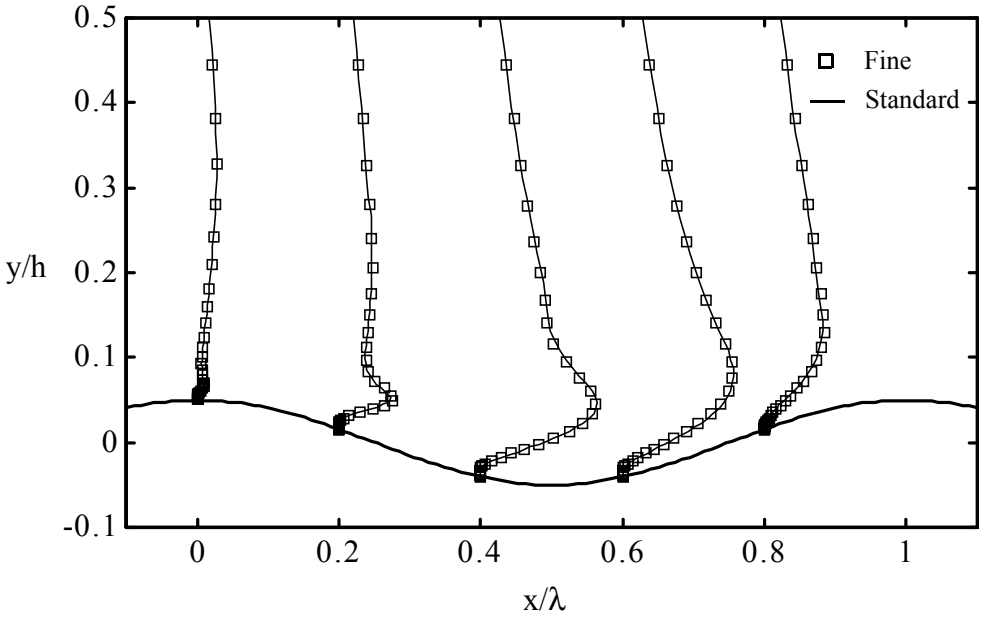

Figure A.24: Predicted $-\overline{uv}$ for the wavy-wall channel for the standard and fine grids.

Figures A.25 and A.26 below show the skin friction coefficient for one-equation near-wall models NR and two-equation near-wall model YS for the standard and fine grids. Clearly, the predictions are insensitive to the doubling of the grid points indicating that the standard grid is sufficiently fine to resolve the flow.

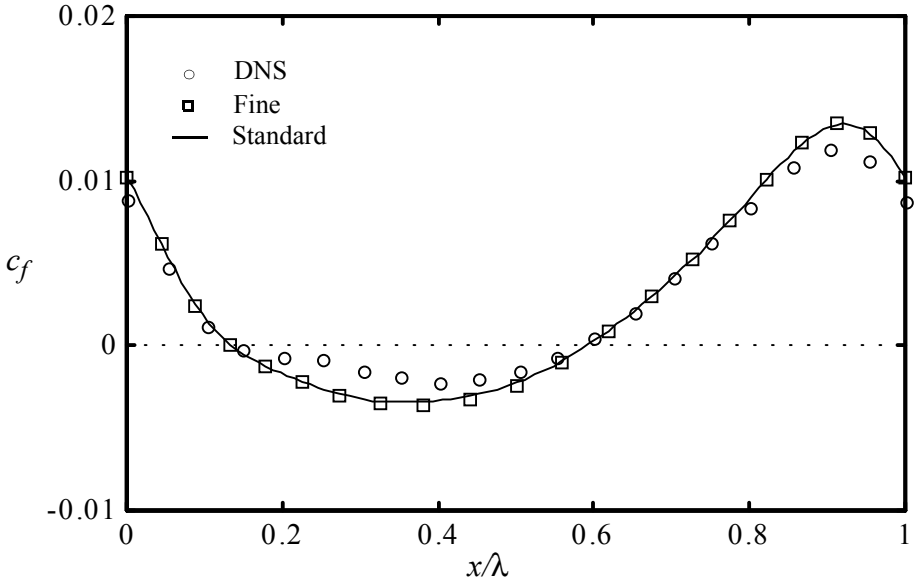

Figure A.25: Predicted c_f at the wavy-wall for one-equation near-wall model NR for the standard and fine grids.

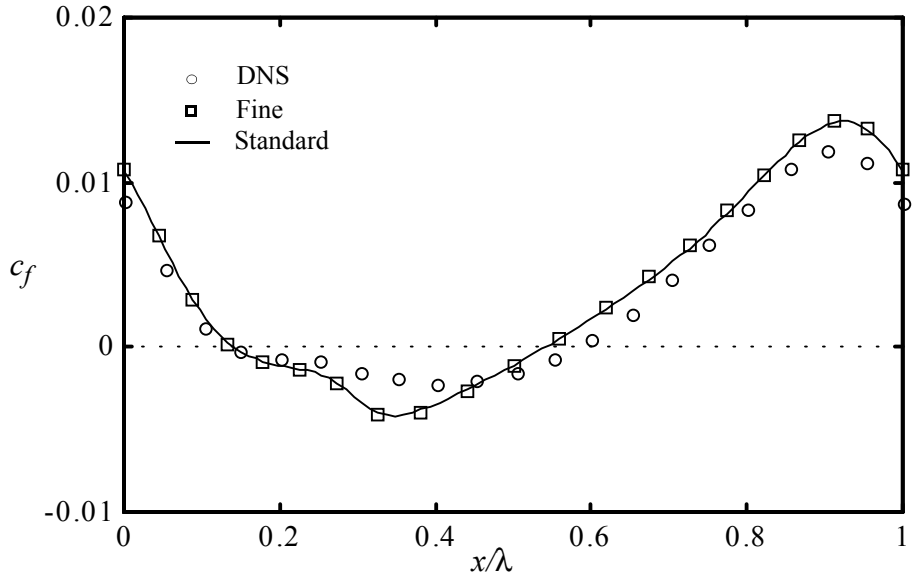

Figure A.26: Predicted c_f at the wavy-wall for two-equation near-wall model YS for the standard and fine grids.

Projection Method

The projection method solves the momentum equations without the pressure gradient term for a pseudo-velocity, solves a Poisson equation for the pressure derived by enforcing the divergence free constraint, and satisfies the continuity equation by projecting the velocity onto the space of divergence free vectors [12, 27]. The resulting flow satisfies both the momentum equations and the continuity equation. The projection method is known by other names including the fractional step method and the pressure correction method. A recent and comprehensive discussion of the projection method can be found in reference 42.

To clearly demonstrate the procedure implemented by the projection method utilized in this work, the formulas are presented as they apply to a uniform orthogonal structured grid within the framework of the finite difference method. The Navier-Stokes equations, normalized appropriately, are

$$U_{,\mathrm{t}} + (U \cdot \nabla)U = -\nabla P + \frac{1}{Re}\nabla^2 U + S \quad . \tag{A.9}$$

These are solved without the pressure gradient term for a pseudo-velocity. Using vector notation, a first-order-in-time method can be written as

$$U^* = U - \Delta t(U \cdot \nabla)U + \Delta t\frac{1}{Re}\nabla^2 U + \Delta t S \quad , \tag{A.10}$$

where S is a source term containing terms such as those arising from the Reynolds stresses. All terms on the right-hand side are at time level k and all variables are normalized appropriately. Figure A.27 shows a typical cell for the finite difference method for two-dimensional and three-dimensional computations. The example flow shown in Figure A.27 is the classic lid-driven cavity commonly used to validate

computational codes [41, 43, 44, 47].

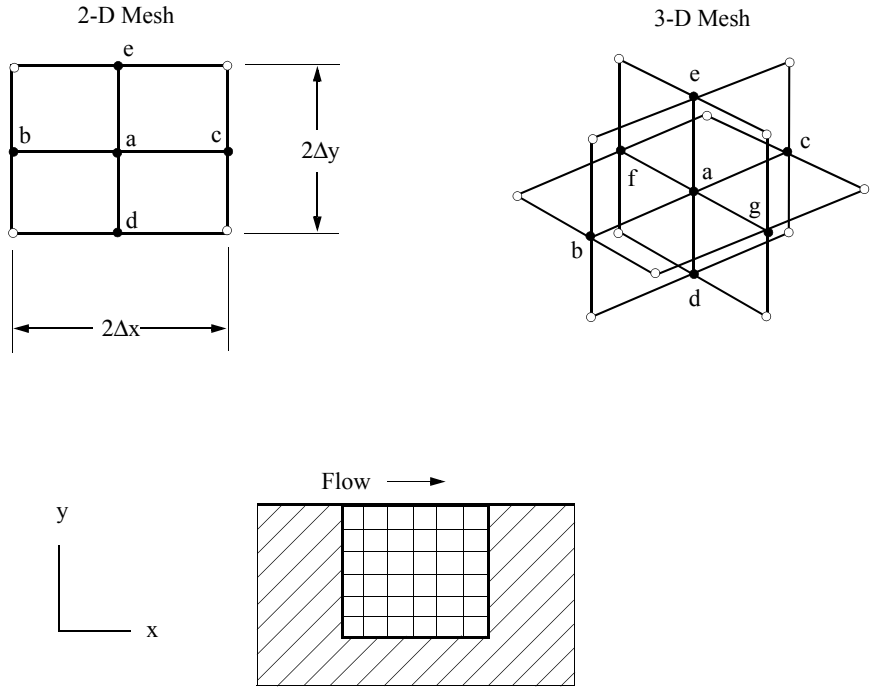

Figure A.27: Discretization of the domain for computations of flow in the lid-driven cavity for the finite difference technique.

A finite differencing of equation (A.10) for u on a three-dimensional orthogonal uniform grid leads to the second-order-accurate-in-space expression

$$u_a^* = u_a + \Delta t\left[-u_a\frac{u_c-u_b}{2\Delta x}-v_a\frac{u_e-u_d}{2\Delta y}-w_a\frac{u_g-u_f}{2\Delta z}\right]+\Delta t D_x+\Delta t s_x, \tag{A.11}$$

where

$$D_x = \frac{1}{Re}\left[\frac{u_b-2u_a+u_c}{\Delta x^2}+\frac{u_d-2u_a+u_e}{\Delta y^2}+\frac{u_g-2u_a+u_f}{\Delta z^2}\right]. \tag{A.12}$$

Quantity Δt is the time step and s_x is a source term described later. The letter subscripts

on u denote different points in space and all terms on the right hand side are at time level k. Equation (A.11) can be written compactly as

$$u_a^* = u_a + \Delta t[c_0 u_a + c_1 u_b + c_2 u_c + c_3 u_d + c_4 u_e + c_5 u_f + c_6 u_g + s_x] \quad . \tag{A.13}$$

For a two-dimensional computation, $c_1 = a_1[1 - P_x/2]/Re$, $c_2 = a_2[1 + P_x/2]/Re$, $c_3 = a_3[1 - P_y/2]/Re$, $c_4 = a_4[1 + P_y/2]/Re$, $c_0 = a_0/Re$ and $c_5 = c_6 = 0$. P is the Peclet number given by $P_x = Re\Delta x u_a$ and $P_y = Re\Delta y u_a$. The number subscripts on the coefficients denote different arrays in contrast to the letter subscripts on u that denote different points in space. For a uniform grid, the coefficients a_1, a_2, a_3, and a_4 are simply $a_1 = a_2 = 1/\Delta x^2$, $a_3 = a_4 = 1/\Delta y^2$, and $a_0 = -2/[\Delta x^2 + \Delta y^2]$. The last coefficient can also be expressed as the negative sum of the first through fourth coefficients. The source term contains additional terms such as the Reynolds stresses. For example, for a two-dimensional computation, $s_x = -(\overline{uu})_{,x} - (\overline{uv})_{,y}$. Substitution of the eddy viscosity relation gives

$$s_x = -\frac{2}{3}k_{,x} + 2\nu_t u_{,xx} + 2\nu_{t,x} u_{,x} + \nu_t(u_{,yy} + v_{,xy}) + \nu_{t,y}(u_{,y} + v_{,x}) \,. \tag{A.14}$$

Some terms in equation (A.14) vanish due to incompressibility while others, resulting from the differencing of equation (A.14), could be included in the coefficients. The time step is subject to the usual constraints for explicit methods [43, 64].

A formulation in terms of coefficients is useful since it allows the code to be easily adapted to use other discretization schemes such as finite volume, exponential convection, and hybrid methods [22, 109, 150]. The formulation above provides coefficients for the most basic finite difference method. The central-differencing of the

convective terms have often been associated with instability arising when computing high Reynolds number flows [151].

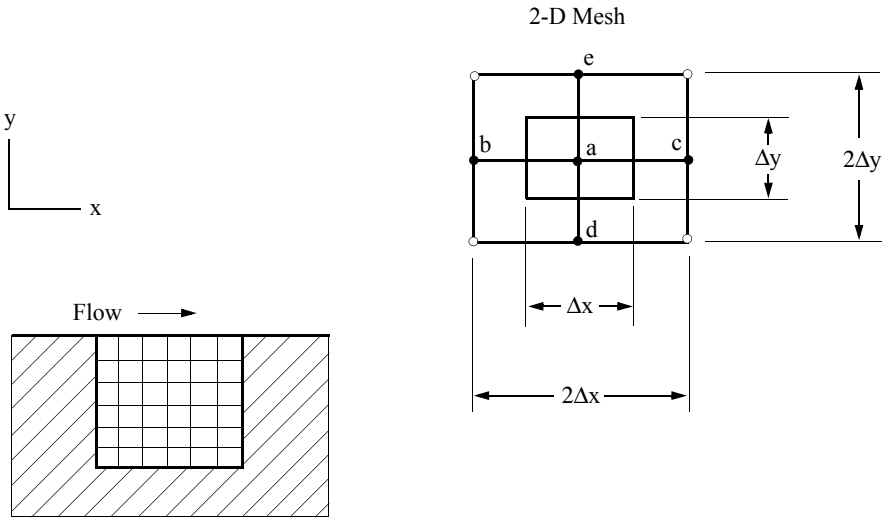

Figure A.28: Discretization of the domain for computations of flow in the lid-driven cavity for the finite volume technique.

The hybrid scheme approximates the exponential convection scheme [109] and circumvents the instability attributed to central-differencing of the convection terms by switching to an up-wind scheme when the Peclet number exceeds the value two. The discretization of the domain for the finite volume technique is shown in Figure A.28. The finite volume method using a hybrid scheme for a two-dimensional computation can be written compactly as $c_1 = a_1[f(|P_b|) + max[0, -P_b]]/Re$, $c_2 = a_2[f(|P_c|) + max[0, P_c]]/Re$, $c_3 = a_3[f(|P_d|) + max[0, -P_d]]/Re$, and $c_4 = a_4[f(|P_e|) + max[0, P_e]]/Re$, where

$$f(P_i) = max\left[e, \left[1 - s\frac{|P_i|}{2}\right]\right]. \tag{A.15}$$

The Peclet number in equation (A.) is subscripted to denote that it is a function of some average *u,* such as 0.5*(u_a+u_b), representing convection into a finite volume centered about point *a* shown in Figure A.28. Similarly, the Peclet number in equation (A.) would be a function of 0.5*(u_a+u_c). Coefficient c_o is the sum of the other coefficients. The coefficients given above can be derived following the discussion provided in reference 109.

The resulting field of u^* given by equation (A.13) is viewed as a pseudo-velocity since it does not necessarily satisfy the continuity equation. To recover the Navier-Stokes equations from equation (A.10), the pseudo-velocity must be related to the velocity through

$$U^* = U^{k+1} + \Delta t \nabla p. \tag{A.16}$$

Since the incompressible flow is divergence free, application of the divergence operator to the relation above gives a Poisson equation for the pressure

$$\nabla^2 p = \frac{1}{\Delta t} \nabla \cdot U^*. \tag{A.17}$$

This can be written in discrete form for a two-dimensional computation as

$$a_0 p_a + a_1 p_b + a_2 p_c + a_3 p_d + a_4 p_e = D. \tag{A.18}$$

The coefficients are as given above. The coefficient a_0 can also be written as the negative sum of the other coefficients. The source term *D* represents the right hand side of equation (A.17). The pseudo-velocity along the boundary, required to solve equation (A.17), is obtained at each time step by solving the discrete form of equation (A.16)

along the boundaries. Pressure along the boundaries is obtained from either a specified pressure gradient or from the Navier-Stokes equations directly. The former is used for pressure driven flows such as the plane channel and the latter is used for external flows such as the boundary layer. Once the pressure has been obtained throughout the flowfield by solving the Poisson equation, the velocity is determined by

$$U^{k+1} = U^{*} - \Delta t \nabla p , \tag{A.19}$$

giving a velocity field that is divergence free to satisfy the continuity equation.

The terms in equation (A.14) are given by the turbulence transport equations and the eddy viscosity model. The transport equation for k for a two-dimensional computation is

$$k_{,\mathrm{t}} + uk_{,\mathrm{x}} + vk_{,\mathrm{y}} = D_k + T_k + P_k - \varepsilon , \tag{A.20}$$

The definitions of the terms on the right hand side are given in Chapter 2. This, along with the dissipation equation, is solved using simple finite differences.

The method above constitutes the first-order-in-time projection method as utilized in this work. For the computations completed for this work, the equations of motion are solved using either finite differences or the hybrid finite volume scheme adapted for curvilinear coordinates using the grid metric transformations given in reference 64. For curvilinear coordinates, the points indicated by the open symbol in Figure A.2 contribute to equation (A.13) in addition to those points indicated by the solid symbol. The stability and rate of convergence of the computation can be enhanced by moving the first term in brackets in equation (A.13) to the left hand side as done in reference 109. This requires modification of equation (A.17). A fully implicit method can also be formulated [76]. A discussion of the numerical accuracy of various formulations can be found in reference

42.

The resolution of the laminar flow in a lid-driven cavity at high Reynolds numbers is considered to be among the most challenging tests for code validation [43, 44, 131]. The geometry consists of a square cavity with boundary conditions of zero velocity on the three walls and a unit horizontal velocity on the upper boundary called the lid. The corresponding experiment would consist of a cavity of effectively infinite dimension in the spanwise direction providing a two-dimensional flow at sufficiently low Reynolds numbers. The flow in the experiment would naturally transition to turbulence at sufficiently high Reynolds numbers.

The solution is typically steady at Reynolds numbers, based on unit depth and height, below seven thousand [43]. At a Reynolds number of ten thousand, the ability to obtain a steady solution may depend on the characteristics of the numerical scheme. This flow is the most common test case used to study the characteristics of computational codes and numerical algorithms [43]. The lid-driven cavity flow tests the capability of the code to resolve flows that are highly skewed with respect to the mesh. Furthermore, since the solution depends highly upon the Reynolds number of the flow, this case indicates whether the numerical scheme suffers from excessive numerical diffusion.

The flow in the lid-driven cavity is computed using the first-order-in-time projection method formulated using the hybrid scheme described above. The computation is completed with a uniform grid having 127 node points in each direction. The streamlines are indicated by contours of the streamfunction ϕ given by the solution of $\nabla^2\phi = \omega$, where ω is the vorticity. The streamfunction is set to a constant along the boundaries since the boundaries form a streamline of the flow. The streamline patterns

for Re=10^3 and velocity along the centerline are shown in Figure A.30. The solution is validated using a stream-function vorticity code with 255 grid points.

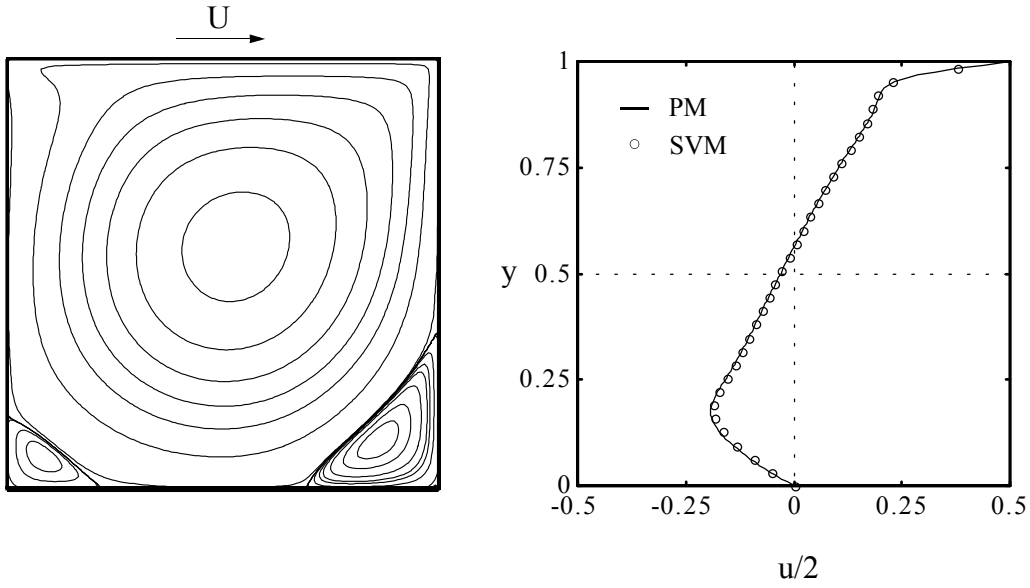

Figure A.29: Streamlines for the lid-driven cavity at a Re=10^3 on the left and *U* along the vertical centerline on the right.

The computation is then completed for Re=10^4 with a uniform grid having 255 node points in each direction and a nonuniform grid having 255 node points and a wall spacing of 20/*Re*. The wall spacing for the nonuniform grid is therefore about one half of that for the uniform grid. The streamfunction is set to a constant along the boundaries since the boundaries form a streamline of the flow. The streamline patterns for Re=10^4 are shown in Figure A.30.

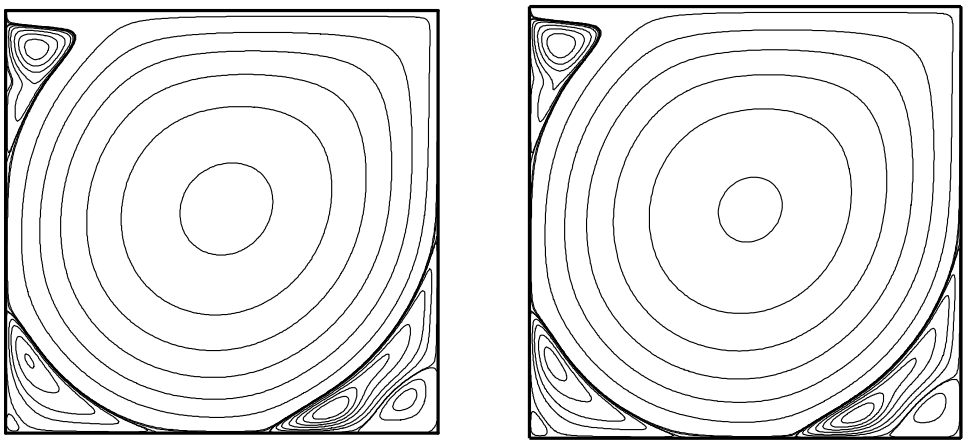

Figure A.30: Streamlines for the lid-driven cavity computed using a uniform grid on the left and nonuniform on the right.

The kinetic energy of the flow increases with time and serves as an indicator of convergence. The kinetic energy is within a few percent of the final value in each case presented above. The streamlines compare well with the frequently referenced classic solution [47] as well as more recent results [41, 43].

It has been stated that a steady solution may not exist at or above a Reynolds number of $1x10^4$ [43]. Many solutions in the open literature appear to have been obtained with a steady-state formulation in which the time derivative appearing in the Navier-Stokes equations has been effectively removed from the computation. The solution computed here using the first-order-in-time projection method exhibits a slight unsteady nature and small variations in the size and form of the vortices can be seen as the computation proceeds. The streamlines shown in the figures correspond to the time-averaged flow.

The computations presented here verifiy that the projection method formulated above resolves the flow for the lid-driven cavity using both a uniform and nonuniform grid. The computations indicates that the projection method can resolve flows that are highly skewed with respect to the computational grid. The computation using the nonuniform grid indicates that the code implements the grid metric transformations correctly. Validation of the projection method code for turbulent flows using several common benchmark flows is described in detail in Chapter 3.

Surveys of projection methods can be found in references 52 and 113. Recent applications of similar methods formulated within the framework of the finite volume technique include the computations of unsteady transitional flow over oscillating airfoils [78] and the simulations of vortex shedding past triangular cylinders [74]. Both applications utilize one of the many existing variations of the k-ε turbulence model to close the RANS equations.

REFERENCES

1. Abid, R., Rumsey, C., Gatski, T., 'Prediction of Nonequilibrium Turbulent Flows with Explicit Algebraic Stress Models', AIAA Journal, Vol. 33, No. 11, 1995

2. Abrams, J., Hanratty, T. J., 'Relaxation effects observed for turbulent flow over a wavy surface', J. Fluid Mech., Vol. 151, 443-455, 1981(1986)

3. Adams, E. W., and Johnston, J. P., 'Flow Structures in the Near-Wall Zone of a Turbulent Separated Flow', AIAA J., Vol.26, No. 8, 932-939, 1988

4. Alexopoupos, G. A., Hassan, H. A., '*k*-Enstophy Compressible Turbulence Model for Mixing Layers and Wall Bounded Flows', AIAA J., Vol. 35, No. 7.

5. Anderson, J. D., 'Fundamentals of Aerodynamics', McGraw-Hill, 2001

6. Armaly, B. F., Durst, F., Pereira, C. F., J. of Fluid Mechanics, Vol. 127, p. 473, 1983

7. Avelino, M. R., Su, J., Freire, A. P., 'An analytical near wall solution for the k-e model for transpired boundary layer flows', Int. J. of Heat and Mass Transfer, Vol. 42, pp. 3085-3096, 1999

8. Baldwin, B. S., Barth, T. J., 'A One-Equation Turbulence Model for High Reynolds Number Wall-Bounded Flows', AIAA Paper 91-0610, 1991

9. Baldwin, B.S., Lomax, H., 'Thin layer Approximation and Algebraic Model for Separated Turbulent Flows', AIAA Paper 78-0257, 1976

10. Bardina, J. E., Huang, P. G., Coakley, T. J., 'Turbulence Modeling Validation, Testing, and Development', NASA Tech. Memorandum 110446, 1997

11. Barlow, J. B., 'Low-Speed Wind Tunnel Testing', Wiley, 1999

12. Bell, J., Colella, P., Glaz, H., 'A Second-Order Projection Method for the Incompresible Navier-Stokes Equations', J. of Fluid Mechnanics, Vol. 85, 1989

13. Bell, J. B., Solomon, J., M., Szymczak, W. G., 'Projection Method for Viscous Incompressible Flow on Quadrilateral Grids', AIAA Journal, Vol. 32, No. 10, 1994

14. Blasius, H., 'Grenzschichten in Flussikeiten mit kleiner Reibung', Z. Angew. Math. Phys., Vol. 56, pp. 1-37, (NACA TM 1256), 1908

15. Bolot, R., Imbert, M., Coddet, C., 'On the use of a low-Reynolds extension to the Chen-Kim *k*-ε model to predict thermal exchanges in the case of an impinging plasma', Int. J. of Heat and Mass Transfer, Vol 44, 1095-1106, 2001

16. Borg, A., Perzon, S., Roditcheva, O., 'On the Influence of the Near Wall Formulation of Turbulence Models for Prediction of Aerodynamic Coefficients for Ground Vehicles', SAE Conf., 2003-01-1317, 337-343, 2003

17. Boussinesq, J., 'Theorie de l'ecoulement tourbillant', Memoires Presentes par Divers Savants Sciences Mathematique at Physiques, Acad. Sciences, Vol. 23, 1877

18. Bradshaw, P., Ferris, D. H., Atwell, N. P., 'Calculation of boundary layer development using the turbulent energy equation', J. Fluid Mech., 159:105, 1967

19. Buckles, J., Hanratty, T. J., Adrian, R. J., 'Turbulent Flow over Large Amplitude Wavy Surfaces', J. Fluid Mechanics, Vol. 140, pp. 27-44, 1984

20. Buning, P. G., Jesperson, D. C., Pulliam, T. H., Chan, W. M., Slotnick, J. P., Krist, S. E., Renze, K., J., 'Overflow User's Manual', NASA Langley, Version 1.7v, 1997

21. Cebeci, T., Smith, A. M. O., 'Analysis of Turbulent Boundary Layers', Academic Press, N.Y., 1974

22. Chen, C. J., ’Fundamentals of Turbulence Modeling’, Taylor and Francis, 1997

23. Chen, H. C., ’ ’, Int. J. Heat Mass Transfer, 43, 1603-1616, 2000

24. Chen, H.C., and Patel, V.C., ‘Near-wall Turbulence Models for Complex Flows Including Separation', AIAA Journal 26, No. 4, pp.641-648, 1988

25. Cherukat, P., Na, Y., Hanratty, T. J., McGlaughlin, J. B., ’Direct Numerical Simulation of a Fully Developed Turbulent Flow over a Wavy Wall’, Theoretical and Computational Fluid Dynamics, Vol. 11, pp. 109-134, 1998

26. Chien, K., ’Predictions of Channel and Boundary-Layer Flows with a Low-Reynolds-Number Turbulence Model’, Vol. 20, No. 1, 1982

27. Chorin, A. J., ’Numerical solution of imcompressible flow problems’, Studies in Numerical Analysis, 2, 64-71, 1968

28. Chorin, A. J., ’Numerical solution of the Navier-Stokes equations’, Math. Comp., 22, 742-762, 1968

29. Chou, P. Y., ’On velocity correlations and the solution of the equations of turbulent fluctuation’, Quart. Appl. Math., 3, 38-54, 1945

30. Coles, D. E., Hirst, E. A., ’Computation of Turbulent Boundary Layers - 1968 AFOSRIFP Stanford Conference", Proc. 1968 Conf., Vol. 2, 1968

31. Computational Dynamics Limited, ’Star-CD version 3.05’, 1998

32. Comte-Bellot, G., Corrsin, S., ’The use of contraction to improve grid generated turbulence’, J.. fo Fluid Mech., 25, 657-682, 1966

33. Daly, B. J., Harlow, F. H., ’Transport eqns in turbulence,’, Phys. Fluids, 13, 1970

34. Davidson, L, Rizzi, A., 'Navier-Stokes Predictions Using an Algebraic Reynolds-Stress Model', J. of Spacecraft and Rockets, Vol. 29, No. 6, 1992

35. Davidson, L., 'Prediction of the Flow Around an Airfoil Using a Reynolds Stress Transport Model', ASME, Vol. 117, 1995

36. De Angelis, V., Lombardi, P., Banerjee, S., ’Direct numerical simulation of turbulent flow over a wavy wall’, Phys. Fluids, 9, 8, 2429-2442

37. Deardoff, J. W., ’3-D numerical study of the height and mean structure of a heated planetary boundary layer’, Boundary-Layer Meteorol., 7, 81-106, 1974

38. Díaz, R. H., Barlow, J. B, ’More Realistic Simulations Explain Aerodynamics of Experimental Aircraft’, Featured Article, NPACI Envision, Vol. 14, No. 3, 1998

39. Durbin, P. A., ’Near-wall Turbulence Closure Modeling Without Damping Functions’, Theoretical and Computational Fluid Dynamics, Vol. 3, No. 1, 1-13, 1991

40. Durbin, P. A., Medic, G., Seo, J. M., Eaton, J. K., Song, S., ’Rough Wall Modification of Two-Layer k-ε’, J. of Fluids Engineering, Vol. 123, 16-21, 2001

41. E. W., Liu, J-G., ’Finite Difference Schemes for Incompressible Flows in the Velocity-Impulse Density Formulation’, J. of Computational Physics, Vol. 130, 67-76, 1997

42. E. W., Liu, J-G., ’Projection Method I: Convergence and Numerical Boundary Layers’, SIAM J. on Numerical Analysis, Vol. 32, Issue 4, 1017-1057, 1995

43. E., W., Liu, J-G., ’Vorticity Boundary Condition and Related Issues for Finite Difference Schemes’, Journal of Computational Physics, Vol. 124, 1996

44. Fletcher, C., ’Computational Techniques for Fluid Dynamics’, Springer, 1991

45. Frederick. K. A., Hanratty, T. J., ’Velocity Measurements for a Turbulent Nonseparated Flow over Solid Waves’, Exp. in Fluids, Vol. 6, pp. 477-486, 1988

46. Gharib, M.,'Perspective: The Experimentalist and the Problem of Turbulence in the Age of Supercomputers', Journal of Fluids Engineering, Vol. 118, 233-241, 1996

47. Goda, K., '', J. Comp. Phys., Vol. 30, pp. 76-95, 1979

48. Goldberg, U. C., 'Derivation and Testing of a One-Equation Model Based on Two Time Scales, AIAA Journal, Vol. 29, No. 8, pp. 1337- 1338, 1991

49. Goldberg, U. , Aspley, D., 'A wall-distance-free low Re k-e turbulence model', Computer Methods in Mechanics and Engineering', Vol. 145, 227-238, 1997

50. Goldstein, R. J., Erickson, V. L., Olson, V. L., Eckert, E. R. G., 'J. of Basic Engineering', Vol. 92, 731-741, 1970

51. Gorski, J. J., Govindan, T. R., Lakshminarayana, B., 'Computation of Three-Dimensional Turbulent Shear Flows in Corners', AIAA Journal, Vol 21, No. 5, pp. 685-692, 1985

52. Gresho, P. M., 'On the theory of semi-implicit projection methods for viscous incompressible flow and its implementation via a finite element method that also introduce a nearly consistent mass matrix', Int. J. Numerical Methods Fluids, 11:587, 1990

53. Hankey, W., Calarese, W., 'Reynolds Stresses for Unsteady Turbulent Flows', AIAA Journal, Vol. 21, No. 1, 1983

54. Hanjalic, K., 'Advanced turbulence closure models: a view of current status and future prospects', Int. J. of Fluid Flow, Vol. 15, No. 3, pp. 178-203, 1994

55. Hanjalic, K., Launder, B. E., 'A Reynolds-stress model of turbulence and its application to thin shear flows', J. Fluid Mech., 52, 609-638, 1972

56. Harlow, F. H., Welch, J. E., 'Numerical Calculation of Time-Dependent Viscous Incompressible Flow with Free Surface', Phys. Fluids, Vol. 8, pp. 2182-2189, 1965

57. Hassid, S., Poreh, M., ‘A Turbulent Energy Dissipation Model for Flows with Drag Reduction', J. Fluids Eng., Vol. 100, No. 1, pp. 107112, 1978

58. Haworth, D. C., Jansen, K., ’Large-eddy simulation on unstructured deforming meshes: toward reciprocating IC engines’, Computers and Fluids 29, 493-524, 2000

59. Head, M. R., Bandyopadhyay, P., ’New aspects of turbulent boundary layer structure’, J. Fluid Mechanics, 107, 297-338

60. Henn, D. S., and Sykes, R. I., ’Large-eddy simulation of flow over wavy surfaces’, J. of Fluid Mechanics, Vol. 383, 1999

61. Henshaw, W., ’A Fourth-Order Accurate Method for the Incompressible Navier-Stokes Equations on Overlapping Grids’, J. of Comp. Physics, Vol. 113, 1994

62. Hinze, J. O., ’Turbulence’, McGraw-Hill, 1975

63. Hirsch, C., ’Numerical Computation of Internal and External Flows’, Wiley, 1988

64. Hoffmann, K., ’Computational Fluid Dynamics for Engineers’, Engineering Education System, Austin, Texas, 1989

65. Hsieh, W. D., Chang K. C., ’Two-Layer Approach Combining Reynolds Stress and Low-Re k-*e* Models’, AIAA Journal, Vol. 37, No. 3, 1999

66. Huang, P. G., Bradshaw, P., ’Law of the wall for Turbulent Flows in Pressure Gradients’, AIAA J., Vol. 33, pp. 624-632, No. 6, 1995

67. Hudson, J., Dykhno, L., Hanratty, T., ’Turbulence production in flow over a wavy wall’, Experiments in Fluids, Vol. 20, 257-265, 1996.

68. Hwang, C. B., Lin C. A., ’Improved low-Re number k-e Model Based on DNS Data’, AIAA Journal, Vol. 36, No. 1, 1998

69. Iacovides, H., Launder, B. E., ’The numerical simulation of flow and heat transfer

in tubes in orthogonal rotation', Proceedings of the 6th Symposium on Turbulent Shear Flows', Toulouse, France, 1990

70. Kawamura, H., Abe, H., Shingai, K., 'DNS of turbulence and heat transport in a channel flow with different Reynolds numbers and Prandtl numbers and boundary conditions', 3rd Int. Symp. on Turbulence, Heat, and Mass Transfer, 15-32, 2000

71. Kwak, INS2D Users Manual', NASA Ames Research Center

72. Jaw, S. Y., Chen, C. J., 'Development of turbulence model including fractal and Kolmogorov scale', Symp. on Advances and Applications in Computational Fluid Dynamics, ASME, November 25-30, 1990

73. Jiménez, J., 'A Selection of Test Cases for the Validation of LES of Turbulent Flows', AGARD-AR-345, 1998

74. Johansson, S., Davidson, L., Olsson, E., 'Numerical simulation of vortex shedding past triangular cylinders at high Reynolds number using a k-e turbulence model', Int. J. for Numerical Methods in Fluids, Vol. 16, 859-878, 1993

75. Jones, W.P., and Launder, B.E., 'The Prediction of Laminarisation with a Two-Equation Model of Turbulence', Int. J. of Heat Trans., 15, pp.301-314, 1972

76. Kim, J., Moin, P., 'Applicaiton of a Fractional-Step Method to Incompressible Navier-Stokes Equations', J. of Computational Physics, Vol. 59, pp. 308-323, 1985

77. Kim, J., Moin, P., Moser, R., 'Turbulence statistics in a fully developed channel flow', J. Fluid Mechanics, Vol. 177, 1987

78. Kim, S. W., Zaman, K. B., Panda, J., 'Calculation of unsteady transitional flow over oscillating airfoil', Separated Flows, ASME, Vol. 149, 1993

79. Klebanhoff, P. S., ' Characteristics of turbulence in a boundary layer with zero pressure gradient', NACA TN 3178, 1954

80. Kolmogorov, A. N., ’The local structure of turbulence in incompressible viscous fluid at very large Reynolds numbers’, C. R. Acad. Sci. 30:301, 1941

81. Kuffer, J., Muller, B., Fannelop, T., 'Implicit Solution Method for Incompressible N-S Equations Including Two-Layer k-t Turbulence Model', AIAA J., 34, 12, 1996

82. Kumarasamy, S., Barlow, J., ’Computation of unsteady over a half-cylinder close to a moving wall’, J. of Wind Engineering and Industrial Aerodynamics, 69-72, 1997

83. Kuzan, J. D., ’Velocity measurements for turbulent separated and nonseparated flow over solid waves’, Ph.D. thesis, Dept. Chem. Eng., U. of Illinois, Urbana, 1986

84. Lakehal, D., Rodi, W., ’Calculation of the flow past a surface-mounted cube with two-layer turbulence models’, J. of Wind Engineering, Vol. 67-68, 1997

85. Lam, C. K. G., Bremhorst, K., ’A modified for of the k-e model for predicting wall turbulence’, Transactions of the American Soc. of Mech. Eng., 103, 456-460, 1981

86. Launder, B. E., Kato, M., ’The modeling of turbulent flow around stationary and vibrating square cylinders’, Proc. 9th Symp. on Turbulent Shear Flow, Kyoto, 1993

87. Launder, B. E., Reece, G.I., Rodi, W., ’Progress in the development of a Reynolds-stress turbulence closure’, J. of Fluid Mechanics, 68, 537-566, 1975

88. Launder, B. E., Sharma, B. I., ’Application of the energy-disspation model of turbulence to the calculation of glow near a spinning disc’, Letters in Heat and Mass Transfer, 1: 131-138, 1974

89. Launder, B. E., Spalding, D. B., ’Mathematical Models of Turbulence, Academic Press, London, 1972

90. Le, H., Moin, P., ’Direct numerical simulation of turbulent flow over a backward-facing step’ Stanford, Center for Turbulence Research, pp. 161-173, 1992

91. Leipmann, H. W., Roshko, A., 'Elements of Gasdynamics', Wiley, 1957

92. Lien, F., Leschziner, M., 'Assessment of turbulence-transport models including non-linear RNG eddy-viscosity formulation and second-moment closure for flow over a backward-facing step', Computers & Fluids, Vol. 23, No. 8, 1994

93. Lilly, D. K., 'The representation of small-scale turbulence in numerical simulation experiments', Proc. IBM Scientific Computing, 1967

94. Lindberg, P. A., 'Near-wall Turbulence Models for 3D Boundary Layers', Applied Scientific Research, Vol. 53, pp. 139-162, 1994

95. Liu, Z., Kareem, A., Yu, D., 'Nunerical Modelling of Flow Over A Rigid Wavy Surface by LES', J. of Wind Eng. and Ind. Aerodynamics, 46 & 47, 245-254, 1993

96. Luo, J., Lakshminarayana, B., 'Analysis of Streamline Curvature Effects on Wall-Bounded Turbulent Flows', AIAA Journal, Vol. 35, No. 8, pp. 1273-1279, 1997

97. Maass, C., Schumann, U., 'Direct numerical simulation of separated turbulent flow over a wavy boundary', Flow Simulation with Higher Performance Computers, (ed. Hirschel), pp. 227-241, 1996

98. Mansour, N., NASA Ames Research Center, private communiction, 1998

99. Mansour, N., Kim, J., Moin, P., 'Near-Wall k-ε Turbulence Modeling', AIAA Journal, Vol. 27, No. 8, 1988

100. Mansour, N., Moser, R., Kim, J., 'Reynolds number effects in low Reynolds number turbulent channels', in preperation, 1997

101. Mentor, F., 'Two-equation eddy-viscosity turbulence models for engineering applications', AIAA J. 32, 1598-1605, 1994

102. Minion, M. L., 'Two Methods for the study of vortex patch evolution on locally

refined grids', Ph.D. Thesis, Dept. of Mathematics, UC Berkeley, CA, 1994

103. Mohammadi, B., 'Complex turbulent compressible flow computation using a two-layer approach', Int. J. for Numerical Methods in Fluids, Vol. 15, 747-771, 1992

104. Mohammadi, B., 'Fluid Dynamics Computation with NSC2KE - User Guide', Institut National de Recherche en Informatique et en Automatique (INRIA), Release 1.0, May 1994

105. Murakami, S., Mochida, A., 'On turbulent vortex shedding flow past 2D square cylinder predicted by CFD', J. of Wind Engineering and INdustrial Aerodynamics', 54/55, 191-211, 1995

106. NATO AGARD Rep. No. AAR-345, April, 1998

107. Nikuradse, J., 'Stromungsgesetze in rauhen Rohren', Forsh. Arb. Ing.-Wes., No. 361, 1933

108. Norris L., Reynolds, W., 'Turbulent channel flow with a moving wavy boundary', Report No. FM-10, Dept. of Mech. Eng., Stanford University, California, 1975.

109. Patankar, S., 'Numerical Heat Transfer and Fluid Flow', McGraw-Hill, 1980

110. Patel, V. C., Chon, J., Yoon, J., 'Turbulent Flow in a Channel with a Wavy Wall', J. of Fluids Engineering, Vol. 113, pp. 579-586, 1991

111. Patel, V. C., Rodi, W., Scheurer, G., 'Turbulence Models for Near-Wall and Low Reynolds Number Flows: A Review', AIAA Journal, Vol. 23, No. 9, 1986

112. Peng, S., Davidson, L., 'Computation of turbulent bouyant flows in enclosures with low-Reynolds-number k-w', Vol. 20, No. 2, pp. 172-184, 1999

113. Peyret, R., Taylor, T. D., 'Computational Methods for Fluid Flow', Springer, 1983

114. Piquet, J., 'Turbulent Flows', Springer-Verlag, 1999

115. Piomelli, U, Liu, J, ’Large Eddy Simulation of rotating turbulence using localized dynamic model’, Physics of Fluids, Vol. 7, No. 839, 1995

116. Pope, S. B.,’ Turbulent Flows’, Cambridge University Press, 2000

117. Prandtl, L., ’Bericht uber Untersuchungen zur ausgebildeten Turbulenz’, Z. Agnew. Math. Mech. 5:136, 1925

118. Prandtl, L., ’Bermerungen zur Theorie der freien Turbulenz’, Z. Angew. Math. Mech. 5136, 1942

119. Rai, M., Moin, P., ’Direct simulation of turbulent flows using finite-difference schemes’, J. Computational Physics, 96, 15-53, 1991.

120. Rautaheimo, P., Sikonen, T., ’Improved Solid-Boundary Treatment in Low-Reynolds-Number Turbulence Models,’, AIAA Journal, Vol. 39, No. 5, 2001

121. Rodi, W., ’A new algebraic relation for calculating the Reynolds stresses’, Z. Angew. Math. Mech., 56 T219, 1976

122. Rodi, W., ’Experience with Two-Layer Models Combining the k-e Model with a One-Equation Model Near the Wall’, AIAA Paper 91-0216, 29th Aerospace Sciences Meeting, Reno, NV, Jan. 7-10, 1991

123. Rodi, W., 'Comparison of LES and RANS calculations of the flow around bluff bodies', J. Wind Eng. and Industrial Aerodynamics, 67-71, 1997

124. Rodi, W., Mansour, N. N., Michelassi, V., ’One-equation near-wall turbulence modeling with the aid of direct siulation data’, J. Fluids Engineering, 115, 1993

125. Rotta, J., ’Statistical Theory of Inhomogeneous Turbulence, Part I’, Zeitschrift fur Physik, Vol. 129, pp. 257-572, 1951

126. Saffman, P. G., ’A model for inhomogeneous turbulent flow’, Proc. R. Soc. London,

A 317, 417-433

127. Saniei, N., Dini, S., ’Heat Transfer Characteristics in a Wavy-Walled Channel’, J. of Heat Transfer, Vol. 115, pp. 788-789, 1993

128. Sarkar, A., So. B. M., ’A critial evaluation of near-wall two-equation models against direct numerical simulation data’, Int. Journal of Heat and Fluid Flow’, Vol. 18, No. 2, pp. 197-207, 1997

129. Schlichting, H., ’Boundary-Layer Theory’, McGraw-Hill, 1979

130. Sengupta, T. K., Lekoudis, S. G., ’Calculation of Two-Dimesional Turbulent Boundary Layers over Rigid and Moving Wavy Surfaces;, AIAA J., 21, 4, 1985

131. Shankar, P. N., Deshpande, M. D., ’Fluid Mechanics in the Driven Cavity’, Annual Revue of FLuid Mechanics, 32, 93-136, 2000

132. Sigal, A., ’An Experimental Investigation of the Turbulent Boundary Layer over a Wavy Wall, Ph.D. Dissertation, California Institute of Technology, CA, 1971

133. Sinha, S. N., Gupta, A. K., Oberai, N. M., AIAA Journal, Vol. 19, 1527-1530, 1981

134. Smagorinsky, J., ’General circulation esperiments with primative equations: I. The basic equations’, Mon. Weather Rev., 91, 99-164, 1963

135. So, R., Lai, Y., Zhang, H., Hwang, B., 'Second-Order Near-Wall Turbulence Closures: A Review', AIAA J., Vol. 29, No. 11, 1991

136. Spalart, P., ’Direct simulation of a turbulent boundary layer up to Re_theta=1410’, J. of Fluid Mechanics, Vol. 187, 61-98, 1988

137. Spalart, P. R., Allmaras, S. R., ’A One-Equation Turbulence Model for Aerodynamic Flows’, AIAA Paper 92-0439, 1992

138. Speziale, C. G., ’On nonlinear k-l and k-ε models of turbulence’, J. of Fluid

Mechanics, Vol. 178, 459-475, 1987

139. Speziale, C. G., 'Comparison of Explicit and Traditional Algebraic Models of Turbulence', AIAA Journal, Vol. 35, No. 9, 1506-1509, 1997

140. Speziale, C. G., Abid, R., Anderson, E. C., 'Critical Evaluation fof two-equation models for near-wall turbulence', AIAA Journal, Vol. 30, 324-33., 1992

141. Speziale, C. G., Sarkar, S., Gatski, T. B., 'Modelling the pressure-strain correlation of turbulence: an invarient dynamical systems approach', J. Fluid Mech., 227, 245-272, 1991

142. Sorensen, J. N., Nygreen, P. J., 'Unsteady vorticity-streamfunction algorithm for external flows', Computers and Fluids, Vol. 30, 69-87, 2001

143. Tamamidis, P., Assanis, D., N., 'Numerical simulation of turbulent flows in complex geometries using curvature modified k-e models', ASME, Vol. 155, 1993

144. Temam, R., 'Sur l'approximation de la solution des equations de Navier-Stokes par la méthode des fractionnarires II', Arch. Rat. Mech. Analysis, 33, 377-385, 1969

145. Thangam, S., Speziale, C. G., 'Turbulent Flow Past a Backward Facing Step: A Critical Evaluation of Two Equation Models', AIAA Journal, Vol. 30, No. 5, 1992

146. Thom, A., 'Flow Past Circular Cylinders at Low Speeds', Proc. Roy. Soc. london, Vol. 141, pp. 651-669

147. Thorsness, C. B., Morriscoe, P. E., Hanratty, T. J., 'A comparison of Linear Theory and Measurements of the Variation of Shear Stress along a Solid Wave', Chem. Eng. Science, Vol. 33, 579-592, 1978

148. Tsuchiya, M., Murakami, S., Mochida, A., Kondo, K., Ishida, Y., 'Development of a new k-e model for flow and pressure fields around bluff body', J. of Wind Engineering and Industrial Aerodynamics', Vol 67-68, pp. 169-182, 1997

149. Van Driest, E., ‘On turbulent flow near a wall', J. Aero. Science, 23, 1956

150. Versteeg, H. K., Malalasekera, W., ’Introduction to Computational Fluid Dynamics - The Finite Volume Method’, Longman Scientific and Technical, 1995

151. White, F. M., ’Viscous Fluid Flow’, McGraw-Hill, 1991

152. Wilcox, D. C., ’Multiscale model for turbulent flows’, AIAA Journal, Vol. 26, 1988

153. Wilcox, D. C., ’Turbulence Modeling for CFD’, DCW Ind., La Cañada, CA, 1993

154. Wolfshtein, M. ‘The velocity and temperature distribution in one-dimensional flow with turbulence augmentation and pressure gradient', Int. J. Heat Mass Transfer, 12, pp. 301-318, 1969

155. Yakhot, V., Orzag, S. A., ’Renormalization Theory of Turbulence I - Basic Theory’, J. Scientific Computing, 1986

156. Yamamoto, M., ’Investigation of multiple-time-scale Reynolds stress model in homogeneous anisotropic turbulence’, Int. J. of Heat and Mass Flow, 16, 5, 1995

157. Yang, Z., Shih, T., ’New Time Scale Based k-e Model for Near-Wall Turbulence’, AIAA Journal, Vol. 31, No.7, 1993

158. Zhao, Y., Ding, Z. M., ’Computation of shock/boundary-layer interactions in bump channels with transport-type turbulence models’, Computer Methods in Applied Mechanical Engineering, 173, 55-69, 1999

159. Zilker, D. P., Cook, G. W., Hanratty, T. J., Influence of the amplitude of a solid wavy wall on a Turbulent Flow. Part I.’ J. Fluid Mech., Vol. 82, 29-51, 1977

160. Zilker, D., Hanratty, T., ’Influence of the amplitude of a solid wavy wall on a turbulent flow. Part 2. Separated flows’, J. of Fluid Mech., Vol. 90, 257-271, 1979